# Experiment Design for Identification of Structured Linear Systems

**Marcus Gerardus Potters**

.

# EXPERIMENT DESIGN FOR IDENTIFICATION OF STRUCTURED LINEAR SYSTEMS

PROEFSCHRIFT

ter verkrijging van de graad van doctor
aan de Technische Universiteit Delft,
op gezag van de Rector Magnificus prof.ir. K.C.A.M. Luyben,
voorzitter van het College voor Promoties,
in het openbaar te verdedigen op

dinsdag 28 juni 2016, om 12:30 uur

door

**Marcus Gerardus POTTERS**

Master of Science in Mathematics, Universiteit Utrecht
Master of Science in Physics and Climate Science, Universiteit Utrecht
geboren te Wijk bij Duurstede

Dit proefschrift is goedgekeurd door de promotoren:

Prof. dr. ir. P.M.J. Van den Hof en Prof. dr. ir. X. Bombois

Samenstelling promotiecommisie:

| | |
|---|---|
| Rector Magnificus, | voorzitter |
| Prof. dr. ir. P.M.J. Van den Hof, | Technische Universiteit Delft |
| Prof. dr. ir. X. Bombois, | CNRS, France |

Onafhankelijke leden:

| | |
|---|---|
| Prof. dr. ir. R. Pintelon, | Vrije Universiteit Brussel, Belgium |
| Prof. dr. ir. A. Heemink, | Technische Universiteit Delft |
| Prof. dr. ir. R. Babuska, | Technische Universiteit Delft |
| Prof. dr. ir. A.C.P.M. Backx, | Technische Universiteit Eindhoven |
| Dr. Hab. G. Mercère, | Université de Poitiers, France |

Printed in The Netherlands.

*To my brother*

# Acknowledgements

With the completion of this dissertation, the time has come where I may reflect upon the past four years, and thank the many people whom have supported and guided me.

First and foremost, I would like to thank Prof. Paul Van den Hof and Prof. Xavier Bombois for providing me the opportunity to do research under their supervision. After many discussions about analytical versus numerical/practical research, I believe the results in this dissertation encompass both approaches complementary. These discussions have definitely changed my view on conducting research to a more balanced one, for which I would like to thank you both. Xavier, I thank you in particular for your ever-constructive evaluations of my writings; it made me realise time after time how important it is to write as succinctly as possible.

I would also like to express my sincere gratitude to the following people. I am grateful to Dr. B. Kuvshinov for several interesting discussions. I thank my friends and colleagues Marco and Mehdi for their collaboration. Mehdi, I also thank you for our early discussions on challenges in petrophysics; these have shaped a major part of this dissertation. I thank Arne for many discussions about System Identification and for being my running partner at conferences. I thank the Autoprofit team for fun times; especially with Quang, Christian, David, Hernan, and Henriette.

I furthermore thank all my colleagues and friends in Delft and Eindhoven. A special thanks goes to Alfredo, Bart, Yashar, and Zhe from Delft; and Pepijn, Ruxandra, Alrianes, Mohsin, Edwin, and Ruben in Eindhoven, for providing a nice work atmosphere and fun times. To the secretaries Kitty, Heleen, Marieke, Saskia, Esther, and Kiran in Delft; and Barbara and Diana in Eindhoven: thank you for helping me with the many administrative tasks.

Last but certainly not least, I thank my parents and brother for providing me a warm home. I thank the love of my life Ana Maria for always supporting me, and coping with my absence whenever I was absorbed in research problems in evenings and weekends.

*M.G. Potters*
*Delft, June 2016*

# Contents

# 1

# Introduction

*"The best time to do an experiment is after you've done it."* - R.A. Fisher

## 1.1 Introduction

### 1.1.1 System Identification

The ability to construct an accurate parametric mathematical model that exactly describes (or effectively mimics) the behaviour of a dynamical system is an important goal in many fields of science and sociology, mainly because such a model can predict the future state of the system. This is for instance important in an oil refinery, where an accurate model can be used to control the process such that product specifications are met. An example of a dynamical system is shown in Fig. 1.1. An input signal enters the system and a noise-corrupted output is returned. This output may be fed back to the system through a feedback mechanism. The reference signal can be constructed and applied by the user. A system is in *open loop* (*closed loop*) when no feedback (feedback) is present. For open-loop systems the user can manipulate the input, whereas for closed-loop systems the reference signal can be manipulated.

Finding mathematical models that describe dynamical systems is the subject of System Identification. Ljung (2008) provides the following definition:

"*System Identification is the art and science of building mathematical models of dynamical systems from observed input-output data.*"

The subject comprises the following main steps (see also Ljung (1999)):

1. Model Classification. The first step is to find the class of parameterised models that contains either the exact or an approximate representation of the behaviour of the dynamical system. This can be realised using for instance *first-principles* modelling, where the process is described by the laws of physics. (From these governing equations the model structure follows.) Other possibilities are *black-box* and *grey-box* modelling. In the former case no physical knowledge is available or simply discarded, and a (possibly) high-order parametric model is employed to capture the dynamics of the system. In the latter case the model is hybrid: it contains both

1
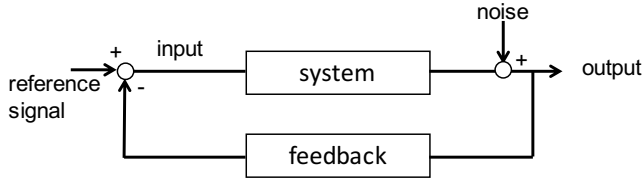
Figure 1.1: An example of a closed-loop system that is frequently used in System Identification.

first-principles (structured) and black-box (unstructured) components[1]. The *true* dynamical system is for all model classes defined by the parametric model using the parameter vector $\theta_0$, i.e., the parameter vector that best represents the true system. It is also referred to as the *true* parameter vector.

2. Experiment Design. This step occurs prior to the actual identification experiment. In it, the experiment length, the signals that need to be measured, and the sampling time are chosen. Furthermore, the reference or input signal that needs to be applied to the system is designed.

3. The Identification Experiment. The identification experiment is performed by applying the designed signal to the system, and input and output data is collected. In this step, the measured signals are corrupted by noise due to random disturbances acting upon the system.

4. Parameter Estimation. Using an identification criterion, usually quadratic, the parameters in the model that best represent the dynamic behaviour of the system are identified using the collected data obtained in the previous step. The parameter estimate is denoted by $\hat{\theta}_N$.

5. Validation. This last step is used to decide whether or not the identified model is acceptable. Part of the validation step is to compare the output simulated with the identified model to the measured output of the true system. Ideally, one should compare these outputs over a time window that does not overlap with the one that is used for the purpose of identification. Many other validation techniques can also be considered.

The parameter estimate $\hat{\theta}_N$ of the identification procedure in step 4 is a random variable - a consequence of the noise-corrupted measurements obtained in step 3. Repeating the identification experiment thus leads to a different estimate. Under conditions that will be revealed in a next chapter, $\hat{\theta}_N$ is normally distributed around the *true* parameter vector $\theta_0$. Due to the random nature of the estimate $\hat{\theta}_N$, the field of System Identification is concomitant with *statistical methods*. We refer to the books of Eykhoff (1974), Goodwin and Payne (1977), Söderström and Stoica (1989), Walter and Pronzato (1997), and Ljung (1999) for many time-domain system identification techniques; and Pintelon and Schoukens (2001) for a frequency-domain approach. In this thesis, we will consider only *linear* systems with a single input and a single output, also called linear SISO systems. Furthermore, we will assume that the model structure is known, or that it can be derived.

---

[1]In some literature, a grey-box model is defined as a model containing only parameters with a physical representation.
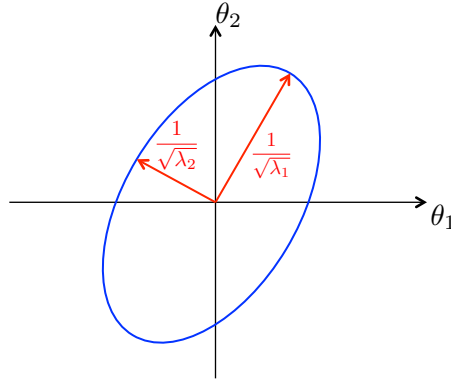
Figure 1.2: The boundary of a two-dimensional confidence ellipse $\boldsymbol{\theta}^T \boldsymbol{P}_{\boldsymbol{\theta}}^{-1} \boldsymbol{\theta} \leq 1$ centered at $\boldsymbol{\theta} = \boldsymbol{\theta}_0 = (0,0)^T$ is shown in blue. The lengths of the principal axes of the ellipse are equal to the reciprocals of the square roots of the eigenvalues $\lambda_i$ of the matrix $\boldsymbol{P}_{\boldsymbol{\theta}}^{-1}$, and are depicted in red. The estimate $\hat{\boldsymbol{\theta}}_N$ will lie inside this ellipse with probability $\alpha \approx 0.39$ (corresponding to $\chi_{\alpha}^2(2) = 1$).

The main body of this thesis is concerned with step 2 in the identification procedure: Experiment Design. In the following section the main concepts of experiment design are introduced. We explain its importance in the field of System Identification and provide a non-exhaustive overview of the existing literature. This will also serve the purpose of revealing the limitations of current Experiment Design methods. We will then proceed with defining the research goal of this thesis.

### 1.1.2 Experiment Design

In the previous section it is mentioned that the parameter estimate $\hat{\boldsymbol{\theta}}_N$ resulting from the parameter estimation step (step 4) is a random variable. Under conditions that will be revealed in Chapter 2, the estimate is normally distributed around the true parameter vector $\boldsymbol{\theta}_0$, with a covariance matrix denoted by $\boldsymbol{P}_{\boldsymbol{\theta}}$. For the sake of simplicity, let us assume that $\boldsymbol{\theta}_0 = \boldsymbol{0}$. Then, as will be formally derived in the next chapter, the estimate $\hat{\boldsymbol{\theta}}_N$ lies with probability $\alpha$ inside the confidence ellipsoid $\boldsymbol{\theta}^T \boldsymbol{P}_{\boldsymbol{\theta}}^{-1} \boldsymbol{\theta} \leq \chi_{\alpha}^2(\kappa)$, where $\kappa = \dim(\boldsymbol{\theta})$ and $\chi_{\alpha}^2(\kappa)$ the $\alpha$-percentile of the $\chi^2$-distribution with $\kappa$ degrees of freedom. The inverse covariance matrix $\boldsymbol{P}_{\boldsymbol{\theta}}^{-1}$ influences the size and orientation of the confidence ellipsoid. A two-dimensional illustration is provided in Fig. 1.2. It will be shown in a future chapter that $\boldsymbol{P}_{\boldsymbol{\theta}}$ is in fact a function of

- the input signal-to-noise ratio (SNR), and

- the system's sensitivity to small variations in model parameters and, in particular, its frequency response.

These two components of the covariance matrix depend on the distribution of the input signal power over the considered frequency range (determined by the bandwidth of the system). The SNR and the system's sensitivity to small variations in model parameters therefore dictate the volume and orientation of the confidence ellipsoid. For instance, a high SNR and sensitivity lead to a small confidence ellipsoid and thus more accurate parameter estimates. These two effects are conceptually explained in Figs. 1.3 and 1.4.
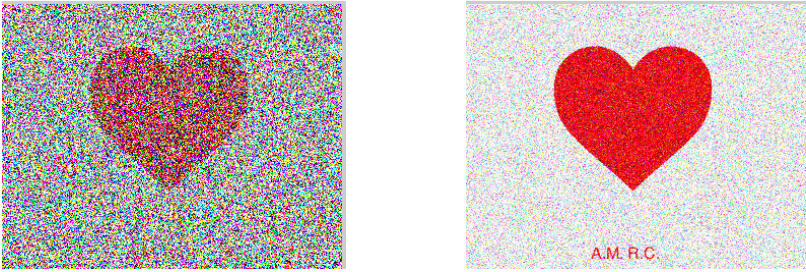
Figure 1.3: Pictures with a low SNR (left panel) and high SNR (right panel) are shown. Notice that a high SNR delivers a much clearer picture, and eases the identification of the objects displayed. In the right panel, we indeed observe the initials A.M.R.C. that are (almost) invisible in the left panel.
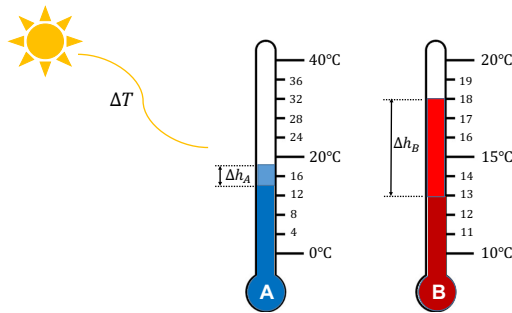


Figure 1.4: Two identical thermometers up to a different liquid and temperature scale are shown. A temperature change $\Delta T$ induces a change in liquid height of $\Delta h_A$ and $\Delta h_B$ for respectively thermometer $A$ and $B$. Suppose we had the task to accurately measure the outdoor temperature, predicted to fluctuate between 10°C and 15°C, and that we had to decide whether to use thermometer $A$ or $B$. It is apparent that thermometer $B$ is better suited for the task since the reference value interval on the scale is smaller on thermometer $B$. Hence, if we would ask many people to read of the temperature on thermometer $A$ and $B$, the variance of the collection of temperature measurements would be lower when using $B$. The underlying question then obviously is: why is $B$ suited with a better temperature scale than $A$? The answer is that the thermometers have liquids with different expansion coefficients. Let $\Delta h_i$ be the increase in height of the liquid in thermometer $i \in \{A, B\}$ upon a temperature increase $\Delta T$. Define the sensitivity $S_i = \Delta h_i / \Delta T$. Clearly, then, if $S_B > S_A$ the liquid column in thermometer $B$ rises more than the liquid column in thermometer $A$ upon the same temperature change $\Delta T$. Stated differently, we can distinguish between small changes in temperature more clearly and with more confidence when using thermometer $B$. In conclusion, a high sensitivity $S_i$ leads to more accurate temperature measurements.

It is the dependence of the estimate's covariance matrix on the input signal that underlies the benefit of doing experiment design. Indeed, designing an input signal containing an optimal set of frequencies can lead to a more precise estimate compared with a white-noise input signal of the same power[2]. Conversely, an equally-precise estimate can be obtained with less power compared with e.g. a white-noise input signal.

We will now give a short historical overview of Experiment Design methods and their aims.

---

[2]A white-noise input signal is characterised by a power spectrum that is flat, i.e., the signal power at each frequency is equal.

### Early Works in Experiment Design

One of the earliest reports on experiment design is due to J.D. Gergonne in 1815 on linear regression problems; see Gergonne (1974) for a republished version of his work, and Pierce (1876) for another notable contribution. These works considered the least squares criterion to estimate the parameters in a polynomial function used to "fit" experimental data. Extensions in regression problems are due to Federov (1972); St John and Draper (1975); Kiefer (1959); Kiefer and Wolfowitz (1959, 1960); Kiefer (1961); Karlin and Studden (1966); Whittle (1973). Their research can be connected to open-loop dynamical systems with linear-in-the-parameters models, e.g., Finite Impulse Response (FIR) and Orthonormal Basis Function (OBF) models (although the latter model type did not exist at that time).

The development of experiment design for dynamical systems (and thus System Identification) started to gain traction in the 1960s with contributions from Levin (1960) for linear time-invariant systems and Levadi (1966) for a linear time-varying system. In the 1970s work on optimal experiment design theory for multiple-input multiple-output (MIMO) systems (Mehra (1973, 1974a)) and general continuous-time linear SISO models were considered. In particular, upper bounds were sought on the number of spectral lines required in the optimal input signal. This quest led to some beautiful mathematical contributions in experiment design (Payne and Goodwin (1974); Zarrop (1979)). For instance, Mehra (1974a) showed that the sample-averaged inverse covariance matrix can be generated with at most $\kappa(\kappa+1)/2+1$ discrete frequencies, where $\kappa$ is the number of unknown parameters. This number can be reduced to only $2\kappa-1$ for parametrically disjoint systems (i.e. where the dynamical system and noise model do not share parameters), see Payne and Goodwin (1974). Sequential non-convex numerical algorithms were furthermore developed to find optimal input signals for open-loop problems (Zarrop (1979); Javaherian (1974)). Javaherian (1974) computed optimal input spectra for a specific optimisation problem and found that for many systems the optimal input signals only required $(\kappa+1)/2$ spectral lines, corresponding to the number required for a persistently exciting input signal (Ljung (1971)).

The optimisation problems that were considered in the above works were of the form:

$$\max_{input} \textit{Accuracy Measure on the Estimated Parameter}$$

subject to

$$\textit{Power or Energy Constraints on Signals},$$

where the accuracy measure and power (or energy) of the system are both a function of the power spectrum of the input signal. Hence, that power spectrum was sought that maximised the accuracy measure under the constraint that the power of the signal did not exceed a user-defined value. The above optimisation problem is quite pervasive in literature.

Oft-considered functionals of $\boldsymbol{P}_{\boldsymbol{\theta}}^{-1}$ defining the accuracy measure are reported in Table 1.1. We elaborate on these accuracy measures to give a conceptual understanding of the above optimisation problems. Minimising the sum of the parameter variances corresponds to maximising $-\text{Tr}(\boldsymbol{P}_{\boldsymbol{\theta}})$, where $\text{Tr}(\cdot)$ is the trace operator. The associated objective function in the above optimisation problem is called the *A*-optimality criterion. Even though the sum of variances is minimised in this type of optimisation problem, it may happen

| Optimality criterion | Measure | Interpretation |
|---|---|---|
| A-optimality | $-\text{Tr}[P_\theta]$ | Sum of parameter variances |
| D-optimality | $\det[P_\theta^{-1}]$ | Inverse of the volume of confidence ellipsoid |
| E-optimality | $\lambda_{min}[P_\theta^{-1}]$ | Largest principal axis of confidence ellipsoid |

Table 1.1: Some optimality criteria used as accuracy measure in optimisation problems with a constraint on power or energy of the input signal.

that one of the parameter variances is very large. A *D*-optimality criterion is used in the above optimisation problem when maximising the determinant of $\boldsymbol{P}_\theta^{-1}$ is of importance. Since the volume of the confidence ellipsoid is inversely proportional to the square root of $\det(\boldsymbol{P}_\theta^{-1})$, the *D*-optimality criterion corresponds to the minimisation of the volume of the confidence ellipsoid. Although this may seem as a good measure to increase the overall accuracy of the estimate $\hat{\boldsymbol{\theta}}_N$, it may occur for particular systems that the confidence ellipsoid is ill-shaped, as remarked by Emery and Nenarokomov (1998). This happens for instance if one of the principal axes of the confidence ellipsoid is not minimised as effectively as the others at the optimal input signal frequencies, resulting in a confidence ellipsoid being fat in one direction yet thin in others. Minimising the ellipsoidal volume can thus be misleading in some cases. Such situations can be avoided with the *E*-optimality criterion. It minimises the largest principal axis of the confidence ellipsoid, and thus maximises $\lambda_{min}(\boldsymbol{P}_\theta^{-1})$ (see for example Fig. 1.2, where the largest axis is inversely proportional to the smallest eigenvalue of the inverse of the covariance matrix.). The *D*-optimality criterion is probably most often used, mainly due to the fact that the computation of a gradient of a determinant is straightforward (gradients are important for fast numerical convergence of the optimisation algorithm). The *E*-optimality criterion is used in Optimal Experiment Design literature, but is less abundant than the *D*-optimality criterion. It also appears in the sensitivity analysis of structural systems (Haug et al. (1986)), although the goal there is optimal structural design, not parameter estimation.

**1990s till State-of-the-Art**

The selection of the accuracy measure in the optimisation problem defined in the previous section is to some extent arbitrary, except for $\kappa = 1$, in which case the *A*-, *C*-, and *D*-optimality criteria are identical. For $\kappa > 1$, the selection of an appropriate measure should be connected to the user's goal with the identified model. However, in the previously mentioned literature no such connection has been made.

This changed with the derivation of the asymptotic expression of $\boldsymbol{P}_\theta^{-1}$ of the parameter estimate for a general linear SISO system in the frequency domain by Ljung (1985), leading to the development of *identification for control*. For this purpose, experiments are designed for model-based control. The parameter estimate resulting from such experiments should be of sufficient quality to ensure high closed-loop performance when used in model-based controllers (Model Predictive Controllers, for instance). At the same time, the experiment should not disrupt the nominal closed-loop operations too much. Hence, in this setting - and in contrast to the optimisation problem introduced previously - the experiment cost should be minimised subject to a constraint on the quality of the parameter estimate, i.e.

$$\min_{input} \textit{Cost of Identification Experiment}$$

subject to

*Accuracy Constraints on Parameters.*

This optimisation problem is loosely speaking the *inverse* of the previous one as the objective function and constraint are swapped. In experiment design literature, it is called a *dual* problem. In this optimisation problem, the cost and accuracy constraint are also a function of the power spectrum of the input signal. The power spectrum is the design variable in the problem.

One of the first optimisation problems of this type is formulated by Bombois et al. (2004) in which the concept of *Least-Costly Experiment Design* (LCED) is introduced; see (Bombois et al. (2006)) for more details. The *cost* of the experiment is a function of perturbations added to the input and output signals caused by the added excitation signal. The accuracy constraint, a function of the input spectrum of the excitation signal, is connected to the model quality and the intended use of the model.

The LCED framework has been extended by Hjalmarsson (2005), who introduced *Applications-Oriented Experiment Design* (AOED), in which different cost functions and accuracy constraints are formulated. The optimisation problems in this framework lead to input designs that result in experiment data sets that reveal the important system properties for the purpose of control, and consequently, estimates that yield good closed-loop performance when used in model-based controllers.

The optimisation problems formulated in (Bombois et al. (2004); Hjalmarsson (2005)) have costs and constraints that are affine in the power spectrum of the to-be-designed input signal, and can be solved with convex numerical algorithms (Boyd and Vandenberghe (2003)). To solve the problems numerically, the power spectrum needs to be parameterised. This can be done by using either *finite-dimensional spectrum parametrisation* (e.g. a multi-sine or filtered white-noise signal) or *partial correlation parametrisation*. In case of the former, the spectrum falls within the class containing e.g. multi-sine or filtered white-noise spectra. Consequently, slightly suboptimal solutions may be found. The second method considers all possible spectra and therefore the optimisation problem finds the optimal solution; see the work of Jansson and Hjalmarsson (2005) for details.

The majority of these works has been formulated in the frequency domain in which the problems are convex. However, important problems cannot be solved in this domain. For instance, time-domain constraints like bounds on the amplitudes of the input and output signals can not be considered, although these are highly relevant in many practical situations. Recently, works have appeared that *do* take time-domain constraints into account, at the expensive of losing convexity (or by using convex relaxations). MPC-X introduced by Larsson et al. (2011) alters the model predictive controller (MPC) by adding a constraint that ensures good model quality while respecting the input and output amplitude bounds set in the MPC; a method that is currently limited to output error (OE) models. A modified version of this method, restricted to open-loop systems, is presented in Ebadat et al. (2014b) (see also Larsson (2014) and references therein) in which the minimal required experiment time is found that satisfies both parameter accuracy constraints and amplitude bounds, using a convex relaxation method introduced by Manchester (2010). This formulation is used to maximise the information content in the experiment data for the intended model use. Manchester (2009) introduced an input design method for *D*-optimal problems with signal amplitude constraints for the class of multi-sine signals based on an algorithm due to Guillaume et al. (1991), although no accuracy constraints are imposed. Manchester

(2009) showed that the additional degree of freedom in the selection of the phases of the multi-sine signal for time-domain problems can be exploited to increase the information density in the experiment data for the purpose of identification.

## 1.2    Limitations of the State-of-the-Art

From the literature overview presented in Section 1.1.2 we extract here the following limitations of the Least-Costly Experiment Design framework.

Firstly, the vast majority of the LCED problems consider black-box (unstructured), discrete-time models that are finite and rational. However, there are many physical systems, i.e. structured systems, that have continuous-time formulations. For instance, diffusion -advection-reaction processes can be modelled by linear Partial Differential Equations with constant coefficients. The latter processes can be represented by continuous-time irrational, infinite-order transfer functions and contain - contrary to unstructured system - only a few parameters that require estimation. The LCED framework is currently only formulated for discrete-time unstructured systems, and is therefore unable to handle physical systems in general. Problems not present in the unstructured systems that need to be accounted for when generalising the LCED framework to structured systems are (i) the order-of-magnitude difference in the physical parameter values, (ii) the discretisation of the physical continuous-time system and their simulation, and (iii) the additional degrees of freedom in the experiment set-up (e.g. actuator and sensor locations) that impose significantly longer computational times as the LCED problem has to be solved for many possible values of the degrees of freedom.

Secondly, the LCED framework relies heavily on convex numerical algorithms. This dependence is a strength but also a weakness of the framework. Its strength is that optimal input signals can be designed for systems with an arbitrary but finite number of to-be-identified parameters. However, the solutions of the numerical algorithms do not provide any interpretation nor understanding of the underlying mechanisms that determine the optimal frequencies and amplitudes of the optimal input signal. Furthermore, the correctness of these numerical solutions (i.e. whether or not they are indeed the correct solutions of the optimisation problem) cannot be tested against analytical solutions, as the latter do not exist in general.

A third limitation is that the vast majority of the problems tackled in these frameworks are only applicable to arbitrary closed-loop systems as long as the controller is known and linear time-invariant. This limits the scope of the frameworks enormously, since many real-life industrial processes use nonlinear controllers. Although solutions for systems regulated by nonlinear controllers exist in the literature (Larsson et al. (2011); Ebadat et al. (2014b); Larsson (2014)), they are all - in one way or another - restricted to specific classes of systems.

The last limitation is as follows. In the LCED framework, the cost function (objective function) in the optimisation problems is of the form of a weighted input spectrum, and the parameter accuracy constraints are Linear Matrix Inequalities (LMIs) affine in the input spectrum. The reason for this formulation is that the optimisation problem is convex, and can therefore be efficiently solved with numerical methods. However, this is only one possible formulation. Indeed, many other possibilities relevant for real-life processes can be considered. For instance, instead of minimising a weighted input power, it might be

relevant to minimise the total experiment time. (The cost is thus experiment time and not a (weighted) input power). Furthermore, many real-life processes are subject to product quality constraints, imposing amplitude bounds on the time-domain input and output signals. Consequently, a relevant problem formulation is to minimise the experiment time subject to parameter accuracy constraints *and* system constraints, where the latter are e.g. input and output amplitude bounds. Such a formulation was recently formulated for open-loop systems by Ebadat et al. (2014b). System constraints are usually imposed for safety or product quality reasons. Consequently, they may influence the economic impact of the experiment. Therefore, these constraints are sometimes referred to as economically-relevant constraints.

## 1.3 Problem Statement and Approach

The limitations revealed in the last section show that there exist more LCED problem formulations than the classical one introduced by Bombois et al. (2006), and that the current framework cannot be applied to all systems. Figure 1.5 gives a high-level schematic overview of many possible LCED problems, defined through the steps I until IV. The classical LCED problem is solvable for unstructured systems (I) without degrees of freedom in the experiment set-up (II)[3], which are either in open loop, or in closed-loop with a known linear time invariant (LTI) controller, and for which an optimisation problem (IV) is solved that minimises a weighted input power subject to parameter accuracy constraints. In this classical LCED problem, the set of design variables $\Xi$ only contains the input power spectrum, and no system constraints are considered.

It is clear from Fig. 1.5 that the classical LCED framework can only solve a limited number of problems. Indeed, a LCED problem consisting of a structured system (I), with possible degrees of freedom in the experiment set-up (II), and which is in closed loop with an unknown or a nonlinear controller (III), has not been investigated. Furthermore, choosing experiment time as the experiment cost, or imposing additional system constraints, have not been considered in full generality (IV).

In light of the above limitations and observations, the research question of this thesis is formulated as follows.

> How can the current Least-Costly Experiment Design framework be extended to include structured and unstructured linear systems regulated by nonlinear controllers while incorporating economically-relevant constraints during experimentation?

Before describing our approach to address this question, let us first clarify some terminology. We consider a system to be structured when its dynamics are described by first principles models (i.e. models containing physical parameters). A structured system may, depending on the application, be in open or closed loop containing unknown linear or (possibly unknown) nonlinear controllers. An economically relevant constraint can be, for instance, amplitude bounds on input and output signals of a system.

In order to address the research question, the following approach is taken. From Fig. 1.5 we observe that in order to extend the LCED framework, the to-be-developed techniques

---

[3]We recall that by degrees of freedom in the set-up, we refer to e.g. actuator and sensor locations.
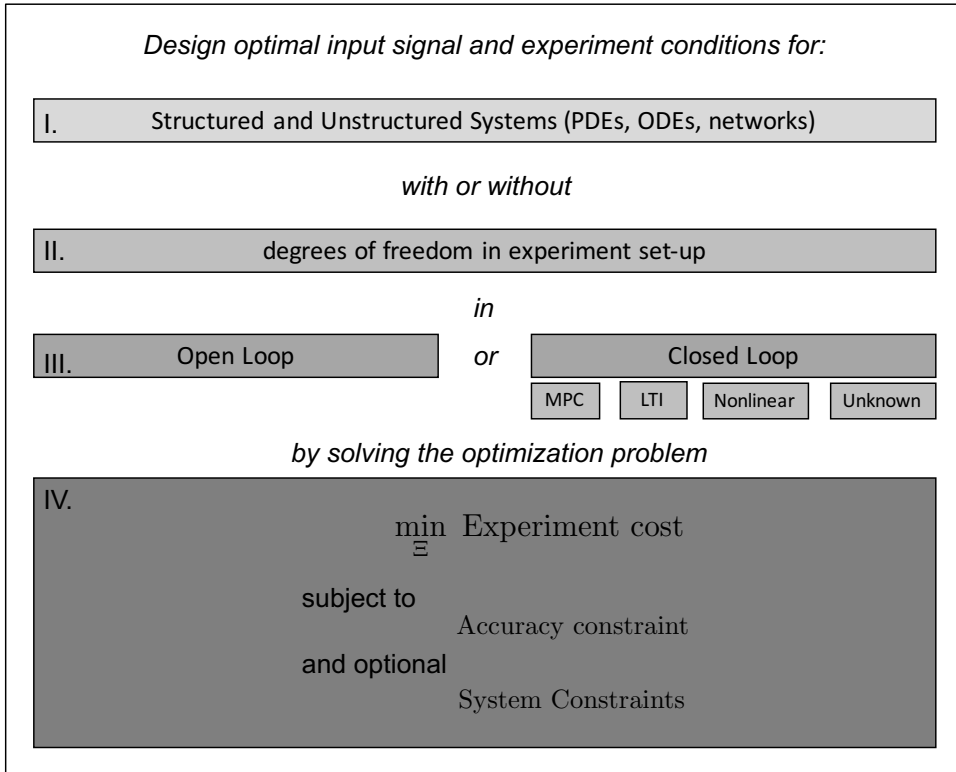
Figure 1.5: This diagram shows the type of experiment design problems that should be solvable. The aim is to solve the optimisation problem IV for any structured or unstructured system, with or without degrees of freedom in the experiment set-up, and that can be in either open- or closed-loop. The symbol $\Xi$ indicates the set of design variables in the optimisation problem, which usually contains only the input spectrum $\Phi_r$, but can also include degrees of freedom of an experiment set-up.

should, in conjunction, be able to solve more of the problems (I)-(IV) than currently possible. Specifically, we should extend the Least-Costly Experiment Design framework to (1) linear structured systems with additional degrees of freedom in the experiment set-up, (2) (un)structured linear systems that are in closed loop with an arbitrary controller, and by (3) considering different economically relevant constraints. In addition to these extensions, we should also (4) provide generic analytical solutions for some LCED problems. The analytical solutions will provide understanding of the numerically generated ones, as mentioned in the previous section. We now discuss in detail the approaches taken to address the points (1)-(4).

**Find generic analytical solutions for some LCED problems**

In Section 1.2 it has been mentioned that the LCED framework suffers from the lack of analytical solutions of its optimisation problems. The motivation for addressing point (4) above is that analytical solutions can be very helpful, even though existing numerical algorithms can already solve the LCED optimisation problems for systems with an arbitrary number of to-be-identified parameters.

First, analytical solutions will expose the mechanisms that are important to minimise the cost while ensuring that parameter accuracy constraints remain satisfied. Consequently, they will provide interpretation of the optimal frequencies and amplitudes that are contained in the optimal input signal.

Second, analytical solutions can speed up the numerical algorithms enormously by e.g. hardcoding them. This, as we shall see in a future chapter, is in fact very useful when not only the input spectrum is designed, but also the degrees of freedom in the experiment set-up. Indeed, in such cases, a LCED problem has to be solved for many possible combinations of values of the degrees of freedom. This leads to a computational burden that can be avoided with analytical results.

Despite these positive features of analytical solutions, one decade after the first formulation of the LCED problem no generic solutions have been calculated. To this end, we take in this thesis a first step towards finding such solutions. We will find analytical solutions for uni- and bi-parametric models, i.e., models in which only one or two parameters are unknown (but multiple occupancy in the model is allowed).

**Develop LCED methods for systems with arbitrary controllers**

Our approach in tackling point (2), i.e. generalising the LCED framework such that it can be applied to (un)structured closed-loop systems with arbitrary controllers, is as follows.

At a technical level, as will be explained in Chapter 5, the LCED problem requires an explicit expression of the LTI sensitivity function, which appears in the covariance matrix expression of the parameter estimate vector. In the case of unknown linear controllers, or (possibly unknown) nonlinear controllers, the sensitivity function is unknown or not LTI. In these cases, the LCED problem cannot be solved. Due to this limitation, we develop in this thesis methods that extend the framework to include other types of controllers.

To this end, we will introduce the novel *Stealth* and *Sensitivity* methods to circumvent the requirement of knowing the sensitivity function. The former method changes the classical closed-loop identification scheme such that the excitation signal is no longer observed by the controller. As will be shown later, this new identification scheme leads to a covariance matrix expression that is no longer a function of the sensitivity function. The

latter method uses the classical closed-loop identification scheme, and approximates the sensitivity function using prior data. This approximate function will then be used in the covariance matrix expression, such that the LCED problem can be solved with existing numerical methods.

### Generalise the LCED framework to structured systems with degrees of freedom in the experiment set-up

The LCED framework has been formulated for discrete-time, black-box (unstructured) systems. However, as already mentioned in Section 1.2, much less attention has been given to physical (structured) systems. This may be due to the fact that such systems are formulated in continuous time, and are driven by partial differential equations (PDEs). Indeed, both differences with unstructured systems make the identification and experiment design problem more difficult.

In this thesis, we will incorporate physical systems driven by linear PDEs with constant coefficients in the LCED framework; hereby addressing point (1) mentioned previously. To this end, we show how to properly simulate these physical systems for the purpose of parameter identification. Furthermore, we show how discrete-time models explicit in the physical parameters can be obtained from the continuous-time PDE equations. These discrete-time models can then be used in the LCED framework. Problems such as stability and ill-shaped covariance matrices will be addressed. Additionally, we will introduce an algorithm that can efficiently deal with the degrees of freedom in the experiment set-up that are concomitant with many physical systems. A case study furthermore reveals the strength of the LCED optimal excitation signals compared to e.g. white noise excitation signals.

### Incorporate other cost definitions and economically-relevant constraints in the LCED framework

We have mentioned in Section 1.2 that the cost function in the LCED framework is formulated as a weighted input power, whereas in practice other ones might be more relevant. Furthermore, we have also mentioned that next to parameter accuracy constraints, other ones are important.

We address this limitation, and thus point (3), as follows. We consider a LCED problem, first formulated by Ebadat et al. (2014b), in which the experiment length is minimised subject to a parameter accuracy constraint and system constraints. The latter type of constraints can be e.g. input and output amplitude bounds (and can be seen as economical constraints). This optimisation problem is no longer convex, in sharp contrast to the classical LCED problem formulations. To this end, we will design the amplitudes and phases of a multi-sine input signal containing fixed frequencies. This is also the main difference with the work of Ebadat et al. (2014a), where the signal is limited to be a stationary process with finite memory and alphabet. In (Ebadat et al. (2014b)) this restriction is not present, but the approach cannot be used for closed-loop identification, unlike the method that is introduced in this thesis. Our method can be applied to open- and closed-loop systems and can treat the general case of multiple accuracy constraints, in contrast to existing methods in the literature. We will illustrate the strength of our non-convex method with three numerical examples. These clearly show that the new methodology can lead to much shorter experiment lengths than the classical formulation (under the exact same constraints).

**Apply the new techniques to a relevant problem in petrophysics**

The novel LCED formulation mentioned above is applied to an important problem in petrophysics. This problem pertains to the estimation of the porosity and permeability values of a porous sample using pressure oscillation experiments. These parameter estimates are e.g. used to calibrate reservoir models, and therefore need to be precise. However, it is clear from the literature that obtaining accurate estimates is a challenge. Furthermore, these lab experiments are expensive mainly due to the required presence of a skilled engineer. Reducing the experiment time is therefore paramount to keeping such experiments viable.

In this thesis, we consider the LCED problem of minimising the experiment time of such experiments under parameter accuracy constraints and bounds on the actuator amplitude of the experiment set-up, by designing the input spectrum of the actuator. As will become clear in Chapter 7, these lab set-ups also have two degrees of freedom. We thus in fact solve the optimisation problem by simultaneously designing the optimal input spectrum and the degrees of freedom. We tackle this optimisation problem analytically (to a large extent). We will show that the experiment times of these type of experiments can be drastically reduced when employing optimal experiment design.

## 1.4 Organisation of this Thesis

This thesis consists of nine chapters in total, five of which provide solutions to the four goals set in the previous section. The novel techniques that will be presented in these chapters are introduced separately, but we stress that these can be used in conjunction to address many of the problems (I)-(IV) in Fig. 1.5.

Chapter 2 describes existing time-domain System Identification techniques, particularly the Direct and Indirect Identification methods.

Chapter 3 describes the classical Least-Costly Experiment Design framework. It shows how the problems in this framework are solved numerically, and provides explanation and examples of several types of frequently considered problems. New in this chapter is a geometric interpretation of some LCED problems. The notations and techniques introduced in Chapters 2 and 3 will be used in the remaining chapters.

Chapter 4 addresses goal (4) set in Section 1.3. We shall derive analytical solutions for the LCED problem formulated in Chapter 3 for uni- and bi-parametric systems and discuss their uniqueness. Parts of this chapter are published in (Potters et al. (2015)) and (Potters et al. (2016a)).

Chapter 5 introduces the *Stealth* and *Sensitivity* Methods, addressing goal (2) in Section 1.3. Both methods generalise the LCED framework such that it can be used for linear systems regulated by arbitrary controllers. This chapter includes several numerical studies in which the methods are applied to a linear system regulated by an MPC, a linear system regulated by a nonlinear controller, and a dynamical network. The chapter is partly based on the article (Potters et al. (2014)).

Chapter 6 addresses goal (1) set in Section 1.3 and introduces a method that generalises the LCED framework such that it can be used for structured systems driven by linear partial differential equations with constant coefficients. An efficient numerical algorithm is developed that can deal with degrees of freedom in the experiment set-up. It also shows how to efficiently and correctly simulate such systems, which is required for parameter

estimation. A case study is provided to show the benefit of experiment design over white-noise experiments. Parts of this chapter are published in (Potters et al. (2016a)).

In Chapter 7 we apply optimal experiment design to a problem in petrophysics. The problem pertains to the estimation of the physical parameters permeability and porosity in a so-called Pressure Oscillation Experiment. We show in this chapter how to minimise the experiment time while respecting amplitude bounds on the actuator of the experiment set-up, as well as respecting bounds on the variances of the two physical parameters. We furthermore compare results between the Direct and Indirect Identification method. The chapter is based on the article (Potters et al. (2016c)).

Chapter 8 introduces a novel algorithm that is applicable to structured and unstructured systems, and addresses goal (3). This algorithm finds the minimal required experiment time such that parameter accuracy constraints and signal amplitude bounds are satisfied. Part of this chapter is published in (Potters et al. (2016b)).

In Chapter 9 conclusions are drawn and recommendations for future research are provided.

# 2

# The Basics of Prediction Error Identification

*"With four parameters I can fit an elephant, and with five I can make him wiggle his trunk."* - J. Von Neumann

## 2.1 Introduction

In this chapter we describe known, basic techniques of system identification for single-input single-output (SISO) systems. These techniques can be generalised and extended to more complex systems, e.g. a network of systems, multiple-input multiple-output (MIMO) systems, and bilaterally-coupled systems.

At the core of each real system lies a continuous-time system $G_0(s)$ that we would like to identify, see Fig. 2.1. This model represents the true dynamics of a process that connects the signal $u$ to the signal $y$, and is based on its equations of motion. As mentioned in Chapter 1, an identified model of the system $G_0(s)$ can be used to design a controller for the true system, or to make predictions on the future state of the process, which is important in e.g. process engineering.

Most processes contain feedback that often has the form of a controller $C(z)$ (designed by the user) that uses the signal $y$ to adapt the signal $u$ that enters the system. In Fig. 2.1 the time-domain, discrete-time signals $r$, $u$, and $y$ are shown. The signal $r$ can be added to the process by the user. The signal $u$ goes through a Digital-to-Analog converter
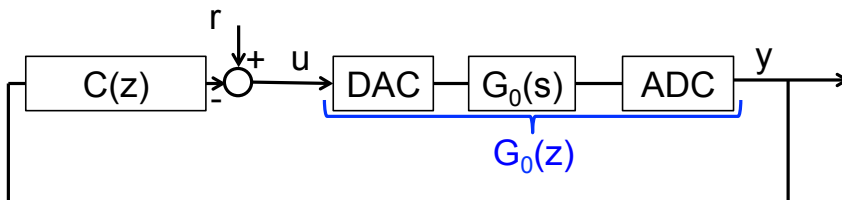


Figure 2.1: A continuous-time system $G_0(s)$ in closed-loop with a linear, time-invariant controller $C(z)$. The signals $r$, $u$, and $y$ are discrete-time. The blocks DAC (Digital-to-Analog Converter), $G_0(s)$, and *ADC* (Analog-to-Digital Converter) define the discrete-time model $G_0(z)$.

before it arrives at the continuous-time process. The continuous-time output that leaves the system $G_0(s)$ then goes through an Analog-to-Digital converter resulting in the discrete-time signal $y$[1]. The DAC, $G_0(s)$, and ADC can be regrouped into a single discrete-time operator: the discrete-time transfer function $G_0(z)$ (see Fig. 2.1).

In this chapter we will describe existing techniques that show how the signals $r$, $u$, and $y$ can be used to identify a discrete-time model of the discrete-time transfer function $G_0(z)$, see Fig. 2.1. The identification experiment is however hampered by noise that can enter the system at various locations. The type of identification method that should be used thus depends on the type of noise and the locations at which it enters the system.

In the remainder of this chapter, we will describe the Prediction Error Method (PEM), the Direct and Indirect Identification methods for discrete-time models. In particular, we describe these for a simple closed-loop transfer function $G_0(z)$. In later chapters, these techniques will also be applied to continuous-time systems, although the concepts remain the same. The PEM is considered in Section 2.2. Sections 2.2.2 and 2.2.3 present the Direct Identification Method and a tailored Indirect Identification Method, which are two different ways to collect experimental data with the aim to identify parameters residing in a parameterised model. These methods will be used in future chapters.

## 2.2   Prediction Error Identification

### 2.2.1   Introduction

The identification framework considered in this thesis is focussed on single-input single-output (SISO) data-generating systems. A discrete-time *data-generating system*, also called the *true system*, is defined as

$$\mathscr{S}: \ y[n] = G_0(q)u[n] + H_0(q)e[n], \tag{2.1}$$

with $y[n]$ the output signal, $u[n]$ the input signal, $e[n]$ a zero-mean white noise signal with variance $\sigma_e^2$, and $n \in \mathbb{N}$ represents discrete time[2]. The functions $G_0(q)$ and $H_0(q)$ are proper rational functions in the shift operator $q$, and $H_0(q)$ is stable and monic. The shift operator is defined as $q^k u[n] = u[n+k]$, where $k \in \mathbb{N}$. The true system is defined by $\mathscr{S} = \{G_0(q), H_0(q)\}$, as these so-called transfer functions determine the dynamic behaviour of the process. The term $H_0(q)e[n]$ represents process and measurement noise. When $H_0(q) = 1$ the noise is called *white* and for all other cases *coloured*.

The input signal in (2.1) is defined by (see Fig. 2.2)

$$u[n] = r[n] - C(q)y[n], \tag{2.2}$$

---

[1]Although incorrect at a formal level, and with slight abuse of notation, we frequently display the system in Fig. 2.1 by a transfer function in the *s*- or *z*-domain, whereas the signals $r$, $u$, and $y$ are in the time domain. This notation should thus be interpreted as the system being *represented* by the transfer function displayed in the block. Furthermore, for notational brevity, the DAC and ADC blocks are often left out with the understanding that these should be included when doing the actual experiment.

[2]We deviate slightly from standard notation in System Identification literature as we need to distinguish between continuous- and discrete-time signals in this thesis. We denote a discrete-time signal with $x[n] = x(nT_s)$, with $T_s$ the sampling time, whereas its continuous-time counterpart is denoted by $x(t)$.
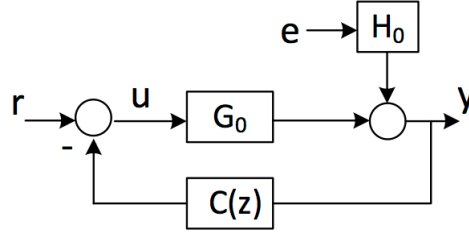
Figure 2.2: Closed-loop configuration of the true, data-generating system $G_0(z)$ regulated by a linear, time-invariant controller $C(q)$. The input is $u[n]$ and the output $y[n]$ is corrupted by an additive noise $v[n] = H_0(q)e[n]$.

where $C(q)$ is a known, linear, time invariant (LTI) controller and $r[n]$ a reference signal. In a later chapter, we will consider other types of controllers as well. The signal $r[n]$ is also called an excitation signal, as it is supplied by the user for the purpose of identification. The controller aims to e.g. reduce the fluctuations in the output due to disturbances by changing the input $u$ through the control action $-C(q)y[n]$. The closed-loop configuration is depicted in Fig. 2.2. Notice that the process noise $H_0(q)e[n]$ affects the measurements, and that it also enters the feedback loop.

In the system identification literature, it is common to assume that the true system lies in a parameterised set of models, defined by

$$\mathcal{M} : y[n;\boldsymbol{\theta}] = G(q,\boldsymbol{\theta})u[n] + H(q,\boldsymbol{\theta})e[n], \ \boldsymbol{\theta} \in \mathbb{R}^{\kappa}, \tag{2.3}$$

where $\kappa = \dim(\boldsymbol{\theta})$, and $G(q,\boldsymbol{\theta})$, $H(q,\boldsymbol{\theta})$ are proper rational transfer functions depending on a real-valued parameter vector $\boldsymbol{\theta}$. With the notation $\mathscr{S} \in \mathscr{M}$ we imply that for some $\boldsymbol{\theta} = \boldsymbol{\theta}_0$ we have that $G_0(q) = G(q,\boldsymbol{\theta} = \boldsymbol{\theta}_0)$ and $H_0(q) = H(q,\boldsymbol{\theta} = \boldsymbol{\theta}_0)$. Under the assumption $\mathscr{S} \in \mathscr{M}$ we see that in order to classify the dynamic behaviour of the data-generating system, only the parameter vector $\boldsymbol{\theta}_0$ needs to be estimated. We make use of this assumption throughout this thesis.

The discrete-time transfer function $G(q,\boldsymbol{\theta})$ in (2.3) is usually a *black-box* model. This representation merely serves to accurately simulate the output as a function of the input, and uses no physical knowledge to define for instance the model structure and order. Consequently, the parameters residing in such models should be interpreted as *fitting* parameters (that may be implicitly linked to physical ones). On the other hand, a *first-principles* model is deduced from the continuous-time governing equations of a process. In this case, the model structure and order follow immediately from the equations of motion. In such models the physical parameters appear explicitly. Lastly, a *grey-box* model consists of first-principles and black-box model components. This model can be used when some parts of the dynamics can be easily deduced from the equations of motion, whereas other parts cannot and therefore need to be modelled in a black-box fashion.

## 2.2.2 Direct Method

The Direct Identification Method, or in short Direct Method, uses the input $u$ (2.2) and output $y$ (2.1) of the data-generating system to identify $\boldsymbol{\theta}_0$. To this end, a known reference signal $r$ is applied to the closed-loop system (2.1)-(2.2) and the input $u$ and output $y$ are

measured and collected in the data set $Z_N = \{u[n], y[n]\}_{n=1}^N$. In the case of an open-loop system, i.e. $C(q) = 0$, a known input signal $r = u$ is applied and the output $y$ is measured.

The data set $Z_N$ is used to determine an estimate of $\theta_0$ in the full-order model structure $\mathcal{M}$ in the following way. We introduce the prediction error between the measured output $y$ and its one-step ahead predictor:

$$\varepsilon[n; \boldsymbol{\theta}] = H^{-1}(q, \boldsymbol{\theta}) \left( y[n] - y_{sim}[n; \boldsymbol{\theta}] \right) = H^{-1}(q, \boldsymbol{\theta}) \left( y[n] - G(q, \boldsymbol{\theta}) u[n] \right). \tag{2.4}$$

In (2.4), we also introduce for further use the symbol $y_{sim}[n; \boldsymbol{\theta}]$, which is the simulated (noise-free) output. It is then a classical procedure to find the best estimate $\hat{\boldsymbol{\theta}}_N$ of $\boldsymbol{\theta}_0$ with the least-squares criterion (Ljung (1999)):

$$\hat{\boldsymbol{\theta}}_N = \arg \min_{\boldsymbol{\theta}} \frac{1}{N} \sum_{n=1}^N \varepsilon^2[n; \boldsymbol{\theta}]. \tag{2.5}$$

Under the assumption $\mathcal{S} \in \mathcal{M}$ (c.f. (2.1), (2.3)) it follows that the estimate $\hat{\boldsymbol{\theta}}_N$ is asymptotically normally distributed around the true parameter vector $\boldsymbol{\theta}_0$. Hence, under certain conditions on the excitation signal (and the controller in closed loop), we have for large $N$ that $(\hat{\boldsymbol{\theta}}_N - \boldsymbol{\theta}_0) \sim \mathcal{N}(\mathbf{0}, \boldsymbol{P}_{N,\boldsymbol{\theta}})$, where $\boldsymbol{P}_{N,\boldsymbol{\theta}}$ is the covariance matrix of the estimate $\hat{\boldsymbol{\theta}}_N$ that is inversely proportional to the experiment length $N$. In the limit $N \to \infty$ the estimate converges in distribution to the true parameter vector, i.e., $\hat{\boldsymbol{\theta}}_N \xrightarrow{d} \boldsymbol{\theta}_0$ w.p. 1. As the estimate is normally distributed around the true parameter $\boldsymbol{\theta}_0$ it follows that the ellipsoid

$$\mathcal{E} = \left\{ \boldsymbol{\theta} \mid (\boldsymbol{\theta} - \hat{\boldsymbol{\theta}}_N)^T \boldsymbol{P}_{N,\boldsymbol{\theta}}^{-1} (\boldsymbol{\theta} - \hat{\boldsymbol{\theta}}_N) \leq \chi_\alpha^2(\kappa) \right\} \tag{2.6}$$

contains the unknown true parameter vector $\boldsymbol{\theta}_0$ with probability $\alpha$. In this expression, $\chi_\alpha^2(\kappa)$ is the $\alpha$-percentile of the $\chi^2$ distribution with $\kappa$ degrees of freedom, and $\boldsymbol{P}_{N,\boldsymbol{\theta}}^{-1}$ the inverse covariance matrix.

**Assumption 2.1** *Notice that from (2.4) and (2.5) that we implicitly assume that the input signal $u$ is either measured without error (no sensor noise), or that the feedback signal $-C(q)y[n]$ in (2.2) is exactly known. If this assumption is not valid, the identification problem is in fact an Errors-in-Variables problem, to which different identification techniques should be applied (Söderström (2007)).*

**Remark 2.1** *The identification method outlined above needs the simulated output as a function of $\boldsymbol{\theta}$. For discrete time models $G(q, \boldsymbol{\theta})$ the simulation is straightforward. However, continuous-time first-principles and grey-box models are not functions of the delay operator $q$. Consequently, $y_{sim}[n; \boldsymbol{\theta}]$ needs to be constructed differently. In Chapter 6 we show that one can e.g. use an input signal that is a sum of sinusoidal signals to easily construct $y_{sim}[n; \boldsymbol{\theta}]$.*

The expression for the inverse of the covariance of $\hat{\boldsymbol{\theta}}_N$ in (2.6) is given by (Ljung (1999))

$$\boldsymbol{P}_{N,\boldsymbol{\theta}}^{-1} = \frac{N}{\sigma_e^2} \overline{E} \left[ \boldsymbol{\psi}[n; \boldsymbol{\theta}] \boldsymbol{\psi}^T[n; \boldsymbol{\theta}] \right]_{\boldsymbol{\theta} = \boldsymbol{\theta}_0}, \tag{2.7}$$

which can be estimated from $\hat{\boldsymbol{\theta}}_N$ and $Z_N$. In this equation, the expectation operator $\bar{E}$ is defined as $\bar{E} f[n] \equiv \lim_{N \to \infty} \frac{1}{N} \sum_{n=1}^N E f[n]$, where $E$ is the usual expectation operator,

and $\sigma_e^2$ is the variance of the noise $e[n]$ defined in the data generating system (2.1)-(2.2). Lastly, $\psi[n;\boldsymbol{\theta}] \equiv -\nabla_{\boldsymbol{\theta}} \varepsilon[n;\boldsymbol{\theta}]$, where $\varepsilon[n;\boldsymbol{\theta}]$ is the prediction error (2.4), and $\nabla_{\boldsymbol{\theta}} = (\partial/\partial\theta_1,\ldots,\partial/\partial\theta_\kappa)^T$ the parameter gradient operator.

Define the sensitivity function of the closed-loop system (2.1)-(2.2) as

$$S(q,\boldsymbol{\theta}) = \frac{1}{1+C(q)G(q,\boldsymbol{\theta})}, \tag{2.8}$$

and define the short-hand notation in the $z$-domain: $S_0(z) = S(z,\boldsymbol{\theta}_0)$, where $z = e^{-i\omega T_s}$, and $\omega$ is the radial frequency. Expression (2.7) can then be transformed into the frequency domain using Parseval's theorem for discrete-time signals and reads (Ljung (1999))

$$\boldsymbol{P}_{N,\theta}^{-1}[\Phi_r] = \boldsymbol{P}_{r,N,\theta}^{-1}[\Phi_r] + \boldsymbol{R}_0 = \frac{NT_s}{2\pi\sigma_e^2} \int_{-\pi/T_s}^{\pi/T_s} \boldsymbol{F}_r(e^{-i\omega T_s})\boldsymbol{F}_r^H(e^{-i\omega T_s})\Phi_r(\omega)\,d\omega + \boldsymbol{R}_0, \tag{2.9}$$

in which the subscript $H$ is the Hermitian conjugate, and where the matrix

$$\boldsymbol{R}_0 = \frac{NT_s}{2\pi} \int_{-\pi/T_s}^{\pi/T_s} \boldsymbol{F}_v(e^{-i\omega T_s})\boldsymbol{F}_v^H(e^{-i\omega T_s})\,d\omega \tag{2.10}$$

represents the contribution of the noise in closed-loop to the certainty in the parameters. Furthermore, the vector functions $\boldsymbol{F}_r(z)$ and $\boldsymbol{F}_v(z)$ are given by

$$\boldsymbol{F}_r(z) = H_0^{-1}(z)S_0(z)\left[\nabla_{\boldsymbol{\theta}}G(z,\boldsymbol{\theta})\right]_{\boldsymbol{\theta}=\boldsymbol{\theta}_0}, \tag{2.11}$$

$$\boldsymbol{F}_v(z) = H_0^{-1}(z)\left[\nabla_{\boldsymbol{\theta}}H(z,\boldsymbol{\theta})\right]_{\boldsymbol{\theta}=\boldsymbol{\theta}_0} - C(z)S_0(z)\left[\nabla_{\boldsymbol{\theta}}G(z,\boldsymbol{\theta})\right]_{\boldsymbol{\theta}=\boldsymbol{\theta}_0}. \tag{2.12}$$

In these expressions $\Phi_r(\omega)$ is the power spectrum of the excitation signal $r[n]$ in (2.2). In the following sections and chapters, we will frequently set $T_s = 1$ for the sake of notational brevity. Notice from (2.9) that the inverse of the covariance matrix is in fact the frequency-averaged accuracy in the parameters over the interval $[-\pi/T_s, \pi/T_s]^3$. It should be stressed that although the covariance matrix is a functional of the power spectrum of the excitation signal $r$, the actual identification (2.5) is done with the collected input $u$ and output $y$ data. Expression (2.9) plays a central role in experiment design as the covariance matrix can be altered by designing the spectrum $\Phi_r$ of the excitation signal $r$. We stress that the expression of the covariance matrix is here defined for a linear LTI controller; in Chapter 5 we will also consider nonlinear controllers.

### 2.2.3 Indirect Method

The Indirect Identification Method, or Indirect Method, uses the applied excitation signal $r[n]$ (2.2) and measured output $y[n]$ (2.1) for the identification of $\boldsymbol{\theta}_0$. This is in contrast to the Direct Method, where the input $u[n]$ and output $y[n]$ were used. The data set in this case is defined by $Z_N = \{r[n],y[n]\}_{n=1}^N$. Substituting (2.2) into (2.1) and using (2.8) shows

---

[3]Indeed, the average value of a function $f(x)$ over the interval $[a,b]$ is given by $< f(x) > = \frac{1}{b-a}\int_a^b f(x)\,dx$.

that the prediction error for the Indirect Method (c.f. (2.4)) reads

$$\varepsilon[n;\boldsymbol{\theta}] = H_{IM}^{-1}(q,\boldsymbol{\theta})\left(y[n] - G_{IM}(q,\boldsymbol{\theta})r[n]\right), \tag{2.13}$$

where

$$H_{IM}(q,\boldsymbol{\theta}) = S(q,\boldsymbol{\theta})H(q,\boldsymbol{\theta}), \tag{2.14}$$

$$G_{IM}(q,\boldsymbol{\theta}) = S(q,\boldsymbol{\theta})G(q,\boldsymbol{\theta}), \tag{2.15}$$

and $G(q,\boldsymbol{\theta})$, $H(q,\boldsymbol{\theta})$, $S(q,\boldsymbol{\theta})$ are defined in (2.3), (2.8). The estimate $\hat{\boldsymbol{\theta}}_N$ is found with $Z_N$ and (2.5), in which instead (2.13) should be used for the prediction error.

The inverse covariance matrix for the Indirect Method is calculated along the same lines as for the Direct Method. The expression is given by (2.9) in which instead

$$\boldsymbol{F}_r(z) = H_{IM}^{-1}(z,\boldsymbol{\theta}_0)\left[\nabla_{\boldsymbol{\theta}}G_{IM}(z,\boldsymbol{\theta})\right]_{\boldsymbol{\theta}=\boldsymbol{\theta}_0}, \tag{2.16}$$

$$\boldsymbol{F}_v(z) = H_{IM}^{-1}(z,\boldsymbol{\theta}_0)\left[\nabla_{\boldsymbol{\theta}}H_{IM}(z,\boldsymbol{\theta})\right]_{\boldsymbol{\theta}=\boldsymbol{\theta}_0}. \tag{2.17}$$

### 2.2.4   Comparison

Let us compare the two identification methods. The Direct Method uses the data $Z_N = \{u[n],y[n]\}_{n=1}^{N}$. The input data contains all the measured feedback dynamics of the system. The Indirect Method, however, is an alternative method that avoids the use of the input signal in the closed-loop system. The estimate $\hat{\boldsymbol{\theta}}_N$ is thus solely based on measurements of $r$ and $y$.

As the data set that is used for identification is different for the two methods, the expression of the inverse covariance matrix (2.9) is also different; compare (2.16)-(2.17) with (2.11)-(2.12). An exception is the case of an open-loop situation, for which $C(z) = 0$ and $S(z) = 1$, leading to identical expressions of $\boldsymbol{F}_r(z)$ and $\boldsymbol{F}_v(z)$ for both methods.

The same input signal $r[n]$ can thus lead to different variances of the parameters in $\hat{\boldsymbol{\theta}}_N$ when employing the Direct or Indirect Method. Clearly, the selection of the signals that are to be used for the identification play a role in the quality of the estimate. We will make use of this property in Chapter 7 in which we compare optimal input signals designed for a Direct and Indirect identification experiment.

**Remark 2.2** *The Indirect Method is actually more general than shown here. We assume that the model structures and orders of $S(q,\boldsymbol{\theta})$, $G(q,\boldsymbol{\theta})$, and $H(q,\boldsymbol{\theta})$ are known. Consequently, we can directly identify $\boldsymbol{\theta}_0$ by employing (2.13) in the least-squares method. In general, the Indirect Method consists of two steps: 1) identifying the models $G_{IM}(q,\boldsymbol{\eta})$ and $H_{IM}(q,\boldsymbol{\eta})$, where $\boldsymbol{\eta}$ is the parameter vector of the closed-loop transfer function $G_{IM}(q,\boldsymbol{\eta})$ that is different from $\boldsymbol{\theta}$, and 2) use knowledge of the controller to calculate $\hat{\boldsymbol{\theta}}_N$ from the relations $\frac{G(\hat{\boldsymbol{\theta}}_N)}{1+C(q)G(q,\hat{\boldsymbol{\theta}}_N)} = G_{IM}(q,\hat{\boldsymbol{\eta}}_N)$ and $\frac{H(\hat{\boldsymbol{\theta}}_N)}{1+C(q)G(q,\hat{\boldsymbol{\theta}}_N)} = H_{IM}(q,\hat{\boldsymbol{\eta}}_N)$. We refer the reader to (Ljung (1999)) for details. The method presented here is thus a tailor-made version of the Indirect Method, but we shall nonetheless refer to it as the Indirect Method as no other version will be used.*

## 2.3 Summary

In this chapter, the Prediction Error Method, the Direct Method, and Indirect Method are described for a discrete-time single-input single-output closed-loop system. Known expressions for the inverse covariance matrices of the parameter estimate of a Direct and Indirect identification experiment are presented. These matrices play a crucial role in Optimal Experiment Design as they are a function of the spectrum of the excitation signal. It is this signal that we will in some sense optimally design in the next chapter.

# 3

# The Basics of Least-Costly Experiment Design

*"I consider that I understand an equation when I can predict the properties of its solutions, without actually solving it."* - Paul A.M. Dirac

## 3.1 Introduction

In the Introduction a non-exhaustive overview of results in the field of experiment design has been given. In the last twenty years many experiment design problems have been formulated and analysed, each with its own application in mind. We focus in this chapter on *Least-Costly Experiment Design* (LCED) problems. The aim of these problems is to find the optimal input signal that leads to some minimal experiment cost, while user-defined accuracy constraints on the to-be-identified parameter vector are satisfied. The solution to such a problem ensures that the experimental data is highly informative for the intended purpose of the identified model by finding frequencies at which a high signal-to-noise ratio and high sensitivity of the system to parameter changes are present (see the two examples in Chapter 1).

One type of LCED problems considers the minimisation of the disruptive effect that the excitation signal induces on the nominal closed-loop system, measured for instance by a weighted power of this signal, such that parameter accuracy constraints are nonetheless satisfied. The design variable in the problem is the power spectrum of the excitation signal; the experiment length is considered fixed.

A related LCED problem is to minimise the experiment length by finding the optimal excitation signal that ensures that a bound on a weighted sum of input and output powers is satisfied. This problem is connected to one in which the experiment length is minimised subject to bounds on the amplitudes of e.g. the input and output signal. We will consider this highly-relevant problem in a later chapter.

In this chapter we consider the classical LCED framework as introduced by Bombois et al. (2006). Section 3.2 introduces this classical framework. We explain how such optimisation problems can be numerically solved, and discuss the so-called chicken-and-egg issue in Section 3.2.2. In Section 3.2.3 we provide several examples of optimisation prob-

lems with specific parameter accuracy constraints that are quite pervasive in literature. In Section 3.3 we provide an extensive geometric interpretation of these problems.

## 3.2 The LCED Framework

### 3.2.1 The Optimisation Problem and Its Solution

We consider the closed-loop system as defined by (2.1)-(2.2) in Chapter 2, see Fig. 2.2. The expression of the inverse covariance matrix (2.9) of the parameter estimate $\hat{\theta}_N$ is a functional of the spectrum of the excitation signal $r$. This expression can thus be used to design an excitation signal that changes the accuracy of the parameter estimate to the wishes of the user. In this section we introduce the classical least-costly experiment design framework that aims to design the excitation leading to a parameter vector estimate (resulting from an identification experiment) that satisfies user-imposed accuracy constraints while nonetheless keeping the experiment cost minimal.

The LCED optimisation problem is defined as follows:

$$\min_{\Phi_r} \frac{T_s}{2\pi} \int_{-\pi/T_s}^{\pi/T_s} \mathscr{L}(e^{-i\omega T_s}, \boldsymbol{\theta}_0) \Phi_r(\omega) \, d\omega \tag{3.1}$$

subject to

$$\forall j = 1, \ldots, J: \ \mathbf{P}_{N,\theta}^{-1}[\Phi_r] \succeq \mathbf{R}_{adm}(j), \tag{3.2}$$

in which $\mathbf{P}_{N,\theta}^{-1}$ the $\kappa \times \kappa$-dimensional inverse covariance matrix defined by (2.9), $\mathbf{R}_{adm}(j)$ an equally-sized symmetric matrix, $T_s$ the sampling time, and $J \in \mathbb{N}^+$ an application-specific constant that sets the number of parameter accuracy constraints. The experiment length $N$ is fixed in this formulation.

The objective function (3.1), or cost functional, is defined as the weighted power of the excitation signal $r$, in which $\mathscr{L}(e^{-i\omega T_s}, \boldsymbol{\theta}_0)$ is an even and positive scalar function. The accuracy constraints (3.2) are matrix inequalities linear in $\Phi_r(\omega)$, and are different for each application. These constraints are called Linear Matrix Inequalities[1]. The symmetric matrices $\boldsymbol{R}_{adm}(j)$ are as-of-yet unspecified and depend on the intended application and user requirements. The LMI $\boldsymbol{P}_{N,\theta}^{-1} \succeq \boldsymbol{R}_{adm}$ means that $\forall \boldsymbol{x}: \ \boldsymbol{x}^T \boldsymbol{P}_{N,\theta}^{-1} \boldsymbol{x} \geq \boldsymbol{x}^T \boldsymbol{R}_{adm} \boldsymbol{x}$. Hence, for any $c \in \mathbb{R}^+$, the volume $\boldsymbol{x}^T \boldsymbol{P}_{N,\theta}^{-1} \boldsymbol{x} \leq c$ lies completely inside the volume $\boldsymbol{x}^T \boldsymbol{R}_{adm} \boldsymbol{x} \leq c$.

Let us elaborate on the objective function (3.1). One of the simplest weighting functions is $\mathscr{L}(e^{-i\omega T_s}, \boldsymbol{\theta}_0) = 1 \, \forall \omega \in [-\pi/T_s, \pi/T_s]$ (or any other constant value). In this case, each frequency is equally weighted and consequently the objective function is defined as the power of the excitation signal $r$. A more common choice of $\mathscr{L}(e^{-i\omega T_s}, \boldsymbol{\theta}_0)$ reads

$$\mathscr{L}(e^{-i\omega T_s}, \boldsymbol{\theta}_0) = \left( \alpha |G_0(e^{-i\omega T_s})|^2 + \beta \right) |S(e^{-i\omega T_s}, \boldsymbol{\theta}_0)|^2, \tag{3.3}$$

which leads to an objective function that is the sum of powers of the input signal component $u_r[n] = S_0(q)r[n]$ (weighted by $\beta \in \mathbb{R}^+$) and output signal component $y_r[n] =$

---

[1]Notice that the objective function (3.1) is linear in $\Phi_r$, and that each constraint in (3.2) is affine in $\Phi_r$ by virtue of the expression of the inverse covariance matrix defined in (2.9).

$S_0(q)G_0(q)r[n]$ (weighted by $\alpha \in \mathbb{R}^+$) induced by the excitation signal $r[n]$ (Bombois et al. (2006)). This is a sensible choice as the perturbations due to the excitation signal are then minimised when using (3.3) in (3.1)-(3.2) - a favourable property when applying the optimal excitation signal resulting from this optimisation problem to for instance industrial processes. Indeed, adding an excitation signal disrupts the nominal operating conditions and can lead to e.g. product quality deterioration. Hence, minimising the power of the induced perturbations is good practice.

**Remark 3.1** *Observe that only the ratio $\alpha/\beta$ influences the solution of (3.1)-(3.2) in the case (3.3). This can be seen by substituting (3.3) in (3.1) and rewriting the resulting expression by moving $\beta$ outside the integral. The cost can increase or decrease, but the solution to the problem does not change.*

In the case of an open-loop system we have $C(z) = 0$ and thus $u = r$ and $S(q,\theta_0) = 1$, see Fig. 2.2. The excitation signal $r$ is thus directly applied to the system (2.2). The expression of $P_{N,\theta}^{-1}$ for open-loop experiments is a special case of its closed-loop expression (2.9). The equivalent of the popular weighting function (3.3) is then given by

$$\mathscr{L}(e^{-i\omega T_s}, \theta_0) = \left( \alpha |G_0(e^{-i\omega T_s})|^2 + \beta \right). \tag{3.4}$$

The optimisation problem (3.1)-(3.2) is convex for open- and closed-loop systems since the objective function and LMI's are affine in the spectrum $\Phi_r(\omega)$. To solve this problem numerically, the infinite-dimensional spectrum $\Phi_r(\omega)$ must first be parameterised. Two possibilities are:

- An input generated as the output of a $M$-th order FIR-filter driven by white noise, having a spectral density

$$\Phi_r(\omega) = \sum_{m=-M}^{M} c_l e^{im\omega T_s} \tag{3.5}$$

  where $c_m = c_{-m}$, $m = 0,\dots,M$ are the decision variables. An additional LMI constraint on the decision variables $\{c_m\}_{m=0}^{M}$ has to be added to ensure $\forall \omega : \Phi_r(\omega) \geq 0$ in the convex algorithm.

- An input parameterised as a multi-sine with $M$ harmonics, defined by a spectral density

$$\Phi_r(\omega) = \frac{\pi}{2T_s} \sum_{m=1}^{M} A_m^2 \left( \delta(\omega - m\omega_f) + \delta(\omega + m\omega_f) \right), \tag{3.6}$$

  where the squared amplitudes $\{A_m^2\}_{m=1}^{M}$ of the time-domain signal are now the decision variables. The fundamental frequency $\omega_f$ of the multi-sine should be chosen a-priori (it is not a decision variable). This signal has a time-domain realisation

$$r[n] = \sum_{m=1}^{M} A_m \sin(m\omega_f n T_s + \phi_m)$$

  in which $\phi_m$ is an arbitrary phase for mode $m$.

With a finite parameterisation, a Matlab toolbox such as CVX can solve the optimisation problem (3.1)-(3.2). In the case of the multi-sine parameterisation this optimisation

problem becomes

$$\min_{\{A_m^2\}_{m=1}^M} \frac{1}{2} \sum_{m=1}^M \mathscr{L}(e^{-im\omega_f T_s}) A_m^2 \tag{3.7}$$

subject to

$$\forall j = 1, \ldots, J : \frac{N}{2\sigma_e^2} \sum_{m=1}^M A_m^2 \mathrm{Re} \left\{ \boldsymbol{F}_r(e^{-im\omega_f T_s}) \boldsymbol{F}_r^H(e^{-im\omega_f T_s}) \right\} + \boldsymbol{R}_0 \succeq \boldsymbol{R}_{adm}(j) \tag{3.8}$$

which is obtained by substituting $\Phi_r(\omega)$ with (3.6) and using (2.9). Notice that this problem is affine in the decision variables $\{A_m^2\}_{m=1}^M$. This particular parametrisation will be often used in future chapters.

In general, i.e. for any parameterisation, the solution to the optimisation problem is used to generate a time-domain excitation signal $r[n] = r_{opt}[n]$, which in turn is used in either the Direct or Indirect identification method explained in Chapter 2.

### 3.2.2 Chicken-and-Egg Issue

The objective function and accuracy constraint in the optimisation problem (3.1)-(3.2) depend on the true parameter vector $\theta_0$ and noise variance $\sigma_e^2$. Yet, prior to the identification experiment, $\theta_0$ and $\sigma_e^2$ are unknown. The optimisation problem thus suffers from the chicken-and-egg dilemma. This should not come as a total surprise, since in order to determine an optimal excitation signal, knowledge about the system must be present. In order to circumvent this problem, it is common to replace the true values of the parameter and variance with some estimates. These can for instance be obtained from prior experiments. More sophisticated techniques are formulated in (Gerencsèr et al. (2009); Larsson et al. (2013); Forgione et al. (2013)).

In the remainder of this work the chicken-and-egg issue will largely be ignored and consequently (3.1)-(3.2) will be solved as if we had full knowledge of the system. However, we will address the chicken-and-egg issue in some case studies and show that optimal experiment design is nonetheless a powerful technique over e.g. white noise signal realisations.

### 3.2.3 Examples of LMI Constraints

Let us now consider some examples of LCED problems. To this end, we will specify for particular applications the matrices $\boldsymbol{R}_{adm}(j)$ that appear in the constraints of (3.1)-(3.2). These examples will be used in future chapters.

#### Performance-relevant Constraints

In many real-life situations an identified model $G(z, \hat{\boldsymbol{\theta}}_N)$ is used to design a controller of a process represented by $G(z, \theta_0)$. For example, the identified parameter can be used in a controller $C(\hat{\boldsymbol{\theta}}_N)$ that depends on the estimate $\hat{\boldsymbol{\theta}}_N$.

Let us assume that the best control performance of the closed loop defined by $(G(z, \theta_0), C(\theta))$ is achieved when $\theta = \hat{\boldsymbol{\theta}}_N = \theta_0$, since the true system in this case is known exactly. We quantify the system's performance degradation by the *application cost* $V_{app}(\boldsymbol{\theta})$. By assumption, the function should attain its minimum value $V_{app}(\boldsymbol{\theta}) = 0$ at $\boldsymbol{\theta} = \theta_0$. To

ensure the function is minimal for this value of $\boldsymbol{\theta}$, it has the additional properties: (i) $[\nabla_{\boldsymbol{\theta}} V_{app}(\boldsymbol{\theta})]_{\boldsymbol{\theta}=\boldsymbol{\theta}_0} = \mathbf{0}$ and (ii) $V_{app}''(\boldsymbol{\theta}_0) \succeq \mathbf{0}$ ($V_{app}''(\boldsymbol{\theta}_0)$ is the Hessian of $V_{app}(\boldsymbol{\theta})$ evaluated at $\boldsymbol{\theta} = \boldsymbol{\theta}_0$).

To quantify whether or not a model is considered of sufficient quality for control we impose the condition $V_{app}(\hat{\boldsymbol{\theta}}_N) \leq \frac{1}{\gamma}$, where $\gamma \in \mathbb{R}^+$ is an application-specific constant. Since the estimate $\hat{\boldsymbol{\theta}}_N$ is asymptotically normally distributed around $\boldsymbol{\theta}_0$, and the experiment length $N$ is generally large, we may consider $V_{app}(\boldsymbol{\theta})$ in the vicinity of $\boldsymbol{\theta}_0$. A second-order Taylor approximation of $V_{app}(\boldsymbol{\theta})$ around $\boldsymbol{\theta}_0$, using properties (i) and (ii), results in (Hjalmarsson (2009))

$$V_{app}(\boldsymbol{\theta}) \approx \frac{1}{2}(\boldsymbol{\theta} - \boldsymbol{\theta}_0)^T V_{app}''(\boldsymbol{\theta}_0)(\boldsymbol{\theta} - \boldsymbol{\theta}_0),$$

where by construction $V_{app}''(\boldsymbol{\theta}_0)$ is symmetric and positive definite. Using this expression, we can define the set

$$\Theta_{app}(\gamma) = \left\{ \boldsymbol{\theta} \mid \frac{1}{2}(\boldsymbol{\theta} - \boldsymbol{\theta}_0)^T V_{app}''(\boldsymbol{\theta}_0)(\boldsymbol{\theta} - \boldsymbol{\theta}_0) \leq \frac{1}{\gamma} \right\}. \tag{3.9}$$

This ellipsoidal region thus contains the model parameters that deliver acceptable performance. Hence, if $\hat{\boldsymbol{\theta}}_N \in \Theta_{app}(\gamma)$ an acceptable model is obtained. Multiplying the inequality in (3.9) on both sides with $\gamma \chi_\alpha^2(\kappa)$, we see from (3.9) and (2.6) that $\hat{\boldsymbol{\theta}}_N \in \Theta_{app}(\gamma)$ with a probability of at least $\alpha$ if the LMI

$$P_{N,\boldsymbol{\theta}}^{-1} \succeq R_{adm} = \frac{\gamma \chi_\alpha^2(\kappa)}{2} V_{app}''(\boldsymbol{\theta}_0) \tag{3.10}$$

is satisfied. The optimisation problem for performance-relevant constraints is thus defined by (3.1)-(3.2) for $J = 1$ in which $R_{adm}$ is given in (3.10).

**Example 3.1** *Consider an industrial plant $G(\boldsymbol{\theta}_0)$ that produces a liquid. The liquid needs to be of high quality for commercial purposes, requiring the amount of impurities in the product to be small. The plant is regulated by a controller $C(\boldsymbol{\theta})$. Let us define the concentration of the impurities in the liquid produced in the closed-loop system $(G(\boldsymbol{\theta}_0), C(\boldsymbol{\theta}))$ at time n by the scalar function $\mathscr{I}[n; G(\boldsymbol{\theta}_0), C(\boldsymbol{\theta})]$. Let us now assume that we obtain the lowest concentration of the impurities when the controller $C(\boldsymbol{\theta}) = C(\boldsymbol{\theta}_0)$, i.e., the closed-loop system operates optimally when the controller utilises the exact plant dynamics (through $\boldsymbol{\theta}_0$). Then, the function $\mathscr{I}[n; G(\boldsymbol{\theta}_0), C(\boldsymbol{\theta}_0)]$ yields the best impurities concentration as a function of time, and can thus serve as a benchmark.*

*The application cost $V_{app}(\boldsymbol{\theta})$ can therefore be defined by*

$$V_{app}(\boldsymbol{\theta}) = \frac{1}{N_{win}} \sum_{n=1}^{N_{win}} (\mathscr{I}[n; G(\boldsymbol{\theta}_0), C(\boldsymbol{\theta})] - \mathscr{I}[n; G(\boldsymbol{\theta}_0), C(\boldsymbol{\theta}_0)])^2,$$

*in which $N_{win}$ sets the length of a user-defined time window, and $\mathscr{I}[n; G(\boldsymbol{\theta}_0), C(\boldsymbol{\theta})]$ is the impurities concentration in the liquid of the closed loop $(G(\boldsymbol{\theta}_0), C(\boldsymbol{\theta}))$ at time n. The application cost $V_{app}(\boldsymbol{\theta})$ thus compares the performance of a closed loop defined by $(G(\boldsymbol{\theta}_0), C(\boldsymbol{\theta}))$ to the (assumed) optimal loop $(G(\boldsymbol{\theta}_0), C(\boldsymbol{\theta}_0))$. The application cost trivially satisfies $V_{app}(\boldsymbol{\theta}_0) = 0$ and the aforementioned properties (i) and (ii). The application cost*

*is computed by simulating the impurities concentration for the closed loops $(G(\theta_0), C(\theta_0))$ and $(G(\theta_0), C(\theta))$. We refer the reader to (Larsson (2014)) for more details.*

**Remark 3.2** *Observe that the constraint matrix $\mathbf{R}_{adm}$ in (3.10) and the $V_{app}(\theta)$ function in Example 3.1 depend on $\theta_0$. These are occurrences of the chicken-and-egg issue that is inherent to optimal experiment design; see Section 3.2.2. However, in practice, one typically replaces $\theta_0$ with an old estimate $\hat{\theta}_N$ that is available from e.g. a previous identification experiment.*

### Variance Constraints

There exist many experiment set-ups that are used to estimate physical parameters of e.g. a solid or liquid. An example is the estimation of porosity and permeability of a sample of rock from a subsurface reservoir (Heller et al. (2002)). In this and many other set-ups a user-designed signal is added and an output signal is measured. These signals are then used to estimate the unknown parameters with for instance a least-squares criterion, see Chapter 2. In order to accurately estimate each parameter of the $J$ entries $\theta_{0,j}$ of the vector $\theta_0$ containing all physical parameters, we can use LCED to design an optimal input signal that minimises the cost while ensuring that

$$\forall j = 1\ldots,J: \ \hat{\theta}_{N,j} \in [-\Delta\theta_j + \theta_{0,j}, \theta_{0,j} + \Delta\theta_j] \text{ w.p. } \alpha. \tag{3.11}$$

These constraints ensure with probability $\alpha$ that the estimates $\hat{\theta}_{N,j}$ lie in the above-defined intervals with the true values $\theta_{0,j}$ as centers. In this equation, the values $\Delta\theta_j$ are defined by the user and determine the size of the interval (i.e. the accuracy). From (2.6) it follows by definition that the size of the interval containing $\hat{\theta}_{N,j}$ with probability $\alpha$ is given by

$$\left[ -\sqrt{\chi_\alpha^2(\kappa)}\sigma_j + \theta_{0,j}, \theta_{0,j} + \sqrt{\chi_\alpha^2(\kappa)}\sigma_j \right], \tag{3.12}$$

where $\sigma_j$ is the standard deviation of $\hat{\theta}_{N,j}$. Equations (3.11) and (3.12) then trivially lead to the constraints $\forall j = 1,\ldots J: \ \sigma_j \leq \Delta\theta_j / \sqrt{\chi_\alpha^2(\kappa)}$, resulting in the variance conditions

$$\forall j = 1,\ldots,J: \ \sigma_j^2 = e_j^T P_{N,\theta} e_j \leq \frac{(\Delta\theta_j)^2}{\chi_\alpha^2(\kappa)}, \tag{3.13}$$

with $e_j$ the $j$-th unit vector and $P_{N,\theta}$ the covariance matrix of the estimate $\hat{\theta}_N$. Using Schur's complement (Boyd and Vandenberghe (2003)) we then write these constraints as

$$\forall j = 1,\ldots,J: \ P_{N,\theta}^{-1}[\mathbf{A}] \succeq \mathbf{R}_{adm}(j) = \mathbf{e}_j \mathbf{e}_j^T \frac{\chi_\alpha^2(\kappa)}{(\Delta\theta_j)^2}, \tag{3.14}$$

where $\mathbf{R}_{adm}(j)$ is symmetric. The optimisation problem for variance constraints is thus defined by (3.1)-(3.2) in which $\mathbf{R}_{adm}(j)$ is defined in (3.13) for $j = 1,\ldots,J$.

**Example 3.2** *Consider the transfer function $G(z, \theta_0) = \frac{az^{-1}}{1+bz^{-1}}$, where $\theta_0 = (a,b)^T$. We wish to perform an identification experiment such that the estimates $\hat{a}_N$ and $\hat{b}_N$ lie with a probability of at least $\alpha = 0.99$ inside the interval $[0.99a, 1.01a]$ and interval $[0.98b, 1.02b]$,*

*respectively. In other words, the estimates $\hat{a}_N$ and $\hat{b}_N$ should not deviate more than respectively 1% and 2% of the true values $a$ and $b$ with a probability of at least $\alpha = 0.99$. Then the variance constraints (3.13) read*

$$\sigma_1^2 \leq \frac{(0.01a)^2}{\chi_{0.99}^2(2)}, \ \sigma_2^2 \leq \frac{(0.02b)^2}{\chi_{0.99}^2(2)},$$

*where we trivially have that $J = 2$ and $\kappa = \dim(\boldsymbol{\theta}_0) = 2$.*

**Frequency-wise Constraints**

Multiple LMI constraints also arise in the case where robustness analysis arguments are used to determine the largest additive uncertainty $r_{adm}(\omega)$ that can be allowed around the frequency response of the identified model to enable satisfactory robust control design. The associated mathematical condition is formulated as

$$\forall \omega : \ |G(e^{-i\omega}, \hat{\boldsymbol{\theta}}_N) - G_0(e^{-i\omega})| < r_{adm}(\omega),$$

where $\omega \in [0, \pi)$. This condition must in theory hold at each frequency, but a grid of the frequency range is often used instead, yielding a finite set of constraints

$$\forall j = 1, \ldots, J : \ |G(e^{-i\omega_j}, \hat{\boldsymbol{\theta}}_N) - G_0(e^{-i\omega_j})| < r_{adm}(\omega_j), \tag{3.15}$$

with $J$ the number of frequencies in the grid. The thresholds $r_{adm}(\omega_j)$ are computed with robust analysis techniques, see for instance the work of Ferreres and Fromion (1997).

    Bombois and Scorletti (2012) aim to ensure (3.15) with probability $\alpha$. For this purpose, using a first-order approximation, the ellipsoid $\mathscr{E}$ containing $\boldsymbol{\theta}_0$ (with probability $\alpha$) is projected in the frequency domain. This projection yields, at each frequency, an ellipse in the Nyquist plane centered at $G(e^{-i\omega}, \hat{\boldsymbol{\theta}}_N)$, defined with the matrix

$$\boldsymbol{P}(\omega) = \chi_\alpha^2(\kappa) \boldsymbol{T}^H \boldsymbol{P}_{N,\theta}[\Phi_r] \boldsymbol{T},$$

where $\boldsymbol{T} = (\text{Re}([\nabla_{\boldsymbol{\theta}} G(e^{-i\omega}, \boldsymbol{\theta})]_{\boldsymbol{\theta}=\boldsymbol{\theta}_0}), \text{Im}([\nabla_{\boldsymbol{\theta}} G(e^{-i\omega}, \boldsymbol{\theta})]_{\boldsymbol{\theta}=\boldsymbol{\theta}_0}))$, see (Bombois and Scorletti (2012)). These ellipsoids contain, with (at least) the same probability $\alpha$, the frequency response of the true system. Consequently, the modulus of the modelling error (i.e. the l.h.s. of 3.15) is bounded by

$$r_{adm}(\omega_j) = \sqrt{\lambda_{max}(\boldsymbol{P}(\omega))}.$$

Expression (3.15) can thus be rewritten as the following matrix inequality:

$$\boldsymbol{T}^H \boldsymbol{P}_{N,\theta} \boldsymbol{T} \leq \frac{r_{adm}^2(j)}{\chi_\alpha^2(\kappa)} \boldsymbol{I}_{2 \times 2},$$

which, via Schur complements, can be rewritten in the form (3.2):

$$\forall j = 1, \ldots J : \ \boldsymbol{P}_{N,\theta}^{-1}[\Phi_r] \succeq \boldsymbol{R}_{adm}(j) = \frac{\chi_\alpha^2(\kappa)}{r_{adm}^2(\omega_j)} \boldsymbol{T} \boldsymbol{T}^H. \tag{3.16}$$

The optimisation problem for frequency-wise constraints is thus defined by (3.1)-(3.2) with $\boldsymbol{R}_{adm}(j)$ defined in (3.16) for $j = 1, \ldots, J$.

## 3.3 Geometric Interpretation

In Section 3.2 it is briefly mentioned that the LMI $\boldsymbol{P}_{N,\boldsymbol{\theta}}^{-1} \succeq \boldsymbol{R}_{adm}$ is equivalent to the statement that $\forall \boldsymbol{x} : \boldsymbol{x}^T \boldsymbol{P}_{N,\boldsymbol{\theta}}^{-1} \boldsymbol{x} \geq \boldsymbol{x}^T \boldsymbol{R}_{adm} \boldsymbol{x}$. Hence, for any $c \in \mathbb{R}^+$, the volume $\boldsymbol{x}^T \boldsymbol{P}_{N,\boldsymbol{\theta}}^{-1} \boldsymbol{x} \leq c$ is fully contained in the volume $\boldsymbol{x}^T \boldsymbol{R}_{adm} \boldsymbol{x} \leq c$. Here, we shall give a more detailed geometric interpretation.

Let us first consider the general case of singular $\boldsymbol{R}_{adm}(j)$'s in (3.2). An example is shown in Fig. 3.1. Here, we have two variance constraints ($J = 2$) as detailed in Section 3.2.3. The variance constraint on parameter $\theta_1$ is shown by the set of vertical lines $l_2$, and the constraint on $\theta_2$ by the set of horizontal lines $l_1$. The blue ellipse indicates the boundary of the confidence region. For the parameter $\theta_i$, we thus only constrain the estimate $\hat{\boldsymbol{\theta}}_N$ in one direction. This is reflected by the set of lines $l_i$ that define a tube (it may also be seen as a degenerate ellipse). However, since we have a constraint on the other parameter as well, the estimate is constrained to lie in the volume that results from the intersection of the tubes defined by the lines $l_1$ and $l_2$. In this particular two-dimensional case, we see that this volume is a rectangle.

In general, i.e. for $\dim(\boldsymbol{\theta}_0) > 2$, the concept remains the same. If we consider the above example for $\dim(\boldsymbol{\theta}) = 3$ the confidence ellipse becomes an ellipsoid, and the sets of lines become sets of two-dimensional planes. The intersections of these sets of planes then generates a three-dimensional box in which the confidence ellipsoid should lie. For even higher dimensions, we cannot visualise how these volumes look like, but the concept remains the same: the confidence hyperellipsoid should be contained in a hyper volume that follows from intersections of hyper-dimensional constraint objects (e.g. the generalisations of the sets of lines and planes).

**A Special Case**

It is insightful to also consider the special case where the matrices $\boldsymbol{R}_{adm}(j)$ are all non-singular, i.e., $\forall j = 1, \ldots, J : \det(\boldsymbol{R}_{adm}(j)) \neq 0$. In this case, the constraints can all be visualised as ellipsoids. For the sake of convenience, in the following we will only consider one constraint and simply denote it by $\boldsymbol{R}_{adm}$. Extension towards more constraints is straightforward.

In the following, we shall denote $\boldsymbol{P} = \boldsymbol{P}_{N,\boldsymbol{\theta}}^{-1}$ and $\boldsymbol{R} = \boldsymbol{R}_{adm}$. We recall that the LMI $\boldsymbol{P} \succeq \boldsymbol{R}$ is equal to

$$\forall \boldsymbol{\theta} : \boldsymbol{\theta}^T \boldsymbol{P} \boldsymbol{\theta} \geq \boldsymbol{\theta}^T \mathbf{R} \boldsymbol{\theta}, \tag{3.17}$$

in which $\kappa = \dim(\boldsymbol{\theta})$. From this expression we see that the LMI constraint means that the confidence ellipsoid defined by the boundary $\boldsymbol{\theta}^T \boldsymbol{P} \boldsymbol{\theta} = c$ should lie inside the ellipsoid $\boldsymbol{\theta}^T \boldsymbol{R} \boldsymbol{\theta} = c$, where $c \in \mathbb{R}^+$ some constant. A two-dimensional example is provided in Fig. 3.2a. The confidence ellipse is shown in red whereas the constraint ellipse is shown in black. The goal of least-costly experiment design is to find the optimal input spectrum such that the confidence ellipsoid lies inside the constraint ellipsoid at minimal cost. We
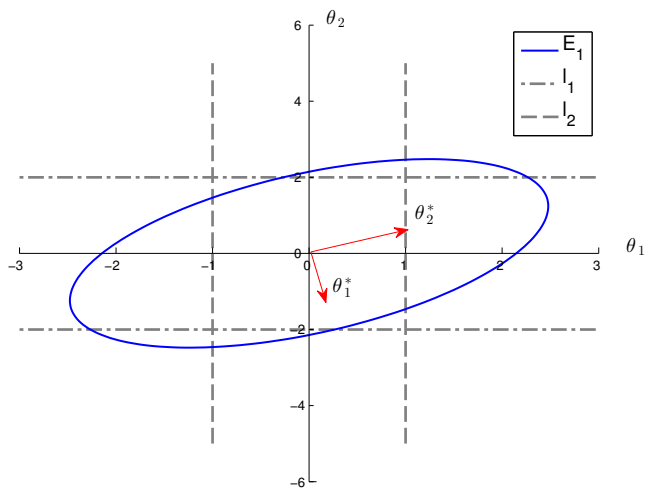
Figure 3.1: The blue ellipse $E_1$ corresponds to the boundary of the confidence region $\boldsymbol{\theta}^T \boldsymbol{P_\theta}^{-1} \boldsymbol{\theta} \leq \chi_\alpha^2(2)$. The dashed and dash-dotted grey line sets correspond to the constraints on parameter $\theta_1$ and $\theta_2$, respectively. The red arrows correspond to the eigenvector directions of $\boldsymbol{P_\theta}^{-1}$, and are orthogonal.
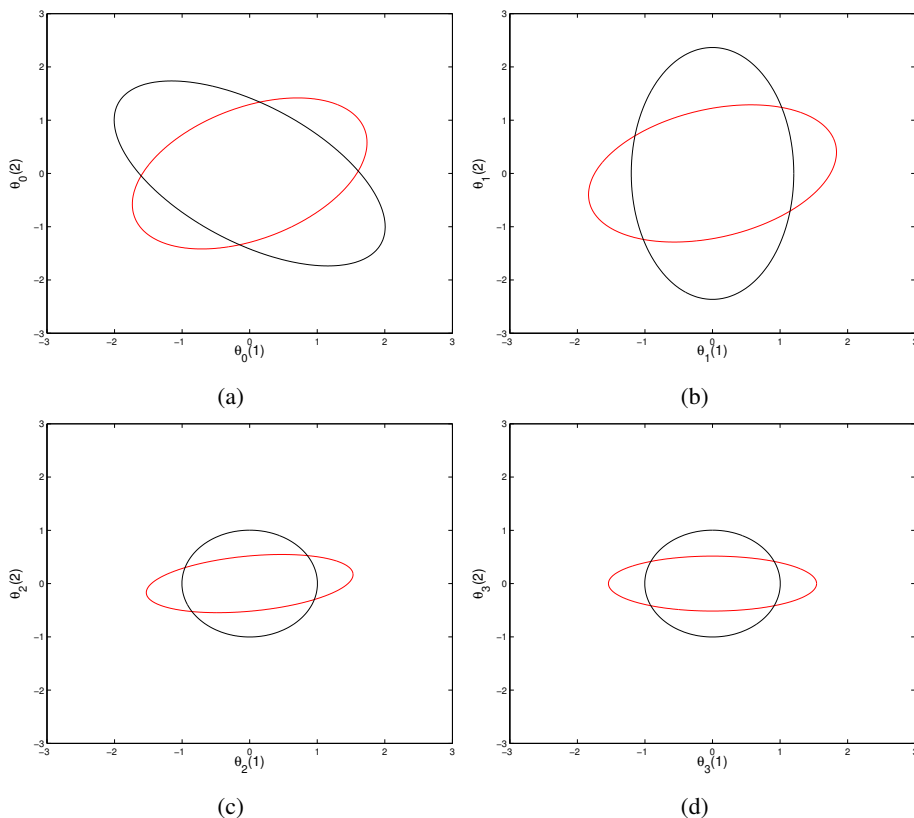


Figure 3.2: An example of the transformations 1-3 in the two-dimensional parameter space. The ellipse $\boldsymbol{\theta}^T \boldsymbol{R}_{adm} \boldsymbol{\theta} = 1$ ($\boldsymbol{\theta}^T \boldsymbol{P_\theta}^{-1} \boldsymbol{\theta} = 1$) is shown in black (red) in all plots. (a) Situation prior to transformations. (b) Ellipses after transformation $\boldsymbol{S}_1$. (c) Ellipses after transformations $\boldsymbol{S}_1$ and $\boldsymbol{S}_2$. (d) Ellipses after transformations $\boldsymbol{S}_1$, $\boldsymbol{S}_2$, and $\boldsymbol{S}_3$.

will now show how to simplify this geometric constraint.

For any dimension of the matrices $\boldsymbol{P}$ and $\boldsymbol{R}$, we apply the following three coordinate transformations in $\boldsymbol{\theta}$-space.

1. Coordinate change $\boldsymbol{\theta}_1 = \mathbf{S}_1\boldsymbol{\theta}$, where $\mathbf{S}_1$ is unitary such that $\mathbf{R}_1 = \mathbf{S}_1^T\mathbf{R}\mathbf{S}_1$ is diagonal. This unitary transformation is guaranteed to exist since $\mathbf{R}$ is symmetric and positive definite. The same transformation yields $\mathbf{P}_1 = \mathbf{S}_1^T\mathbf{P}\mathbf{S}_1$. The resulting matrices $\mathbf{P}_1$ and $\mathbf{R}_1$ are again symmetric and positive definite. An example of such a transformation is shown in Fig. 3.2b. Here, we go from coordinate frame $\boldsymbol{\theta}_0$ (Fig. 3.2a) to coordinate frame $\boldsymbol{\theta}_1$.

2. Coordinate change $\boldsymbol{\theta}_2 = \mathbf{S}_2\boldsymbol{\theta}_1$, where $\mathbf{S}_2 = \mathbf{R}_1^{-1/2}$ is a non-unitary transformation matrix that ensures that $\mathbf{R}_2 = \mathbf{S}_2^T\mathbf{R}_1\mathbf{S}_2 = \mathbf{I}$ is the identity matrix. The same transformation makes $\mathbf{P}_2 = \mathbf{S}_2^T\mathbf{P}_1\mathbf{S}_2$. Both are again symmetric and positive definite. An example of such a transformation is shown in Fig. 3.2c. Here, we go from coordinate frame $\boldsymbol{\theta}_1$ (Fig. 3.2b) to coordinate frame $\boldsymbol{\theta}_2$.

3. Coordinate change $\boldsymbol{\theta}_3 = \mathbf{S}_3\boldsymbol{\theta}_2$, where $\mathbf{S}_3$ is a unitary matrix such that $\mathbf{P}_3 = \mathbf{S}_3^T\mathbf{P}_2\mathbf{S}_3$ is diagonal. This transformation is guaranteed to exist since $\mathbf{P}_2$ is symmetric and positive definite. The same transformation also yields $\mathbf{R}_3 = \mathbf{S}_3^T\mathbf{R}_2\mathbf{S}_3 = \mathbf{R}_2 = \mathbf{I}$. An example of such a transformation is shown in Fig. 3.2d. Here, we go from coordinate frame $\boldsymbol{\theta}_2$ (Fig. 3.2c) to coordinate frame $\boldsymbol{\theta}_3$.

The result of the coordinate transformations 1-3 is as follows. In the $\boldsymbol{\theta}_3$-coordinate system the original ellipsoids $\boldsymbol{\theta}^T\mathbf{P}\boldsymbol{\theta}$ and $\boldsymbol{\theta}^T\mathbf{R}\boldsymbol{\theta}$ are now given by respectively

$$\boldsymbol{\theta}_3^T\mathbf{P}_3\boldsymbol{\theta}_3 \quad = \quad \sum_{i=1}^{\dim(\boldsymbol{\theta})} \lambda_i(\mathbf{P}_3)\theta_{3,i}^2, \tag{3.18}$$

$$\boldsymbol{\theta}_3^T\mathbf{R}_3\boldsymbol{\theta}_3 \quad = \quad \sum_{i=1}^{\dim(\boldsymbol{\theta})} \lambda_i(\mathbf{R}_3)\theta_{3,i}^2 = \sum_{i=1}^{n} \theta_{3,i}^2. \tag{3.19}$$

The transformations have greatly simplified the problem as both ellipsoids now have principal axes that are aligned with the axes of the coordinate system, i.e., the matrices $\mathbf{P}_3$ and $\mathbf{R}_3$ are both diagonal. The LMI $\mathbf{P} \succeq \mathbf{R}$ constraint in $\boldsymbol{\theta}_3$-space is equivalent to, using (3.17), $\forall \boldsymbol{\theta}_3 : \boldsymbol{\theta}_3^T\mathbf{P}_3\boldsymbol{\theta}_3 \geq \boldsymbol{\theta}_3^T\mathbf{R}_3\boldsymbol{\theta}_3$. From (3.18)-(3.19), this generates the constraints

$$\forall i = 1,\ldots,\dim(\boldsymbol{\theta}) : \quad \lambda_i(\mathbf{P}_3) \geq \lambda_i(\mathbf{R}_3) = 1, \tag{3.20}$$

where $n$ is the total number of eigenvalues.

The next step is to prove that the eigenvalues of $\mathbf{P}_3$ are equal to the eigenvalues of $\mathbf{P}\mathbf{R}^{-1}$. In what follows we shall consider the eigenvalue $\lambda_i$, but the computations hold for all eigenvalues $i = 1,\ldots,n$.

First, we show that $\lambda_i(\mathbf{P}_2) = \lambda_i(\mathbf{P}_3)$. Starting from the characteristic equation of matrix $\mathbf{P}_2$

$$\det(\mathbf{P}_2 - \lambda_i\mathbf{I}) = 0, \tag{3.21}$$

we see that by multiplying it by $\det(\mathbf{S}_3^T)$ on the left and by $\det(\mathbf{S}_3)$ on the right we obtain

$$\det(\mathbf{S}_3^T)\det(\mathbf{P}_2 - \lambda_i\mathbf{I})\det(\mathbf{S}_3) = \det(\mathbf{S}_3^T\mathbf{P}_2\mathbf{S}_3 - \lambda_i\mathbf{I}) = 0, \tag{3.22}$$

where we used that $\mathbf{S}_3^T \mathbf{S}_3 = \mathbf{I}$ and note that $\mathbf{S}_3^T \mathbf{P}_2 \mathbf{S}_3 = \mathbf{P}_3$, see (iii). Hence, the eigenvalues are the same which is a consequence of the unitary transformation in step (iii).

Secondly, the matrix $\mathbf{P}_2$ is defined in step (ii) as $\mathbf{P}_2 = \mathbf{S}_2^T \mathbf{P}_1 \mathbf{S}_2$, where $\mathbf{S}_2 = \mathbf{R}_1^{-1/2}$. Hence, we have by definition that

$$\det(\mathbf{P}_2 - \lambda_i \mathbf{I}) = 0 \Leftrightarrow \det(\mathbf{S}_2^T \mathbf{P}_1 \mathbf{S}_2 - \lambda_i \mathbf{I}) = 0. \tag{3.23}$$

As $\mathbf{S}_2 = \mathbf{R}_1^{-1/2}$ is diagonal we have that $\mathbf{S}_2^T = \mathbf{S}_2$. Multiplying (3.23) on the l.h.s. with $\det(\mathbf{S}_2^{-1})$ and on the r.h.s. by $\det(\mathbf{S}_2)$ results in

$$\det(\mathbf{S}_2^{-1}) \det(\mathbf{S}_2^T \mathbf{P}_1 \mathbf{S}_2 - \lambda_i \mathbf{I}) \det(\mathbf{S}_2) = \det(\mathbf{P}_1 \mathbf{R}_1^{-1} - \lambda_i \mathbf{I}) = 0. \tag{3.24}$$

At this point we have proven that $\lambda_i(\mathbf{P}_3) = \lambda_i(\mathbf{P}_2) = \lambda_i(\mathbf{P}_1 \mathbf{R}_1^{-1})$.

Lastly, we substitute $\mathbf{P}_1 = \mathbf{S}_1^T \mathbf{P} \mathbf{S}_1$ and $\mathbf{R}_1 = \mathbf{S}_1^T \mathbf{R} \mathbf{S}_1$, see step (i), into (3.24) and find that

$$\det(\mathbf{P}_1 \mathbf{R}_1^{-1} - \lambda_i \mathbf{I}) = \det(\mathbf{S}_1^T \mathbf{P} \mathbf{S}_1 (\mathbf{S}_1^T \mathbf{R} \mathbf{S}_1)^{-1} - \lambda_i \mathbf{I}) = \det(\mathbf{S}_1^T (\mathbf{P} \mathbf{R}^{-1}) \mathbf{S}_1 - \lambda_i \mathbf{I}) = 0.$$

Since $\mathbf{S}_1$ is a unitary matrix it is clear that, as shown in (3.21) for the unitary matrix $\mathbf{S}_3$, that $\lambda_i(\mathbf{P}_1 \mathbf{R}_1^{-1}) = \lambda_i(\mathbf{P} \mathbf{R}^{-1})$. Hence, we have now proven that $\lambda_i(\mathbf{P}_3) = \lambda_i(\mathbf{P}_2) = \lambda_i(\mathbf{P}_1 \mathbf{R}_1^{-1}) = \lambda_i(\mathbf{P} \mathbf{R}^{-1})$.

The constraints (3.20) can thus be written as $\forall i : \lambda_i(\mathbf{P} \mathbf{R}^{-1}) \geq 1$. All these constraints can however be captured by a single one, i.e.,

$$\lambda_{min}(\mathbf{P} \mathbf{R}^{-1}) \geq 1. \tag{3.25}$$

Indeed, if the smallest eigenvalue $\lambda_{min}(\mathbf{P} \mathbf{R}^{-1}) \geq 1$, then all other eigenvalues are clearly also greater than or equal to unity. Finally, replacing by definition $\mathbf{P} = P_{N,\boldsymbol{\theta}}^{-1}$ and $\mathbf{R} = R_{adm}$ in (3.25) yields the expression

$$\lambda_{min} \left( P_{N,\boldsymbol{\theta}}^{-1} [\Phi_r] R_{adm}^{-1} \right) \geq 1. \tag{3.26}$$

This equation has a clear geometric meaning. From the above transformations we see that the previous equation corresponds to the situation that, in $\boldsymbol{\theta}_3$-space, the largest principal axis of the confidence ellipsoid (inversely proportional to the square root of the eigenvalue in (3.26)) is smaller than the largest principal axis of the constraint ellipse in the same space (which in $\boldsymbol{\theta}_3$-space takes the form of a ball). In fact, for the LCED problems, we have the optimality condition that equality should hold for (3.26).

## 3.4 Summary

In this chapter we have described the framework of Least-Costly Experiment Design framework. We have provided several examples that show how to find optimal input signals that minimise an experiment cost subject to e.g. constraints on the variance of the to-be-estimated parameters. We have furthermore provided a novel geometric interpretation of such constraints.

# 4

# An Analytical Treatment of Least-Costly Experiment Design

*"It's not that I'm so smart, it's just that I stay with problems longer."* - Albert Einstein

## 4.1 Introduction

With the advent of fast convex algorithms least-costly experiment design (LCED) problems like (3.1)-(3.2) could be efficiently solved (Bombois et al. (2006)). Over the years, many problems have been considered in literature and their optimal input spectra have been reported. However, questions like 'What mechanisms underlie the selection of the optimal input spectrum?', 'Do the optimal frequencies depend on the location(s) that the parameters occupy in the transfer function?' are difficult if not impossible to address numerically. [1]

   A major remaining challenge from a theoretical point of view is, thus, the interpretation of the optimal power spectra that result from these numerical algorithms. Analytical solutions to the LCED problems will enhance our understanding of the problem and provide insight into the mechanisms that should be exploited to find the optimal input signal. Additionally, these analytical solutions can be used to check the solutions of the numerical algorithms, and could in fact be hard-coded into an algorithm to provide solutions quicker than currently possible.

In this chapter steps are taken that provide understanding of the solutions of a select few LCED problems by solving them analytically. We shall in particular derive analytical solutions for uni- and bi-parametric models. Examples of the former type are

$$G(z, \theta_0) = \frac{a_1 z^{-1}}{1 + \theta_0 z^{-1} + b_2 z^{-2}}, \text{ and } G(z, \theta_0) = \frac{\theta_0 z^{-1}}{1 + \theta_0 z^{-1} + b_2 z^{-2}},$$

in which the scalar parameters $a_1$ and $b_2$ are known. Notice that $\theta_0$ only occupies one position in the first transfer function, whereas it occupies multiple positions in the second one.

---

[1] Parts of this chapter have been published in (Potters et al. (2015, 2016a)).

In general, $\theta_0$ may occupy an arbitrary number of positions. Examples of bi-parametric models are

$$G(z, \boldsymbol{\theta}_0) = \frac{\theta_1 z^{-1}}{1 + \theta_2 z^{-1}} \text{ and } G(z, \boldsymbol{\theta}_0) = \frac{a_1 z^{-1} + \theta_1 z^{-2}}{1 + \theta_1 z^{-1} + \theta_2 z^{-2} + b_3 z^{-3}},$$

in which the elements of $\boldsymbol{\theta}_0 = (\theta_1, \theta_2)^T$ may appear only once (the first example) or multiple times in the transfer function (the second example).

Admittedly, the appearance of uni- and bi-parametric *black-box* models are limited in the System Identification literature. However, they are quite pervasive in other domains such as medical imaging (Bombois et al. (2011); Manchester (2012)), reservoir engineering (Heller et al. (2002); Mansoori et al. (2014); Jansen (2013)), material sciences (Gabano and Poinot (2009)), etc.. This is mainly due to the fact that, in sharp contrast to black-box parameters, many physical parameters (e.g. the density of water, the speed of light) are precisely known and thus need not be identified. Frequently, these physical systems can be represented by continuous-time, irrational transfer functions. We will show in Chapter 6 that the result we will present in the sequel for discrete-time systems can be easily extended to the case of continuous-time systems.

Analytical solutions for some uni-parametric LCED problems have already been reported in the literature. Probably one of the first contributions is due to Zarrop, who proved that a single sine is a solution for uni-parametric models (Zarrop, 1979, p. 35-36). However, the optimal frequency provided in this book is only given for a special case due to normalisation, and no interpretation is given. Wahlberg et al. (2011) provide a specific solution for a uni-parametric LCED problem with one constraint by studying an open-loop output-error system. Malti et al. (2014) give a specific solution for a uni-parametric fractional model and consider a *D*-optimality criterion.

In this chapter we find analytical solutions for the LCED problem (3.1)-(3.2) for both uni- and bi-parametric systems when the optimal excitation signal is restricted to the class of a single sinusoid. More precisely, we provide an analytical expression for the amplitude and frequency of this optimal sinusoidal excitation. In the uni-parametric case, we furthermore show that this single sinusoid is in fact also the solution of (3.1)-(3.2) when no restriction whatsoever is imposed on the spectrum. For the bi-parametric case, we also provide arguments as to why this parametrisation of the spectrum as one sinusoid is not too restrictive in practice.

We thus find solutions to the generic LCED optimisation problem (3.1)-(3.2) that considers an arbitrary but finite number of parameter accuracy constraints, and which is valid for both open- and closed-loop identification problems (either the Direct or Indirect Method).

The outline of this chapter is as follows. Section 4.2 is dedicated to the derivation of the analytical solutions of (3.1)-(3.2) for both uni- and bi-parametric models. Interpretation of these solutions is given in Section 4.3 in which we also consider several illustrative examples.

## 4.2 Analytical Solutions

### 4.2.1 The Two Model Types

We consider the identification of plant transfer functions $G_0(z)$ using a model structure $G(z,\boldsymbol{\theta})$ containing one or two unknown parameters. The noise model $H(z,\boldsymbol{\theta}) = H(z)$ in (2.3) is assumed fixed for simplicity (i.e. it does not contain any parameter that requires identification). Since two parameters have to be identified in $G(z,\boldsymbol{\theta})$, the theory on persistency of excitation (Ljung (1999)) states that these parameters can be identified consistently with an excitation signal made up of one sinusoid. This is true for both open- and closed-loop identification. As a result, the obtained covariance matrix (2.9) is non-singular with this type of excitation. To nevertheless avoid pathological cases, we make the following assumption.

**Assumption 4.1** *We consider uni- and bi-parametric models for which an identification experiment using single sinusoid as excitation signal leads (assymptotically) to a non-singular covariance matrix.*

Since by assumption a single sinusoid is sufficient to generate a non-singular covariance matrix, we will design the optimal excitation as such and show that we can determine both the frequency and the amplitude of this signal. We consider thus the following parametrisation $\Phi_1$ for the optimal signal (we take a sampling time of $T_s = 1$ seconds throughout this chapter without loss of generality):

$$\Phi_1(\omega) = \frac{\pi A^2}{2} \sum_{l=\{-1,1\}} \delta(\omega + l\overline{\omega}). \tag{4.1}$$

where both $\overline{\omega}$ and $A$ are design variables. This spectrum has the following time-domain realisation:

$$r[n] = A\sin(\overline{\omega}n + \phi), \tag{4.2}$$

where $\phi$ can be chosen freely (it does not influence the spectrum). Note that, unlike in (3.6), we also optimise the frequency of the sinusoid.

One could wonder whether considering a multi-sine as in (3.6) or, more generic, a sum of sines (instead of a single sinusoid), would not lead to a smaller cost[2]. This is a relevant question. We show in the sequel that, for the uni-parametric case, one single sinusoid is indeed optimal (i.e. this signal leads to the global minimum of (3.1)-(3.2)). For the bi-parametric case, this result is not formally proven in this chapter as it would be quite involved. However, examples in (Zarrop (1979)) and (Javaherian (1974)) suggest that the optimal signal of optimisation problems like (3.1)-(3.2) are indeed made up of only one sinusoid. We furthermore give a heuristic argument in a future section.

### 4.2.2 Bi-Parametric Models

Let us particularise the optimisation problem (3.1)-(3.2) to the case of the identification of a bi-parametric model, and for which the spectrum is restricted to be in the class $\Phi_1$

---

[2]It should be stressed that adding additional sines to an input signal is often done in practice when the model order is not known exactly.

defined in (4.1). Let us first rewrite the optimisation problem as

$$\min_{\Phi_r \in \Phi_1} \frac{1}{2\pi} \int_{-\pi}^{\pi} \mathcal{L}(e^{-i\omega}) \Phi_r(\omega) \, d\omega \tag{4.3}$$

subject to

$$\forall j = 1, \ldots, J : \; P_{r,N,\theta}^{-1}[\Phi_r] \succeq R_{adm}(j) - R_0, \tag{4.4}$$

where the matrices in (4.4) are two-dimensional, and we made use of the definition of $P_{N,\theta}$ in (2.9) to move the term $R_0$ in the expression of the inverse covariance matrix to the right hand side of the LMIs, and in which $\Phi_1$ is the class of all single-sine spectra being a subset of all the possible spectra $\Phi_{tot}$.

An analytical solution is given in the theorem below, which requires the following lemma.

**Lemma 4.1** *Consider the $\kappa \times \kappa$-dimensional symmetric matrices $A \succ 0$ and $B \succeq 0$ and a positive scalar $\alpha$. Then the following statements are equivalent:*

1. *$\alpha A \succeq B$,*

2. *$\alpha \geq \lambda_{max} \left( A^{-1} B \right)$.*

**Proof:** Define $A^{-1/2} = (A^{-1/2})^T$ as the square root of the inverse of $A$. The inequality (1) is by definition equivalent to $\forall \theta : \; \alpha \theta^T A \theta \geq \theta^T B \theta$, where $\dim(\theta) = \kappa$. Define the transformation $\theta_1 = S_1 \theta$, where $S_1 = A^{1/2}$. Then (1) may be written as $\forall \theta : \; \alpha \theta_1^T I \theta_1 \geq \theta_1^T A^{-1/2} B A^{-1/2} \theta_1$, which is equivalent to

$$\alpha \geq \lambda_{max} \left( A^{-1/2} B A^{-1/2} \right). \tag{4.5}$$

The eigenvalues $\lambda$ of the matrix in (4.5) are found by solving

$$\det \left( A^{-1/2} B A^{-1/2} - \lambda I \right) = 0.$$

Multiplying this equation from the left with $\det(A^{-1/2})$ and with $\det(A^{1/2})$ from the right and using $A^{-1/2} A^{1/2} = I$ results in

$$\det(A^{-1/2}) \det \left( A^{-1/2} B A^{-1/2} - \lambda I \right) \det(A^{1/2}) = 0 =$$
$$\det(A^{-1} B - \lambda A^{-1/2} I A^{1/2}) = \det(A^{-1} B - \lambda I),$$

which shows that $\forall i = 1, \ldots, \kappa : \lambda_i \left( A^{-1/2} B A^{-1/2} \right) = \lambda_i \left( A^{-1} B \right)$. In particular, it follows that $\lambda_{max} \left( A^{-1/2} B A^{-1/2} \right) = \lambda_{max} \left( A^{-1} B \right)$. Substitution of this equality in (4.5) proves the equivalence between (1) and (2). $\qquad \square$

**Theorem 4.1** *Consider the optimisation problem (4.3)-(4.4) corresponding to the least-costly identification of a bi-parametric model for which Assumption 4.1 holds. Then the solution of this optimisation problem is given by*

$$\Phi_{r,opt}(\omega) = \frac{\pi \sigma_e^2}{N} \max_j \lambda_{max} \left( \left[ Re \left\{ F(e^{-i\omega_{opt}}) \right\} \right]^{-1} R(j) \right) \sum_{l=\{-1,1\}} \delta(\omega + l\omega_{opt}) \tag{4.6}$$

*in which*

$$\omega_{opt} = \arg\min_{\overline{\omega}} \left[ \mathscr{L}(e^{-i\overline{\omega}}, \boldsymbol{\theta}_0) \max_j \lambda_{max} \left( \left[ \operatorname{Re} \left\{ \boldsymbol{F}(e^{-i\overline{\omega}}) \right\} \right]^{-1} \boldsymbol{R}(j) \right) \right], \qquad (4.7)$$

$\sigma_e^2$ *is the variance of the white noise, and where* $\boldsymbol{F}(e^{-i\omega}) = \boldsymbol{F}_r(e^{-i\omega}) \boldsymbol{F}_r^H(e^{-i\omega})$ *and* $\boldsymbol{R}(j) = \boldsymbol{R}_{adm}(j) - \boldsymbol{R}_0$.

**Proof:** Let us start by a change of variables, i.e., define

$$\Phi_\xi(\omega) = \mathscr{L}(e^{-i\omega}, \boldsymbol{\theta}_0)\Phi_r(\omega). \qquad (4.8)$$

If $\Phi_r(\omega) \in \Phi_1$, then the spectrum $\Phi_\xi(\omega)$ defined in (4.8) also lies in $\Phi_1$, i.e., $\Phi_\xi(\omega) \in \Phi_1$, and is defined as

$$\Phi_\xi(\omega) = \frac{\pi C^2}{2} \sum_{l=\{-1,1\}} \delta(\omega + l\overline{\omega}). \qquad (4.9)$$

Moreover, the spectrum $\Phi_\xi(\omega)$ (4.8) has the same frequency $\overline{\omega}$ as $\Phi_r(\omega)$ and a squared amplitude that is related to the one of $\Phi_r(\omega)$ through $A^2 = C^2/\mathscr{L}(e^{-i\overline{\omega}}, \boldsymbol{\theta}_0)$. Using this change of variables we simplify the optimisation problem (4.3)-(4.4) to

$$\min_{\Phi_\xi \in \Phi_1} \frac{1}{2\pi} \int_{-\pi}^{\pi} \Phi_\xi(\omega) d\omega \qquad (4.10)$$

subject to

$$\forall j = 1, \ldots, J : \ \boldsymbol{P}_{r,N,\theta}^{-1} \left[ \frac{\Phi_\xi(\omega)}{\mathscr{L}(e^{-i\omega}, \boldsymbol{\theta}_0)} \right] \succeq \boldsymbol{R}_{adm}(j) - \boldsymbol{R}_0. \qquad (4.11)$$

Next, we inject the spectrum (4.9) in (4.10)-(4.11), and use (2.9) or (3.8) to obtain the optimisation problem

$$\min_{C^2, \overline{\omega}} \frac{1}{2} C^2 \qquad (4.12)$$

subject to

$$\forall j = 1, \ldots, J : \ \frac{NC^2}{2\sigma_e^2 \mathscr{L}(e^{-i\overline{\omega}}, \boldsymbol{\theta}_0)} \operatorname{Re} \left\{ \boldsymbol{F}_r(e^{-i\overline{\omega}}) \boldsymbol{F}_r^H(e^{-i\overline{\omega}}) \right\} \succeq \boldsymbol{R}_{adm}(j) - \boldsymbol{R}_0. \qquad (4.13)$$

We then rewrite the above $J$ LMI constraints as

$$C^2 \geq \frac{2\sigma_e^2 \mathscr{L}(e^{-i\overline{\omega}}, \boldsymbol{\theta}_0)}{N} \max_j \lambda_{max} \left( \left[ \operatorname{Re} \left\{ \boldsymbol{F}(e^{-i\overline{\omega}}) \right\} \right]^{-1} \boldsymbol{R}(j) \right), \qquad (4.14)$$

where $\boldsymbol{F}(e^{-i\omega})$ and $\boldsymbol{R}(j)$ are defined in the statement of the theorem, and where from Lemma 4.1 it follows that the LMIs $\forall j = 1, \ldots, J : \ \boldsymbol{A} \succeq \boldsymbol{B}(j)$ are equivalent to the scalar inequality $\max_j \lambda_{max}(\boldsymbol{A}^{-1} \boldsymbol{B}(j)) \leq 1$, where $\boldsymbol{A}$ is invertible. Note that $\operatorname{Re}\{\boldsymbol{F}(e^{-i\overline{\omega}})\}$ is invertible by virtue of Assumption 4.1.

At this point we obtained the simpler optimisation problem (4.12)-(4.13) that is formulated for the signal $\xi[n]$. In order to minimise the objective function (4.12) we clearly have the optimality condition that the left hand side of (4.14) should be equal to its right hand side. Furthermore, to minimise (4.12) we should minimise $C^2$ (4.14), which is achieved

by selecting the frequency $\omega_{opt}$ as defined in (4.7). The optimal input spectrum $\Phi_{\xi,opt}$ that solves the problem (4.12)-(4.13) is thus given by (4.9) with $\overline{\omega} = \omega_{opt}$ defined in (4.7) and $C^2 = C^2_{opt}$ given by

$$C^2_{opt} = \frac{2\sigma_e^2 \mathscr{L}(e^{-i\omega_{opt}}, \theta_0)}{N} \max_j \lambda_{max} \left( \left[ \mathrm{Re}\left\{ F(e^{-i\omega_{opt}}) \right\} \right]^{-1} R(j) \right).$$

The last step in the proof is to find the optimal spectrum that solves the intended optimisation problem (4.3)-(4.4). It is clear from (4.8) that $\Phi_{r,opt}(\omega)$ is given by (4.1) with $\overline{\omega} = \omega_{opt}$ and squared amplitude $A^2_{opt} = C^2_{opt}/\mathscr{L}(e^{-i\overline{\omega}}, \theta_0)$, i.e.,

$$A^2_{opt} = \frac{C^2_{opt}}{\mathscr{L}(e^{-i\omega_{opt}}, \theta_0)} = \frac{2\sigma_e^2}{N} \max_j \lambda_{max} \left( \left[ \mathrm{Re}\left\{ F(e^{-i\omega_{opt}}) \right\} \right]^{-1} R(j) \right). \tag{4.15}$$

We have thus obtained the solution (4.6)-(4.7).[3]                                                    □

## 4.2.3   Uni-Parametric Models

When only one parameter has to be identified in the transfer function $G(z, \theta)$ of the model structure, the covariance matrix $P_{N,\theta}$ and the matrices $\{R_{adm}(j)\}_{j=1}^J$ all reduce to scalars. The vector of transfer functions $F_r(z)$ also reduces to a single transfer function. Consequently, we can rewrite the optimisation (4.3)-(4.4) as

$$\min_{\Phi_r \in \Phi_1} \frac{1}{2\pi} \int_{-\pi}^{\pi} \mathscr{L}(e^{-i\omega}, \theta_0) \Phi_r(\omega) \, d\omega \tag{4.16}$$

subject to

$$\frac{N}{2\pi\sigma_e^2} \int_{-\pi}^{\pi} |F_r(e^{-i\omega})|^2 \Phi_r(\omega) \, d\omega \geq R, \tag{4.17}$$

where we recall that $\Phi_1$ is the class containing all single-sine spectra, and the $J$ constraints have been absorbed into one constraint using the notation $R = -R_0 + \max_j R_{adm}(j)$.

The analytical solution of this problem can be deduced in the same way as for the bi-parametric case.

**Corollary 4.1** *The solution of the optimisation problem (4.16)-(4.17) is given by*

$$\Phi_{r,opt}(\omega) = \frac{\pi\sigma_e^2 R}{N|F_r(e^{-i\omega_{opt}})|^2} \sum_{l=\{-1,1\}} \delta(\omega + l\omega_{opt}), \tag{4.18}$$

*with*

$$\omega_{opt} = \arg\min_{\overline{\omega}} \frac{\mathscr{L}(e^{-i\overline{\omega}}, \theta_0)}{|F_r(e^{-i\overline{\omega}})|^2}. \tag{4.19}$$

**Proof:** The proof follows along the same lines as for Theorem 4.1.                          □

---

[3]Note that $\mathscr{L}(e^{-i\overline{\omega}}, \theta_0)$ is replaced by $\mathscr{L}(e^{-i\omega_{opt}}, \theta_0)$ in $A^2_{opt}$ (4.15). This is allowed due to the presence of the Dirac delta function that is centered at $\overline{\omega} = \pm\omega_{opt}$.

**Remark 4.1** *For the case of the identification of one parameter, the optimal frequency (4.19) could also be equal to zero. The optimal excitation signal corresponding to the spectrum (4.18) is then no longer a sinusoid but a constant signal equal to $\forall n = 1, \ldots, N$:*

$$\sqrt{\frac{\sigma_e^2 R}{N|F_r(0)|^2}}.$$

**Remark 4.2** *Note that, when the objective function is the power of the excitation signal ($\mathcal{L}(e^{-i\omega}, \theta_0) = 1$), the optimal sinusoid has a frequency $\omega_{opt}$ that is the frequency for which the modulus of $F_r(e^{-i\omega})$ is maximal. Given the fact that the derivative of the prediction error (c.f. (2.4)) with respect to parameter $\theta$ can be expressed as $F_r(q)r[n] + F_v(q)e[n]$, this particular excitation signal leads to a prediction error with the highest sensitivity to variations in the to-be-identified parameter $\theta$.*

**Remark 4.3** *The frequency function $\mathcal{L}(e^{-i\omega}, \theta_0)/|F_r(e^{-i\omega})|^2$ could reach its global minimum at distinct frequencies. The optimal signal can then be a single sinusoid at one of these possible frequencies, or a superposition of sinusoids at these different frequencies. Note that this could also have been the case for (4.7). In the sequel, we will disregard this possibility for simplicity.*

Corollary 4.1 gives the solution of the LCED optimisation problem for the restricted class of spectra (4.1), i.e., $\Phi_r(\omega) \in \Phi_1$. However, we show below that, for the uni-parametric case, the spectrum (4.18) is also the general solution of (3.1)-(3.2), i.e., the solution when the spectrum $\Phi_r$ is sought in the complete set of all possible spectra $\Phi_{tot}$. We consider thus the optimisation problem

$$\min_{\Phi_r \in \Phi_{tot}} \frac{1}{2\pi} \int_{-\pi}^{\pi} \mathcal{L}(e^{-i\omega}, \theta_0)\Phi_r(\omega) \, d\omega \qquad (4.20)$$

subject to the scalar constraint (4.17).

**Theorem 4.2** *Suppose that $\mathcal{L}(e^{-i\omega}, \theta_0)/|F_r(e^{-i\omega})|^2$ in (4.19) reaches its global minimum at one single frequency. Consider the optimisation problem (4.20)-(4.17). A solution of this optimisation problem is the spectrum (4.18).*

**Proof:** Let us remark that, given the nature of the optimisation problem (4.20)-(4.17), the scalar inequality constraint (4.17) must be active at the optimum. Indeed, substituting the spectrum (4.18) into (4.17) we find that

$$\frac{N}{2\pi\sigma_e^2} \int_{-\pi}^{\pi} |F_r(e^{-i\omega})|^2 \Phi_{r,opt}(\omega) \, d\omega = R.$$

Furthermore, note that for the spectrum (4.18), the objective function in (4.20) is given by

$$\frac{1}{2\pi} \int_{-\pi}^{\pi} \mathcal{L}(e^{-i\omega}, \theta_0)\Phi_{r,opt}(\omega) \, d\omega = \frac{\sigma_e^2}{N} R \frac{\mathcal{L}(e^{-i\omega_{opt}}, \theta_0)}{|F_r(e^{-i\omega_{opt}})|^2}.$$

We now prove the theorem by contradiction. Suppose that the solution of (4.20)-(4.17) is a spectrum $\overline{\Phi}(\omega) \in \Phi_{tot}$ different from (4.18). This spectrum should obey the condition

$$\frac{1}{2\pi} \int_{-\pi}^{\pi} \mathcal{L}(e^{-i\omega}, \theta_0)\overline{\Phi}(\omega) \, d\omega < \frac{\sigma_e^2}{N} R \frac{\mathcal{L}(e^{-i\omega_{opt}}, \theta_0)}{|F_r(e^{-i\omega_{opt}})|^2}. \qquad (4.21)$$

In other words, the objective function with $\overline{\Phi}(\omega)$ is smaller than with $\Phi_{r,opt}(\omega)$. Since $\overline{\Phi}(\omega)$ is a solution of the optimisation problem, the inequality constraint (4.17) must also be active, i.e.,

$$\frac{N}{2\pi\sigma_e^2}\int_{-\pi}^{\pi}|F_r(e^{-i\omega})|^2\overline{\Phi}(\omega)\,d\omega = R. \tag{4.22}$$

Replacing $R$ in (4.21) with its expression in (4.22) we obtain the inequality

$$\int_{-\pi}^{\pi}\mathscr{L}(e^{-i\omega},\theta_0)\overline{\Phi}(\omega)\,d\omega < \frac{\mathscr{L}(e^{-i\omega_{opt}},\theta_0)}{|F_r(e^{-i\omega_{opt}})|^2}\int_{-\pi}^{\pi}|F_r(e^{-i\omega})|^2\overline{\Phi}(\omega)\,d\omega,$$

which, after multiplying both sides with $\frac{|F_r(e^{-i\omega_{opt}})|^2}{\mathscr{L}(e^{-i\omega_{opt}},\theta_0)}$ and rearranging terms, yields

$$\int_{-\pi}^{\pi}\frac{|F_r(e^{-i\omega_{opt}})|^2}{\mathscr{L}(e^{-i\omega_{opt}},\theta_0)}\mathscr{L}(e^{-i\omega},\theta_0)\overline{\Phi}(\omega)\,d\omega < \int_{-\pi}^{\pi}\frac{|F_r(e^{-i\omega})|^2}{\mathscr{L}(e^{-i\omega},\theta_0)}\mathscr{L}(e^{-i\omega},\theta_0)\overline{\Phi}(\omega)\,d\omega.$$

By virtue of (4.19) we have that $\forall\omega:\ \frac{|F_r(e^{-i\omega_{opt}})|^2}{\mathscr{L}(e^{-i\omega_{opt}},\theta_0)} > \frac{|F_r(e^{-i\omega})|^2}{\mathscr{L}(e^{-i\omega},\theta_0)}$. Therefore, the above inequality never holds for any $\overline{\Phi}(\omega)$. We have thus proven by contradiction that the spectrum (4.18) leads to the smallest cost given the constraint (4.17).　□

## 4.3　Interpretation

### 4.3.1　Motivation

In this section we provide interpretation of the analytical solutions in the previous section. For bi-parametric models we will study in particular the curiosity as to why a single sine is usually the optimal solution. We give a fictive example that shows that two sines can in fact lead to a smaller cost than a single sine. We also motivate why a solution consisting of two sines in practice hardly occurs. We show how the chicken-and-egg problem can be easily analysed using the analytical solution, and compare this solution to a numerical one. For uni-parametric models we analyse how the occupancy of the parameter $\theta_0$ in a model affects the optimal frequency, and compare the analytical and numerical solutions.

We shall for convenience restrict our analysis in this section to Direct Identification experiments.

### 4.3.2　Bi-Parametric Models

Theorem 4.1 provides the optimal spectrum to (3.1)-(3.2) when restricting the solution space to that of single-sine spectra. Unlike for the uni-parametric case, we have however not proven that a single-sine solution is the optimal solution out of all possible spectra. Nonetheless, it is often the optimal spectrum out of all possible ones. This statement is supported with numerical simulations in (Javaherian (1974)) and, as we will see, in an example of Chapter 6. In the sequel, we will also give an example. We will also provide heuristic arguments that explain this curiosity.

We will use the following example throughout this section.

**Example 4.1** *Consider the system defined by* $G(z, \boldsymbol{\theta}_0) = \frac{\theta_1 z^{-1}}{1+\theta_2 z^{-1}}$, *where* $\boldsymbol{\theta}_0 = (4, -0.6)^T$, *a noise filter* $H(z) = 1$, *and noise variance* $\sigma_e^2 = 4$. *This system is operated and identified in open-loop:* $\boldsymbol{R}_0 = \boldsymbol{0}_{2\times 2}$. *We furthermore consider the LCED problem (3.1)-(3.2) with* $N = 500$, $\mathcal{L}(e^{-i\omega}, \boldsymbol{\theta}_0) = 1$, $J = 1$, *and* $\boldsymbol{R}_{adm} = 100\boldsymbol{I}_{2\times 2}$.

### Analytical vs Numerical Solution

Consider Example 4.1. Let us compare the analytical solution (4.6)-(4.7) of the LCED problem (4.3)-(4.4), in which the power spectrum of the excitation signal is restricted to single-sine spectra, to the numerical solution of (3.1)-(3.2), in which the power spectrum is not restricted.

We first consider the analytical solution. The magenta curve in Fig. 4.1 gives, as a function of $\omega$, the amplitudes $A$ of the excitation sine $r[n] = A\sin(\omega n)$ at frequency $\omega$ that is required to satisfy (4.4). The points are computed using (4.15) in which $\omega_{opt}$ is replaced with $\omega$, and where we used the true parameter vector $\boldsymbol{\theta}_0$ defined in Example 4.1. The curve attains its minimum $A^2 = A_{opt}^2 = 0.8116$ (c.f. (4.15)) at the frequency $\omega = \omega_{opt} = 0.4932$ (c.f. (4.7)). This point thus defines the optimal spectrum (4.6).

Denote $\boldsymbol{P}_{N,\theta}^{-1} = A^2 \boldsymbol{P}^{-1}(\omega)$ as the inverse covariance matrix of the single sine $r[n] = A\sin(\omega n)$, where $\boldsymbol{P}^{-1}(\omega) = \frac{N}{2\sigma_e^2}\text{Re}\left\{\boldsymbol{F}_r(e^{-i\omega})\boldsymbol{F}_r^H(e^{-i\omega})\right\}$, and define the boundary of the confidence ellipse (2.6) for a single sine as

$$E_{conf}(\omega) : \boldsymbol{\theta}^T A^2 \boldsymbol{P}^{-1}(\omega)\boldsymbol{\theta} = 1. \tag{4.23}$$

The ellipse $E_{conf}(\omega_{opt})$ is shown for $A = A_{opt}$ in Fig. 4.2a. In this figure several other ellipses $E_{conf}(\omega')$ using $A = A_{opt}$ at frequencies $\omega' \neq \omega_{opt}$ are also shown. The ellipse $R : \boldsymbol{\theta}^T \boldsymbol{R}_{adm}\boldsymbol{\theta} = 1$ is shown in black, and defines the boundary of the area in which the confidence ellipse should lie. For our example this ellipse is in fact a circle, since $\boldsymbol{R}_{adm} = 100\boldsymbol{I}_{2\times 2}$. Notice that the major axis of the magenta ellipse (corresponding to the optimal frequency $\omega_{opt}$) is smaller than that of all other (shown) ellipses. For the optimisation problem we consider here, we know from Section 3.3 that the optimality condition $A_{opt}^2 \lambda_{min}(\boldsymbol{P}^{-1}(\omega_{opt})\boldsymbol{R}_{adm}) = A_{opt}^2 \lambda_{min}(\boldsymbol{P}^{-1}(\omega_{opt})) = 1$ should hold. Geometrically, it means that the major axis of the confidence ellipse should be as long as the radius of the black circle, i.e., the confidence ellipse is internally tangent to the black ellipse. Since the objective function (4.3) for Example 4.1 is $\frac{1}{2}A^2$, it is clear from Fig. 4.2a that the magenta ellipse requires the smallest scaling $A^2$ such that the confidence ellipse $E_{conf}(\omega_{opt})$ is internally tangent to the black ellipse; and that it satisfies the optimality condition. Indeed, for all other ellipses, a squared amplitude $A^2 > A_{opt}^2$ is required to ensure internal tangency, leading to a suboptimal cost (4.3).

Consider now the numerical solution obtained by solving (3.1)-(3.2), in which the input spectrum is parameterised as a multi-sine (3.6) with $M = 50$ harmonics and fundamental frequency $\omega_f = \pi/M$, and where we used the true parameter vector $\boldsymbol{\theta}_0$ of Example 4.1 in the covariance matrix expression. The solution is shown in black in Fig. 4.1. Notice that the solution consists of only one spectral line at $\omega = 0.5027$ with an amplitude of 0.812. This optimal frequency and squared amplitude are almost equal to their respective values of the analytical solution (where the magenta curve attains its minimum). We conclude

that, for Example 4.1, the single-sine analytical solution is also the solution of (3.1)-(3.2).

Let us analyse the accuracy of the numerical solution by solving (3.1)-(3.2) with a multi-sine using different values of $M$. The results are summarised in Table 4.1. Observe that for $M \geq 25$ the numerical optimal frequency and squared amplitude are close to the analytical ones. At $M = 500$ the frequency grid is sufficiently detailed to yield an optimal frequency that is almost identical to $\omega_{opt} = 0.4932$.

| $M$ | Numerical $\omega_{opt}$ | Numerical $A_{opt}$ |
|-----|--------------------------|---------------------|
| 10  | 0.6283                   | 0.838               |
| 25  | 0.5027                   | 0.812               |
| 50  | 0.5027                   | 0.812               |
| 100 | 0.5027                   | 0.812               |
| 500 | 0.4901                   | 0.812               |

Table 4.1: The numerical solution of the LCED problem (3.1)-(3.2) is solved using a multi-sine parameterisation (3.6) for several values of $M$ and fundamental frequencies $\omega_f = \pi/M$. All solutions consist of a single spectral line at the tabulated frequencies.
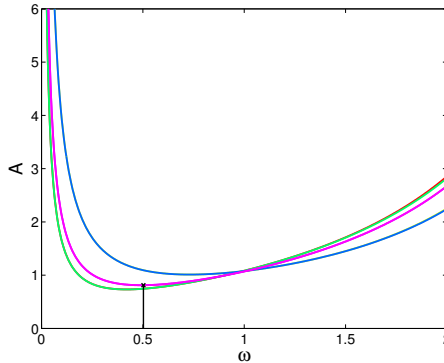


Figure 4.1: The squared amplitude $A^2$ (4.15) required to satisfy (4.4) as a function of frequency for $\boldsymbol{\theta} = (3.6, -0.65)^T$ (green), $\boldsymbol{\theta} = (4.2, -0.45)^T$ (blue), and $\boldsymbol{\theta} = \boldsymbol{\theta}_0 = (4.0, -0.6)^T$ (magenta). The optimal frequency for each value of $\boldsymbol{\theta}$ is given by that value of $\omega$ at which the corresponding curve attains its minimum.

### Why is a Single Sine Often Optimal?

Let us address this question now. To this end, we recall that $A^2 \boldsymbol{P}^{-1}(\omega)$ is defined as the inverse covariance matrix corresponding to the single sine $r[n] = A\sin(\omega n)$, where $\boldsymbol{P}^{-1}(\omega)$ is defined above. Note that the matrix $\boldsymbol{P}^{-1}(\omega)$ is, thus, essentially the building block in order to generate a confidence ellipse based on an inverse covariance matrix that is a superposition of the $M$ sines $r_m = A_m \sin(\omega_m n)$, i.e., $\boldsymbol{P}^{-1}_{N,\boldsymbol{\theta}} = \sum_{m=1}^{M} A_m^2 \boldsymbol{P}^{-1}(\omega_m)$.

Consider now again Example 4.1. In Fig. 4.2a we have shown in blue, red, magenta, green, and cyan the ellipses $\boldsymbol{\theta}^T A^2 \boldsymbol{P}^{-1}(\omega)\boldsymbol{\theta} = 1$ for respectively the frequencies $\omega = \{0.157, 0.31, \omega_{opt}, 1.0, 2.0\}$ and for $A^2 = 1$. Since $A^2 = 1$ for all these ellipses, they all correspond to an objective function (3.1) equal to $\frac{1}{2}$.

In Fig. 4.2b we show for Example 4.1 the optimal ellipse $\boldsymbol{\theta}^T \boldsymbol{P}^{-1}(\omega_{opt})\boldsymbol{\theta} = 1$ in magenta, and several grey ellipses. The latter are all combinations of a superposition of two ellipses displayed in Fig. 4.1, for which we ensured that the objective function is also

(a)　　　　　　　　　　　　　(b)
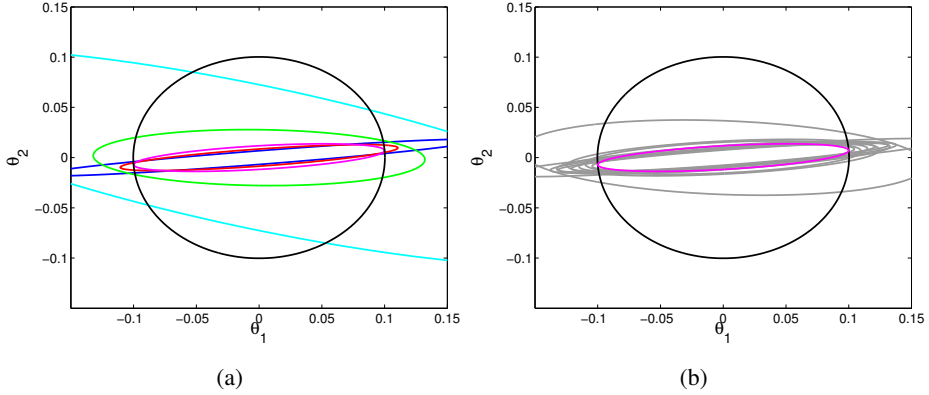
Figure 4.2: (a) The ellipse $R : \boldsymbol{\theta}^T \boldsymbol{R}_{adm} \boldsymbol{\theta} = 1$ is shown in black. The set of ellipses $E_{conf}(\omega) : \boldsymbol{\theta}^T \boldsymbol{P}^{-1}(\omega)\boldsymbol{\theta} = 1$ are shown in blue, red, magenta, green, and cyan for respectively $\omega = \{0.157, 0.31, 0.49, 1.0, 2.0\}$ at $A = 1$. For all non-black ellipses the objective function (4.3) is equal to $\frac{1}{2}$. (b) Superpositions of combinations of two ellipses shown in (a) for which the value of the objective function (4.3) is equal to $\frac{1}{2}$. The magenta ellipse and black circle are defined in (a).

equal to $\frac{1}{2}$. Notice that the major axes of all these grey ellipses remain larger than that of the single-sine optimal solution (magenta). Thus, a single-sine solution is optimal for Example 4.1, as was already known from the numerical solution obtained previously. Since Zarrop (1979) has shown that the optimal signal can always be expressed as a multi-sine, we can indeed conclude that the numerical solution with $M = 500$ is very close to the optimal spectrum.

The cause as to why a single sine is optimal, as opposed to two or more superimposed sines, has to do with the following. We have seen in Fig. 4.1 that at different frequencies $\omega$, the confidence ellipse $\boldsymbol{\theta}^T \boldsymbol{P}^{-1}(\omega)\boldsymbol{\theta} = 1$ has (i) a different orientation, and (ii) a different shape. However, we notice a relatively small difference in orientation, but large difference in shape, between these ellipses. In order to ensure that two sines deliver the optimal solution, the variability in points (i) and (ii) as a function of frequency should *both* be considerable. We illustrate this with the following example.

**Example 4.2** *Consider the problem (3.1)-(3.2) for $\boldsymbol{R}_{adm} = \boldsymbol{I}$, $\boldsymbol{R}_0 = \boldsymbol{0}_{2\times 2}$, and a weighting function $\mathscr{L}(e^{-i\omega}, \boldsymbol{\theta}_0) = 1$. We consider a fictive system for which the inverse covariance matrix for a single sine $u[n] = A\sin(\omega n)$ is denoted by $A^2 \boldsymbol{X}(\omega)$. For this problem, we have the optimality condition that $A^2 \lambda_{min}(\boldsymbol{X}(\omega)) = 1$. Suppose that we have a single-sine solution to this optimisation problem, defined by the optimal amplitude $A_{opt} = \frac{1}{\sqrt{2}}$ and optimal frequency $\omega_{opt}$ such that $\lambda_{min}(A_{opt}^2 \boldsymbol{X}(\omega_{opt})) = 1$, where $\boldsymbol{X}(\omega_{opt}) = \begin{pmatrix} 4 & 0 \\ 0 & 2 \end{pmatrix}$. Note that $\lambda_{min}(\boldsymbol{X}(\omega_{opt})) = 2$. Now, consider two sines with amplitudes $A_1 = A_2 = \frac{1}{\sqrt{6}}$, $\omega_1 = \omega_{opt}$, $\omega_2 \neq \omega_1$ and suppose $\boldsymbol{X}(\omega_2) = \begin{pmatrix} 2 & 0 \\ 0 & 4 \end{pmatrix}$. We thus have two ellipses that are rotated 90 degrees with respect to each other. It follows that the inverse covariance matrix of the input signal $u[n] = A_1 \sin(\omega_1 n) + A_2 \sin(\omega_2 n)$ is given by*

$$\lambda_{min}\left(A_1^2 \boldsymbol{X}(\omega_1) + A_2^2 \boldsymbol{X}(\omega_2)\right) = \lambda_{min}\left(\frac{1}{6}\boldsymbol{X}(\omega_{opt}) + \frac{1}{6}\boldsymbol{X}(\omega_2)\right) = 1.$$

*Hence, a two-sine solution leads to a lower cost than a single-sine. Indeed, the objective function (3.1) for the two-sine solution is $\frac{1}{2}\sum_{i=1}^{2}A_i^2 = \frac{1}{6}$, yet $\frac{1}{2}A_1^2 = \frac{1}{2}A_{opt}^2 = \frac{1}{4}$ for the single-sine solution.*

In this fictive example the superposition of two ellipses (two sines) led to a smaller cost than when using only a single ellipse (one sine). This was possible since the two eigenvalues of $X$ differed by a factor two, and because the confidence ellipse corresponding to $X(\omega_2)$ was rotated 90 degrees with respect the confidence ellipse that corresponding to $X(\omega_{opt})$, i.e. no parameter correlation. Consequently, the accuracy in the direction of the major axis of the confidence ellipse of $X(\omega_{opt})$ could be much improved by adding another sine. Indeed, the major axis corresponding to the superimposed matrices is a factor $\sqrt{3}$ times smaller than of $X(\omega_{opt})$.

For realistic model structures such as Box-Jenkins, Output-Error, FIR, etc., the variability in orientation and shape as a function of frequency (i.e. points (i) and (ii) mentioned above) is much more limited than in our fictive example. Indeed, from (2.9) it is clear that the plant model $G(z, \theta_0)$ determines the orientation and shape of the ellipse through the elements of the covariance matrix, e.g. the gradient $[\nabla_{\theta} G(z, \theta)]_{\theta=\theta_0}$. Apparently, for these model structures, the orientation is limited to such an extent that a single-sine solution is better than a multi-sine one. This is confirmed by Example 4.1, the case study in Chapter 6, and examples in (Javaherian (1974)). It is probably possible to give exact conditions when a multi-sine solution is better than a single-sine, but such an analysis is not considered here.

### Chicken-and-Egg Issue

Another benefit of the analytical solution (4.6)-(4.7) for bi-parametric models is the ease with which the chicken-and-egg issue (c.f. Section 3.2.2) can be studied.

Let us consider again Example 4.1. In the calculation of the analytical solution in the previous section, we have made use of the true unknown parameter vector $\theta_0 = (4.0, 0.6)^T$ in the expression of the inverse covariance matrix that is used in (4.4). Obviously, as we intend to estimate this parameter, we should in reality replace this parameter with an estimate $\theta_g$. To this end, we calculate the required amplitude $A^2$ to satisfy (4.4) as a function of frequency using (4.15) for three vectors $\theta_g$, see Fig. 4.1. The magenta curves corresponds to $\theta_g = \theta_0$. Notice that for the green curve corresponding to $\theta_g = (3.6, -0.65)^T$, we would obtain an optimal squared amplitude that is lower than for $\theta = \theta_0$, whereas a larger one would be obtained for the blue curve, corresponding to $\theta_g = (4.2, -0.45)^T$. In the former case, we would not satisfy the constraint (4.4) whereas in the latter case we would (at the expensive of a larger experiment cost).

**Remark 4.4** *The analytical curves in Fig. 4.1 can also be used to find the second best solution in case the optimal frequency cannot be used in practice. For instance, in the case of the magenta curve, we see that the second best solution would be to use the first allowed frequency higher than $\omega_{opt} = 0.4932$.*

## 4.3.3   Uni-Parametric Models

We now turn to the interpretation of the analytical solution for uni-parametric models. We will consider here the effect of the location of the unknown parameter on the optimal

excitation frequency, and compare the analytical solution with the one that is obtained using the convex numerical method explained in Chapter 3. More extensive interpretation can be found in (Potters et al. (2015)).

**Parameter Location**

Let us consider the identification in open- or closed-loop of a system with a fixed noise model $H(z)$ and a plant transfer function $G(z)$ given by

$$G(z) = \frac{B(z)}{1+A(z)} = \frac{\sum_{r=1}^{n_b} b_r z^{-r}}{1+\sum_{m=1}^{n_f} a_m z^{-m}}, \tag{4.24}$$

in which $\{b_r\}_{r=1}^{n_b}$, $\{a_m\}_{m=1}^{n_f}$ are the coefficients of the polynomials $B(z)$, $A(z)$. Suppose, now, that all these coefficients are known except one. Note that this is a restriction from the general case we have considered so far. This unknown coefficient can either reside in the numerator or denominator. In the former case, the unknown coefficient $\theta_0 = b_{r'}$ for some $\mathbb{N} \ni r' \in [1, n_b]$, whereas for the latter case the unknown coefficient $\theta_0 = a_{m'}$ for some $\mathbb{N} \ni m' \in [1, n_f]$. We write (4.24) as

$$G(z, \theta_0) = \frac{B(z, \theta_0)}{1+A(z)}, \quad \text{or } G(z, \theta_0) = \frac{B(z)}{1+A(z, \theta_0)},$$

if the unknown coefficient resides respectively in the numerator or denominator.

We pose the following question: *Will the optimal frequency $\omega_{opt}$ (4.19) depend on the location of the parameter in this transfer function?*

In order to answer this question, we recall the expression of $\omega_{opt}$ (4.19) for the case of a Direct Identification experiment (see Chapter 2):

$$\omega_{opt} = \arg\min_{\omega} \frac{\mathcal{L}(e^{-i\omega}, \theta_0)|H(e^{-i\omega})|^2}{|[\nabla_\theta G(e^{-i\omega}, \theta)]_{\theta=\theta_0}|^2 |S_0(e^{-i\omega})|^2}. \tag{4.25}$$

First, note that the noise filter is independent of $\theta_0$. Second, the expressions $\mathcal{L}(e^{-i\omega}, \theta_0)$ (see for instance (3.3)) and $S_0(e^{-i\omega})$ (c.f. (2.8)) are also invariant with respect to the position of $\theta_0$ in (4.24). Indeed, these functions are simply evaluated at the true value $\theta_0$; their frequency responses therefore do not change. Consequently, the optimal frequency does not change due to these terms.

We now show, however, that the derivative of $G(z, \theta)$ appearing in (4.25) *does* influence the optimal frequency. To this end, we calculate the derivative of (4.24) for the case in which the unknown parameter resides in solely the numerator, and in solely the denominator. Choosing the arbitrary locations $r' \in [1, n_b]$ and $m' \in [1, n_f]$ for the position of $\theta_0$ in these respective cases, the derivative of (4.24) evaluated at $\theta = \theta_0$ then respectively reads

$$|\nabla_\theta G(z, \theta)|_{\theta=\theta_0}^2 = \frac{1}{|1+A(e^{-i\omega})|^2}, \tag{4.26}$$

and

$$|\nabla_\theta G(z, \theta)|_{\theta=\theta_0}^2 = \frac{|B(e^{-i\omega})|^2}{|1+A(e^{-i\omega}, \theta_0)|^4}. \tag{4.27}$$

From these two expressions we observe the following. First, (4.26) and (4.27) do not depend on $r'$ and $m'$, respectively. Thus, if the unknown parameter resides in the numerator (denominator), the optimal frequency is the same for all $r' \in [1, n_b]$ (resp. $m' \in [1, n_f]$), i.e., is invariant to the position of $\theta_0$ in the numerator (resp. denominator). Second, observe that the expression (4.26) and (4.27) are different. From these two observation we conclude that there are only two different optimal frequencies: one in the case in which $\theta_0$ resides in the numerator, and one in the case where $\theta_0$ resides in the denominator.

**Remark 4.5** *It is typical in black-box modelling to consider all the coefficients $\{b_r\}_{r=1}^{n_b}$ and $\{a_m\}_{m=1}^{n_f}$ as independent parameters. However, some rational transfer functions $G(z, \theta_0)$ arise from discretising a set of partial differential equations that describe a physical process (we will see examples in Chapter 6). For such systems, the coefficients in the transfer function $G(z, \theta_0)$ are a function of the physical parameters and therefore not independent. The above analysis then no longer holds: the optimal frequency will depend on the locations these physical parameters occupy in the numerator and/or denominator.*

**Remark 4.6** *This analysis only holds for discrete-time systems.*

### Numerical Illustration

The aim of this section is to compare our uni-parametric analytical solution of Section 4.2 with the solution of the convex numerical method detailed in Chapter 3. To this end, we consider the true system

$$G_0(e^{-i\omega}) = \frac{a_1(1 - \theta_0)e^{-i\omega}}{1 - \theta_0 e^{-i\omega}},$$

and $H(e^{-i\omega}) = 1$, where $a_1 = 10$ is the steady-state gain, $\sigma_e^2 = 4.0$ is the variance of the noise $e[n]$, and $\theta_0 = 0.45$ is the unknown parameter that we need to identify with a least-costly experiment. We first consider the closed-loop setting with a PI controller $C(z)$ defined by the constants $K_p = 0.00853$ and $K_i = 0.0171$. With this controller $R_0 = 3.0826$.

The optimisation problem we consider is (4.16)-(4.17), with $\mathcal{L}(e^{-i\omega}, \theta_0)$ given by (3.3). The parameters defining the optimisation problem are: $N = 200$, $\alpha = 0.1$, $\beta = 0.7$, and $R_{adm} = 1000$.

We first consider the theoretical predictions. The optimal excitation is here equal to $r_{opt}[n] = 0.5033 \sin(\omega_{opt} n + \phi)$ with an arbitrary phase shift $\phi$ and with $\omega_{opt} = 1.8903$ $rad/s$. The frequency $\omega_{opt}$ can be determined by inspection of the frequency response of (4.25) or, alternatively, via straightforward but tedious algebraic manipulations leading to the expression

$$\omega_{opt} = \arccos\left[1 - \frac{(1 - \theta_0)^2}{2\beta\theta_0}\sqrt{\beta(\beta + \alpha a_1^2)}\right].$$

The cost of the identification corresponding to this identification is equal to $J_{opt} = 0.4580$.

We will compare this optimal excitation with the excitation that we obtain via convex optimisation. The LCED problem is solved with an FIR parameterisation (c.f. (3.5)): $\Phi_r(\omega) = \sum_{m=-M}^{M} c_m e^{-i\omega m}$, where $c_{-m} = c_m$ are to-be-determined coefficients and $M$ the order. Note that, for finite $M$, this class does not contain all possible spectra and, in particular, does not contain the optimal spectra (4.18).

We have solved the LCED problem in this example using this numerical routine for different values of $M$, i.e., $M = \{10, 25, 50, 75\}$. The obtained spectra are depicted in Fig.
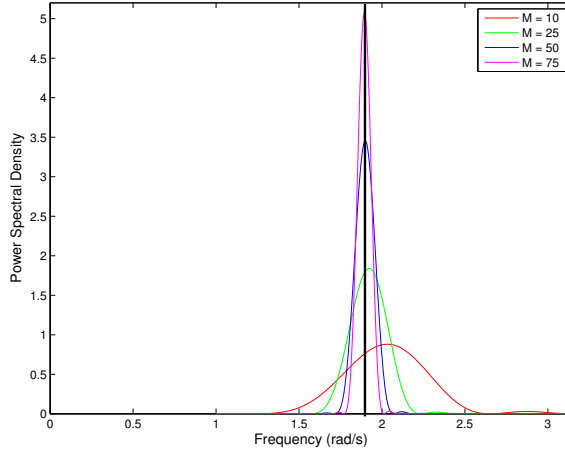
Figure 4.3: Optimal excitation spectra for $M = 10$ (red), $M = 25$ (green), $M = 50$ (blue), and $M = 75$ (purple). The black vertical line is the analytical optimal spectrum. The parameter values for the simulations are $\theta_0 = 0.45$, $N = 200$, $a_1 = 10$, $\sigma_e^2 = 4.0$, and $R_{adm} = 1000$. Observe that when $M$ is increased, the numerical spectra converge to the analytical solution.

4.3 and we observe that, for small values of $M$, the obtained spectra are relatively far from the optimal one which is a Dirac pulse at $\omega_{opt} = 1.8903 \; rad/s$. This discrepancy is also observed in the optimal identification cost that are respectively given by $J_{opt} = \{0.4601, 0.4584, 0.4581, 0.4580\}$ for these four values of $M$. We see that only for the large values of $M$ the cost converges to the optimal one, i.e., the one obtained with the sinusoid excitation.

## 4.4 Summary

In this chapter we have derived analytical solutions for uni- and bi-parametric models. These are models in which respectively one or two parameters are unknown. In particular, these solutions have provided insight into the selection of the optimal frequency and amplitude. The analytical solutions can be used to speed up the numerical methods by hard-coding the solutions into the LCED algorithms, and to e.g. easily address the chicken-and-egg issue discussed in Chapter 3. This is particularly useful in LCED problems containing additional design variables next to the spectrum $\Phi_r$, e.g. degrees of freedom in the experiment set-up that we will face in Chapter 7. In such a case, the LCED problem needs to be solved many times. Thus, for uni- and bi-parametric models, the analytical solutions can be used in such situations and deliver the optimal design variables faster than is currently possible.

There remain several problems that need to be solved. First, it would be fruitful to have a condition that states when the single-sine solution for bi-parametric models is not optimal. Second, it would be interesting to find analytical solutions for models with three or four unknown parameters. Since no generic analytical expressions exists for eigenvalues of matrices of dimension four or higher, it is probably unlikely that analytical LCED solutions exist for models with more than four unknown parameters. A formal proof of this hypothesis is an interesting subject for future work.

# 5

# Handling Unknown and Nonlinear Feedback Controllers in LCED

---

*"Every great and deep difficulty bears in itself its own solution. It forces us to change our thinking in order to find it."* - Niels Bohr

## 5.1  Introduction

The previous chapters assumed that an open-loop system is closed by a feedback mechanism containing a known, linear time-invariant (LTI) controller $C(z)$. As a result, the Least-Costly Experment Design (LCED) problem (3.1)-(3.2) is affine in the power spectrum $\Phi_r$ of the to-be-designed excitation signal $r[n]$. The optimisation problem is therefore convex can consequently be solved by parameterising the power spectrum as e.g. a multisine (3.6) or filtered white-noise signal (3.5); see Chapter 3.[1]

There are however two important conditions that must be met in order to solve (3.1)-(3.2). First, as explained in Section 3.2.2, the inverse covariance matrix (2.9) is a function of the true parameter vector $\boldsymbol{\theta}_0$, which we do not know and intend to estimate. This chicken-and-egg issue can be resolved by replacing $\boldsymbol{\theta}_0$ with an initial estimate $\boldsymbol{\theta}_{init}$ that is obtained from a previous experiment. The presence of such an estimate is thus the first condition. Secondly, the inverse covariance matrix is a function of the sensitivity function of the closed-loop system, see (2.11). Thus, the sensitivity function must also be known, and is the second condition.

As seen in the previous chapters, when the system is in closed loop with a known LTI controller the sensitivity function is trivially calculated. The LCED problem is then affine in $\Phi_r$ and therefore convex. However, there are many systems that are in closed loop with an unknown or nonlinear controller. For instance, industrial processes regulated by Model Predictive Controllers, which are not LTI; and a dynamical network, in which the feedback from the output to the input consists of many unknown LTI transfer functions that are connected in parallel and/or in series. In such complex systems, an expression for the inverse covariance matrix that is linear in $\Phi_r$ cannot be calculated with the steps taken in Section 2.2.2. Consequently, this limits the applicability of the LCED framework to systems with

---

[1]Parts of this chapter have been published in (Potters et al. (2014)).

known LTI controllers.

This chapter is therefore concerned with the generalisation of the LCED framework to systems that are regulated by unknown linear, and unknown and/or implicit nonlinear controllers. We will consider only the LCED problem (3.1)-(3.2) for the Direct Method, see Section 2.2.2. An advantage of this identification technique is that the identification procedure does not require the knowledge of the controller present in the loop during the identification experiment, and can thus be applied to systems with any type of stabilising controllers (e.g. unknown, implicit, piece-wise linear, or nonlinear). To this end, we introduce two approaches to tackle the problem. Both methods make use of a prior experiment from which, among other things, an initial estimate $\theta_{init}$ is obtained that is subsequently used to replace $\theta_0$ in the inverse covariance matrix expression in the constraints (3.2). We have thus satisfied the first condition described above.

The first approach, called the Sensitivity Method, pertains to the estimation of the sensitivity function $S_0(z)$ with the use of the closed-loop input $u$ and (non-optimal) excitation data $r$ from the experiment that is used to find the initial estimate $\theta_{init}$. The estimate $S_{init}(z)$ is used to replace the unknown true sensitivity function $S(z, \theta_0)$ in the inverse covariance matrix. The LCED problem is then again convex can be solved numerically. This approach is introduced in Section 5.3.1.

The second approach, introduced in Section 5.3.2, is the Stealth Method. It involves modifying the feedback mechanism in the classical closed-loop identification scheme in such a way that the (possibly unknown, implicit and/or nonlinear) controller does not sense the excitation signal (hence the name *Stealth*). If this is the case, the signal $r$ is applied in an open-loop fashion to the nominal closed-loop system $G_0$ and, consequently, the dependence of $P_{N,\theta}^{-1}$ on $\Phi_r$ becomes independent of the expression of the controller (i.e., the sensitivity function effectively becomes $S_0(z) = 1$). The inverse covariance matrix expression is then again affine in the power spectrum $\Phi_r$, and convex optimisation techniques can be readily applied, even though the true system is operated by an unknown, implicit or nonlinear controller. For the above property to hold, we will show that the feedback signal to the controller should be changed to $y - G(q, \theta_0)r$. Evidently, this scheme requires the knowledge of the unknown system $G_0 = G(z, \theta_0)$. We will replace $G(z, \theta_0)$ by the initial estimate $G_{id}(z) = G(z, \theta_{init})$ of $G_0$, where $\theta_{init}$ is the initial estimate from the first experiment that is used to tackle the chicken-and-egg issue.

The chapter is organised as follows. After the introduction of the two approaches in Sections 5.3.1 and 5.3.2, we consider three numerical studies. The first one illustrates the use of Stealth Identification on a linear system in closed loop with an MPC. The second study pertains to a system regulated by a nonlinear controller, and in which we compare our two approaches. The same is done in the third study, but instead a comparison is performed on a linear dynamical network.

## 5.2 Reminder: Experiment Design in Closed Loop with Known LTI Controller

This section shows how LCED can be applied to known linear controllers. To this end, we briefly recapitulate the Direct Method for the closed loop as shown in Fig. 5.1, and recall
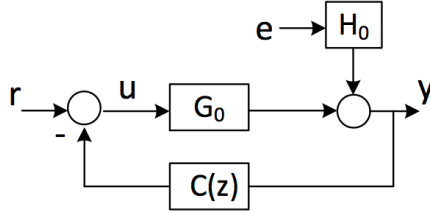
Figure 5.1: Schematic overview of the true closed-loop system. The input $u$ enters the true system $G_0$. The resulting signal that leaves the system is perturbed with the coloured noise $H_0 e$, leading to the output $y$. This output is fed back to the system through the controller $C$.

how the LCED framework is formulated for this closed loop; see also Chapter 2.

We consider the case of a LTI controller $C(z)$ regulating a single-input single-output (SISO) LTI true system $\mathscr{S}$, consisting of the output $y[n]$ and input $u[n]$:

$$
\begin{aligned}
y[n] &= G(q,\boldsymbol{\theta}_0)u[n] + H(q,\boldsymbol{\theta}_0)e[n], & (5.1)\\
u[n] &= r[n] - C(q)y[n]. & (5.2)
\end{aligned}
$$

Here, $\boldsymbol{\theta}_0$ is the unknown true parameter vector with $\dim(\boldsymbol{\theta}_0) = \kappa$, $e[n]$ is white noise with variance $\sigma_e^2$; $G(z,\boldsymbol{\theta}_0) = G_0$ and $H(z,\boldsymbol{\theta}_0) = H_0$ are stable, discrete-time transfer matrices; and $H(z,\boldsymbol{\theta}_0)$ is monic and minimum-phase. Lastly, we assume that $G_0(q)$ or $C(q)$ has at least one sample delay. Equations (5.1)-(5.2) may also be written as

$$
\begin{aligned}
y[n] &= S(q,\boldsymbol{\theta}_0)G(q,\boldsymbol{\theta}_0)r[n] + S(q,\boldsymbol{\theta}_0)H(q,\boldsymbol{\theta}_0)e[n], & (5.3)\\
u[n] &= u_r[n] + u_e[n] = S(q,\boldsymbol{\theta}_0)r[n] - S(q,\boldsymbol{\theta}_0)C(q)H(q,\boldsymbol{\theta}_0)e[n], & (5.4)
\end{aligned}
$$

upon introducing the sensitivity function of the closed-loop system $(G(q,\boldsymbol{\theta}),C(q))$:

$$
S(q,\boldsymbol{\theta}) = \frac{1}{1+C(q)G(q,\boldsymbol{\theta})}. \qquad (5.5)
$$

We define $S_0(z) = S(z,\boldsymbol{\theta}_0)$ as the sensitivity function of the closed-loop system $(G_0(z), C(z))$. As can be seen from (5.2) (see also Fig. 5.1), the closed-loop system is excited via an external signal $r[n]$ that is added to the output $u_C[n] = -Cy$ of the controller. Applying the excitation signal $r[n]$ for $n = 1,\dots,N$ to the system and measuring the signals $Z_N = \{u[n],y[n]\}_{n=1}^N$, a model $\{G(z,\hat{\boldsymbol{\theta}}_N),H(z,\hat{\boldsymbol{\theta}}_N)\}$ of the true system can be identified. The parameter vector $\hat{\boldsymbol{\theta}}_N$ is defined as $\hat{\boldsymbol{\theta}}_N = \arg\min_{\boldsymbol{\theta}} V_{id}(\boldsymbol{\theta})$, with

$$
V_{id}(\boldsymbol{\theta}) = \frac{1}{N}\sum_{n=1}^N \varepsilon^2[n;\boldsymbol{\theta}], \qquad (5.6)
$$

where

$$
\begin{aligned}
\varepsilon[n;\boldsymbol{\theta}] &= H^{-1}(q,\boldsymbol{\theta})\left(y[n] - G(q,\boldsymbol{\theta})u[n]\right) & (5.7)\\
&= \frac{G_0(q) - G(q,\boldsymbol{\theta})}{H(q,\boldsymbol{\theta})}S_0(q)r[n] + \frac{H_0(q)}{H(q,\boldsymbol{\theta})}\frac{1+C(q)G(q,\boldsymbol{\theta})}{1+C(q)G_0(q)}e[n] & (5.8)
\end{aligned}
$$

is the prediction error; see (2.4). We assume that $r$ is sufficiently exciting and that the model has been identified in a model structure $\mathcal{M}$ containing the true system (5.1)-(5.2), i.e., $\mathscr{S} \in \mathcal{M}$. In this way, the parameter vector $\hat{\boldsymbol{\theta}}_N$ identified through (5.7) and (5.6) will be asymptotically normally distributed around the true parameter vector $\boldsymbol{\theta}_0$; see Chapter 2. From this last equation, we obtain the gradient $\psi[n;\boldsymbol{\theta}'] = \nabla_{\boldsymbol{\theta}} \varepsilon[n;\boldsymbol{\theta}] \mid_{\boldsymbol{\theta}=\boldsymbol{\theta}'}$ evaluated at $\boldsymbol{\theta} = \boldsymbol{\theta}_0$:

$$\psi[n;\boldsymbol{\theta}_0] = \boldsymbol{F}_r(\boldsymbol{\theta}_0)r[n] + \boldsymbol{F}_v(\boldsymbol{\theta}_0)e[n], \tag{5.9}$$

in which the vectors $\boldsymbol{F}_r$ and $\boldsymbol{F}_v$ are defined by (2.11) and (2.12). We recall these expressions here for convenience:

$$\boldsymbol{F}_r(q,\boldsymbol{\theta}_0) = H_0^{-1}(q)S_0(q)[\nabla_{\boldsymbol{\theta}}G(q,\boldsymbol{\theta})]_{\boldsymbol{\theta}=\boldsymbol{\theta}_0} \tag{5.10}$$

$$\boldsymbol{F}_v(q,\boldsymbol{\theta}_0) = H_0^{-1}(q)[\nabla_{\boldsymbol{\theta}}H(q,\boldsymbol{\theta})]_{\boldsymbol{\theta}=\boldsymbol{\theta}_0} - C(q)S_0(q)[\nabla_{\boldsymbol{\theta}}G(q,\boldsymbol{\theta})]_{\boldsymbol{\theta}=\boldsymbol{\theta}_0}. \tag{5.11}$$

Notice that both expressions depend on the controller $C(q)$ and/or the controller-dependent term $S_0(q)$. Since the signals $r[n]$ and $e[n]$ are independent, the expressions (5.9), (5.10)-(5.11) lead to the strictly positive definite covariance matrix $\boldsymbol{P}_{N,\boldsymbol{\theta}}$ (c.f. (2.7)) of which the inverse in the frequency domain is given by (2.9), i.e.,

$$\boldsymbol{P}_{N,\boldsymbol{\theta}}^{-1} = \boldsymbol{P}_{r,N,\boldsymbol{\theta}}^{-1} + \boldsymbol{R}_0 = \frac{N}{2\pi\sigma_e^2} \int_{-\pi}^{\pi} \boldsymbol{F}_r(e^{i\omega},\boldsymbol{\theta}_0)\boldsymbol{F}_r^H(e^{i\omega},\boldsymbol{\theta}_0)\Phi_r(\omega)\,d\omega \tag{5.12}$$

$$+ \frac{N}{2\pi} \int_{-\pi}^{\pi} \boldsymbol{F}_v(e^{i\omega},\boldsymbol{\theta}_0,\boldsymbol{\theta}_0)\boldsymbol{F}_v^H(e^{i\omega},\boldsymbol{\theta}_0)\,d\omega,$$

with $\boldsymbol{F}_r(e^{-i\omega},\boldsymbol{\theta}_0)$ and $\boldsymbol{F}_v(e^{-i\omega},\boldsymbol{\theta}_0)$ defined in (2.11) and (2.12), and $\Phi_r(\omega)$ is the spectrum of the excitation signal. The matrix $\boldsymbol{R}_0$ is defined by the second integral on the right hand side of (5.12).

With the expression (5.12) we can solve the LCED problem (3.1)-(3.2), which we here recall for convenience:

$$\min_{\Phi_r} \frac{1}{2\pi} \int_{-\pi}^{\pi} \mathscr{L}(e^{-i\omega},\boldsymbol{\theta}_0)\Phi_r(\omega)\,d\omega \tag{5.13}$$

subject to

$$\forall j = 1,\ldots,J: \ \mathbf{P}_{N,\boldsymbol{\theta}}^{-1}[\Phi_r] \succeq \mathbf{R}_{adm}(j), \tag{5.14}$$

in which $\mathbf{P}_{N,\boldsymbol{\theta}}^{-1}$ the $\kappa \times \kappa$-dimensional inverse covariance matrix defined by (5.12), $\mathbf{R}_{adm}(j)$ equally-sized matrices, and $J \in \mathbb{N}^+$ an application-specific constant that sets the number of constraints. Examples of LMI constraints can be found in Section 3.2.3.

A parameterisation such as (3.5) or (3.6) should be chosen; in that case the problem can be solved with efficient numerical methods, as explained in Chapter 2. Due to the chicken-and-egg issue (see Section 3.2.2) the vector $\boldsymbol{\theta}_0$ should be replaced by an initial estimate $\boldsymbol{\theta}_{init}$ obtained from a previous experiment. Furthermore, the LTI controller $C(z)$ should be known. Indeed, otherwise, the operators $\boldsymbol{F}_r(e^{-i\omega})$ and $\boldsymbol{F}_v(e^{-i\omega})$ cannot be evaluated. The LCED problem can in that case not be solved.

To obtain an initial estimate $\boldsymbol{\theta}_{init}$, a short identification experiment is performed prior to the actual optimal identification experiment. To this end, we apply an excitation signal
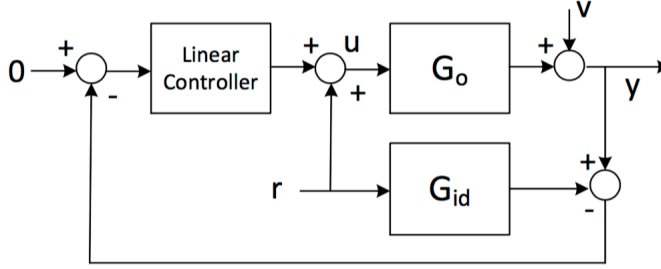
Figure 5.2: Schematic overview of the stealth identification set up for a closed-loop system with a linear (possibly implicit or unknown) controller. The excitation signal $r$ is added to the input $u$, which subsequently enters the true system $G_0$. The output $y - G_{id}r$ enters the linear controller. The output is disturbed with the coloured noise $v$.

$\{r_{init}[n]\}_{n=1}^{N_{init}}$ and collect the data $\{u_{init}[n]\}_{n=1}^{N_{init}}$ and $\{y_{init}[n]\}_{n=1}^{N_{init}}$ and subsequently use (5.6) to obtain $\boldsymbol{\theta}_{init} = \hat{\boldsymbol{\theta}}_{N_{init}}$.

In the sequel, we will give two methods to approximate the dependence of $\boldsymbol{P}_{N,\boldsymbol{\theta}}$ as a function of $\Phi_r$, i.e., $\boldsymbol{P}_{r,N,\boldsymbol{\theta}}^{-1}$. First we consider the case of an unknown LTI controller and then in the case of a (possibly unknown) nonlinear controller. Subsequently, we will give methods to determine the component $\boldsymbol{R}_0$ appearing in $\boldsymbol{P}_{N,\boldsymbol{\theta}}^{-1}$, i.e., the contribution to the parameter accuracies due to the noise $e$.

## 5.3 Unknown LTI controllers

### 5.3.1 Sensitivity Method

In the expression of $\boldsymbol{F}_r$ (5.10), the only dependence on $C(q)$ is the sensitivity function $S_0(q)$. Consequently, if we would estimate $S_0$, we could use this estimate in the expression of $\boldsymbol{F}_r$ and be able to design an optimal spectrum $\Phi_{r,opt}(\omega)$.

For this purpose, we can use the same experiment as the one that yielded $\boldsymbol{\theta}_{init}$. Indeed, from (5.4) and the obtained data $\{r_{init}[n], u_{init}[n]\}_{n=1}^{N_{init}}$, we can identify $S_0$ using open loop prediction error identification. This identification yields the model $S_{init}$ that can be used together with $\boldsymbol{\theta}_{init}$ in the expression of $\boldsymbol{F}_r$.

This approach does not allow us to find an expression of $\boldsymbol{R}_0$ since $\boldsymbol{F}_v$ is a function of $C(q)$ too. However, since $\boldsymbol{R}_0 \succeq \boldsymbol{0}$, we can e.g. neglect it for experiment design ((5.14) is then replaced by $\boldsymbol{P}_{r,N,\boldsymbol{\theta}}^{-1} \succeq \boldsymbol{R}_{adm}(j)$ for all $j$). The matrix $\boldsymbol{R}_0$ can however also be estimated via the methods given in Section 5.5.

We can thus solve (5.13)-(5.14) and obtain an optimal input spectrum $\Phi_{r,opt}$. A realisation of the spectrum can then be applied to the closed-loop and a model can be identified using the Direct Method. Since $r_{opt}$ can be parameterised as a filtered white noise signal, it will be of sufficient high order of excitation and thus we can guarantee a consistent estimate. However, due the approximation above ($S_{init} \approx S_0$; $\boldsymbol{\theta}_{init} \approx \boldsymbol{\theta}_0$), we cannot fully guarantee that the constraints (5.14) are satisfied. This was also the case in Section 5.2, where for linear known controllers an initial estimate is also required.

## 5.3.2  Stealth Method

Let us now consider an alternative manner to circumvent the LCED requirement of knowing the controller $C(q)$. Instead of estimating the sensitivity function as done in the previous section, we here modify the feedback mechanism in the classical closed-loop identification scheme in such a way that the unknown controller does not sense the excitation signal (hence the name *Stealth*). If this is the case, the signal $r$ is applied in an open-loop fashion to the nominal closed-loop system $G_0$ and, consequently, the dependence of $P_{N,\theta}^{-1}$ on $\Phi_r$ becomes independent of the expression of the controller.

To this end, consider Fig. 5.2 where $G_{id}$ is given by $G(z, \theta_{init})$, and in which $\theta_{init}$ is the initial guess of $\theta_0$ (see end of Section 5.2). The input-output relations are for this case defined by

$$
\begin{aligned}
u[n] &= u_r[n] + u_e[n] = \frac{1 + C(q)G_{id}(q)}{1 + C(q)G_0(q)} r[n] - \frac{C(q)H_0(q)}{1 + C(q)G_0(q)} e[n], \\
y[n] &= y_r[n] + y_e[n] \\
&= G_0(q) \frac{1 + C(q)G_{id}(q)}{1 + C(q)G_0(q)} r[n] + \frac{H_0(q)}{1 + C(q)G_0(q)} e[n],
\end{aligned}
\tag{5.15}
$$

where $y_e[n]$ and $u_e[n]$ are the output and input signals that are generated by the closed loop $(G_0(z), H_0(z), C(z))$ without the presence of the excitation signal $r[n]$. Notice the difference between the above equations and (5.3)-(5.4).

To be able to design $\Phi_r$ when $C(z)$ is unknown we will make the assumption that $G_{id} = G(z, \theta_{init}) = G_0(z)$. This is the same assumption as in Section 5.2: $\theta_{init} \approx \theta_0$. With these assumptions, (5.15) becomes

$$
u[n] = r[n] - \frac{C(q)H_0(q)}{1 + C(q)G_0(q)} e[n],
\tag{5.16}
$$

$$
y[n] = G_0(q)r[n] + \frac{H_0(q)}{1 + C(q)G_0(q)} e[n].
\tag{5.17}
$$

We observe the following from these last two equations. The signal $r[n]$ is now applied as if it was in open loop identification (the controller does not see $r[n]$!). The contribution of the noise $e$ is as in classical closed-loop identification (see (5.3)-(5.4)). Substituting the above two relations into (5.7) yields

$$
\varepsilon[n; \theta] = \frac{G_0(q) - G(q, \theta)}{H(q, \theta)} r[n] + \frac{H_0(q)}{H(q, \theta)} \frac{1 + C(q)G(q, \theta)}{1 + C(q)G_0(q)} e[n],
$$

from which it follows that

$$
\psi[n, \theta_0] = \overline{F}_r(q, \theta_0)r[n] + \overline{F}_v(q, \theta_0)e[n] = \frac{\nabla_\theta G(q, \theta) \mid_{\theta = \theta_0}}{H_0(q)} r[n] + F_v(\theta_0)e[n].
$$

Note that $\overline{F}_v = F_v$ is the same as its expression in Section 5.2. From the above equation the inverse covariance matrix for the Stealth identification scheme reads

$$
P_{N,\theta}^{-1} = \frac{N}{2\pi\sigma_e^2} \int_{-\pi}^{\pi} \overline{F}_r(z, \theta_0)\overline{F}_r^H(z, \theta_0)\Phi_r(\omega)\,d\omega + R_0,
\tag{5.18}
$$

with $R_0$ identical to the one defined in Section 5.2. This approach does not allow us to find an expression of $R_0$ since $F_v$ is a function of $C(q)$. However, like in the previous section, since $R_0 \succeq 0$, we can e.g. neglect it for experiment design ((5.14) is then replaced by $P_{r,N,\theta}^{-1} \succeq R_{adm}(j)$ for all $j$). The matrix $R_0$ can however also be estimated via the methods given in Section 5.5.

Using (5.18) in the LCED optimisation problem then leads to an optimal input signal $r_{opt}$ that will be applied as shown in Fig. 5.2 on the true system. Here we will use $G_{id}(z) = G(z, \theta_{init})$. Since $r_{opt}$ is filtered white noise the data will be sufficiently informative. Theorem (5.1) shows that the estimate will be consistent for all stable $G_{id}$ when $r_{opt}$ is a filtered white noise.

**Theorem 5.1** *Assume that the true system $\mathscr{S}$ is operated as in Fig. 5.2 and that the considered closed loop is stable (condition D1 in (p. 249, Ljung (1999))). Consider a model set $\mathscr{M}(\theta) := \{G(z, \theta), H(z, \theta)\}$ that contains the true model, i.e., $\mathscr{S} \in \mathscr{M}$. Furthermore, we assume that our dataset $Z_N$ is sufficiently informative w.r.t. $\mathscr{M}$, that there is a delay in either the controller or in both $G_0(z)$ and $G(z, \theta)$, and that $\mathscr{M}(\theta)$ is globally identifiable at $\theta_0$.*

*Then, the stealth identification scheme yields a consistent estimate of the true parameter vector $\theta_0$, even when $G_{id} \neq G_0$.*

**Proof:** Under the above assumptions, we have (cf. Theorem 8.2 in (Ljung (1999))) that $\hat{\theta}_N \to D_c$ w.p. 1 as $N \to \infty$, where

$$D_c = \arg\min_{\theta} \bar{V}(\theta) = \left\{ \theta \mid \bar{V}(\theta) = \min_{\theta'} \bar{V}(\theta') \right\},$$

with

$$\bar{V}(\theta) = \bar{E}\frac{1}{2}\varepsilon^2[n; \theta].$$

The set $D_c$ contains all parameter vectors $\theta^*$ that minimise the quadratic criterion. For consistency, we now need to prove that the set $D_c$ only contains the true parameter $\theta_0$, i.e. $D_c = \{\theta_0\}$. In other words, that $\theta_0$ is the unique minimiser of the quadratic criterion (cf. Theorem 8.3 in Ljung (1999)).

The prediction error corresponding to the Stealth identification method follows straightforwardly from (5.15) and reads

$$\varepsilon[n; \theta] = \frac{G_0(q) - G(q, \theta)}{H(q, \theta)} \left( \frac{1 + C(q)G_{id}(q)}{1 + C(q)G_0(q)} \right) r[n] + \frac{H_0(q)}{H(q, \theta)} \left( \frac{1 + C(q)G(q, \theta)}{1 + C(q)G_0(q)} \right) e[n].$$
$$(5.19)$$

Using the assumption on the presence of a delay in either $C(z)$ or in both $G(z, \theta)$ and $G_0(z)$, the power of $\varepsilon$ reaches its minimum at $\theta = \theta_0$. It is furthermore a unique minimiser due to the assumption of an informative data set.

The above result is in fact straightforward. Indeed, (5.19) is almost equivalent to the expression (5.8) of $\varepsilon[n; \theta]$ as a function of $r$ and $e$ for classical Direct closed-loop identification. The only difference is that the transfer function $(1 + CG_{id})/(1 + CG_0)$ is replaced by $S_0$. Since both $S_0$ and $(1 + CG_{id})/(1 + CG_0)$ are fixed (i.e. independent of $\theta$) and non-zero transfer functions, the consistency properties are the same in both cases. $\square$
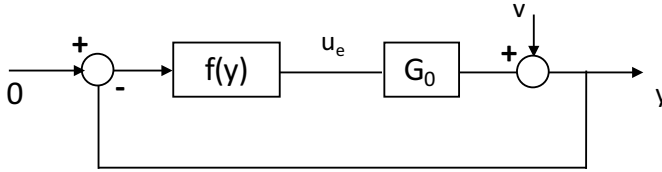
Figure 5.3: Stealth identification method with a zero excitation signal.

**Remark 5.1** *The proof also holds for other identification criteria; see (Ljung (1999)) for details. Furthermore, when $G_{id}(z) = 0$, the prediction error (5.19) reduces to the expression one would have obtained from the Direct Method for a closed-loop system. Additionally, when $G_{id}(z) = G_0(z)$, we see that the first term on the right hand side becomes $H^{-1}(z, \boldsymbol{\theta})(G_0(z) - G(z, \boldsymbol{\theta})r[n])$. This term is now equivalent to the one which would have been obtained with identification of an open-loop system.*

## 5.4   Nonlinear Controllers

### 5.4.1   Sensitivity Method

In the case of linear systems regulated by nonlinear controllers we evidently have nonlinear sensitivities (i.e., rational, finite-order transfer functions $S(q)$ do not exist). Even though it will of course lead to suboptimal values for the excitation spectrum, we can still apply the Sensitivity Method as introduced in Section 5.3.1 to such systems, by estimating a linear approximation $S(q, \boldsymbol{\theta}_{init})$ of the nonlinear sensitivity.

### 5.4.2   Stealth Method

The Stealth Method as introduced in Section 5.3.2 still holds for nonlinear controllers. Indeed, if $G_{id} = G_0$ in Fig. 5.4, the input signal $u$ is given by

$$u[n] = r[n] + u_e[n],$$

where $u_e[n] = f(y[n])$ is the input signal when $r = 0$; see Fig. 5.3. The signals $r$ and $u_e$ are thus independent. Consequently, we may write the prediction error as

$$\varepsilon[n; \boldsymbol{\theta}] = \frac{G_0(q) - G(q, \boldsymbol{\theta})}{H(q, \boldsymbol{\theta})} r[n] + \frac{G_0(q) - G(q, \boldsymbol{\theta})}{H(q, \boldsymbol{\theta})} u_e[n] + \frac{H_0(q)}{H(q, \boldsymbol{\theta})} e[n]$$

since the term in $r$ is independent of the rest. The contribution of $\Phi_r$ to $P_{N,\boldsymbol{\theta}}^{-1}$ can be approximated as in the linear case. The contribution of the noise, $\boldsymbol{R}_0$, is once again the contribution when $r = 0$. Using similar arguments as for the LTI controller case and using the results in (Ljung (1978)), we will obtain a consistent estimate of $\boldsymbol{\theta}_0$ even if $G_{id} \neq G_0$.
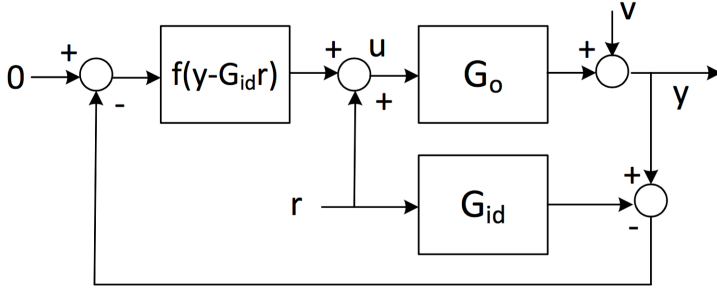
Figure 5.4: Schematic overview of the Stealth identification scheme for nonlinear controllers. The classical closed-loop scheme is adapted by subtracting the signal $G_{id}r$ from the output $y$ that would normally directly enter the nonlinear controller $f(y)$. With the Stealth scheme, the signal $y - G_{id}r$ enters the controller.

## 5.5 The Matrix $R_0$

In the above cases of least-costly experiment design for closed-loop systems with (possibly unknown) linear and nonlinear controllers, the matrix $R_0$ is the contribution of the noise to the covariance matrix for a Direct closed-loop identification with $r = 0$. Here we provide several options to compute this matrix:

1. As already mentioned above, the positive-definite matrix $R_0$ can be neglected. In this case, we consider the LMI $P_{r,N,\theta}^{-1} \succeq R_{adm}$ in the problem (5.13)-(5.14). The optimal input signal will have a higher power than the solution resulting from the problem with the LMI $P_{N,\theta}^{-1} \succeq R_{adm}$. However, the parameter accuracy constraints will be satisfied.

2. We can collect data in normal operation (i.e. $r = 0$ in the identification experiment), and subsequently estimate $\hat{\theta}_N$ if the collected data is sufficiently informative. The resulting covariance matrix is $R_0^{-1}$.

3. If the system cannot be estimated with $r = 0$ (i.e. with data generated from normal operation), we can add a non-zero excitation signal $r$ to the closed-loop system, identify $\hat{\theta}_N$, and estimate $P_{N,\theta}^{-1}$ (using the collected data). Using the known spectrum of the excitation signal, the initial estimate $\theta_{init}$ and the contribution $P_{r,N,\theta}^{-1}$ can be computed using either (5.18) in the Stealth situation or (5.12) in other situations. In this latter case, the initial estimate $S_{init}(q)$ of the sensitivity function can be used to evaluate $F_r(q)$. Finally, $R_0$ can be estimates as:

$$R_0 \approx \hat{P}^{-1} - P_{r,N,\theta}^{-1},$$

where $\hat{P}$ is the estimate of the covariance matrix computed with the data. Note that the initial experiment (i.e. the one leading to $\theta_{init}$) could also be used to estimate $R_0$ in this way.

## 5.6     Numerical Study 1: A System Controlled by MPC

### 5.6.1     Introduction

In this section we test the Stealth identification framework on a SISO system regulated by a model predictive controller. We verify whether the least-costly framework can indeed yield models that obey $P_{N,\theta}^{-1} \succeq R_{adm}$ for $G_{id} = G_0$ as well as $G_{id} \neq G_0$ by comparing four identification experiment types. For each experiment type we perform Monte Carlo simulations. We will limit ourselves to only the Stealth method as we will explore the sensitivity estimation method in the next numerical studies. In the following subsections, we introduce the data-generating system, the least-costly experiment design problem, and finally we show the identification results.

### 5.6.2     The Data-Generating System

We consider a data-generating system (5.1)-(5.2) embedded in a Box-Jenkins (BJ) model structure $\mathscr{M} = \{M(\theta), \theta \in \mathbb{R}^6\}$. The family of models $M(\theta)$ in this structure is given by

$$G(z,\theta) = \frac{\theta_1 z^{-1} + \theta_2 z^{-2}}{1 + \theta_5 z^{-1} + \theta_6 z^{-2}}, \text{ and } H(z,\theta) = \frac{1 + \theta_3 z^{-1}}{1 + \theta_4 z^{-1}}.$$

A Gaussian white-noise signal $e[n]$ with variance $\sigma_e^2 = 0.5$ is added through the filter $H(z,\theta_0)$, yielding $v = H(q,\theta_0)e[n]$. The noise realisation $e[n]$ is identical for all four experiment types during a single Monte Carlo step. At each new Monte Carlo step a new white-noise signal is randomly generated. This allows us to compare precisely the identification results. The true system is defined as $\mathscr{S}_0 = M(\theta_0) \in \mathscr{M}$, where $\theta_0 = (0.5, 0, 0, -0.6, -0.6, 0.8)^T$ ($\kappa = \dim(\theta_0) = 6$). The sampling times $T_s = 1$ second.

**MPC algorithm**

The data-generating system (5.1)-(5.2) is operated in closed loop with an MPC controller (Maciejowski (2002)) based on our commissioning model $(G_{init}, H_{init}) \in \mathscr{M}$, where $\theta_{init} = (0.15, 0.05, 0.92, 0.92, -0.30, 0.71)^T$. We denote this controller by $C(G_{init})$. A Bode diagram of $G_{init}$ and the data-generating system from Section 5.6.2 is shown in Fig. 5.5.

    The MPC is tuned so that we get sufficient performance for the commissioning model $(G_{init}, H_{init})$. We define the model predictive controller with the MPC function in Matlab. The MPC is set to have a prediction horizon of $N_y = 40$ and a control horizon of $N_u = 20$. The output variable $y$ has a weight of $Q = 1.0$, and the input a weight of $R = 0.1$. The constraint on the input $u$ is $-3 \leq u \leq 3$. However, as we want to add an excitation signal to nominal operation, we reduce the bounds to $-2.5 \leq u \leq 2.5$ to allow system excitation. There are no constraints on the output. The cost function of the MPC is of standard form (i.e. output reference tracking).
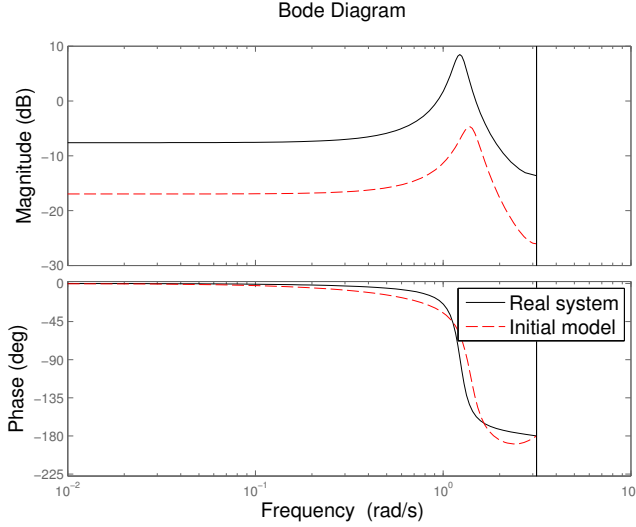
Figure 5.5: Bode diagram of the data-generating $G(z, \boldsymbol{\theta}_0)$ system (black) and commissioning model $G(z, \boldsymbol{\theta}_{init})$ (red).

### 5.6.3 Least-Costly Experiment Design

We now define the least-costly experiment design problem. The chosen objective function of our LCED problem is given by (5.20) and is of the form (3.3), i.e., we choose

$$\mathscr{P}_{y_r} + \mathscr{P}_r = \frac{1}{2\pi} \int_{-\pi}^{\pi} (\Phi_{y_r} + \Phi_r) \, d\omega, \tag{5.20}$$

where $\mathscr{P}_{y_r}$ and $\mathscr{P}_r$ are the power of $y_r[n] = G_0(q)r[n]$ and of $r[n]$, respectively. It represents the cost of the induced perturbations on $u$ and $y$ when we assume $G_{id} = G_0$ in the Stealth framework (see (5.16)-(5.17)). The LCED constraint (3.2) is a performance-relevant one, defined in Section 3.2.3. In particular, we chose the same application cost as in Example 3.1, i.e.,

$$V_{app}(\boldsymbol{\theta}) = \frac{1}{N_{win}} \sum_{n=1}^{N_{win}} (y[n; G(\boldsymbol{\theta}_0), C(\boldsymbol{\theta})] - y[n; G(\boldsymbol{\theta}_0), C(\boldsymbol{\theta}_0)])^2, \tag{5.21}$$

where the noise-free output $y[n; G(\boldsymbol{\theta}_0), C(\boldsymbol{\theta})]$ represents the closed-loop output of the closed loop $(G(\boldsymbol{\theta}_0), C(\boldsymbol{\theta}))$ at time instance $n$. For example, $y[n; G(\boldsymbol{\theta}_0), C(\boldsymbol{\theta}_{init})]$ is the output at time instance $n$ from the above-defined data-generating system and MPC controller. The constraint $\boldsymbol{P}_{N,\boldsymbol{\theta}}^{-1} \succeq \boldsymbol{R}_{adm}$ for the performance-relevant constraint is then given by (3.10), i.e.,

$$\boldsymbol{P}_{N,\boldsymbol{\theta}}^{-1} \succeq \boldsymbol{R}_{adm} = \frac{\gamma \chi_{\alpha}^2(6)}{2} V_{app}''(\boldsymbol{\theta}_0),$$
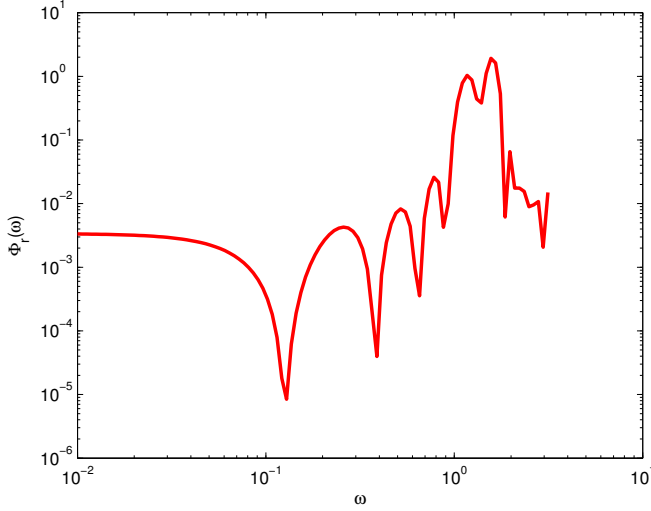
Figure 5.6: Optimal excitation spectrum $\Phi_{r,opt}(\omega)$ that is calculated in Section 5.6.3.

in which we choose $N = 10^4$, $\alpha = 0.99$, $\gamma = 400$, and $V''_{app}(\boldsymbol{\theta}_0)$ the Hessian of (5.21) at $N_{win} = 100$. The resulting matrix $\boldsymbol{R}_{adm}$ then reads

$$\boldsymbol{R}_{adm} = \begin{pmatrix} 1.195 & -0.0352 & 0.0124 & 0.0202 & -0.066 & -0.2207 \\ -0.0352 & 1.5146 & -0.004 & 0.0065 & -0.439 & 0.429 \\ 0.0124 & -0.004 & 0.00067 & 0.0004 & 0.0087 & 0.0087 \\ 0.0202 & 0.0065 & -0.0004 & 0.011 & -0.0102 & 0.0063 \\ -0.066 & -0.439 & 0.0087 & -0.0102 & 0.0395 & -0.74 \\ -0.2207 & 0.429 & 0.0087 & 0.0063 & -0.74 & 0.4501 \end{pmatrix}.$$

We have now defined all terms in the LCED problem (3.1)-(3.2). The problem is now solved using a finite-dimensional parameterisation of the spectrum $\Phi_r(\omega)$ and by replacing $\boldsymbol{\theta}_0$ with $\boldsymbol{\theta}_{init}$ in order to circumvent the chicken-and-egg issue. We choose the 30-th order FIR filter defined by (3.5), which defines the term $\boldsymbol{P}_{r,N,\boldsymbol{\theta}}^{-1}[\Phi_r]$ (c.f. (5.18)) in $\boldsymbol{P}_{\boldsymbol{\theta}}^{-1}[\Phi_r] = \boldsymbol{P}_{r,N,\boldsymbol{\theta}}^{-1}[\Phi_r] + \boldsymbol{R}_0$. The matrix $\boldsymbol{R}_0$ is estimated with an identification experiment in nominal closed-loop operation simulation (i.e. $r = 0$ for the entire experiment). The experiment length is $N = 10^4$ (when $r \neq 0$). Hence, the optimal excitation spectrum $\Phi_r$ is computed such that $\boldsymbol{P}_{r,N,\boldsymbol{\theta}}^{-1}[\Phi_r] \succeq \boldsymbol{R}_{adm} - \boldsymbol{R}_0$. The optimal spectrum $\Phi_{r,opt}$ is shown in Fig. 5.6.

## 5.6.4   Identification Results

We now compare different identification experiments. Experiments I and II use the same optimal excitation signal as shown in Fig. 5.6, whereas experiments III and IV use a white-noise excitation signal. We validated that the input constraints $-3 \leq u \leq 3$ were not violated. The identification results are compared with the various measures shown in Table 5.1; its values are averages over 250 Monte Carlo simulations (each Monte Carlo

| Experiment | I | II | III | IV |
|---|---|---|---|---|
| $10^4\|\|\hat{\boldsymbol{\theta}}_N - \boldsymbol{\theta}_0\|\|^2$ | 2.45 | 8.28 | 4.15 | 2.95 |
| $\lambda_{min}(\boldsymbol{P}_{N,\boldsymbol{\theta}}^{-1} - \boldsymbol{R}_{adm})$ | 267 | 174 | -3003 | -3029 |

Table 5.1: The different measures calculated for four types of experiments. The tabulated values are averaged over 250 Monte Carlo simulations. The first row gives the error between the estimate $\hat{\boldsymbol{\theta}}_N$ and the true parameter vector $\boldsymbol{\theta}_0$. The second row indicates whether or not the constraint $\boldsymbol{P}_{N,\boldsymbol{\theta}}^{-1} \succeq \boldsymbol{R}_{adm}$ is satisfied: when the minimal eigenvalue is positive (negative) the above constraint is satisfied (not satisfied).

simulation has a different noise realisation on the simulated output)[2]. The first row in the table shows the average mean-square error of the identified parameter vector $\hat{\boldsymbol{\theta}}_N$ compared with the true vector $\boldsymbol{\theta}_0$. The second row shows the averaged minimal eigenvalue $\lambda_{min}(\boldsymbol{P}_{N,\boldsymbol{\theta}}^{-1} - \boldsymbol{R}_{adm})$. When it is negative, the constraint in the optimisation problem, i.e., $\boldsymbol{P}_{N,\boldsymbol{\theta}}^{-1} \succeq \boldsymbol{R}_{adm}$, is not satisfied. We now describe the experiments I-IV in detail.

### Experiment I. Optimal input signal $r_{opt}$ and $G_{id}(z) = G_0(z)$

The first identification experiment considers $G_{id} = G_0$, see Fig. 5.4. This is an experiment in which the controller will not notice the excitation signal at all. As excitation signal, we add $r_{opt}$ as computed in Section 5.6.3 and collect the data $Z_N = \{u[n], y[n]\}_{n=1}^N$. This data is used in (5.6) to obtain an estimate $\hat{\boldsymbol{\theta}}_N$ of the true parameter vector $\boldsymbol{\theta}_0$. We performed 250 Monte Carlo simulations of this experiment type, the results of which are reported in Table 5.1. From this table, we see that the average estimation error is small, and that, on average, the estimated model $G(z, \hat{\boldsymbol{\theta}}_N)$ is sufficiently accurate for performance-relevant control. Indeed, the related performance-relevant constraint in the LCED optimisation problem used in the previous section is satisfied, since the average minimum eigenvalue of the matrix $\boldsymbol{P}_{N,\boldsymbol{\theta}}^{-1} - \boldsymbol{R}_{adm}$ is positive; see Table 5.1.

### Experiment II. Optimal input signal $r_{opt}$ and $G_{id}(z) = G(z, \boldsymbol{\theta}_{init})$

This second identification experiment is identical to Experiment I, with the difference being that we instead use $G_{id} = G(z, \boldsymbol{\theta}_{init})$, i.e., the initial guess $\boldsymbol{\theta}_{init}$ available at commissioning was used. (It is the same parameter vector that is used in the MPC controller, see Section 5.6.2). The excitation spectrum is equal to that of experiment I. The Monte Carlo results are depicted in Table 5.1. Notice that again a good model is found that satisfies $\boldsymbol{P}_{N,\boldsymbol{\theta}}^{-1} \succeq \boldsymbol{R}_{adm}$, although the estimation error is larger than for Experiment I.

### Experiment III. White-noise input signal and $G_{id}(z) = G(z, \boldsymbol{\theta}_{init})$

This third experiment type is different from the above two in the sense that we no longer use the optimal input signal $r_{opt}$ as computed in Section 5.6.3. Instead, we generate a zero-mean Gaussian white-noise input signal with a power that is equal to that of the optimal input signal used above. Experiment III considers $G_{id}(z) = G(z, \boldsymbol{\theta}_{init})$, see Fig. 5.4. Analogous to experiments I and II, we apply in this case the white-noise input signal for the same duration as the previous two experiments, and collect the input-output data in $Z_N = \{u[n], y[n]\}_{n=1}^N$. This data is used with (5.6) to obtain an estimate $\hat{\boldsymbol{\theta}}_N$. Table

---

[2]We use Monte Carlo simulations to validate accuracy constraints since a closed-form analytical expression of the inverse covariance matrix is not available for systems with nonlinear controllers.

5.1 shows the Monte Carlo averages of e.g. the estimation error. Although a consistent estimate is obtained, we observe that the average minimum eigenvalue is negative. Thus, the performance-relevant constraint $P_{N,\theta}^{-1} \succeq R_{adm}$ is not satisfied, even though we used the same input power as in Experiments I and II. This clearly illustrates the benefit of LCED: with equal power, higher parameter accuracies can be obtained.

**Experiment IV. White-noise input signal and $G_{id}(z) = 0$**

This last experiment type is identical to Experiment type III, the difference being that we instead use $G_{id}(z) = 0$. It means that the excitation signal will be noticed by the controller. We observe from the Monte Carlo averages in Table 5.1 that also in this case the parameter accuracy constraint is not satisfied.

From Table 5.1, we conclude that the least-costly signals deliver precise models of the true system satisfying $P_{N,\theta}^{-1} \succeq R_{adm}$. The converse holds for the equally-powered white-noise signal excitations. These latter signals deliver consistent parameter estimates, but do not lead to the user-imposed required model accuracies.

# 5.7    Numerical Study 2: A System Regulated by a Nonlinear Controller

## 5.7.1    Introduction

In this section we apply the Stealth Method to a linear system that is regulated by an explicit nonlinear controller. In particular, we look at a P controller that is preceded by a nonlinear filter on the system's output, see Fig. 5.7. This set-up is inspired by the work of Fromion and Scorletti (2002). In this figure, the dashed block defines the nonlinear controller, $G_0$ is the true system, $v[n]$ is coloured noise, $y[n]$ is the noise-disturbed output, $r[n]$ the excitation signal, and $G_{id}$ a transfer function that lies in the same model family as $G_0$. The diagram without the block $G_{id}$ represents the classical closed-loop identification scheme. We will also consider in this case study the Sensitivity Method introduced in Section 5.2. For this method, we can use the same set-up, but in which $G_{id} = 0$.

   As in the previous numerical study, we first define the data-generating system, the least-costly experiment design problem, and then discuss the identification results.

## 5.7.2    The Data-Generating System

We consider the model set $\mathscr{M} = \{G(z,\boldsymbol{\theta}), H(z,\boldsymbol{\theta})\}$, where

$$G(z,\boldsymbol{\theta}) = \frac{\theta_1 z^{-1} + \theta_2 z^{-2}}{1 + \theta_3 z^{-1} + \theta_4 z^{-2}}, \; H(z,\boldsymbol{\theta}) = \frac{1 + \theta_5 z^{-1} + \theta_6 z^{-2}}{1 + \theta_7 z^{-1} + \theta_8 z^{-2}}.$$

The true system, denoted $\mathscr{S} \in \mathscr{M}$, is then defined by setting $\boldsymbol{\theta} = \boldsymbol{\theta}_0 = (0.0852, 0.049$ $-1.735, 0.7513, 0.067, -0.04, -0.817, -0.155)^T$. The noise model $H(z, \boldsymbol{\theta}_0)$ then defines the coloured noise, being $v[n] = H(q, \boldsymbol{\theta}_0)e[n]$, where $e[n]$ is a zero-mean Gaussian white noise realisation with variance $\sigma_e^2 = 7.5 \times 10^{-4}$. The transfer function $G_{id} = G(z, \boldsymbol{\theta}_{init})$, where $\boldsymbol{\theta}_{init}$ is a user-defined initial guess of $\boldsymbol{\theta}_0$. The sampling time is $T_s = 1$ second.
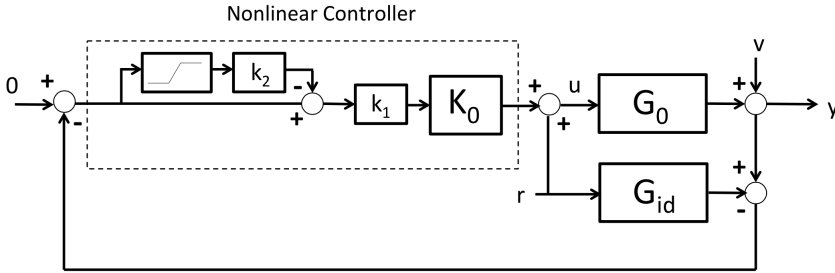
Figure 5.7: The closed-loop system as used by Fromion and Scorletti (2002), but in which the Stealth scheme is implemented. If $G_{id} = 0$, we obtain the original closed loop (to which the Sensitivity Method is applied). The true system is indicated by $G_0$ and the nonlinear controller by the elements in the dashed square.

## Nonlinear controller

Next, we define the nonlinear controller. The block $K_0$ in Fig. 5.7 represents a traditional PI controller with the following structure:

$$K_0(z) = \frac{\tau_z z + 1}{z(\tau_c z + 1)^2},\tag{5.22}$$

with $\tau_z$ and $\tau_c$ tuneable constants. The terms proceeding the block $K_0$ in Fig. 5.7 act as a variable gain that is a function of the output $y[n]$. This variable gain, denoted $k(y[n])$, reads

$$k(y[n]) = k_1 \left( y[n] - k_2 \text{sat}(y[n]) \right),\tag{5.23}$$

with $k_1 = k_{max}$, $k_2 = 1 - k_{min}/k_{max}$, and where the saturation function is defined by

$$\text{sat}(y[n]) = \begin{cases} k_{min} & \text{if } y[n] \geq k_{min} \\ y[n] & \text{if } |y[n]| \leq k_{min} \\ -k_{min} & \text{if } y[n] \leq -k_{min}. \end{cases}$$

We will define the constants $k_{min}$ and $k_{max}$ later. The relation between the input $u[n]$ and the signal noise-disturbed output $y[n]$ is thus given by (see Fig. 5.7):

$$u[n] = r[n] - k(y[n])K_0(z)y[n],$$

from which we clearly see that we have a nonlinear controller $k(y[n])K_0(z)$. The nonlinear controller is defined by the values $k_{min} = 0.02$, $k_{max} = 1.45$, $\tau_z = \frac{1}{8}$, and $\tau_c = \frac{1}{100}$.

At this point, an obvious question is: What is the advantage of such a controller over a classical PI(D) controller with a constant gain $k$? It is known that the gain $k$ of a linear controller is used to either reduce the noise effect on the input and output, or to shorten output perturbation rejection. When the gain $k = k_{min}$ is small, we speak of a low-gain controller, whereas when $k = k_{max}$ we speak of a high-gain controller. A low-gain controller can attenuate the noise effect on the input and output at the cost of a longer perturbation rejection time at the output. Conversely, a high-gain controller generates a quick perturbation rejection, but bad noise attenuation. Clearly, the ability to use properties of both low-

and high-gain controllers would be advantageous. For this reason, the nonlinear controller $k(y[n])K_0(z)$ is designed as depicted in Fig. 5.7. Depending on $y[n]$, the gain $k(y[n])$ is chosen to reduce perturbation rejection time and increase noise attenuation at the same time.

### 5.7.3  Least-Costly Experiment Design Problem

The LCED problem we consider is as follows. We minimise a weighted sum of input and output power subject to a frequency-wise bound on the estimated transfer function $G(z, \hat{\boldsymbol{\theta}}_N)$. Mathematically, we solve the problem

$$\min_{\Phi_r} \frac{1}{2\pi} \int_{-\pi}^{\pi} \left( \overline{\alpha} |G_0(e^{-i\omega}, \boldsymbol{\theta}_0)|^2 + \overline{\beta} \right) |S_0(e^{-i\omega})|^2 \Phi_r(\omega) \, d\omega$$

subject to

$$\forall \omega : \ |G(e^{-i\omega}, \boldsymbol{\theta}_0) - G(e^{-i\omega}, \hat{\boldsymbol{\theta}}_N)| < \gamma(\omega) |G(e^{-i\omega}, \boldsymbol{\theta}_0)| \ \text{w.p.} \ \alpha, \qquad (5.24)$$

where we choose $\forall \omega : \ \gamma(\omega) = 0.1$. The optimisation problem above is used for the Sensitivity Method, whereas the above objective function in the Stealth approach considers $S_0 = 1$. We thus require that at every frequency the relative error in the estimated transfer function and the true system is less than or equal to 10% with probability $\alpha$. Furthermore, $S(z, \boldsymbol{\theta}_0)$ is the sensitivity function of the true system $(G_0(z), C(z))$. We choose $\overline{\alpha} = \overline{\beta} = 1$ in the objective function. In order to solve this problem, we furthermore uniformly grid the frequency range $[0, \pi)$ into $J = 40$ points, such that (5.24) can be written as a finite set of frequency-wise constraints (see Section 3.2.3), and choose $\alpha = 0.99$. The experiment length is furthermore set to $N = 3 \times 10^4$ and we recall that $\sigma_e^2 = 7.5 \times 10^{-4}$.

The resulting optimisation problem is of the form (3.1)-(3.2); the weighting function $\mathcal{L}(e^{-i\omega}, \boldsymbol{\theta}_0)$ in the objective function is given by (3.3), and the $J = 40$ frequency-wise constraints are of the form (3.16). The excitation spectrum $\Phi_r(\omega)$ in $P_{N,\theta}^{-1}$ is parameterised by a 40th-order FIR filter, see (3.5). The optimisation problem is now finite and can be solved, see Chapter 3.

In order to circumvent the chicken-and-egg issue, we replace $\boldsymbol{\theta}_0$ - following the previous numerical study - by an initial estimate $\boldsymbol{\theta}_{init} = (0.0793, 0.0699, -1.6695, -1.0874, 0.1263, -1.9422, 0.9442)^T$ that is obtained by performing a short ($N = 10^3$) Direct Method identification experiment (see Section 2.2.2) on the system shown in Fig. 5.7 (with $G_{id} = 0$) with a white-noise excitation signal. A Bode diagram of the data-generating system $G(z, \boldsymbol{\theta}_0)$ and the initial model $G(z, \boldsymbol{\theta}_{init})$ is shown in Fig. 5.8.

We can now solve the optimisation for the Stealth Method and the Sensitivity Method. In the former case, we use $G_{id} = G(z, \boldsymbol{\theta}_{init})$, whereas in the latter case we have $G_{id}(z) = 0$ and use $\boldsymbol{\theta}_{init}$ to obtain an estimate $S_{init}(z)$; see Section 5.3. The Box-Jenkins model structure $S_{init}(z)$ is of order three (which would be its order if there was no saturation in the controller). The optimal spectra for the two cases are shown in Fig. 5.9a in respectively red and blue. Observe that the spectra are quite similar. Furthermore, the costs of the experiments of the Stealth and Sensitivity methods are the same.
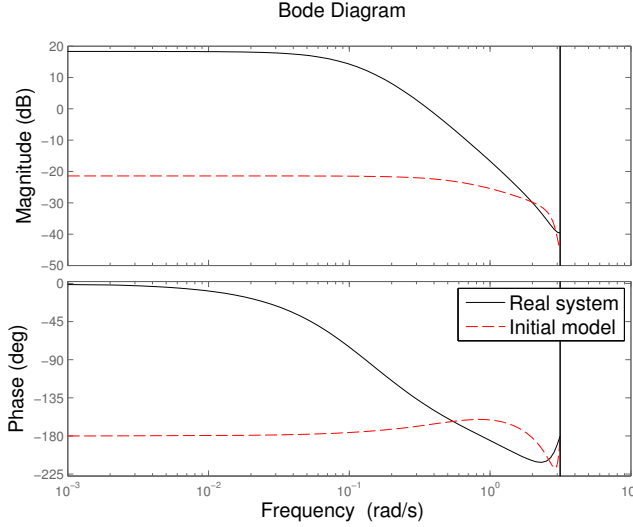
Figure 5.8: Bode diagram of the data-generating $G(z, \boldsymbol{\theta}_0)$ system (black) and initial model $G(z, \boldsymbol{\theta}_{init})$ (red) for numerical study 2.

### 5.7.4  Identification Results

For the identification of the true system $\mathscr{S}$, the optimal excitation signals are translated into the time domain, and applied as follows. For the Stealth Method, the corresponding optimal excitation signal $\{r_{opt}[n]\}_{n=1}^N$ is applied to the system shown in Fig. 5.7 where $G_{id}(z) = G(z, \boldsymbol{\theta}_{init})$. For the Sensitivity Method, we apply the corresponding optimal excitation signal to the system in Fig. 5.7 in which now $G_{id} = 0$.

Next, we collect in both cases the input and output data in a set $Z_N = \{u[n], y[n]\}_{n=1}^N$ and use (5.6) to obtain two estimates $\hat{\boldsymbol{\theta}}_N$. Figures 5.9b,c show respectively the Bode diagrams of the identified transfer functions $H(z, \hat{\boldsymbol{\theta}}_N)$ and $G(z, \hat{\boldsymbol{\theta}}_N)$ for the Stealth (red) and Sensitivity (blue) methods. Observe that we obtain models that are very close to the true frequency responses $G_0(e^{-i\omega})$ and $H_0(e^{-i\omega})$, both indicated with dashed black curves (both lie under the blue and red curves).

We also ran fifty Monte Carlo simulations and calculated the distance between the true model and the estimated model at each frequency, and took the worst case from the fifty simulations. (These distances could also be calculated analytically.) The result is shown in Fig. 5.9d, from which we see that in both cases the relative error between $G(z, \hat{\boldsymbol{\theta}}_N)$ and $G_0(z)$ is less than 10%, as required.

## 5.8  Numerical Study 3: A Dynamical Network

### 5.8.1  Introduction

The previous two numerical studies pertained to a single-input single-output system with an MPC (piece-wise affine controller) and explicit nonlinear controller. In this last numerical study, we will show how to use the Stealth and Sensitivity Method in order to apply experiment design on linear dynamical networks; see the works of Van den Hof et al.
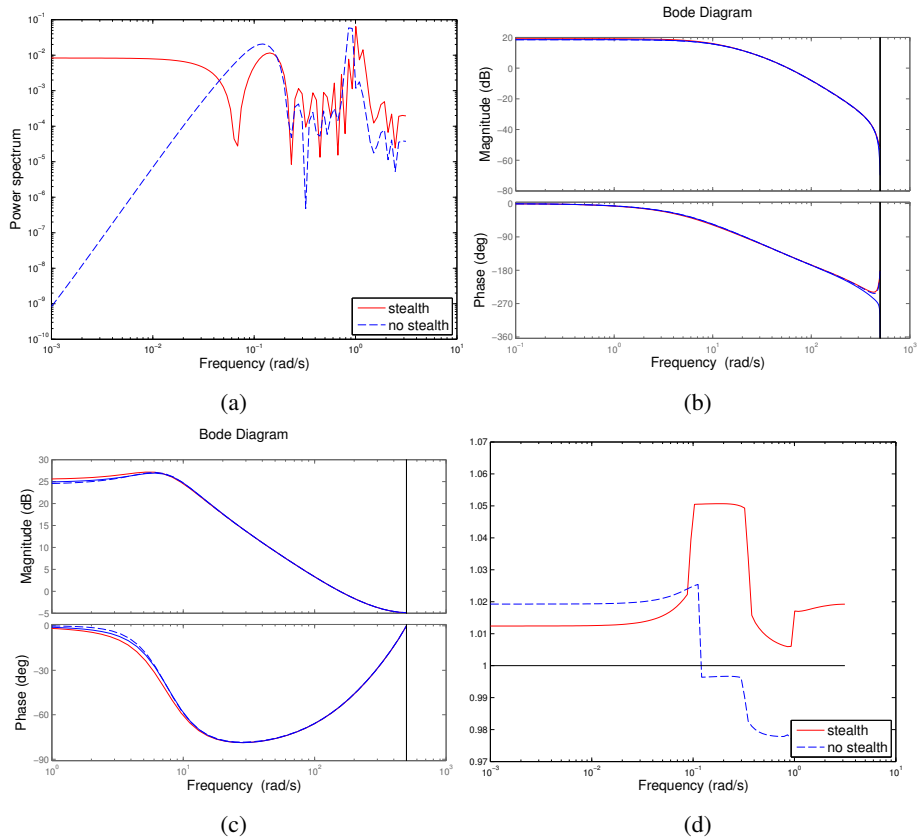
Figure 5.9: The figures above all pertain to one Monte Carlo experiment. (a) Optimal excitation spectra corresponding to the Stealth Method (red) and the Sensitivity Method (blue). (b) Bode diagram of the estimated transfer function $H(z, \hat{\boldsymbol{\theta}}_N)$ for the Stealth (red) and Sensitivity Method (blue). The true transfer function is shown in black, dashed. (c) Bode diagram of estimated $G(z, \hat{\boldsymbol{\theta}}_N)$ and true transfer function $G_0(z)$. Same colour coding as top figures. (d) Relative error between estimated $G(z, \hat{\boldsymbol{\theta}}_N)$ and true transfer function $G_0(z)$ for the Stealth (red) and Sensitivity (blue) methods. At all frequencies the relative error is less than 10%: the parameter accuracy constraints are thus satisfied.
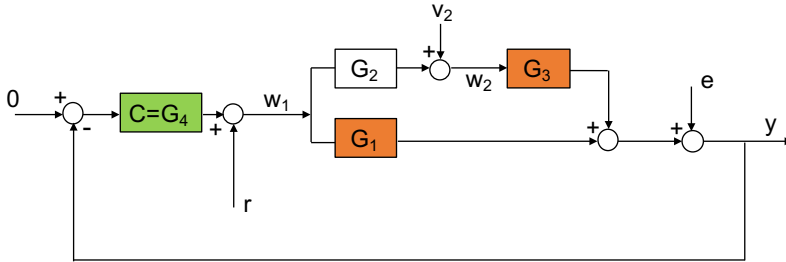
Figure 5.10: Schematic representation of the network. The controller $C = G_4(z)$ contains all feedback from the output $y$ to the input $w_1$. The signal $v_2$ is an external signal uncorrelated the noise signal $e$. The transfer function $G_4$ is unknown but will not be identified. Transfer function $G_2(z)$ is known. The transfer functions $G_1(z, \boldsymbol{\theta}_0)$ and $G_3(z, \boldsymbol{\theta}_0)$ are unknown, and for which the parameters $\boldsymbol{\theta}_0$ need to be estimated.

(2013); Dankers (2014) for an introduction to this topic.

Estimating a single transfer function (or even a subset of parameters in it) in a dynamical network consisting of many transfer functions can be a daunting task, predominantly due to the interconnected nature that is inherent to networks. To estimate a single transfer function, the user is left with several choices, one of which is the selection of input(s) and output(s) that are be used in the prediction error method (see Chapter 2). For simplicity, we will consider in this section a single output that is measured, and furthermore fix the input and output variables.

The network we consider is shown in Fig. 5.10. The input signal is $w_1$ and the output $y$; the other variables will be defined later. We are interested in identifying the parameters of transfer function $G_1(z)$. We assume that $G_2(z)$ is known, but that $G_3(z)$ and $G_4(z)$ are unknown (all these functions will be defined below). The latter transfer function should be understood as the total transfer function that describes the dynamics between the output $y$ and the input $w_1$; it is a superposition of serial- and parallel-coupled transfer function between these two signals. It can be interpreted as a controller, which contains a huge number of unknown parameters.

Our aim is to design an optimal excitation signal $r_{opt}$ so that we can identify the parameters in the transfer function $G_1(z)$ with a certain accuracy. In order to use LCED, we recall from the introduction that we require an explicit and known expression of the controller $C(z)$, in this case $G_4(z)$. However, since $G_4(z)$ can be made up of a very complex interconnection of systems, the transfer function $G_4(z)$ will be unknown. Fortunately, we can use the Stealth and Sensitivity method introduced in this chapter to circumvent the requirement of knowing $C(z) = G_4(z)$.

## 5.8.2 The Data-Generating System

The network is depicted in Fig. 5.10. All transfer functions are stable and rational, and are defined as follows:

$$G_1(z, \boldsymbol{\theta}) = \frac{\theta_1}{1 + \theta_2 z^{-1}}, \; G_2(z) = \frac{1}{1 - 0.25 z^{-1}}, \; G_3(z, \boldsymbol{\theta}) = \frac{\theta_3}{1 + \theta_4 z^{-1}}, \; G_4(z) = \frac{1}{1 - 0.65 z^{-1}},$$

where it should be understood that $\boldsymbol{\theta} = (\theta_1, \ldots, \theta_4)^T$, that $G_2(z)$ is known, and where $G_4(z)$ is unknown but does not need to be identified. The signal $r$ is the excitation signal

and $v_2$ and $e$ are two unknown and independent Gaussian white noise signals of respective variances $\sigma_{v_2}^2$ and $\sigma_e^2$. The true system is defined by $\boldsymbol{\theta}_0 = (0.1, -0.9, 0.67, -0.21)^T$. The transfer functions $G_1(z, \boldsymbol{\theta}_0)$ is unknown and needs to be identified such that the variances of the parameter estimates respect user-chosen constraints. However, as will be discussed below, to obtain a consistent estimate of $G_1(z, \boldsymbol{\theta}_0)$ the unknown transfer function $G_3(z, \boldsymbol{\theta}_0)$ also needs to be identified, although no restrictions are put on the variances of its parameters. It is for this reason that $\boldsymbol{\theta}_0$ contains both the parameters of $G_1(z)$ and $G_3(z)$.

### 5.8.3   The Sensitivity Method

In order to be able to identify $G_1$ consistently, Dankers (2014) has shown that both $G_1$ and $G_3$ need to be identified. Dankers (2014) furthermore showed that, to this end, it is sufficient to use the input data $w_1, w_2$ (see Fig. 5.10). The considered prediction error is

$$\varepsilon[n; \boldsymbol{\theta}] = y[n] - G_1(q, \boldsymbol{\theta})w_1[n] - G_3(q, \boldsymbol{\theta})w_2[n]. \tag{5.25}$$

For experiment design, we will need an expression of $\boldsymbol{P}_{N,\boldsymbol{\theta}}$. For this purpose, let us express (5.25) as a function of the external and independent signals $r$, $e$, and $v_2$. Denoting

$$\tilde{S}(q, \boldsymbol{\theta}) = \frac{1}{1 + G_4(q)(G_1(q, \boldsymbol{\theta}) + G_2(q)G_3(q, \boldsymbol{\theta}))}$$

as the transfer function between $r$ and $w_1$, we obtain

$$\varepsilon[n; \boldsymbol{\theta}] = ((G_1(q, \boldsymbol{\theta}_0) - G_1(q, \boldsymbol{\theta})) + G_2(q)(G_3(q, \boldsymbol{\theta}_0) - G_3(q, \boldsymbol{\theta}))) \tilde{S}_0(q)r[n] + \varepsilon_e[n] + \varepsilon_{v_2}[n],$$

where $\varepsilon_e$ and $\varepsilon_{v_2}$ are terms dependent on $e$ and $v_2$. We define for convenience $\tilde{S}_0(q) = \tilde{S}(q, \boldsymbol{\theta}_0)$.

Consequently, we see that the contribution of $r$ to the inverse covariance matrix is given by

$$\boldsymbol{P}_{r,N,\boldsymbol{\theta}}^{-1} = \frac{N}{2\pi\sigma_e^2} \int_{-\pi}^{\pi} \boldsymbol{F}_r(e^{-i\omega}, \boldsymbol{\theta}_0) \boldsymbol{F}_r^H(e^{-i\omega}, \boldsymbol{\theta}_0) \Phi_r(\omega) \, d\omega, \tag{5.26}$$

where $\boldsymbol{F}_r(e^{-i\omega}, \boldsymbol{\theta}') = \left(\nabla_{\boldsymbol{\theta}} G_1(e^{-i\omega}, \boldsymbol{\theta}) \mid_{\boldsymbol{\theta}=\boldsymbol{\theta}'} + G_2(e^{-i\omega})\nabla_{\boldsymbol{\theta}} G_3(e^{-i\omega}, \boldsymbol{\theta}) \mid_{\boldsymbol{\theta}=\boldsymbol{\theta}'}\right) \tilde{S}(e^{-i\omega}, \boldsymbol{\theta}_0)$. Thus, in order to be able to design $\Phi_r$, we need to perform an initial experiment with an initial $\{r_{init}[n]\}_{n=1}^{N_{init}}$ leading to data $\{u_{init}[n], y_{init}[n]\}_{n=1}^{N_{init}}$. With these data, we can identify the models $G_1(q, \boldsymbol{\theta}_0)$ and $G_3(q, \boldsymbol{\theta}_0)$. Using the data $\{r_{init}[n], u_{init}[n]\}_{n=1}^{N_{init}}$, we can also identify a model of $\tilde{S}(q, \boldsymbol{\theta}_0)$ which allows to design $\Phi_r$ optimally using (5.26). The contribution of $v_2$ and $e$ to the information matrix can be either neglected or estimated using similar techniques as in Section 5.5.

### 5.8.4   The Stealth Method

The Stealth Method requires, just as the Sensitivity Method, an initial estimate of $G_1$ and $G_3$ that can be deduced from an initial experiment. These models $G_{1,init}$ and $G_{3,init}$ can be used to determine

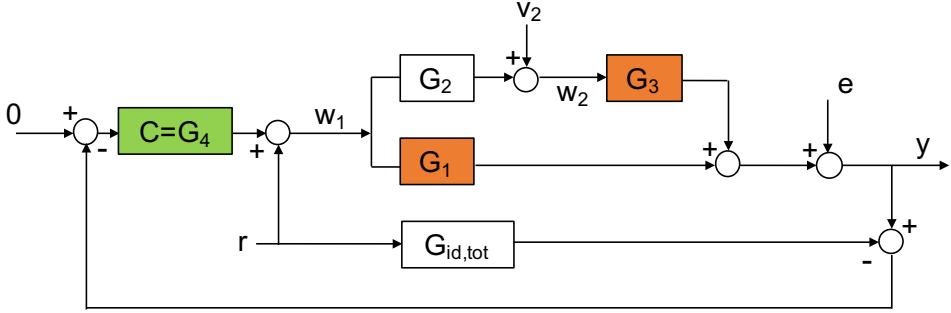$$G_{id,tot}(q) = G_{1,init}(q) + G_2(q)G_{3,init}(q).$$

Figure 5.11: Schematic representation of the network. The controller $C = G_4$ contains all feedback from the output $y$ to the input $w_1$. The signal $v_2$ is an external signal uncorrelated the the noise signal $e$ that is required in the identification procedure. In the case the Stealth Method is used, the block $G_{id,tot}$ is a non-zero rational, finite-order transfer function. The transfer function $G_4$ is unknown but will not be identified. Transfer function $G_2(z)$ is known. The transfer functions $G_1(z, \theta_0)$ and $G_3(z, \theta_0)$ are unknown, and for which the parameters $\theta_0$ need to be estimated.

This transfer function $G_{id,tot}$ is used to modify the network in such a way that $r$ is not sensed by the unknown 'controller' $G_4$. This is shown in Fig. 5.11. Assuming as in Section 5.3.2 that $G_{1,init} = G_1$ and $G_{3,init} = G_3$, the prediction error is then given by (c.f. (5.25))

$$\varepsilon[n; \theta] = ((G_1(q, \theta_0) - G_1(q, \theta)) + G_2(q)(G_3(q, \theta_0) - G_3(q, \theta))) r[n] + \varepsilon_e[n] + \varepsilon_{v_2}[n]$$

and the contribution of $r$ to the inverse covariance matrix, i.e., $P_{r,N,\theta}$ (c.f. (5.26)) becomes

$$P_{r,N,\theta}^{-1} = \frac{N}{2\pi\sigma_e^2} \int_{-\pi}^{\pi} \overline{F}_r(e^{-i\omega}, \theta_0) \overline{F}_r^H(e^{-i\omega}, \theta_0) \Phi_r(\omega) \, d\omega, \tag{5.27}$$

where $\overline{F}_r(e^{-i\omega}, \theta') = \left( \nabla_\theta G_1(e^{-i\omega}, \theta) \big|_{\theta=\theta'} + G_2(e^{-i\omega}) \nabla_\theta G_3(e^{-i\omega}, \theta) \big|_{\theta=\theta'} \right)$. This last expression is thus no longer a function of $\tilde{S}(q, \theta_0)$ or $G_4$. Consequently, the optimal input spectrum $\Phi_r$ can be determined (using $G_{1,init}$ and $G_{3,init}$).

## 5.8.5 Least-Costly Experiment Design Problem

We recall that our aim is to estimate the parameters $\theta_1$ and $\theta_2$ in transfer function $G_1(z, \theta)$ of the network in Fig. 5.11. Consequently, even though we will identify the parameters in both $G_1$ and $G_3$, we only impose constraints on the variances of the parameters in $G_1$:

$$\sigma_{\hat{\theta}_1}^2 \leq \frac{(0.01\theta_1)^2}{9} = 1.1 \times 10^{-7}, \text{ and } \sigma_{\hat{\theta}_2}^2 \leq \frac{(0.01\theta_2)^2}{9} = 9.0 \times 10^{-6}, \tag{5.28}$$

see Section 3.2.3. The LCED problem we solve is thus (5.13)-(5.14), in which $J = 2$, the above constraints are of the form (3.14), and $\mathscr{L}(e^{-i\omega}, \theta_0) = 1$; see also Example 3.2. The inverse covariance matrix $P_{N,\theta}^{-1}$ that is used to solve this problem is given by (5.26) for the Sensitivity Method, and by (5.27) for the Stealth Method. In other words, we will neglect the contribution $R_0$ to the accuracy of the estimates. We parameterise the input spectrum in both cases as $\Phi_r(\omega)$ with a multi-sine (3.6) defined by $T_s = 1$, $M = 105$ and $\omega_f = 0.03$ rad/s. The experiment length is $N = 10^5$, and the noise variances are $\sigma_e^2 = 0.05$ and $\sigma_{v_2}^2 = 0.075$.
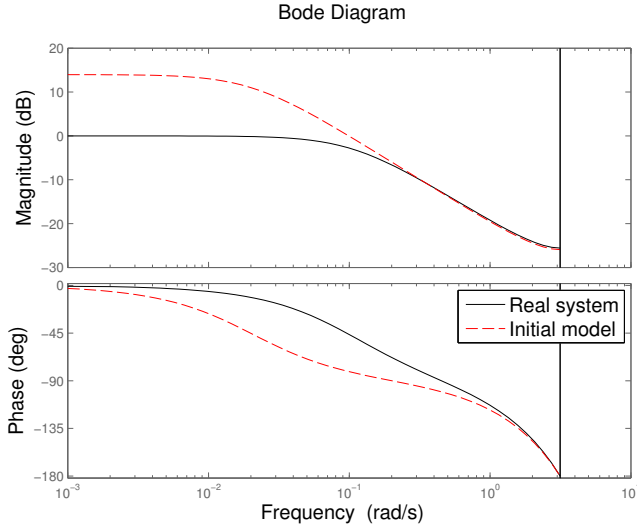
Figure 5.12: Bode diagram of the data-generating $G(z, \theta_0)$ system defined in Section 5.8.2 (red) and the initial model $G(z, \theta_{init})$ (red).

Regardless of Stealth or Sensitivity methods that we shall consider, one experiment using a white-noise excitation signal of variance 36 and length $N_{init} = 10^5$ samples is performed. The data $Z_{N_{init}} = \{w_1[n], w_2[n], y[n]\}_{n=1}^{N_{init}}$ is used with (5.25) to obtain the initial estimate $\theta_{init} = (0.1, -0.98, 0.75, -0.25)^T$, which will replace $\theta_0$ in $P_{N,\theta}^{-1}$. A Bode diagram of $G(z, \theta_{init})$ and $G(z, \theta_0)$ is shown in Fig. 5.12. The same experiment data is used to provide an estimate of the sensitivity function between $w_1[n]$ and $r[n]$, and is denoted by $S_{init}(z)$. The true sensitivity function $\tilde{S}_0(z)$ and the estimated $S_{init}(z)$ are shown in respectively black and blue in Fig. 5.13a. The model order of $S_{init}$ is equal to the one of the true sensitivity, and the delay is zero. Observe that a relatively good fit is obtained, except for the phase at frequencies exceeding 0.1 rad/s (at higher frequencies, more power is apparently required to obtain a better fit of the phase).

Neglecting the contributions of the noise signals $e[n]$ and $v_2[n]$ to the parameter accuracy, we construct the optimal input spectrum $\Phi_{r,opt}(\omega)$ based on the following four situations:

## I. Sensitivity Method with $\theta_{init}$

This first LCED problem considers the approximation of the sensitivity function through the Sensitivity Method detailed in Section 5.8.3. The optimisation problem is solved by substituting the previously estimated sensitivity $S_{init}(q)$ in the inverse covariance matrix (5.26), and by replacing furthermore $\theta_0$ with $\theta_{init}$ in all of its other terms. The resulting optimal amplitude of $r$ for this problem is shown in Fig. 5.13b as a function of frequency in dark blue. Observe that it contains two sinusoids, corresponding with the requirement of obtaining a consistent estimate of four parameters (Ljung (1971)).

**II. Sensitivity with $\theta_0$**

This second LCED problem is similar to LCED Experiment I. The difference, however, is that instead of substituting the true parameter vector with the initial estimate $\theta_{init}$, we compute the optimal input spectrum as if we had full knowledge of the true system. In other words, we use $\tilde{S}(q, \theta_0)$ in (5.26), of which all other terms are also evaluated at $\theta_0$. The result is shown in Fig. 5.13b in cyan. We can now compare the optimal amplitudes found from LCED problem I (that considered the realistic scenario of replacing the unknown true parameter with an estimate) with the true optimal one (computed here). Notice that also two sinusoids are present, although both are slightly shifted to a higher frequency. This clearly shows that the optimal frequencies when using the estimate $\theta_{init}$ in the LCED problem are chosen too low.

**III. Stealth Method with $\theta_{init}$**

This LCED problem is concerned with the Stealth identification framework as displayed in Fig. 5.11. We replace the true vector $\theta_0$ by the initial estimate $\theta_{init}$ and define $G_{id}(z) = G(z, \theta = \theta_{init})$. This leads to an inverse covariance matrix expression in which the contribution of $\Phi_r$ no longer contains a sensitivity function; see (5.27). The resulting optimal amplitude as a function of frequency is shown in dark red in Fig. 5.13b. Not surprisingly, two spectral lines are present in order to consistently estimate the four parameters in $\theta_0$. Notice that these two peaks are close to the ones obtained with the LCED problem I.

**IV. Stealth Method with $\theta_0$**

This LCED problem is identical to III, with the exception that we use the true parameter vector $\theta_0$ in the inverse covariance matrix (5.27) that is present in the LCED problem, and consequently use $G_{id}(z) = G_0(z)$. The resulting optimal input spectrum is shown in magenta in Fig. 5.13b. Similar to the comparison between LCED problems I and III, we observe that the LCED problems II and IV have spectral lines that occur at similar frequencies. It should be noted however that the highest frequency of the current experiment is quite a bit lower than the one of LCED problem II, and is due to the fact that no controller is present in the design of the optimal input signal using the Stealth Method, leading to a different optimal frequency.

Comparing the LCED problems I and II with III and IV in Fig. 5.13b, we observe that the power of the excitation signals of III and IV are less than those of I and II. This is due to the fact that the Stealth implementation reduces the impact of the feedback $G_4(z)$ on the loop. Indeed, From Fig. 5.13a we see that at the excitation frequencies the amplitude of the excitation signal is reduced as the sensitivity is less than unity. Consequently, for the traditional loop in which the stealth block $G_{id}(z)$ is not present (i.e. the Sensitivity Method), the power of the excitation signal must be higher in order to increase the signal-to-noise ratio. This in turn ensures that the variance constraints are satisfied.

Furthermore, we find that in all four experiments two sinusoids are required. We have already explained that this is in agreement with the requirement of obtaining consistent estimates of four parameters. Nonetheless, this seems to contradict the heuristic arguments in Chapter 4 and results from Javaherian (1974), which suggest that in order to estimate $\kappa$ parameters with an optimal input signal, it is almost always true that only $\kappa/2$ sinu-

soids are required. However, the situation here is different. Indeed, in this network, we want to accurately estimate the two parameters $\theta_1$ and $\theta_2$ residing in $G_1$. Constraints have therefore been put on the variances of the estimates $\hat{\theta}_1$ and $\hat{\theta}_2$. However, we also need to identify the parameters in $G_3$ to obtain consistent estimates of the parameters in $G_1$. We thus have $\kappa = 4$ unknown parameters, of which only $J = 2 < \kappa$ parameters have constraints on their estimates. Consequently, the variance $\sigma_{\hat{\theta}_i} = e_i^T P_{N,\theta} e$ of the estimate $\hat{\theta}_i$ is a function of the $4 \times 4$ covariance matrix. To ensure that the variances of all the estimates, and in particular of $\hat{\theta}_1$ and $\hat{\theta}_2$, are finite, the inverse covariance matrix $P_{N,\theta}^{-1}$ must be full rank. Indeed, the variance of each estimate is inversely proportional to the determinant of the inverse covariance matrix, which is only non-zero if $P_{N,\theta}^{-1}$ has full rank. Thus, the optimal input spectrum requires two sines to ensure the full rank condition (Ljung (1971)). The LCED optimisation problem for this network case thus finds the optimal amplitudes and frequencies of the two required sinusoids. Had we only needed to estimate $\kappa = 2$ parameters, each with a variance constraint ($J = 2$), the optimal input signal would probably contain only one sine.

### 5.8.6 Identification Results

In the previous section we have computed four optimal spectra. LCED problems I and II correspond to a Sensitivity Method identification experiment, see Section 5.8.3, and the problems III and IV correspond to a Stealth identification experiment, see Section 5.8.4. We will now use these optimal spectra and perform identification experiments. We recall that all experiments are done on the same network defined above.

For LCED problems I and II, we consider the identification scheme as displayed in Fig. 5.10. The signal $\{r_{i,opt}[n]\}_{n=1}^N$, corresponding to the optimal input signal computed with LCED problem $i \in \{I, II\}$, is applied to the true closed-loop system (defined in the previous sections), and we collect the data $Z_N = \{w_1[n], w_2[n], y[n]\}_{n=1}^N$. This data is used to obtain an estimate $\hat{\theta}_N$ using (5.25) and (5.6). Repeating this procedure using Monte Carlo simulations (i.e. using varying noise realisations), we obtain a set of one hundred estimates, i.e. $\{\hat{\theta}_{k,N}\}_{k=1}^{100}$. We take the first two components of each estimate in this set, and compute their respective variances; see Table 5.2. Note that these variances obtained with the signals $r_{I,opt}$ and $r_{II,opt}$ satisfy the required accuracy constraints (5.28). Note that when using $r_{II,opt}$ - constructed on the basis of full knowledge of the system - leads to lower variances of $\theta_1$ and $\theta_2$ than when using $r_{I,opt}$.

For the LCED problems III and IV, we consider the Stealth identification scheme as displayed in Fig. 5.11. The signal $\{r_{i,opt}[n]\}_{n=1}^N$, corresponding to the optimal input signal computed with LCED problem $i \in \{III, IV\}$, is applied to the true closed-loop system. In the case $i = III$, the Stealth block $G_{id}(z) = G(z, \theta_{init})$, and in the case $i = IV$ we use $G_{id}(z) = G_0(z)$. As for the previous two experiments, we collect the data $Z_N = \{w_1[n], w_2[n], y[n]\}_{n=1}^N$ to obtain an estimate $\hat{\theta}_N$ using (5.25) and (5.6). The variances of the estimates of $\theta_1$ and $\theta_2$ are also obtained from one-hundred Monte Carlo simulations, and are shown in Table 5.2. We again find that the variance constraints (5.28) are respected, and that the variances using the full knowledge of the system are lower than when using the estimate $\theta_{init}$ in the optimisation problems.

Comparing identification experiments I and II with III and IV, we see that the variances using the Stealth Method are higher (but still satisfy the constraints). However, the optimal spectra of $r_{III,opt}$ and $r_{IV,opt}$ shown in Fig. 5.13b have a lower power, and thus lead to a

| Identification Experiment | Variance $\theta_1$ | Variance $\theta_2$ | Mean $\hat{\theta}_1$ | Mean $\hat{\theta}_2$ |
|---|---|---|---|---|
| I | $3.335 \times 10^{-8}$ | $7.386 \times 10^{-8}$ | 0.1 | -0.9 |
| II | $3.253 \times 10^{-8}$ | $6.071 \times 10^{-8}$ | 0.1 | -0.9 |
| III | $4.602 \times 10^{-8}$ | $2.097 \times 10^{-7}$ | 0.1 | -0.9 |
| IV | $4.587 \times 10^{-8}$ | $2.462 \times 10^{-7}$ | 0.1 | -0.9 |

Table 5.2: Variances and means of the estimated parameters of transfer function $G_1(z, \boldsymbol{\theta})$ obtained from identification experiments using the optimal input spectra shown in Fig. 5.9b. Observe that the variances from the Stealth experiments III and IV are higher than from experiments I and II. However, all experiments obey the variance constraints (5.28).



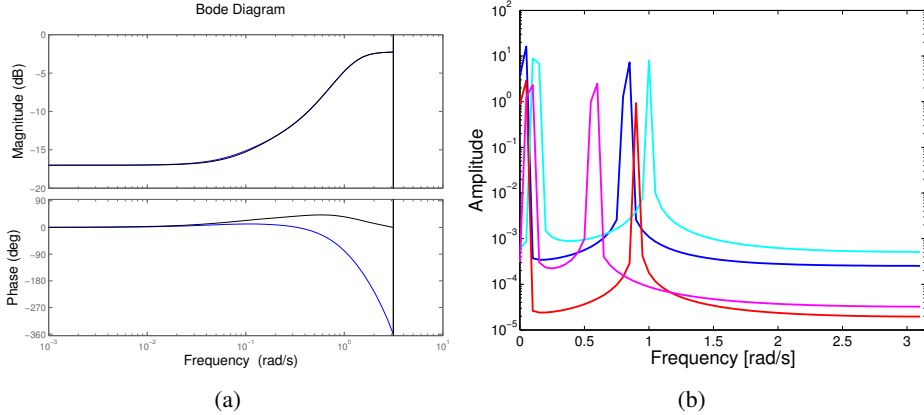(a)                                                    (b)

Figure 5.13: (a) Bode diagram of the estimated sensitivity function (blue) and the true sensitivity function (black). Note that the magnitudes match very well, but the phase is poorly matches after about $10^{-1}$ rad/s. (b) The optimal input spectra for $r[n]$ in the case of an estimated sensitivity (dark blue), the true sensitivity based on $\boldsymbol{\theta}_0$ (cyan), the stealth method based on prior estimate (dark red), and the stealth method using $\boldsymbol{\theta}_0$ (magenta). Note that both results from the stealth method deliver less powerful input signals.

lower experiment cost (5.13). The Stealth Method thus slightly outperforms the Sensitivity Method in this case.

Notice furthermore that all the variances are lower than required. This is due to the fact that we have neglected the contribution of the noise $e$ and $v_2$ in our design of the optimal spectra. Consequently, the optimal spectra are more powerful than required in order to satisfy the variance constraints.

## 5.9   Summary

In this chapter we have generalised the Least-Costly Experiment Design framework, such that it can now also be applied to linear systems with a (possible unknown) nonlinear or unknown linear controller. To this end, we have introduced the Stealth Method, which adapts the classical closed-loop scheme such that the controller no longer senses the excitation signal. We also introduced the Sensitivity Method that estimates the (nonlinear) sensitivity function of a closed-loop system. This sensitivity function estimate can then be used in the Least-Costly Experiment Design framework to replace the unknown, true sensitivity function. Three numerical studies have shown the strength of these two methods. In all studies, optimal input spectra are computed that lead to estimates that satisfy user-chosen accuracy constraints, even when the true parameter vector is not used in the

LCED problem.

There are still many open research questions to address. For instance, how can we position the Stealth block in a network as smartly as possible in order to estimate a particular transfer function in it? If the network contains multiple transfer functions that require identification, how should we place one or more Stealth blocks in it?

# 6

# LCED for Structured Systems Governed by Linear PDEs

*"Nothing in life is to be feared, it is only to be understood. Now is the time to understand more, so that we may fear less."* - Marie Curie

## 6.1  Introduction

It is mentioned in Section 3.2.3 that accuracy estimation of key physical parameters in a system is an important problem. We give some examples: a material can be characterised by its conductivity and diffusivity constants in heat transfer studies (Gabano and Poinot (2009)), realistic groundwater contamination simulations require accurate estimates of diffusivity and advection constants (Yeh (1986); Wagner (1997)), permeability and porosity of rock aid in oil extraction from subsurface reservoirs (Mansoori et al. (2014)), etc. In this context, we consider in this chapter the problem of optimally designing the identification experiment leading to the estimates of these physical parameters. More particularly, we design the least-intrusive excitation signal that nevertheless leads to parameter estimates with variances that do not exceed certain given (user-chosen) limits. Physical systems can have different structures. In this chapter, we are particularly interested in those systems that can be described by linear partial differential equations (PDEs) with spatially-independent coefficients.[1]

Such systems are characterised by equations that not only contain time derivatives but also spatial ones. In the System Identification literature they are usually referred to as distributed systems. The phenomena described by such equations are quite pervasive in the physical world (convection, diffusion, diffusion-advection-reaction, wave phenomena). Consequently, it is of importance to be able to design experiments that will allow identification of physical parameters in those systems in an accurate manner. Unfortunately, as their dynamics are described by PDEs, the classical optimal experiment design[2] techniques that have been developed for systems described by ordinary differential equations (ODEs) cannot be directly applied, see e.g. (Jansson and Hjalmarsson (2005); Bombois

---

[1]Parts of this chapter have been published in (Potters et al. (2016a)).

[2]For a general introduction to optimal experiment design, we refer the reader to the nice historical review by Mehra (1974b).

et al. (2006)). The classical approach in Chapter 3 will therefore have to be adapted. This is one of the contributions of the present chapter. Moreover, the particular structure of the systems described by PDEs allows us to analyze an additional design aspect that is usually not considered in optimal (least-costly) experiment design: the location of the actuator that will excite the system and the location of the sensor that will measure the output of the system for the purpose of identification. Indeed, as mentioned in the recent book of Uciński (2004), most literature on optimal sensor and actuator location in distributed systems deals with state estimation, but few works actually address parameter identification. Yet, finding such locations can greatly improve the accuracy of the estimates, as shown by Rensfelt et al. (2008) on an elasticity estimation problem. This chapter addresses the problem of finding the optimal sensor and actuator locations *as well as* finding the optimal spectrum of the input signal.

Before addressing optimal experiment design for systems decribed by PDEs, let us first discuss how we will perform the identification of the physical parameter vector $\boldsymbol{\theta}_0$ of such a system. Like all physical systems, systems described by PDEs are continuous-time systems. Since we assume linearity, the relation between the continuous-time input and output is given by a continuous-time transfer function $G(s, \boldsymbol{\theta}_0)$ in the Laplace variable $s$ ($\boldsymbol{\theta}_0$ appears explicitly in $G(s, \boldsymbol{\theta}_0)$). However, for systems described by PDEs, this continuous-time transfer function is not rational in $s$ (it can be e.g. $G(s) = \cosh(\sqrt{s})$). A closed-form expression of $G(s, \boldsymbol{\theta}_0)$ can be derived if the PDE is analytically tractable, although this is in general not possible for complicated (high-order, coupled) systems. Because the data that will be used for the identification are discrete, we need a discrete-time representation of $G(s, \boldsymbol{\theta}_0)$ that is also explicit in $\boldsymbol{\theta}_0$. However, such a representation does not exist in practice (it would be of infinite order). To circumvent this problem, spatio-temporal discretisation is generally applied and yields a finite-order approximation $G(z, \boldsymbol{\theta}_0)$ of the discrete-time transfer function between the discrete-time input and output data. The approximation consists of dividing the spatial dimension into a finite number of intervals in which the states of the systems are supposed constant. The order of $G(z, \boldsymbol{\theta}_0)$ is then related to the number of intervals in the grid. This spatio-temporal discretisation yields a transfer function that is still explicit in $\boldsymbol{\theta}_0$. Different discretisation schemes exist. In this chapter, we propose to use the Crank-Nicolson stencil (Crank and Nicolson (1947)), which is unconditionally stable, and also ensures that the finite-order approximation $G(z, \boldsymbol{\theta}_0)$ is stable. Once we have the description of the system in the form of the transfer function $G(z, \boldsymbol{\theta}_0)$, it is straightforward to use the input-output data to identify the parameter vector $\boldsymbol{\theta}_0$ using prediction-error techniques.

   A second method to simulate/identify the system explicit in $\boldsymbol{\theta}$ exists. When the PDE is analytically tractable, we can make use of the linearity of the system to calculate the system response (Ljung (1999)). However, this method is only applicable for an input signal that is a superposition of sines.

   These two approaches are not the only ones possible to identify the physical parameter vector $\boldsymbol{\theta}_0$. A rational or fractional black-box model can also be first identified and then the physical parameters be deduced from the parameters of the black-box model (see for instance (Poinot et al. (2002); Poinot and Trigeassou (2003); Gabano and Poinot (2011); Aoun et al. (2004))). However, these approaches require models with many parameters that are implicitly coupled to the physical ones. As such, the identification procedure will be numerically heavy. If the continuous-time transfer function $G(s, \boldsymbol{\theta}_0)$ can be expressed

in closed form, frequency-domain approaches can also be used to identify $\boldsymbol{\theta}_0$ from the collected data (see for instance (Pintelon et al. (2005))). Recently, a nice instrumental variable method has also been proposed by Schorsch et al. (2013). However, we have chosen the approach via $G(z, \boldsymbol{\theta}_0)$ (or $G(s, \boldsymbol{\theta}_0)$), since it is the most general, the most straightforward, and useful for Optimal Experiment Design.

We have now defined our identification method and we have an expression of the true plant transfer function as a function of the physical parameters (which in general is also a function of the sensor and actuator locations, or other design variables). When a discrete-time plant transfer function $G(z, \boldsymbol{\theta}_0)$ is considered, we can then use the classical optimal experiment design technique introduced in Chapter 3 to optimally design the input signal for the identification of the physical parameter vector $\boldsymbol{\theta}_0$. The to-be-designed optimal signal therefore needs to be parametrised. Generally, it is parametrised as a superposition of sinusoids (e.g. a multi-sine) or a filtered white noise. These parametrisations make the optimal experiment design problem convex and finite-dimensional. The transfer function $G(z, \boldsymbol{\theta}_0)$ being generally of large order, it is more practical to parametrise the to-be-designed optimal input signal as a multi-sine (with fixed frequencies, but free amplitudes). Indeed, in this particular case, only the frequency response of the gradient of $G(z, \boldsymbol{\theta}_0)$ with respect to $\boldsymbol{\theta}_0$ is required for optimal experiment design[3]. In the case where a closed-form expression of $G(s, \boldsymbol{\theta}_0)$ exists, the frequency response of the gradient of this usually simpler continuous-time transfer function can be used instead in the optimal experiment design procedure.

The approach above can be applied for each sensor/actuator location in a very easy way and the optimal experiments (in the sense of experiment cost) for each location can be compared, from which the optimal locations can be determined.

We apply our methodology to one-dimensional, second-order linear PDEs with spatially-independent coefficients. Diffusion-advection-reaction processes in real life can be modelled with this family of equations. We stress that our methodology is applicable to higher-dimensional, higher-order PDE systems with different boundary conditions (as long as a discrete-time transfer function between input and output can be determined). We introduce and scale the continuous-time physical models in Section 6.2 and 6.2.2. The unscaled physical model represents the (continuous-time) true system which will be used to identify the physical parameters $\boldsymbol{\theta}_0$ with the use of our optimal input signal. The scaled model will be used for optimal input signal design and in the identification procedure. This procedure, together with the generation of discrete-time input and output signals, is explained in Section 6.3. The identification procedure requires simulation of the output as a function of $\boldsymbol{\theta}$ and is introduced in Section 6.3.2. The experiment design framework is explained in Section 6.4 and shows how to generate the optimal input signal for given choice of sensor and actuator locations. We generalise the least-costly experiment design framework in Section 6.4.3, where now also optimal sensor and actuator locations are computed. In Section 6.5, we apply our methodology to a diffusion process in which two material properties are identified with a front-face experiment.

---

[3]The gradient is indeed used to compute the covariance matrix of the identified parameter vector.

## 6.2    Diffusion-Advection-Reaction Processes

### 6.2.1    The Governing Equations

The diffusion-advection-reaction equation typically contains only a few key physical parameters, the most important one being the so-called diffusivity parameter, i.e., the hydraulic diffusivity parameter in flow through porous media, the conductivity coefficient in conductive heat transfer, the diffusion parameter in mass transfer, etc. Although this lumped parameter is a function of microscopic properties of the system, it effectively characterises the observed macroscopic dynamic behaviour of the system. Hence, using macroscopic measurements of the system, it is possible to estimate such parameters. We shall use the family of diffusion-advection-reaction processes as a showcase of our methodology, but we remind the reader that it is applicable to higher-order linear PDE processes. Furthermore, we make a particular choice of boundary conditions, but many others exist that can also be applied within our framework. However, it is important to note that we restrict attention to systems with physical parameters that are not spatially dependent.

   Diffusion-advection-reaction processes are described by the following family of second-order linear partial differential equations:

$$\frac{\partial f(x,t)}{\partial t} = \theta_1 \frac{\partial^2 f(x,t)}{\partial x^2} + \theta_2 \frac{\partial f(x,t)}{\partial x} + \theta_3 f(x,t), \qquad (6.1)$$

where $f(x,t)$ represents a macroscopic physical quantity at continuous time $t$ and continuous position $x$. The coefficients $\theta_1 > 0$, $\theta_2$, $\theta_3$ are physical parameters. The spatial domain is defined by $\mathcal{D} = [0,L]$, where $L$ the domain length. We assume zero initial conditions at $t = 0$. The boundary conditions are:

$$-\theta_4 \left.\frac{\partial f(x,t)}{\partial x}\right|_{x=x_u} = u(t), \; y_{nf}(t) = f(x_y,t) \text{ and } f(L,t) = 0 \, \forall t. \qquad (6.2)$$

The physical parameters are collected in the vector $\boldsymbol{\theta} = (\theta_1, \theta_2, \theta_3, \theta_4)^T$. The first boundary condition in (6.2) is of the $2^{nd}$ kind, known as the Neumann boundary condition. It expresses the flow rate across the boundary at position $x = x_u$ induced by the influx $u(t)$. We define $u(t)$ as the user-imposed (known) input signal to the physical system and therefore call $x_u \in \mathcal{D}$ the input location. The second boundary condition defines the noise-free output $y_{nf}(t)$ being equal to the physical quantity $f(x,t)$ at the output measurement location $x = x_y \in \mathcal{D}$. We thus consider a single-input, single-output system. The third boundary condition states that the physical quantity $f(x,t)$ at location $x = L$ is equal to zero at all times.

**Definition 6.1** *The data-generating system is defined by equations (6.1)-(6.2) and setting* $\boldsymbol{\theta} = \boldsymbol{\theta}_0$, *where* $\boldsymbol{\theta}_0$ *are the true physical parameter values.*

If the system of equations (6.1)-(6.2) is analytically tractable, then a Laplace transform of (6.1)-(6.2) allows us to relate the input $u(t)$ and output $y_{nf}(t)$ of the data-generating system through

$$Y_{nf}(s) = G_{x_u,x_y}(s,\boldsymbol{\theta}_0)U(s), \qquad (6.3)$$

where $s$ is the Laplace variable, $Y_{nf}(s) = \mathscr{L}\left\{f(x_y,t)\right\}$ the Laplace transform of $y_{nf}(t)$,

$U(s) = \mathscr{L}\{u(t)\}$ the Laplace transform of $u(t)$, and $G_{x_u,x_y}(s,\boldsymbol{\theta}_0)$ is defined as their transfer function[4]. The subscripts $x_u, x_y$ indicate that the transfer function depends on the input and output locations. Hence, the above relation shows that the physical system may be interpreted as a linear, time-invariant system defined through input $U(s)$, output $Y_{nf}(s)$, and transfer function $G_{x_u,x_y}(s,\boldsymbol{\theta}_0)$. As mentioned in the Section 6.1, this transfer function will be irrational and of infinite order in $s$.

### 6.2.2 Non-dimensionalisation

An inherent feature of physical systems is the order-of-magnitude difference between the input and output values, and between the physical parameters values. Numerical simulation of the unscaled system (6.1)-(6.2) is prone to numerical difficulties, especially when considering the optimal experiment design algorithm, which uses a covariance matrix expression of the parameters. Without scaling, this matrix is usually ill-conditioned and consequently the algorithm cannot find a solution to the optimisation problem.

To avoid these difficulties we non-dimensionalise equations (6.1)-(6.2) as follows:

1. Scale parameter vector $\boldsymbol{\theta}$: $\tilde{\boldsymbol{\theta}} = \boldsymbol{\Theta}_s^{-1}\boldsymbol{\theta}$, where $\boldsymbol{\Theta}_s = \mathrm{diag}(\theta_{s,1},\ldots,\theta_{s,4})$ is a diagonal matrix containing the scaling factors for each element $\theta_i$ in the vector $\boldsymbol{\theta}$,

2. Non-dimensionalise all variables:

$$\tilde{f} = \frac{f}{f_s}, \; \tilde{u} = \frac{u}{u_s}, \; \tilde{x} = \frac{x}{x_s}, \; \tilde{t} = \frac{t}{t_s}, \tag{6.4}$$

    where $f_s$, $u_s$, $x_s$, and $t_s$ are as-of-yet undecided scaling values,

3. Rewrite (6.1)-(6.2) in terms of the non-dimensional parameters and variables defined in step 1 and 2:

$$\frac{\partial \tilde{f}(\tilde{x},\tilde{t})}{\partial \tilde{t}} = \tilde{\theta}_1 \frac{\theta_{s,1}t_s}{x_s^2} \frac{\partial^2 \tilde{f}(\tilde{x},\tilde{t})}{\partial \tilde{x}^2} + \tilde{\theta}_2 \frac{\theta_{s,2}t_s}{x_s} \frac{\partial \tilde{f}(\tilde{x},\tilde{t})}{\partial \tilde{x}} + \tilde{\theta}_3 \theta_{s,3}t_s \tilde{f}(\tilde{x},\tilde{t}), \tag{6.5}$$

    with boundary conditions

$$-\tilde{\theta}_4 \frac{\theta_{s,4}f_s}{u_s x_s} \frac{\partial \tilde{f}(\tilde{x},\tilde{t})}{\partial \tilde{x}}\Big|_{\tilde{x}=\tilde{x}_u} = \tilde{u}(\tilde{t}), \; \tilde{y}_{nf}(\tilde{t}) = \tilde{f}(\tilde{x}_y,\tilde{t}), \; \text{and } \tilde{f}(\frac{L}{x_s},\tilde{t}) = 0 \forall \tilde{t}, \tag{6.6}$$

4. Select $f_s$, $u_s$, $x_s$, and $t_s$ such that as many as possible terms in (6.5)-(6.6) are solely a function of $\tilde{\boldsymbol{\theta}}$, and therefore of $O(1)$. The selection is not unique. One possible choice is to freely choose $f_s$ and determine $x_s$, $t_s$, and $u_s$ as the solution of the following three equations: $t_s = x_s^2/\theta_{s,1}$, $x_s = \theta_{s,2}t_s$, and $u_s = \theta_{s,4}f_s/x_s$. This leads to $x_s = \theta_{s,1}/\theta_{s,2}$, $t_s = \theta_{s,1}/\theta_{s,2}^2$ and $u_s = \theta_{s,4}\theta_{s,2}f_s/\theta_{s,1}$. If some $\tilde{\theta}_i$ are zero, more freedom is available.

Step 1 ensures that the dimensionless parameters are of $O(1)$; a necessary step in order to apply experiment design. Although we don't know the actual values of $\boldsymbol{\theta}_0$, we do know their order of magnitude. Consequently, each element in the scaled vector $\boldsymbol{\theta}$ can be made

---

[4]For some simple diffusion processes an analytical solution exists, and therefore also an analytical expression of $G_{x_u,x_y}$.

of order one. Step 4 simplifies the non-dimensional system and shows which processes (i.e. diffusion, advection, or reaction) are dominant[5]. Substitution of $\theta = \theta_0$ in step 1 and following the scaling procedure then defines the scaled equivalent of the *data-generating system* as detailed in Definition 6.1.

The relation between the scaled output $\tilde{y}_{nf}(\tilde{t})$ and scaled input $\tilde{u}(\tilde{t})$ for the family of scaled physical systems reads

$$\tilde{Y}_{nf}(\tilde{s}) = \tilde{G}_{\tilde{x}_u, \tilde{x}_y}(\tilde{s}, \tilde{\theta}) \tilde{U}(\tilde{s}), \tag{6.7}$$

where now $\tilde{Y}_{nf}(\tilde{s}) = \mathscr{L}\left\{\tilde{f}(\tilde{x}_y, \tilde{t})\right\}$, $\tilde{U}(\tilde{s}) = \mathscr{L}\left\{\tilde{u}(\tilde{t})\right\}$ and $\tilde{s} = st_s$. This equation is the scaled equivalent of equation (6.3) for $\tilde{\theta} = \tilde{\theta}_0 \equiv \Theta_s^{-1}\theta_0$.

## 6.3   Identification and Simulation

### 6.3.1   Introduction

In the previous sections we have defined the continuous-time *data-generating system*, see Definition 6.1. This system represents the true physical process of which we want to identify the physical parameters $\theta_0$. To accomplish this, we will here consider open-loop identification, i.e., the excitation signal will be applied directly to the input of the system: $r = u$. We will suppose in the sequel that this applied excitation is a continuous-time signal, e.g. a continuous-time multi-sine[6]. This continuous-time input signal yields a continuous-time noise-free output signal $y_{nf}(t)$.

Since the prediction error identification method requires discrete-time data, we will choose a certain sampling time $T_s$. If the input signal $u(t)$ contains frequencies higher than the corresponding Nyquist frequency $\pi/T_s$, the input and output data are first filtered by an anti-aliasing filter. The sampling time $T_s$ is generally chosen such that the Nyquist frequency is a decade above all dynamics of the system (i.e. the system's bandwidth).

With a sampling time $T_s$ chosen, we can deduce the discrete-time input signal $u_D[n] = u(t = nT_s)$, $n = 1, \ldots, N$, with $NT_s$ the experiment length expressed in seconds. The discrete-time output $y_D[n]$ is obtained by measuring the continuous-time output $y_{nf}(t)$ at time instants $t = T_s$, $t = 2T_s, \ldots, t = NT_s$. This measurement process is assumed to be corrupted by a zero-mean white noise with variance $\sigma_e^2$. In other words

$$y_D[n] \equiv y_{nf}(t = nT_s) + e[n], \tag{6.8}$$

where $e[n]$ represents the zero-mean white noise with variance $\sigma_e^2$. Following this procedure we obtain the data set $Z_N = \{u_D[n], y_D[n]\}_{n=1}^N$.

### 6.3.2   Identification Procedure

We identify the physical parameter vectors $\theta_0$ using the collected data. First, we scale the dataset $Z_N$ using (6.4) to $\tilde{Z}_N = \left\{\frac{u_D[j]}{u_s}, \frac{y_D[j]}{f_s}\right\}$, where now our data points are shifted

---

[5]The scaling procedure explained here is classical, except that usually in the literature the parameters are (assumed to be) known. In such cases, one can make most terms equal to unity in step 4, rather than of $O(1)$.

[6]If the chosen excitation is generated by a computer as for e.g. a white noise signal, the discrete-time signal is then first transformed in a continuous-time signal using a DAC as in Fig. 2.1.
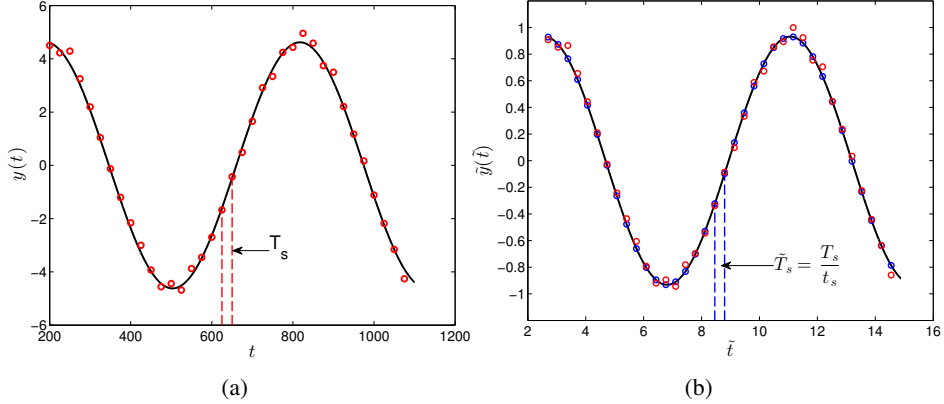
Figure 6.1: (a) Unscaled continuous-time output signal as a function of time (black) and the noise-corrupted measured discrete-time signal (red). (b) Scaled continuous-time output (black), scaled noise-corrupted measured discrete-time signal (red), and scaled simulated output data (blue).

in time to $\tilde{t} = jT_s/t_s$. The scaled continuous-time noise-free output $\tilde{y}_{nf}(\tilde{t})$ is depicted in Fig. 6.1b in black, whereas the scaled measured data points $y_D[j]/f_s$ are shown in red. Observe that due to the time scaling the temporal distance between the data points has become $\tilde{T}_s = T_s/t_s$. The scaled true physical parameter $\tilde{\theta}_0 = \Theta_s^{-1}\theta_0$ can now be estimated with the least-squares criterion (see Chapter 2)[7]:

$$\hat{\tilde{\theta}}_N = \arg\min_{\tilde{\theta}} \frac{1}{N} \sum_{j=1}^{N} \left( \frac{y_D[j]}{f_s} - \tilde{y}_{sim}[j;\tilde{\theta}] \right)^2, \tag{6.9}$$

where $\tilde{y}_{sim}[j;\tilde{\theta}]$ is the sampled version of the output $\tilde{y}_{nf}(\tilde{t})$ of the scaled system (6.5)-(6.6) for an arbitrary $\tilde{\theta}$ and $y_D[j]/f_s$ is the scaled measured output from the data-generating system. The unscaled estimate can then easily be retrieved by calculating $\hat{\theta}_N = \Theta_s \hat{\tilde{\theta}}_N$ (step 1 in Section 6.2.2). It is apparent from (6.9) that we require an expression for $\tilde{y}_{sim}[j;\tilde{\theta}]$ for estimation.

To simulate the noise-free scaled output $\tilde{y}_{nf}(\tilde{t})$ (c.f. (6.6)) for arbitrary values of the physical parameters $\tilde{\theta}$ we can use two methods.

**Method 1**

If the input signal is chosen to be a superposition of sinusoids, its scaled form being

$$\tilde{u}(\tilde{t}) = \sum_{m=1}^{M} \tilde{A}_m \sin(\omega_m t_s \tilde{t}) = \sum_{m=1}^{M} \tilde{A}_m \sin(\tilde{\omega}_m \tilde{t}),$$

---

[7]If the noise corrupting (6.8) is not white, the corresponding noise model $H(z)$ could be used in (6.9) in the same way as in (2.4)-(2.5).

where $\tilde{\omega}_m = \omega_m t_s$ and $\tilde{A}_m = A_m / u_s$, then the continuous-time simulated output reads (Ljung (1999))

$$\tilde{y}_{sim}(\tilde{\boldsymbol{\theta}}, \tilde{t}) = \sum_{m=1}^{M} \tilde{A}_m |\tilde{G}_{\tilde{x}_u, \tilde{x}_y}(i\tilde{\omega}_m, \tilde{\boldsymbol{\theta}})| \sin(\tilde{\omega}_m \tilde{t} + \alpha_m),$$

where $\alpha_m = \angle \tilde{G}_{\tilde{x}_u, \tilde{x}_y}(i\tilde{\omega}_m, \tilde{\boldsymbol{\theta}})$, the transfer function $\tilde{G}_{\tilde{x}_u, \tilde{x}_y}$ defined in (6.7), and $M$ a positive integer. Sampling this signal with the scaled sampling time $T_s / t_s$ generates $\tilde{y}_{sim}[j; \tilde{\boldsymbol{\theta}}]$ that is used in (6.9)[8].

## Method 2

Discretise equation (6.5)-(6.6) using a finite-difference method which is detailed in Section 6.3.2. This method discretises time and space at an interval of $\Delta \tilde{t}$ and $\Delta \tilde{x}$, respectively. The constant $\Delta \tilde{t}$ is called the time integration step. Let us choose $\Delta \tilde{t} = \tilde{T}_s = T_s / t_s$. Then we can apply an arbitrary input signal $u(t)$ to the data-generating system. The sampled scaled input $\tilde{u}_D$ from $\tilde{Z}_N$ can then be used to simulate the output $\tilde{y}_{sim}[j; \tilde{\boldsymbol{\theta}}]$ of which the samples are separated at an interval of $T_s / t_s$. The simulated points are shown in blue for $\tilde{\boldsymbol{\theta}} = \boldsymbol{\Theta}_s^{-1} \boldsymbol{\theta}_0$ and as can be observed, they occur at the same time instance as the scaled measured output data from $\tilde{Z}_N$.

Method 1 can only be used for sinusoidal input signals, and if a closed-form expression of $\tilde{G}_{\tilde{x}_u, \tilde{x}_y}$ exists. Method 2 is the most generic one as it can be used when the $\tilde{G}_{\tilde{x}_u, \tilde{x}_y}$ does not have a closed-form expression and/or the input signal is not a sum of sinusoids. Since Method 2 is more involved, we give more details concerning this method. First, we show in the next section how to generate $\tilde{y}_{sim}[j; \tilde{\boldsymbol{\theta}}]$ for Method 2.

### Simulation of the Data-generating System using a Finite-Difference Scheme

In this section we show how we generate the simulated output $\tilde{y}_{sim}[j; \tilde{\boldsymbol{\theta}}]$ that is used in (6.9) using Method 2 above. To this end, we discretise the scaled PDE equations (6.5)-(6.6), which will serve two purposes. On the one hand, it provides us a way to generate $\tilde{y}_{sim}$. On the other hand, the discretisation delivers a state-space model explicit in the physical parameters, which in turn can be converted into a discrete-time transfer function that is required for optimal experiment design.

Partial differential equations like (6.5)-(6.6) are sometimes refered to as *stiff equations*. Applying the wrong integration scheme can result in exponential growth of numerical errors. Most explicit methods, such as the forward Euler method, will only provide a stable solution under restrictive conditions on the spatial and temporal integration steps. To avoid such issues, we have adopted the implicit Crank-Nicolson algorithm, which is known to be unconditionally stable regardless of the temporal and spatial integration steps. A second benefit of this method is that the temporal truncation error is of $(\Delta t)^2$ instead of $\Delta t$ for the Euler methods.

We recall that we will simulate a scaled version of the data-generating system in Def. 6.1. The conversion between the continuous-time physical models (6.1)-(6.2) and (6.5)-(6.6) is defined through (6.4). Using these definitions, the scaled spatial domain becomes

---

[8]In Method 1, the discrete-time input $u_D[n]$ are not explicitly used in the identification criterion.

$\tilde{\mathcal{D}} = [0, \frac{L}{x_s}]$, which we discretise in $V$ parts of size $\Delta \tilde{x}^9$. This results in a spatial resolution of $\Delta \tilde{x} = \frac{L}{x_s V}$. The time integration step is chosen equal to $\Delta \tilde{t} = \frac{T_s}{t_s}{}^{10}$. The scaled time is then represented by $\tilde{t} = j\Delta \tilde{t}$, where $j \in \mathbb{N}^+$. We use index $i \in \mathbb{N}^+$ to denote the position on the lattice, i.e., $x_i = i\Delta \tilde{x}$. At location $i\Delta \tilde{x}$ and at time $j\Delta \tilde{t}$, the input and macroscopic field are $\tilde{u}_i^j = \tilde{u}(i\Delta \tilde{x}, j\Delta \tilde{t})$ and $\tilde{f}_i^j = \tilde{f}(i\Delta \tilde{x}, j\Delta \tilde{t})$, respectively. Using these definitions, the scaling steps in Section 6.2.2, discretisation of (6.5) and (6.6) results in

$$\frac{\tilde{f}_i^{j+1} - \tilde{f}_i^j}{\Delta \tilde{t}} = \frac{1}{2} \sum_{l=\{0,1\}} \left( \tilde{\theta}_1 \frac{\tilde{f}_{i+1}^{j+l} - 2\tilde{f}_i^{j+l} + \tilde{f}_{i-1}^{j+l}}{(\Delta \tilde{x})^2} + \tilde{\theta}_2 \frac{\tilde{f}_{i+1}^{j+l} - \tilde{f}_{i-1}^{j+l}}{\Delta \tilde{x}} + \tilde{\theta}_3 \theta_{s,3} t_s \tilde{f}_i^{j+l} \right), \quad (6.10)$$

$$\tilde{u}_{i_u}^j = -\tilde{\theta}_4 \frac{\tilde{f}_{i_u+1}^j - \tilde{f}_{i_u}^j}{\Delta \tilde{x}}, \tilde{y}_{nf}^j = \tilde{f}_{i_y}^j \text{ and } \tilde{f}_{L/x_s}^j = 0 \,\forall j, \quad (6.11)$$

where on the r.h.s. of the first equation we took the average of a forward- and backward-Euler method to ensure stability of the simulation for any $\Delta \tilde{t}$ and $\Delta \tilde{x}$ (it will also ensure stability of the transfer function $G$ that we will derive shortly). Lastly, $t_s$ is defined in step 4 in Section 6.2.2. This discretisation method is known as the Crank-Nicolson method. We remark that the actuator and sensor positions $\tilde{x}_u$ and $\tilde{x}_y$ in (6.6) determine the resolution $\Delta \tilde{x}$ to ensure that $i_u = \tilde{x}_u/\Delta \tilde{x}, i_y = \tilde{x}_y/\Delta \tilde{x}$ in (6.11) are integers.

We rewrite the first of the above equations as

$$\tilde{f}_i^{j+1} - \tilde{f}_i^j = \tilde{\lambda}_1 \left( \tilde{f}_{i+1}^{j+1} - 2\tilde{f}_i^{j+1} + \tilde{f}_{i-1}^{j+1} + \tilde{f}_{i+1}^j - 2\tilde{f}_i^j + \tilde{f}_{i-1}^j \right)$$
$$+ \tilde{\lambda}_2 \left( \tilde{f}_{i+1}^{j+1} - \tilde{f}_{i-1}^{j+1} + \tilde{f}_{i+1}^j - \tilde{f}_{i-1}^j \right) + \tilde{\lambda}_3 \left( \tilde{f}_i^{j+1} + \tilde{f}_i^j \right) \quad (6.12)$$

where the $\tilde{\lambda}$'s are defined as

$$\tilde{\lambda}_1(\tilde{\theta}) = \tilde{\theta}_1 \frac{\Delta \tilde{t}}{2(\Delta \tilde{x})^2}, \quad \tilde{\lambda}_2(\tilde{\theta}) = \tilde{\theta}_2 \frac{\Delta \tilde{t}}{2\Delta \tilde{x}}, \quad \tilde{\lambda}_3(\tilde{\theta}) = \tilde{\theta}_3 \theta_{s,3} t_s \frac{\Delta \tilde{t}}{2}, \quad (6.13)$$

and where we recall that $t_s$ is defined in step 4 in Section 6.2.2. With these expressions, we will now show how to approximate $\tilde{y}_{nf}(\tilde{t})$ at discrete-time instances $\tilde{t} = jT_s/t_s$ using the input we applied to the data-generating system $\tilde{u}_{i_u}^j$. To this end, let us denote the vector $\tilde{f}[j+1] = \left( \tilde{f}_0^{j+1}, \ldots, \tilde{f}_V^{j+1} \right)$, which contains the value of the macroscopic field at locations $i = 0, \ldots, V$ at time $j+1$. Similarly, we define $\tilde{f}[j] = \left( \tilde{f}_0^j, \ldots, \tilde{f}_V^j \right)$ for time $j$. Lastly, we let $\tilde{u}[j+1] = \tilde{u}_{i_u}^{j+1}$ and $\tilde{u}[j] = \tilde{u}_{i_u}^j$. Imposing the boundary conditions (6.11) and grouping all terms of $j+1$ in (6.12) on the l.h.s. and all terms at time $j$ at the r.h.s. results in the *descriptor state-space* form

$$\tilde{\mathcal{E}}(\tilde{\theta})\tilde{f}[j+1] = \tilde{\mathcal{A}}(\tilde{\theta})\tilde{f}[j] + \tilde{\mathcal{B}}(\tilde{\theta})(\tilde{u}[j+1] + \tilde{u}[j]), \quad (6.14)$$
$$\tilde{y}_{sim}[j;\tilde{\theta}] = \tilde{\mathcal{C}}\tilde{f}[j], \quad (6.15)$$

---

[9]The number $V$ is usually chosen through simulations of the discretized system. A trade-off can be made between computational time and accuracy of the numerical solution.

[10]The simulation accuracy is thus $O(\Delta \tilde{t})^2$. If $\Delta \tilde{t}$ turns out to be large, define the integer $\gamma$ such that the time integration step becomes $\Delta \tilde{t}/\gamma$. This generates $\gamma$ times more points in the considered simulation time interval. In the identification procedure, one then has to downsample the simulated output by a factor $\gamma$.

in which

$$
\tilde{\mathcal{E}}(\tilde{\boldsymbol{\theta}}) \;=\; \begin{pmatrix}
w_{0,0} & w_1 & 0 & \cdots & \cdots & 0 \\
w_{-1} & w_{0,1} & w_1 & 0 & \cdots & 0 \\
0 & \ddots & \ddots & \ddots & \ddots & \vdots \\
\vdots & 0 & \ddots & \ddots & \ddots & 0 \\
\vdots & \vdots & \ddots & w_{-1} & w_{0,V-1} & w_1 \\
0 & 0 & \cdots & 0 & w_{-1} & w_V
\end{pmatrix}, \tag{6.16}
$$

$$
\tilde{\mathcal{A}}(\tilde{\boldsymbol{\theta}}) \;=\; \begin{pmatrix}
w_{2,0} & -w_1 & 0 & \cdots & \cdots & 0 \\
-w_{-1} & w_{2,1} & -w_1 & 0 & \cdots & 0 \\
0 & \ddots & \ddots & \ddots & \ddots & \vdots \\
\vdots & 0 & \ddots & \ddots & \ddots & 0 \\
\vdots & \vdots & \ddots & -w_{-1} & w_{2,V-1} & -w_1 \\
0 & 0 & \cdots & 0 & -w_{-1} & w_{2,V}
\end{pmatrix}, \tag{6.17}
$$

$$
\tilde{\mathcal{B}}(\tilde{\boldsymbol{\theta}}) = \frac{2\Delta\tilde{x}}{\tilde{\theta}_4}(\tilde{\lambda}_2 - \tilde{\lambda}_1)\left( w_{3,0}, w_{3,1}, \cdots, w_{3,V} \right)^T, \text{ and } \tilde{\mathcal{C}} = (\delta_{i,i_y}, \delta_{i,i_y}, \ldots, \delta_{i,i_y}). \tag{6.18}
$$

Matrices $\tilde{\mathcal{E}}$ and $\tilde{\mathcal{A}}$ are two $(V+1) \times (V+1)$ matrices, $\tilde{\mathcal{B}}$ a $(V+1)$ column vector, and $\tilde{\mathcal{C}}$ a $(V+1)$ row vector. Furthermore,

$$
\begin{aligned}
w_{0,i} &= 1 + (2 - \delta_{i,i_u})\tilde{\lambda}_1(\tilde{\boldsymbol{\theta}}) - \tilde{\lambda}_3(\tilde{\boldsymbol{\theta}}), w_1 = -\tilde{\lambda}_1(\tilde{\boldsymbol{\theta}}) - \tilde{\lambda}_2(\tilde{\boldsymbol{\theta}}), \ w_{-1} = -\tilde{\lambda}_1(\tilde{\boldsymbol{\theta}}) + \tilde{\lambda}_2(\tilde{\boldsymbol{\theta}}), \\
w_{2,i} &= 1 - (2 - \delta_{i,i_u})\tilde{\lambda}_1(\tilde{\boldsymbol{\theta}}) + \tilde{\lambda}_3(\tilde{\boldsymbol{\theta}}), w_{3,i} = \delta_{i,i_u}.
\end{aligned} \tag{6.19}
$$

In the expressions of $w_{0,i}$, $w_{2,i}$, and $w_{3,i}$ the symbol $\delta_{i,i_u}$ is the Kronecker delta function, defined by $\delta_{kl} = 1$ if $k = l$ and $\delta_{kl} = 0$ for $k \neq l$. It means that the values of $w_{0,i}$, $w_{2,i}$, and $w_{3,i}$ differ at the row index $i = i_u$, which is a consequence of the boundary conditions. We remark that the matrices $\tilde{\mathcal{E}}$ and $\tilde{\mathcal{A}}$ are tri-diagonal since we are dealing with a second-order PDE (c.f. (6.1)). Consequently, we can compute the vector $\tilde{f}[j]$ with $O(V)$ complexity with Thomas' algorithm (Thomas (1949)) (a simplified version of Gaussian elimination that can solve tri-diagonal systems of equations).

We now return to the problem of identification in Section 6.3. To simulate the scaled continuous-time output $\tilde{y}_{nf}(t)$ defined in equation (6.6), we first compute the vector $\tilde{f}[j]$ using (6.14)-(6.19) and the scaled input data points from $\tilde{Z}_N$ defined in Section 6.3, i.e. we compute the macroscopic field $f(x,t)$ at the discrete spatial locations $i\Delta\tilde{x}$ for $i = 0, \ldots, V$, and times $j\Delta\tilde{t} = jT_s/t_s$ for $j = 1, \ldots, N$. Equation (6.15) then takes the element of this vector corresponding to location $\tilde{x}_y$. Indeed, $\tilde{y}_{sim}[j]$ is then equivalent to $\tilde{y}_{sim}[j] = \tilde{f}(\tilde{x} = \tilde{x}_y, \tilde{t} = jT_s/t_s)$. We can now identify the physical parameters using equation (6.9), the scaled outputs from $\tilde{Z}_N$, and our simulated output $\tilde{y}_{sim}[j]$. This way of simulating generates the entire macroscopic field $\tilde{f}(x,t)$ at discrete positions $i\Delta\tilde{x}$. The computational time scales linearly with $\Delta\tilde{t}$ due to the tri-diagonal algorithm, which allows for very high temporal resolution in the least-squares identification method.

Lastly, we show how the descriptor state-space form can be converted into a discrete-time transfer function. First, we rewrite (6.14)-(6.15) in its *state-space* form

$$
\begin{aligned}
\tilde{\boldsymbol{f}}[j+1] &= \tilde{A}(\tilde{\boldsymbol{\theta}})\tilde{\boldsymbol{f}}[j] + \tilde{B}(\tilde{\boldsymbol{\theta}})\tilde{u}_D[j] \\
\tilde{y}_{sim}[j;\tilde{\boldsymbol{\theta}}] &= \tilde{C}\tilde{\boldsymbol{f}}[j],
\end{aligned}
\tag{6.20}
$$

where $\tilde{A}(\tilde{\boldsymbol{\theta}}) = \tilde{\boldsymbol{\mathcal{E}}}^{-1}\tilde{\boldsymbol{\mathcal{A}}}$, $\tilde{B}(\tilde{\boldsymbol{\theta}}) = \tilde{\boldsymbol{\mathcal{E}}}^{-1}\tilde{\boldsymbol{\mathcal{B}}}(1+\tilde{z})$, and $\tilde{C} = \tilde{\boldsymbol{\mathcal{C}}}$. Here, $\tilde{z} = e^{i\tilde{\omega}\tilde{T}_s}$. From this state-space form we can trivially compute the discrete-time transfer function (the discrete-time equivalent of (6.7)), being

$$
\tilde{G}_{i_u,i_y}(\tilde{z},\tilde{\boldsymbol{\theta}}) = \tilde{C}\left[\tilde{z}\boldsymbol{I} - \tilde{A}(\tilde{\boldsymbol{\theta}})\right]^{-1}\tilde{B}(\tilde{\boldsymbol{\theta}}).
\tag{6.21}
$$

In this equation, $\boldsymbol{I}$ is the $(V+1) \times (V+1)$ identity matrix, $\tilde{z} = e^{i\tilde{\omega}\tilde{T}_s}$, and $\tilde{\omega} = \omega t_s$ the scaled frequency. Note that this transfer function is not causal. However, since we only need its frequency response later, and $u(t)$ is fully known, this is not an issue. The discrete-time scaled input and output signals are then related by

$$
\tilde{y}_{sim}[j;\tilde{\boldsymbol{\theta}}] = \tilde{G}_{i_u,i_y}(\tilde{z},\tilde{\boldsymbol{\theta}})\tilde{u}_D[j].
$$

We recapitulate what we have done so far. We have defined the data-generating system to which we apply an analog input signal, usually a superposition of sinusoids, and measure the noise-corrupted output at an interval of $T_s$ seconds. We have shown how to identify the physical parameters by scaling the dataset $Z_N$ and simulating the scaled continuous-time model of the data-generating system as defined in Definition 6.1. What we have not yet defined is how to design the input signal that minimises the cost of the experiment while guaranteeing user-imposed constraints on the variances of the physical parameters. This question will be addressed in the next section.

## 6.4 Least-Costly Optimal Experiment Design

### 6.4.1 Introduction

We recall that we wish to estimate the $\kappa$-dimensional true parameter vector $\boldsymbol{\theta}_0$ of the data-generating system (see def. 6.1) in such a way that the cost of the experiment is minimal, while at the same time guaranteeing with high probability that the variances of the elements of our scaled estimate $\hat{\tilde{\boldsymbol{\theta}}}_N$ remain below certain user-defined constraints. The cost and the constraints need to be a function of the to-be-designed input signal in order to find the optimal one. We first assume that the sensor and actuator locations $i_y$ and $i_u$ are fixed. In all that follows we consider the scaled system, but conversion to the unscaled system is done with (6.4). We restrict our attention to a multi-sine input signal.

### 6.4.2 Fixed Sensor and Actuator Locations

We start by defining the constraints. The joint confidence region containing an estimate $\hat{\tilde{\boldsymbol{\theta}}}_N$ with a user-defined probability $\alpha$ is described by the ellipsoid (c.f. (2.6))

$$
E = \left\{ \tilde{\boldsymbol{\theta}} \mid (\tilde{\boldsymbol{\theta}} - \tilde{\boldsymbol{\theta}}_0)^T P_{N,\tilde{\boldsymbol{\theta}}}^{-1}[\tilde{\Phi}_{\tilde{u}}](\tilde{\boldsymbol{\theta}} - \tilde{\boldsymbol{\theta}}_0) \le \chi_\alpha^2(\kappa) \right\},
$$

in which $\chi_\alpha^2(\kappa)$ is the quantile of the Chi-squared distribution function for a probability $\alpha$, and $\kappa = \dim(\tilde{\boldsymbol{\theta}})$. Furthermore, the inverse covariance matrix $P_{N,\tilde{\boldsymbol{\theta}}}^{-1}$ when using the scaled input signal $\tilde{u}_D[n]$ with spectrum $\tilde{\Phi}_{\tilde{u}}$ in the frequency-domain reads (see Chapter 2)

$$\tilde{\boldsymbol{P}}_{N,\tilde{\boldsymbol{\theta}}}^{-1} = \frac{N\tilde{T}_s}{2\pi\tilde{\sigma}_e^2} \int_{-\pi/\tilde{T}_s}^{\pi/\tilde{T}_s} \left[ \nabla_{\tilde{\boldsymbol{\theta}}} \tilde{G}_{i_u,i_y}(e^{-i\tilde{\omega}\tilde{T}_s}, \tilde{\boldsymbol{\theta}}) \right]_{\tilde{\boldsymbol{\theta}}=\tilde{\boldsymbol{\theta}}_0} \left[ \nabla_{\tilde{\boldsymbol{\theta}}} \tilde{G}_{i_u,i_y}(e^{-i\tilde{\omega}\tilde{T}_s}, \tilde{\boldsymbol{\theta}}) \right]_{\tilde{\boldsymbol{\theta}}=\tilde{\boldsymbol{\theta}}_0}^{H} \tilde{\Phi}_{\tilde{u}}(\tilde{\omega}) \, d\tilde{\omega},$$
(6.22)

where $\tilde{\sigma}_e^2 = \sigma_e^2/f_s^2$ is the scaled noise variance, $\tilde{G}_{i_u,i_y}(e^{-i\tilde{\omega}\tilde{T}_s}, \tilde{\boldsymbol{\theta}})$ the discrete-time transfer function defined in (6.21), $\tilde{T}_s$ the scaled sampling time, and $\tilde{\Phi}_{\tilde{u}}(\tilde{\omega})$ the spectrum of input signal.

We now wish to put bounds on the variances of the estimates. To this end, we consider the LMI in Section 3.2.3 and adapt it to the scaled estimate. The resulting variance constraints are then easily retrieved and read

$$\forall j = 1,\ldots,J \leq \kappa: \ \tilde{\sigma}_j^2 = e_j^T \tilde{\boldsymbol{P}}_{N,\tilde{\boldsymbol{\theta}}} e_j \leq \frac{(\Delta\tilde{\theta}_j)^2}{\chi_\alpha^2(\kappa)}.$$
(6.23)

The second component to formulate the least-costly experiment design problem is to define the cost of the experiment. We define the scaled cost of the experiment, denoted $\tilde{\mathcal{J}}_{cost}$, as the power of the as-of-yet undetermined scaled input signal:

$$\tilde{\mathcal{J}}_{cost}[\tilde{\Phi}_{\tilde{u}}] = \frac{\tilde{T}_s}{2\pi} \int_{-\pi/\tilde{T}_s}^{\pi/\tilde{T}_s} \tilde{\Phi}_{\tilde{u}}(\tilde{\omega}) \, d\tilde{\omega}.$$
(6.24)

Note that this expression is the scaled equivalent of (3.1) for $\mathcal{L}(e^{-i\omega}, \boldsymbol{\theta}_0) = 1 \, \forall \omega$. The least-costly experiment design problem is thus formulated as

$$\min_{\tilde{\Phi}_{\tilde{u}}} \tilde{\mathcal{J}}_{cost}[\tilde{\Phi}_{\tilde{u}}]$$
(6.25)

subject to the constraints (6.23) that are equivalent to (c.f. (3.14))

$$\forall j = 1,\ldots,J: \ \tilde{\boldsymbol{P}}_{N,\tilde{\boldsymbol{\theta}}}^{-1}[\tilde{\Phi}_{\tilde{u}}] \succeq e_j e_j^T \frac{\chi_\alpha^2(\kappa)}{(\Delta\tilde{\theta}_j)^2}$$
(6.26)

Observe that we have rewritten constraints (6.23) into (6.26) by invoking Schur's complement in order to ensure that all constraints are linear in the spectrum $\tilde{\Phi}_{\tilde{u}}$, i.e., we have Linear Matrix Inequalities (LMI). Consequently, since the cost is also linear in the spectrum, the optimisation problem (6.25)-(6.26) is linear in the design variable $\tilde{\Phi}_{\tilde{u}}$. The optimisation problem is thus convex. Its solution, denoted $\tilde{\Phi}_{\tilde{u},opt}$, is the spectrum that minimises the cost while honouring the constraints. In order to solve this problem numerically we have to parameterise the input spectrum $\tilde{\Phi}_{\tilde{u}}(\tilde{\omega})$. To this end, we can use the parameterisation (3.6) where the excitation signal is constrained to be a multi-sine. For this purpose, we discretise the frequency domain into $M \in \mathbb{N}^+$ parts. Defining $\tilde{\omega}_f = \frac{\pi}{M\tilde{T}_s}$ as the fundamental frequency, we have that $\tilde{\omega}_m = m\tilde{\omega}_f$, for $m = 1,\ldots,M_{ex}$, where $M_{ex} \leq M$ is the number of

sinusoids used in experiment design[11]. Furthermore, the spectrum is given by

$$\tilde{\Phi}_{\tilde{u}}(\tilde{\omega}) = \frac{\pi}{2\tilde{T}_s} \sum_{m=1}^{M_{ex}} \tilde{A}_m^2 \left[ \delta(\tilde{\omega} - \tilde{\omega}_m) + \delta(\tilde{\omega} + \tilde{\omega}_m) \right], \tag{6.27}$$

which corresponds to a $M\tilde{T}_s/2$-periodic discrete-time multi-sine

$$\tilde{u}[j] = \tilde{u}(j\tilde{T}_s) = \sum_{m=1}^{M_{ex}} \tilde{A}_m \sin(\tilde{\omega}_m j\tilde{T}_s). \tag{6.28}$$

Substitution of (6.27) into the cost (6.25) and the expression of the covariance matrix (6.22) gives

$$\tilde{\mathcal{J}}_{cost}[\tilde{\Phi}_{\tilde{u}}] = \frac{1}{2} \sum_{m=1}^{M_{ex}} \tilde{A}_m^2 \tag{6.29}$$

and

$$\tilde{P}_{N,\tilde{\theta}}^{-1} = \frac{N}{2\tilde{\sigma}_e^2} \sum_{m=1}^{M_{ex}} \tilde{A}_m^2 \mathrm{Re} \left\{ \left[ \nabla_{\tilde{\theta}} \tilde{G}_{i_u,i_y}(e^{-i\tilde{\omega}_m \tilde{T}_s}, \tilde{\theta}) \right]_{\tilde{\theta}=\tilde{\theta}_0} \left[ \nabla_{\tilde{\theta}} \tilde{G}_{i_u,i_y}(e^{-i\tilde{\omega}_m \tilde{T}_s}, \tilde{\theta}) \right]_{\tilde{\theta}=\tilde{\theta}_0}^H \right\}. \tag{6.30}$$

The above two equations show that the cost and covariance matrix are now linear in the amplitudes $\tilde{A}_m^2$. Substitution into the optimisation problem (6.25)-(6.26) then yields a convex finite-dimensional problem in $\tilde{A}_m^2$, see also Chapter 3. The integer $M$ determines the accuracy of the solution. In Appendix 6.B we show how to compute the gradient $\nabla_{\tilde{\theta}} \tilde{G}_{i_u,i_y}$ efficiently. The solution to the optimisation problem generates the set $\left\{ \tilde{A}_{m,opt} \right\}_{m=1}^{M_{ex}}$. Substitution of these amplitudes in (6.28) then delivers the scaled optimal input signal $\tilde{u}_{opt}[j]$. The unscaled optimal input signal is easily retrieved via (6.4), i.e. $A_{m,opt} = \tilde{A}_{m,opt} u_s$ and $\omega_m = \tilde{\omega}_m/t_s$. The resulting unscaled signal is the analog of (6.28).

**Remark 6.1** *The above procedure pertains to Method 2 of Section 6.3.2. If Method 1 is used for the identification, a very similar procedure can be followed. However, the gradient of the continuous-time transfer function $\tilde{G}(i\tilde{\omega}, \tilde{\theta}_0)$ can be used in (6.30) instead of the gradient of the discrete-time transfer function. This is allowed due to the data generation procedure presented in Section 6.3.*

**Remark 6.2** *Notice that the true parameter vector $\tilde{\theta}_0$ appears in both the constraints (6.23) and the inverse covariance matrix (6.30). This so-called chicken-and-egg problem, discussed in Section 3.2.2, is in practice circumvented by replacing $\tilde{\theta}_0$ in these equations by an initial guess, $\tilde{\theta}_g$. Admittedly, this will result in different experiment costs and different parameter variances. Nevertheless, under equal input power, the framework can deliver signals that result in variances of the parameters that are lower than obtained with an arbitrary input signal. An illustration will follow in Section 6.5.*

**Remark 6.3** *We have mentioned in the introduction that scaling is of importance in the least-costly experiment design framework for physical systems. We comment further on this now. Suppose we want to identify two physical parameters, denoted $\theta_1$ and $\theta_2$. Their*

---

[11]Since the Nyquist frequency is chosen a decade above the system's bandwidth it is generally not necessary to cover the whole frequency range $[0, \pi/\tilde{T}_s]$

*values can easily differ by ten orders of magnitude, resulting in variances (that are on the diagonal of $\boldsymbol{P}_{N,\theta}$) that differ by twenty orders of magnitude. Consequently, the matrix $\boldsymbol{P}_{N,\theta}^{-1}$ is ill-posed, and the convex methods can no longer solve such problems. However, with scaling, the parameters are of the same order, resolving the badly-scaled matrix.*

**Remark 6.4** *We mention that in the numerical procedure we require an expression for $\nabla_{\tilde{\boldsymbol{\theta}}}\tilde{G}_{i_u,i_y}(\tilde{z},\tilde{\boldsymbol{\theta}})$. The transfer function $\tilde{G}_{i_u,i_y}(\tilde{z},\tilde{\boldsymbol{\theta}}_0)$ being of high order for fine spatial grids, this can lead to a heavy computational load. Note that nevertheless, as previously mentioned, this load can be eased by the method described in Appendix 6.B. Moreover, it is also to be noted that this gradient computation can be achieved before solving the LMI problem. Finally, this load becomes negligible if an explicit continuous-time expression for $\tilde{G}_{i_u,i_y}(i\tilde{\omega},\tilde{\boldsymbol{\theta}}_0)$ exists, i.e., if we use Method 1. Indeed, as already mentioned above, the discrete-time transfer function in (6.22) can then be replaced by its much simpler continuous-time equivalent. We give an example in Section 6.5.*

### 6.4.3 Actuator and Sensor Locations as Design Variables

In the previous section we formulated the LCED framework but assumed that the actuator and sensor locations $i_u$ and $i_y$ were given. Since the derivatives of $\tilde{G}_{i_u,i_y}$ (6.21) depend explicitly on the actuator and sensor locations, we can also attempt to decrease the cost even further by optimally choosing these locations. Due to the explicit dependence of the derivatives on the locations the optimal frequencies change with the locations. Consequently, we have to solve the LCED optimisation problem formulated in the previous section for many combinations of $i_u$ and $i_y$. To this end, consider Algorithm 1. The solution of this algorithm is given by the set of values $\{\tilde{\boldsymbol{x}}_{opt}, \tilde{\boldsymbol{A}}_{opt}, \tilde{\mathcal{J}}_{opt}\}$ containing the optimal actuator and sensor location, as well as the optimal amplitudes and the optimal cost. Conversion to the unscaled signal is described in the previous section.

The algorithm makes use of progressive subdivision. The algorithm starts by dividing the $(x_u,x_y)$-plane into four equally-sized squares. For each square, the optimisation problem is solved at the coordinates that correspond to the centre of the square. From these four solutions the one that delivers the smallest cost $\mathcal{J}_{cost}$ is selected. At step $k+1$ that square is subsequently divided into four equally-sized squares for which we again find the least-costly solution. This procedure is repeated until $N_{sim}$ divisions have taken place. This subdivision algorithm is important if the number of variables such as $\tilde{x}_u$ and $\tilde{x}_y$ increases. The algorithm is easily adapted if only one spatial degree is considered (only input or output location).

The algorithm speed can be improved drastically in cases where $\dim(\boldsymbol{\theta}) \leq 2$, for which we derived analytical solutions in Chapter 4. A properly chosen frequency grid can improve the speed further.

## 6.5 Case Study: Estimation of diffusivity and conductivity parameters in front-face experiments

### 6.5.1 Introduction

In this section we apply the optimal experiment design framework to the identification of thermal parameters. The experimental set-up is inspired by work of Gabano and Poinot

Set $N_{sim}$ as total number of iterations ;
Set $\alpha$ and $\Delta\theta_i$'s to set constraints;
Set $Q$ determining the lowest frequency $\omega_f = \frac{\pi}{MT_s}$ ;
Set array $\tilde{\mathbf{A}}_{opt} = \{\tilde{A}_m\}_{m=1}^{M_{ex}}$;
Set array $\tilde{\mathbf{x}}_{opt} = [\tilde{x}_u, \tilde{x}_y]$;
Set cost $\tilde{\mathcal{J}}_{opt} = 1 \times 10^8$ (a high value);
$\tilde{x}_{u,sub} = \frac{1}{2}, \tilde{x}_{y,sub} = \frac{1}{2}$;
$k = 0$;
**while** $k < N_{sim}$ **do**
$\quad$ $\Delta x_{u,k} = \tilde{x}_{u,sub}, \Delta x_{y,k} = \tilde{x}_{y,sub}$ ;
$\quad$ **for** $i = 1$ *to* $2$ **do**
$\quad\quad$ $x_u = (i-1)\Delta x_{u,k} + \frac{1}{2}\Delta x_{u,k}$ ;
$\quad\quad$ **for** $j = 1$ *to* $2$ **do**
$\quad\quad\quad$ $x_y = (j-1)\Delta x_{y,k} + \frac{1}{2}\Delta x_{y,k}$ ;
$\quad\quad\quad$ Solve (6.25)-(6.26) using (6.27) and use solution $\tilde{A} = \{\tilde{A_m}\}_{m=1}^{M_{ex}}$ to compute cost $\tilde{\mathcal{J}}_{cost}[\tilde{A}]$ (6.24);
$\quad\quad\quad$ **if** $\tilde{\mathcal{J}}_{cost}[\tilde{A}] < \tilde{\mathcal{J}}_{opt}$ **then**
$\quad\quad\quad\quad$ $\tilde{x}_{u,sub} = x_u, \ \tilde{x}_{y,sub} = x_y$;
$\quad\quad\quad\quad$ $\tilde{\mathbf{A}}_{opt} = \tilde{\mathbf{A}}$;
$\quad\quad\quad\quad$ $\tilde{\mathcal{J}}_{opt} = \tilde{\mathcal{J}}_{cost}$;
$\quad\quad\quad$ **end**
$\quad\quad$ **end**
$\quad$ **end**
$\quad$ $\boldsymbol{x}_{opt} = [x_{u,sub}, x_{y,sub}]$;
$\quad$ $k = k+1$;
**end**

**Algorithm 1:** Progressive subdivision algorithm that finds the minimal experiment cost by designing the optimal input spectrum and optimal sensor and actuator locations.
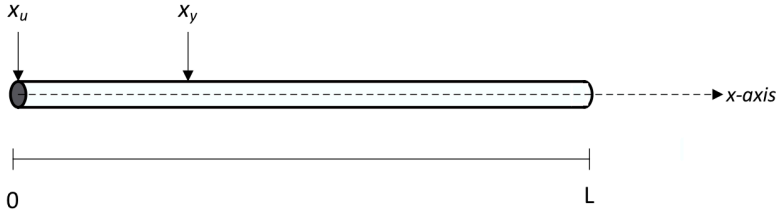
Figure 6.2: Sketch of the experimental set-up. A rod with length $L$ is heated at the user-chosen actuator position $x_u$. The temperature is measured at the user-chosen sensor location $x_y$.

(2009) and simulated with the computer. We first introduce the data-generating system and its scaled equivalent in Section 6.5.2. We then set up the experiment and define the constraints on the variances of the estimates and compute the optimal input signal in Section 6.5.3. We solve the optimisation problem using CVX (Boyd and Grant (2013)). We also show what the optimal actuator and sensor locations are. In Section 6.5.4 the optimal input signal is applied to the data-generating system (in a simulation environment) and with the collected data we identify the physical parameters. In order to test if the variance constraints are honoured we simulate $2 \times 10^4$ experiments. We also analyze what happens to the optimal input signal when we replace $\tilde{\theta}_0$ by an initial guess $\tilde{\theta}_g$ in (6.30).

### 6.5.2 Data-generating System

We consider a homogeneous rod of length $L = 0.05$ m oriented along the spatial coordinate $x$, see Fig. 6.2. We place the left side of the rod at $x = 0$, such that the spatial domain we consider is $\mathcal{D} = [0, L]$. During the experiment, we heat the cross-sectional area of the rod uniformly at the user-chosen location $x = x_u$ with a heat flux $u(t)$ and keep the temperature constant at the right boundary ($x = L$), here equal to zero[12]. We measure the temperature $T(x,t)$ at the user-chosen position $x = x_y \in \mathcal{D}$. If $x_u = x_y = 0$ the experiment is called a front-face experiment (Gabano and Poinot (2009)). The optimal actuator and sensor positions ($x_u$ and $x_y$) are determined with Optimal Experiment Design, and are thus design variables. We assume zero initial conditions.

The dynamics are governed by the equations

$$\frac{\partial T(x,t)}{\partial t} = \alpha_0 \frac{\partial^2 T(x,t)}{\partial x^2}, \tag{6.31}$$

$$-\lambda_0 \left.\frac{\partial T(x,t)}{\partial x}\right|_{x=x_u} = u(t), \, y_{nf}(t) = T(x_y,t), \text{ and } T(L,t) = 0 \, \forall t, \tag{6.32}$$

in which $\lambda_0 = 111$ W m$^{-1}$ °C$^{-1}$ is the thermal conductivity and $\alpha_0 = 3.38 \times 10^{-5}$ m$^2$ s$^{-1}$ the thermal diffusivity. We collect the physical parameters in the vector $\theta_0 = (\alpha_0, \lambda_0)^T$. This data-generating system corresponds to the continuous-time second-order PDE (6.1)-(6.2) for the macroscopic field $f(x,t) = T(x,t)$, input location $x = x_u$, $\theta_{1,0} = \alpha_0$, and $\theta_{4,0} = \lambda_0$. Our goal is to identify the physical parameters $\theta_0 = (\alpha_0, \lambda_0)^T = (3.38 \times 10^{-5}, 111)^T$.

---

[12]If $x_u = 0$ we can easily heat the cross-sectional area. If $x_u \neq 0$ the rod can be heated locally with a thin thermal band wrapped around the rod

**Non-dimensionalisation**

Following Section 6.2.2, we introduce the non-dimensional variables $\tilde{T}(\tilde{x},\tilde{t}) = \frac{T(x,t)}{y_s}$, $\tilde{x} = \frac{x}{x_s}$, $\tilde{u}(\tilde{t}) = \frac{u(t)}{u_s}$, $\tilde{t} = \frac{t}{t_s}$, and non-dimensional parameters $\tilde{\alpha}_0 = \frac{\alpha_0}{\alpha_s}$, $\tilde{\lambda}_0 = \frac{\lambda_0}{\lambda_s}$. Choosing $y_s = 1$, $x_s = L = 0.05$, $t_s = \frac{L^2}{\alpha_0} = 73.96$, $u_s = \frac{L}{\lambda_0 y_s} = 4.5 \times 10^{-4}$, $\alpha_s = \alpha_0$, $\lambda_s = \lambda_0$ and substituting the non-dimensional variables in (6.31)-(6.32) results in the non-dimensional model

$$\frac{\partial \tilde{T}(\tilde{x},\tilde{t})}{\partial \tilde{t}} = \tilde{\alpha}_0 \frac{\partial^2 \tilde{T}(\tilde{x},\tilde{t})}{\partial \tilde{x}^2}, \tag{6.33}$$

$$-\tilde{\lambda}_0 \left.\frac{\tilde{T}(\tilde{x},\tilde{t})}{\partial \tilde{x}}\right|_{\tilde{x}=\tilde{x}_u} = \tilde{u}(\tilde{t}), \; \tilde{y}_{nf}(\tilde{t}) = \tilde{T}(\tilde{x}_y,\tilde{t}), \; \text{and} \; \tilde{T}(1,\tilde{t}) = 0 \forall \tilde{t} \tag{6.34}$$

Note that we have used an initial guess $\boldsymbol{\theta}_g = \boldsymbol{\theta}_0$ for convenience. This results in an unscaled true parameter vector, $\tilde{\boldsymbol{\theta}}_0$, that is of $O(1)$.

The non-dimensional continuous-time transfer function $\tilde{G}_{\tilde{x}_u,\tilde{x}_y}(\tilde{s},\tilde{\boldsymbol{\theta}}_0)$ that couples $\tilde{u}(\tilde{t})$ to the output $\tilde{y}_{nf}(\tilde{t})$ (c.f. (6.7)) is derived in Appendix 6.A and reads

$$\tilde{G}_{\tilde{x}_u,\tilde{x}_y}(\tilde{s},\tilde{\boldsymbol{\theta}}_0) = \frac{1}{\tilde{\lambda}_0} \sqrt{\frac{\tilde{\alpha}_0}{\tilde{s}}} \frac{\sinh\left(\sqrt{\frac{\tilde{s}}{\tilde{\alpha}_0}}(1-\tilde{x}_y)\right)}{\cosh\left(\sqrt{\frac{\tilde{s}}{\tilde{\alpha}_0}}(1-\tilde{x}_u)\right)} \tag{6.35}$$

In this equation, the Laplace variable has also been scaled according to (6.4), i.e. $\tilde{s} = t_s s = sL^2/\alpha_0$. Since we consider a multi-sine excitation signal, we will use this transfer function in the experiment design procedure for Method 1 in Section 6.3.

## 6.5.3 Experiment Preliminaries

In this section we define the experiment. We choose the same parameters as in (Gabano and Poinot (2009)), mainly to compare the excitation frequencies. We remark that we did not have an actual physical set-up to generate data. Instead, the noise-corrupted output data is generated with the computer. We set the experiment length at $2000 + 9000$ samples, where the first 2000 samples are not used in the identification, i.e. we wait until transients died out. The sampling time is set at $T_s = 0.1$ seconds. The optimal input signal (which we will compute shortly) generates the measured output of the data-generating system, given by

$$y_D[n] = y_{nf}(nT_s) + e[n], \tag{6.36}$$

where we assumed that the output of the data-generating system $y_{nf}(nT_s)$ is corrupted by zero-mean Gaussian white noise $e[n]$ with variance $\sigma_e^2 = 0.05$ (see also (6.8)).

**Optimal Experiment Design**

Gabano and Poinot (2009) collected the thousand estimates $\{\hat{\alpha}_N\}$ and $\left\{\hat{\lambda}_N\right\}$, which were distributed around their respective true values $\alpha_0 = 3.38 \times 10^{-5}$ and $\lambda_0 = 111$ (identical to the parameters used in this section) with $\sigma_\alpha = 0.02\alpha_0/3$ and $\sigma_\lambda = 0.01\lambda_0/3$. Following

Section 6.4, we cast these values in the scaled variance constraints (6.23):

$$\tilde{\sigma}_{\tilde{\alpha}}^2 \equiv \tilde{\sigma}_1^2 \leq \left(\frac{0.02}{3}\right)^2, \tilde{\sigma}_{\tilde{\lambda}}^2 \equiv \tilde{\sigma}_2^2 \leq \left(\frac{0.01}{3}\right)^2, \tag{6.37}$$

where it is understood that the probability $\alpha \approx 0.99$, and that $\chi^2_{0.99}(2) \approx 9$. The optimal experiment design problem is formulated by (6.25)-(6.26). Choosing (6.27) to represent the scaled spectrum the above constraints, the scaled optimisation problem for this experiment reads[13]

$$\min_{\{\tilde{A}_m\}} \frac{1}{2} \sum_{m=1}^{M_{ex}} \tilde{A}_m^2 \tag{6.38}$$

subject to the constraints

$$\tilde{P}_{N,\tilde{\theta}}^{-1} \succeq e_1 e_1^T \tilde{\sigma}_{\tilde{\alpha}}^{-2}, \ \tilde{P}_{N,\tilde{\theta}}^{-1} \succeq e_2 e_2^T \tilde{\sigma}_{\tilde{\lambda}}^{-2}. \tag{6.39}$$

The expression of $\tilde{P}_{N,\tilde{\theta}}^{-1}$ is given by (6.30), in which we substituted $\tilde{G}_{i_u,i_y}(\tilde{z}, \tilde{\theta})$ with the continuous-time transfer function $\tilde{G}_{\tilde{x}_u,\tilde{x}_y}(\tilde{s}, \tilde{\theta})$ in equation (6.35), and used as initial guess $\theta_g = \theta_0$, i.e., $\tilde{\theta}_0 = (1.0, 1.0)^T$.

We use Algorithm 1 to find the optimal locations and the optimal input signal for those locations. To this end, we thus solve (6.25)-(6.26) with the LMI approach. We take $M = M_{ex} = 100$. For each combination $(\tilde{x}_u, \tilde{x}_y)$ it turns out that the optimal input signal is a single sinusoid. Interestingly, we find that the lowest cost, i.e. $\tilde{\mathcal{J}}_{cost} = \frac{1}{2}\tilde{A}_{opt}^2$ is obtained at $(\tilde{x}_u, \tilde{x}_y) = (0, 0.12)$. In unscaled length, this corresponds to $x_y = 0.12L$. The optimal amplitude $\tilde{A}_{opt}$ at $\tilde{x}_u = 0$ as a function of $\tilde{x}_y$) is depicted in Fig. 6.3b. In practice, front-face experiments ($x_u = x_y = 0$) are common. However, this study suggests that this is not best practice, as a lower cost (proportional to $\tilde{A}^2$) of about 6% can be obtained at $\tilde{x}_y = 0.12$. Equivalently, for the same cost, the variances in the parameters will be about 6% lower since $\tilde{P}_{N,\tilde{\theta}}^{-1}$ is proportional to $\tilde{A}^2$. Furthermore, observe that the curve increases rapidly as $\tilde{x}_y$ increases. Although not shown in the figure, when $\tilde{x}_y \to 1$, the optimal amplitude $\tilde{A}_{opt} \to \infty$. This is a consequence of the boundary condition $\tilde{T}(1, \tilde{t}) = 0 \forall \tilde{t}$ (c.f. (6.34)). Hence, the informativeness of the data at any frequency is zero at this location.

Although the best estimate can be obtained at $(\tilde{x}_u, \tilde{x}_y) = (0, 0.12)$, we shall however use the optimal input signal for $\tilde{x}_u = 0$ and sensor location $\tilde{x}_y = 0$ to compare with previous works. In this case, the optimal input signal is computed to be

$$\tilde{u}_{opt}(\tilde{t}) = 1.7067 \sin(1.571\tilde{t}), \tag{6.40}$$

which in unscaled variables translates (using the conversion defined in Section 6.5.2) into the optimal input signal[14]

$$u(t) = 3.789 \times 10^3 \sin(0.0212t). \tag{6.41}$$

---

[13]The parameter $N$ in (6.39) is chosen equal to $N = 9000$. The actual experiment length is 2000+9000, but we will discard the first 2000 samples in the identification procedure. We thus set $N = 9000$ in the optimal experiment design problem.

[14]This optimal input signal has a different optimal frequency than the case $\tilde{x}_y = 0.12$.
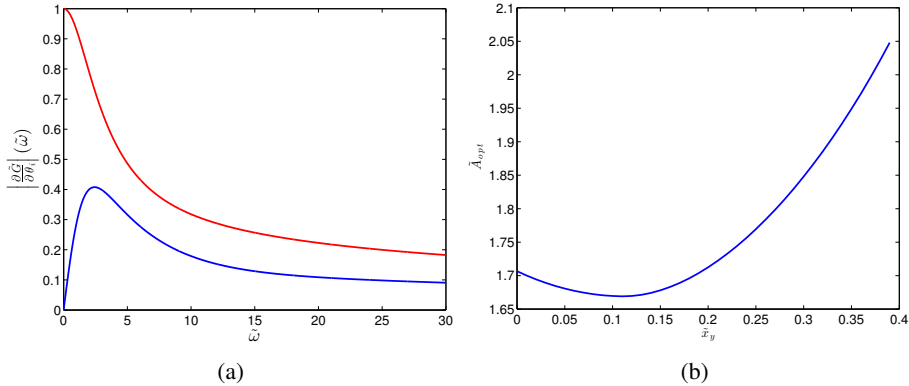
Figure 6.3: (a) Derivatives $\partial \tilde{G}_{\tilde{x}_u,\tilde{x}_y}(i\tilde{\omega},\tilde{\boldsymbol{\theta}})/\partial \tilde{\alpha}$ (red) and $\partial \tilde{G}_{\tilde{x}_u,\tilde{x}_y}(i\tilde{\omega},\tilde{\boldsymbol{\theta}})/\partial \tilde{\lambda}$ (blue) for $\tilde{x}_u = \tilde{x}_y = 0$ of the transfer function (6.35). (b) The scaled optimal amplitude $\tilde{A}_{opt}$, i.e. the solution of (6.25)-(6.26), is plotted as a function of scaled output location $\tilde{x}_y$ for $\tilde{x}_u = 0$.

Observe from Figure 6.3a that the scaled optimal frequency $\tilde{\omega} = 1.571$ lies in between the two maxima of the derivatives of $\tilde{G}_{\tilde{x}_u,\tilde{x}_y}$. This is an intuitively pleasing result, as high values for the derivatives lead to a large accuracy, see (6.30).

### Chicken-and-Egg Problem

The optimal input signal designed in the previous section was designed by using the true parameter vector $\tilde{\boldsymbol{\theta}}_0$. In practice, however, we obviously don't know this vector as we in fact want to estimate it. As mentioned in Section 6.4, the problem of finding the optimal signal to identify the parameter vector requires the parameter vector itself. This so-called chicken-and-egg problem can be circumvented by replacing $\tilde{\boldsymbol{\theta}}_0$ in (6.30) with a previous estimate or guess $\tilde{\boldsymbol{\theta}}_g$. This inevitably leads to a designed input signal that is not optimal. Optimal input design can however still be used and will generally lead to better estimates than arbitrary signals under the same experiment cost.

A central question is the sensitivity of the cost of the experiment to the initial guess $\tilde{\boldsymbol{\theta}}_g$, and whether or not the constraints will still be honoured. To this end we computed the optimal amplitude and frequency for many values of $\tilde{\boldsymbol{\theta}}_g$ using (6.38)-(6.39). The range in which these values lie is larger than the desired accuracy of estimates from the identification experiment. In Fig. 6.4a the optimal amplitude is shown for values of $\tilde{\lambda}$ and $\tilde{\alpha}$ around 10% of $\tilde{\lambda}_0 = 1$ and $\tilde{\alpha}_0 = 1$ (the case for which $\boldsymbol{\theta}_g = \boldsymbol{\theta}_0$). Observe that within this range the optimal amplitudes can differ up to 30% from the one obtained with $\tilde{\boldsymbol{\theta}}_0 = \tilde{\boldsymbol{\theta}}_g$, i.e., $A_{opt} = 1.7067$ (c.f. (6.40)). The cost of the experiment is thus rather sensitive to the guess $\tilde{\boldsymbol{\theta}}_g$. In Fig. 6.4b the optimal frequencies as a function of $\tilde{\boldsymbol{\theta}}_g$ are shown. It can be observed that the optimal frequency is not sensitive to a wrong guess $\tilde{\alpha}_g$ for a given guess $\tilde{\lambda}_g$. To test whether the constraints will still be honoured, and how large the error in the estimates is when using the optimal input signal designed with $\boldsymbol{\theta}_g \neq \boldsymbol{\theta}_0$, we proceed as follows. For each guess $\tilde{\boldsymbol{\theta}}_g$ we use the corresponding optimal amplitude and frequency of Figs. 6.4a and 6.4b, and apply this input signal to the true system. We then obtain the variances in the estimates $\hat{\tilde{\alpha}}_N$ and $\hat{\tilde{\lambda}}_N$ as a function of $\tilde{\boldsymbol{\theta}}_g$. We use the following measure

(a)



(b)



(c)

Figure 6.4: (a) The optimal amplitude resulting from the optimisation problem (6.38)-(6.39) is plotted as a function of the initial estimate $\tilde{\boldsymbol{\theta}}_g = (\tilde{\alpha}, \tilde{\lambda})^T$. This initial estimate is used to circumvent the chicken-and-egg iss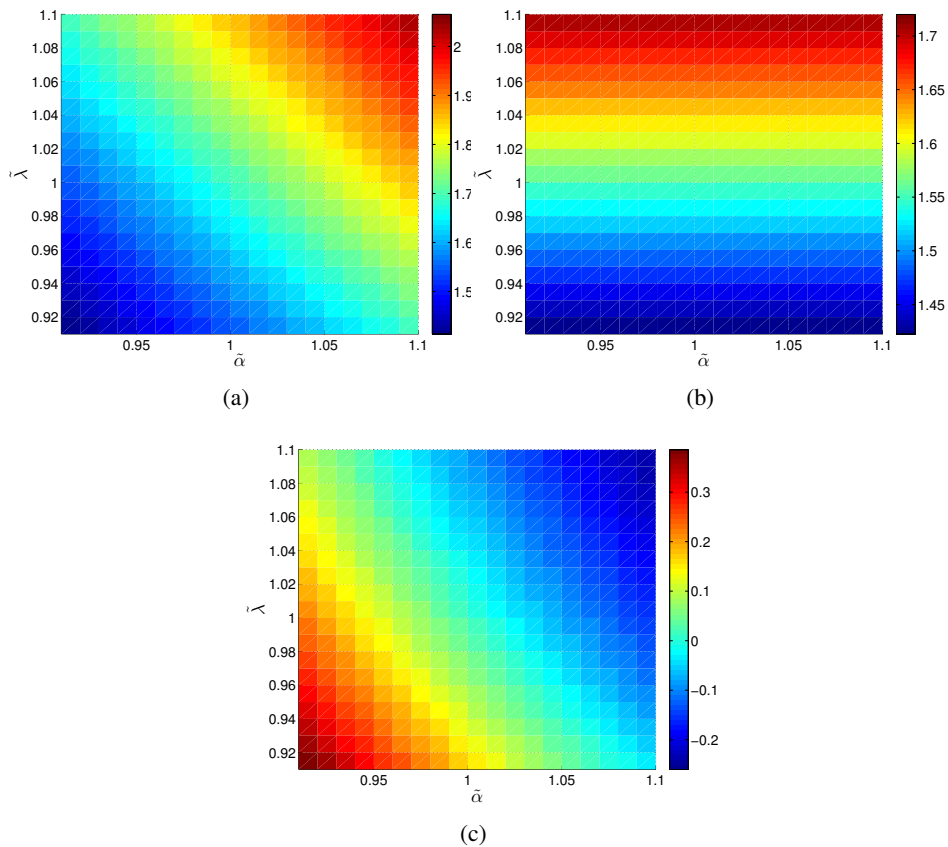ue. (b) The optimal frequency resulting from the optimisation problem (6.38)-(6.39) is plotted as a function of the initial estimate $\tilde{\boldsymbol{\theta}}_g = (\tilde{\alpha}, \tilde{\lambda})^T$. (c) The relative error (6.42) is plotted as a function of the initial estimate $\tilde{\boldsymbol{\theta}}_g$.

of error:

$$e(\tilde{\boldsymbol{\theta}}_g) = \frac{1}{2} \left[ \frac{\text{var}\hat{\tilde{\alpha}}_N(\tilde{\alpha}_g) - \text{var}\hat{\tilde{\alpha}}_N(\tilde{\alpha}_0)}{\text{var}\hat{\tilde{\alpha}}_N(\tilde{\alpha}_0)} + \frac{\text{var}\hat{\tilde{\lambda}}_N(\tilde{\lambda}_g) - \text{var}\hat{\tilde{\lambda}}_N(\tilde{\lambda}_0)}{\text{var}\hat{\tilde{\lambda}}_N(\tilde{\lambda}_0)} \right] \qquad (6.42)$$

We found that the relative error in the considered interval lies between 0 and 30%, see Fig. 6.4c. Also, it is clear that a strong correlation exists with Fig. 6.4a: if the optimal amplitude is larger or equal to $\tilde{A}_{opt} = 1.7067$ $((\tilde{\alpha}, \tilde{\lambda}) = (1, 1))$ we obtain variances that are smaller or equal to the case $\boldsymbol{\theta}_g = \boldsymbol{\theta}_0$. Conversely, we do not satisfy the constraints if the optimal amplitude is smaller than $\tilde{A}_{opt} = 1.7067$. This result could have been anticipated based on the analytical solution for bi-parametric models in Chapter 4.

## 6.5.4 Identification Results

In this section we identify the physical parameters $\tilde{\boldsymbol{\theta}}_0$ with the optimal input signal computed in the previous section (6.40). We use Method 2 as detailed in Section 6.3. The resulting unscaled data set $Z_N$ is defined by scaling (6.36) and the scaled sampled equivalent of the input (6.41). We remind the reader that we consider the case $x_u = x_y = 0$. The data set $\tilde{Z}_N = \left\{ \frac{u_D[j]}{u_s}, \frac{y_D[j]}{y_s} \right\}_{j=2001}^{11000}$, where $u_s$ and $y_s$ are defined in Section 6.5.2. Note that we discard the first 2000 samples to remove transients. Simulation of the scaled noise-free output $\tilde{y}_{nf}(\tilde{t})$ (6.34) is done according to Section 6.3.2 where we chose $\Delta\tilde{t} = T_s/t_s$ and $M = 200$. The simulated noise-free output $\tilde{y}_{sim}[j]$ for $j = 2001, \ldots, 11000$ is then used together with the scaled measured data $y_D[j]/y_s$ in $\tilde{Z}_N$ in the least-squares procedure (6.9). For one experiment we found the scaled estimates resulting from this procedure to be $\hat{\tilde{\alpha}}_N = 1.01$ and $\hat{\tilde{\lambda}}_N = 1.005$, corresponding to unscaled estimates $\hat{\alpha}_N = 3.414 \times 10^{-5}$ m$^2$ s$^{-1}$ and $\hat{\lambda}_N = 111.56$ W m$^{-1}$ °C$^{-1}$. These estimates fall within the respective intervals $[\lambda_0 - 0.01\lambda_0, \lambda_0 + 0.01\lambda_0]$ and $[\alpha_0 - 0.02\alpha_0, \alpha_0 + 0.02\alpha_0]$ that we set in Section 6.5.3.

### Monte Carlo Simulations, Experiment 1: Validating the Variance Constraints

To validate whether the variance constraints are honoured, we ran $2 \times 10^4$ Monte Carlo simulations to identify the scaled physical parameters $\tilde{\alpha}_0 = 1$ and $\tilde{\lambda}_0 = 1$ with the optimal signal (6.40). (In other words, twenty thousand data sets $Z_N$ were generated and for each the identification procedure was applied). The identified parameters $\tilde{\alpha}_N$ and $\tilde{\lambda}_N$ for all experiments are shown in Fig. 6.5. The mean value of the coordinate $\hat{\boldsymbol{\theta}}_N = (\tilde{\alpha}_0, \tilde{\lambda}_0)^T$ is indicated by the red cross. The constraints set in Section 6.5.3 are visualised by the square resulting from intersection horizontal and vertical dashed black lines.

Observe that almost none of the estimates $\tilde{\boldsymbol{\theta}}_N$ lies outside the region of constraints. The computed variance for $\tilde{\alpha}_N$ and $\tilde{\lambda}_N$ are respectively $\text{var}(\tilde{\alpha}_N) = 3.615 \times 10^{-5}$ and $\text{var}(\tilde{\lambda}_N) = 1.1108 \times 10^{-5}$. Clearly, the optimal input signal designed in the previous section honours the constraints. The experiment design procedure ensured that the confidence ellipse 'touches' the horizontal constraints, whereas the variance in $\tilde{\alpha}_N$ is in fact a bit smaller. This is not surprising, as explained in Chapter 4.

Under the same experiment length, parameter values $\alpha_0, \lambda_0$, and rod length $L$, Gabano and Poinot (2009) obtained estimates with slightly lower accuracy in the estimates. However, they used more input signal power than is used in our experiment. The input signal
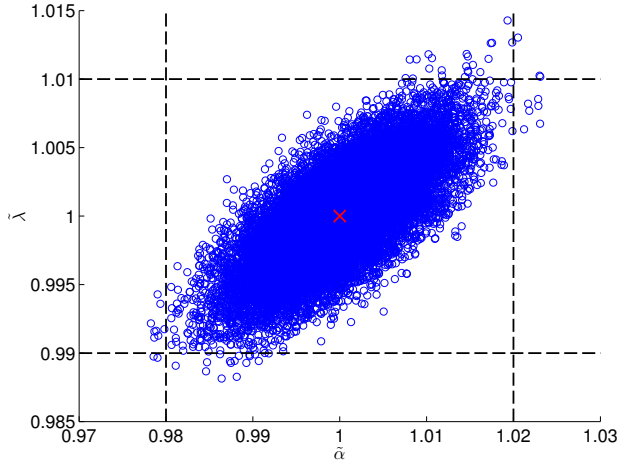
Figure 6.5: Twenty thousand identified vectors $\tilde{\theta}_N$ are indicated by the blue open circles, the mean value of $\tilde{\theta}_N$ over all Monte Carlo simulations by the red cross, and the constraints on the parameters $\tilde{\alpha}_N$ and $\tilde{\lambda}_N$ by the square generated through the intersection of the dashed black lines.

they considered was a pseudo-random binary excitation signal with a power distribution in the higher frequencies, up to $20\,rad/s$. Our result suggests that one should instead use a very low excitation frequency, i.e. 0.02 rad/s to get the most accurate estimates. As shown in Fig. 6.4b, choosing high frequencies leads to matrix $P_{N,\bar{\theta}}^{-1}$ that is much smaller than using one that is close to the maxima of the derivatives. Intuitively, it means that the system is not sensitive to high-frequency input signals.

Our results also suggest that higher accuracy can be obtained by measuring at $\tilde{x}_y = 0.12$ as shown in Figure 6.4a. The ratio of the optimal amplitude between $\tilde{x}_y = 0$ and $\tilde{x}_y = 0.12$ is 1.03. As $\tilde{P}_{N,\bar{\theta}}^{-1}$ is proportional to $\tilde{A}^2$, it means that $1.03^2$ higher accuracies can be obtained using the same input power.

### Monte Carlo Simulations, Experiment 2: Chicken-and-Egg Problem Revisited

In Section 6.4 we mentioned that LCED suffers from the chicken-and-egg problem. In this section we show that we can still find estimates that honour the user-imposed constraints, even if we don't know exactly $\tilde{\theta}_0$.

To this end suppose that we start without any prior knowledge on $\theta_0$. We run an experiment of length $N/2$ and apply a white-noise input signal[15] with high variance $\tilde{\sigma}_{wn}^2 = 25$. This delivers us an estimate $\hat{\bar{\theta}}_{wn}$. At this point, we compare two scenarios: (i) we apply optimal experiment design to find the optimal input signal that guarantees the constraints (6.37) based on the initial guess $\tilde{\theta}_g = \hat{\bar{\theta}}_{wn}$ for an experiment length of $N/2$, or (ii) continue with applying a white-noise signal that has the same power as the optimal input signal and equal experiment length. Both scenarios thus have equally-powered input signals and the experiments have equal length.

Using Monte Carlo simulations, we first generate 500 white-noise realisation with vari-

---

[15]Note that we now can only use Method 2 of Section 6.3 because the input signal is no longer periodic, whereas in Experiment 1 we could have also opted for Method 1 since the input signal is periodic and a closed-form transfer function exists.
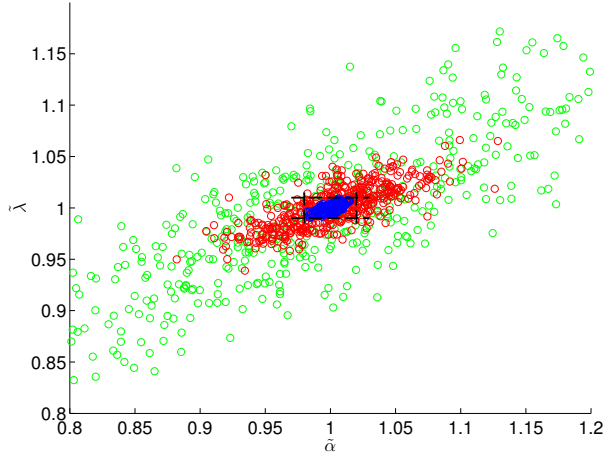
Figure 6.6: Monte Carlo simulations. The red circles correspond to initial estimates resulting from identification experiments in which white-noise excitation signals were used. For each initial guess (red circles), a LCED problem is solved in which the true parameter vector has been replaced by the estimate. The resulting optimal input signal is subsequently applied and the new experiment data is used to compute a new estimate. These estimates are shown in blue. The green circles are a collection of estimates obtained by applying white-noise excitation signals, each having the same power as one of the optimal input signals (used to obtain the blue estimates).

ance $\tilde{\sigma}_{wn}^2 = 25$ that generate 500 estimates $\hat{\tilde{\theta}}_{wn}$, which we collect in the set $\left\{ \hat{\tilde{\theta}}_{wn} \right\}$. These estimates are shown in red in Fig. 6.6. Next, for each of the estimates, we run scenario (i) and (ii). The estimates resulting from scenario (i) and (ii) are shown in blue and green in Fig. 6.6, respectively. We find that the variances of the estimates in scenario (i) are $\text{var}(\hat{\tilde{\alpha}}_{N/2}) = 3.1381 \times 10^{-5}$ and $\text{var}(\hat{\tilde{\lambda}}_{N/2}) = 9.2074 \times 10^{-6}$, which are both smaller than the required variances of respectively $4.44 \times 10^{-5}$ and $1.11 \times 10^{-5}$. The equally-powered white noise realisations of scenario (ii) deliver much worse estimates.

Since both scenarios generate signals that are equally long and equally-powered, these Monte Carlo simulations clearly illustrate the advantage of optimal experiment design.

The above approach is the classical approach to tackle the chicken-and-egg problem. More involved approaches exist. In these approaches, the initial guess and the optimal spectrum are adapted throughout the experiment; see e.g. the works of Gerencsèr et al. (2009), Larsson et al. (2013), and Forgione et al. (2013).

## 6.6   Summary

The main novelty of this chapter is the introduction of a systematic way to identify physical parameters in linear physical systems in a least-intrusive manner while guaranteeing accuracy on the to-be-identified parameters. We have in particular shown how to apply the theory of least-costly experiment design to structured processes governed by linear PDEs with constant coefficients.

To this end, we made use of a discretisation using the Crank-Nicolson stencil to truncate the continuous-time model to find a discrete-time transfer function that couples the input and output. This transfer function is then also guaranteed to be stable. This integration scheme is not only unconditionally stable, but also more accurate than the Euler

stencil. The resulting truncated model is a state-space realisation that is explicit in the physical parameters. We then showed how optimal experiment design can be applied. The second novelty of this chapter is the generalisation of the experiment design framework to find not only optimal amplitudes and frequencies, but also optimal actuator and sensor locations.

We applied our methodology to the estimation of two thermal parameters in a front-face experiment. This study showed that current practice, i.e. placing the sensor and actuator at position $x = 0$, in fact does not deliver the best possible estimates. Our study suggests that placing the sensor location at a distance of 12% of the total length of the rod from the actuator position yields estimates that are 6% better. Applying the optimal input signals designed in the case study furthermore shows that the input power can be reduced considerably in comparison to previous experiments.

Future work could be focussed on generalising the method to nonlinear PDEs, since many physical systems in real-life are in fact nonlinear. For these systems, one can analyse whether or not linearisation is feasible. If it is not feasible, it would be interesting to generalise the LCED framework to Linear Parameter Varying systems. Such systems can be used to approximate a nonlinear system while still having excess to the powerful linear methods.

## 6.A Derivation of continuous-time transfer function of 1D diffusion equation

We consider the one dimensional problem of a diffusion process on a line with domain $\mathcal{D} = [0, L]$. The physical parameters are collected in the vector $\theta = (\theta_1, \theta_2)^T$. The problem is defined by

$$\frac{\partial f(x,t)}{\partial t} = \theta_1 \frac{\partial^2 f(x,t)}{\partial x^2} \tag{6.43}$$

subject to the boundary conditions

$$\phi(x,t) = -\theta_2 \frac{\partial f(x,t)}{\partial x}, \quad f(L,t) = 0 \forall t$$

We define the input of the system by $u(t) = \phi(x_u, t)$ and the output $y_{nf}(t) = f(x_y, t)$, where $x_u, x_y \in \mathcal{D}$ denote the input and output location on the line. To solve the problem, we first apply the Laplace transform to the above equations:

$$sF(x,s) = \theta_1 \frac{\partial^2 F(x,s)}{\partial x^2} \tag{6.44}$$

$$\Phi(x,s) = -\theta_2 \frac{\partial F(x,s)}{\partial x}. \tag{6.45}$$

The general solution to (6.44) reads

$$F(x,s) = c_1 e^{\sqrt{\frac{s}{\theta_1}} x} + c_2 e^{-\sqrt{\frac{s}{\theta_1}} x}, \tag{6.46}$$

where $c_1$ and $c_2$ are real constants that will be determined from the boundary conditions. From this equation, it follows that (6.45) becomes

$$\Phi(x,s) = -\theta_2 \sqrt{\frac{s}{\theta_1}} \left\{ c_1 e^{\sqrt{\frac{s}{\theta_1}} x} - c_2 e^{-\sqrt{\frac{s}{\theta_1}} x} \right\}. \tag{6.47}$$

We also have that the input and output in the Laplace domain read $U(s) = \Phi(x_u, s)$ and $Y_{nf}(s) = F(x_y, s)$. We can thus write

$$U(s) = \Phi(x_u, s) = -\theta_2 \sqrt{\frac{s}{\theta_1}} \left\{ c_1 e^{\sqrt{\frac{s}{\theta_1}} x_u} - c_2 e^{-\sqrt{\frac{s}{\theta_1}} x_u} \right\}$$

from which follows that

$$c_1 = e^{-\sqrt{\frac{s}{\theta_1}} x_u} \left\{ -\frac{1}{\theta_2} \sqrt{\frac{s}{\theta_1}} U(s) + c_2 e^{-\sqrt{\frac{s}{\theta_1}} x_u} \right\}. \tag{6.48}$$

Furthermore, from (6.46) and the boundary condition $F(L, s) = 0 \; \forall s$ we get

$$F(L, s) = c_1 e^{\sqrt{\frac{s}{\theta_1}} L} + c_2 e^{-\sqrt{\frac{s}{\theta_1}} L} = 0 \;\; \rightarrow \;\; c_2 = -c_1 e^{2\sqrt{\frac{s}{\theta_1}} L}. \tag{6.49}$$

We can now combine (6.48) and (6.49) to find that

$$c_1 = -\frac{1}{\theta_2} \sqrt{\frac{\theta_1}{s}} \frac{e^{-\sqrt{\frac{s}{\theta_1}} x_u}}{1 + e^{2\sqrt{\frac{s}{\theta_1}} (L - x_u)}} U(s),$$

$$c_2 = \frac{1}{\theta_2} \sqrt{\frac{\theta_1}{s}} \frac{e^{-\sqrt{\frac{s}{\theta_1}} (x_u - 2L)}}{1 + e^{2\sqrt{\frac{s}{\theta_1}} (L - x_u)}} U(s).$$

Next, we can write the expression for $Y_{nf}(s) = F(x_y, s)$ which reads

$$\begin{aligned}
Y_{nf}(s) &= c_1 e^{\sqrt{\frac{s}{\theta_1}} x_y} + c_2 e^{-\sqrt{\frac{s}{\theta_1}} x_y} \\
&= -\frac{1}{\theta_2} \sqrt{\frac{\theta_1}{s}} \frac{e^{-\sqrt{\frac{s}{\theta_1}} (x_u - x_y)}}{1 + e^{2\sqrt{\frac{s}{\theta_1}} (L - x_u)}} \left\{ 1 - e^{2\sqrt{\frac{s}{\theta_1}} (L - x_y)} \right\} U(s).
\end{aligned}$$

Hence, the transfer function between input and output reads

$$G_{x_u, x_y}(s, \boldsymbol{\theta}) = \frac{Y_{nf}(s)}{U(s)} = -\frac{1}{\theta_2} \sqrt{\frac{\theta_1}{s}} \frac{e^{-\sqrt{\frac{s}{\theta_1}} (x_u - x_y)}}{1 + e^{2\sqrt{\frac{s}{\theta_1}} (L - x_u)}} \left\{ 1 - e^{2\sqrt{\frac{s}{\theta_1}} (L - x_y)} \right\},$$

which can be further simplified to

$$G_{x_u, x_y}(s, \boldsymbol{\theta}) = \frac{1}{\theta_2} \sqrt{\frac{\theta_1}{s}} \frac{\sinh\left[ \sqrt{\frac{s}{\theta_1}} (L - x_y) \right]}{\cosh\left[ \sqrt{\frac{s}{\theta_1}} (L - x_u) \right]}.$$

Substitution of $f(x,t) = T(x,t)$ in (6.43) and following the same calculations yields the equation above. Finally, setting $\theta_1 = \alpha_0$ and $\theta_2 = \lambda_0$ results in $G_{x_u,x_y}(s,\boldsymbol{\theta}_0)$, in which $\boldsymbol{\theta}_0 = (\alpha_0, \lambda_0)^T$. In a similar fashion the continuous-time transfer function between the scaled input and scaled output can be derived for (6.33)-(6.34), yielding

$$\tilde{G}_{\tilde{x}_u,\tilde{x}_y}(\tilde{s},\tilde{\boldsymbol{\theta}}) = \frac{1}{\tilde{\theta}_2}\sqrt{\frac{\tilde{\theta}_1}{\tilde{s}}}\,\frac{\sinh\left[\sqrt{\frac{\tilde{s}}{\tilde{\theta}_1}}(1-\tilde{x}_y)\right]}{\cosh\left[\sqrt{\frac{\tilde{s}}{\tilde{\theta}_1}}(1-\tilde{x}_u)\right]}.$$

This equation is equal to (6.35) after substitution of $\tilde{\boldsymbol{\theta}} = \tilde{\boldsymbol{\theta}}_0 = (\tilde{\alpha}_0, \tilde{\lambda}_0)^T$.

## 6.B    Computation of the Gradient

n this appendix we show how to compute the gradient $\partial G_{i_u,i_y}/\partial\boldsymbol{\theta}$ in (6.30) evaluated at $\boldsymbol{\theta} = \boldsymbol{\theta}_0$ for given $i_u$, $i_y$. We start from equation (6.30), which we here recall for convenience:

$$G_{i_u,i_y}(z,\boldsymbol{\theta}) = \boldsymbol{C}\left[z\boldsymbol{I} - \boldsymbol{A}(\boldsymbol{\theta})\right]^{-1}\boldsymbol{B}(\boldsymbol{\theta}). \qquad (6.50)$$

In this equation, $\boldsymbol{I}$ is the $(V+1) \times (V+1)$ identity matrix, $\boldsymbol{A}(\boldsymbol{\theta}) = \boldsymbol{\mathcal{E}}^{-1}\boldsymbol{\mathcal{A}}$, $\boldsymbol{B}(\boldsymbol{\theta}) = \boldsymbol{\mathcal{E}}^{-1}\boldsymbol{\mathcal{B}}(1+z)$, and $\boldsymbol{C} = \boldsymbol{\mathcal{C}}$. Here, $z = e^{i\omega T_s}$ and $\boldsymbol{\mathcal{E}}$, $\boldsymbol{\mathcal{A}}$, $\boldsymbol{\mathcal{B}}$, and $\boldsymbol{\mathcal{C}}$ are given by (6.16)-(6.18). Making use of the identities $\frac{\partial U^{-1}}{\partial x} = -U^{-1}\frac{\partial U}{\partial x}U^{-1}$ and $\frac{\partial(UV)}{\partial x} = U\frac{\partial V}{\partial x} + \frac{\partial U}{\partial x}V$, where $U, V$ equally-sized matrices and $x$ a scalar, we find that the derivative of (6.50) with respect to parameter $\theta_i$ reads

$$\frac{\partial G_{i_u,i_y}(z,\boldsymbol{\theta})}{\partial\theta_i} = \boldsymbol{C}\left[z\boldsymbol{I} - \boldsymbol{A}(\boldsymbol{\theta})\right]^{-1}\left\{\frac{\partial\boldsymbol{B}(\boldsymbol{\theta})}{\partial\theta_i} + \frac{\partial\boldsymbol{A}(\boldsymbol{\theta})}{\partial\theta_i}\left[z\boldsymbol{I} - \boldsymbol{A}(\boldsymbol{\theta})\right]^{-1}\boldsymbol{B}(\boldsymbol{\theta})\right\}. \quad (6.51)$$

The derivatives of $\boldsymbol{A}(\boldsymbol{\theta}) = \boldsymbol{\mathcal{E}}^{-1}(\boldsymbol{\theta})\boldsymbol{\mathcal{A}}(\boldsymbol{\theta})$ and $\boldsymbol{B}(\boldsymbol{\theta}) = \boldsymbol{\mathcal{E}}^{-1}(\boldsymbol{\theta})\boldsymbol{\mathcal{B}}(\boldsymbol{\theta})[1+z]$ w.r.t. $\theta_i$ are

$$\frac{\partial\boldsymbol{A}(\boldsymbol{\theta})}{\partial\theta_i} = -\boldsymbol{\mathcal{E}}^{-1}(\boldsymbol{\theta})\frac{\partial\boldsymbol{\mathcal{E}}(\boldsymbol{\theta})}{\partial\theta_i}\boldsymbol{\mathcal{E}}^{-1}(\boldsymbol{\theta})\boldsymbol{\mathcal{A}}(\boldsymbol{\theta}) + \boldsymbol{\mathcal{E}}^{-1}(\boldsymbol{\theta})\frac{\partial\boldsymbol{\mathcal{A}}(\boldsymbol{\theta})}{\partial\theta_i}, \qquad (6.52)$$

$$\frac{\partial\boldsymbol{B}(\boldsymbol{\theta})}{\partial\theta_i} = \left(-\boldsymbol{\mathcal{E}}^{-1}(\boldsymbol{\theta})\frac{\partial\boldsymbol{\mathcal{E}}(\boldsymbol{\theta})}{\partial\theta_i}\boldsymbol{\mathcal{E}}^{-1}(\boldsymbol{\theta})\boldsymbol{\mathcal{B}}(\boldsymbol{\theta}) + \boldsymbol{\mathcal{E}}^{-1}(\boldsymbol{\theta})\frac{\partial\boldsymbol{\mathcal{B}}(\boldsymbol{\theta})}{\partial\theta_i}\right)[1+z]. \quad (6.53)$$

Substitution of (6.52) and (6.53) into (6.51) finally gives

$$\frac{\partial G_{i_u,i_y}(z,\boldsymbol{\theta})}{\partial\theta_i} =$$

$$\boldsymbol{C}\left[z\boldsymbol{I} - \boldsymbol{A}(\boldsymbol{\theta})\right]^{-1}\boldsymbol{\mathcal{E}}^{-1}(\boldsymbol{\theta})(1+z)\left\{\left(\frac{\partial\boldsymbol{\mathcal{B}}(\boldsymbol{\theta})}{\partial\theta_i} + \frac{\partial\boldsymbol{\mathcal{A}}(\boldsymbol{\theta})}{\partial\theta_i}\left[z\boldsymbol{I} - \boldsymbol{A}(\boldsymbol{\theta})\right]^{-1}\boldsymbol{\mathcal{E}}^{-1}(\boldsymbol{\theta})\boldsymbol{\mathcal{B}}(\boldsymbol{\theta})\right)\right.$$

$$\left. -\frac{\partial\boldsymbol{\mathcal{E}}(\boldsymbol{\theta})}{\partial\theta_i}\boldsymbol{\mathcal{E}}^{-1}(\boldsymbol{\theta})\left(\boldsymbol{\mathcal{B}}(\boldsymbol{\theta}) + \boldsymbol{\mathcal{A}}(\boldsymbol{\theta})\left[z\boldsymbol{I} - \boldsymbol{A}(\boldsymbol{\theta})\right]^{-1}\boldsymbol{\mathcal{E}}^{-1}(\boldsymbol{\theta})\boldsymbol{\mathcal{B}}(\boldsymbol{\theta})\right)\right\}$$

$$(6.54)$$

In this equation, the derivatives can be found analytically using (6.16), (6.18). To evaluate this equation at $\boldsymbol{\theta} = \boldsymbol{\theta}_0$ for all parameters $\theta_i \in \boldsymbol{\theta}$ it is most efficient to follow these steps:

1. Calculate all terms independent of $z$ in (6.54) for $\boldsymbol{\theta} = \boldsymbol{\theta}_0$ once and store these.

2. Evaluate for $\boldsymbol{\theta}_i$ the expression (6.54) at frequency $\omega$ by substituting $z = \exp(i\omega T_s)$

3. Repeat step (2) for all other $i = 1, \ldots, \dim(\boldsymbol{\theta})$.

4. Repeat step (2)-(3) until the gradient is computed for all required frequencies $\omega$.

Combining the derivatives of each element in the parameter vector then gives the gradient.

# 7

# LCED for Core-Scale Pressure Oscillation Experiments

*"Prediction is very difficult, especially if it's about the future."* - Niels Bohr

## 7.1   Introduction

In this chapter, we will use the concepts introduced in Chapter 6 and apply them on a relevant problem in petrophysics. We define this problem below.[1]

Two key parameters influencing fluid flow in a porous medium are permeability (i.e. inverse resistance) and porosity (i.e. storage capacity). These parameters are important to characterise fluid flow in underground water resources (Cardiff et al. (2013)), contaminated water disposal in underground storages (Song and Renner (2007)), and subsurface hydrocarbon reservoirs (Wang and Knabe (2011)). Indeed, permeability and porosity estimates are used to initialise reservoir simulations, optimise the number of wells and their locations, and drilling and completion procedures.

Estimation of both parameters locally can be carried out by performing an experiment on a cylindrically-shaped core sample of the porous medium, using either steady-state (SS), unsteady-state (USS), or pressure oscillation (PO) measurements. In an SS experiment a constant pressure difference is applied across the axis of the core sample and subsequently the flow rate is measured after the SS condition has been established. Permeability is then estimated based on the relationship between the flow rate and the pressure drop. In an USS experiment an impulse or step pressure change is applied at the upstream side of the sample while the pressure change is recorded downstream. The observed response is then analysed either graphically or numerically to estimate the unknown parameter(s). Similarly, in a PO experiment, the recorded downstream pressure response is analyzed for parameter estimation - the difference being that an oscillatory pressure signal is applied upstream. The attenuation and phase shift between the up- and downstream signals are then translated into parameter estimates (Fischer (1992); Heller et al. (2002)). The oscillatory signal is usually a single sinusoid with a frequency and amplitude specified by the experimenter. The amplitude of the upstream signal is however bounded by the limits

---

[1]Parts of this chapter have been published in (Potters et al. (2016c)).

of the actuator. In cases where a rather high actuator frequency is necessary to take into account geometrical and physical properties of the sample, Boitnott (1997) suggested the use of input signals with complex shapes including the required high frequencies.

The consensus in the literature is that a PO experiment has several advantageous properties not shared by its SS and USS counterparts, e.g., less experiment time, less stress on the core sample, and the possibility of simultaneously estimating permeability and porosity (Bernabé and Evans (2006); Song and Renner (2007)). The effectiveness of PO experiments for the estimation of permeability has been demonstrated in different set-ups (Heller et al. (2002); Wang and Knabe (2011); Suri et al. (1997); Hasanov and Batzle (2013); Boitnott (1997)). Despite its advantageous properties, however, it is observed that measurements can result in large uncertainties in the estimates, particularly for porosity (Bernabé and Evans (2006); Song and Renner (2007); Wang and Knabe (2011)). Porosity estimates with an uncertainty exceeding an order of magnitude, or that have negative values, have been reported by e.g. Song and Renner (2007) and Bernabé and Evans (2006). One cause is measurement noise, but in this chapter we show that other ones also play an important role.

Furthermore, it is important to be able to reduce the experiment time without loss of accuracy. In such a case, more core samples can be analysed in a given time, which consequently reduces the experiment costs. Analogously, given a maximum experiment time, it is important to get the best possible estimates.

Clearly, the challenge of estimating permeability and porosity with high accuracy remains, especially in evaluating the production potential of tight formations in unconventional hydrocarbon reservoirs (Wang and Knabe (2011)) or the sealing characteristics of the cap rock in underground storage (Song and Renner (2007)).

Motivated by the above problems we raise the question whether we can, for a PO experiment, design the applied upstream pressure signal in order to increase parameter accuracies. The dependence of the accuracy of the estimates on the selected driving frequency has been first pointed out by Kranz et al. (1990), although no investigation into this topic was pursued. Besides the optimisation of the excitation signal, we will also optimise simultaneously the degrees of freedom (DOF) in the experiment set-up to further improve the results. This is similar to what we have done in Chapter 6 where the optimisation of the actuator and sensor locations were used for the same objective.

We will formulate the optimal experiment problem in a slightly different way than in the previous chapters. This alternative formulation is motivated by the limitation of the amplitude of the actuator. As a consequence we define the following optimisation problem: find the minimal experiment time required to guarantee user-imposed variance constraints on the estimates by utilising DOF in the experiment set-up as well as designing the to-be-applied upstream pressure signal, ensuring that this signal has an amplitude that honours the actuator limits.

In a PO experiment, the actuator can generally only generate excitation signals in the form of a single sinusoid or a square wave (Heller et al. (2002)). We shall thus limit ourselves to the design of such actuator signals.

We apply our method to the Dynamic Darcy Cell experiment set-up, as detailed in (Heller et al. (2002)), but we stress that our methodology can be applied to many other set-ups as well. The DOF in the Dynamic Darcy Cell set-up are the inlet volume and outlet volume.

We introduce the Dynamic Darcy Cell in Section 7.2 and show how to apply sinusoidal and square wave signals to the set-up. Two types of measurements are then introduced: inlet pressure/outlet pressure measurements (Direct Method) and actuator position/outlet pressure measurements (Indirect Method). The former is one of the current ways to estimate parameters (Heller et al. (2002)), in particular using sinusoidal signals. The latter has, to the best of our knowledge, not been investigated before. For both cases, we focus on square wave input signals, for which we prove that shorter experiment lengths than for sinusoidal ones can be obtained. We explain the data collection and estimation procedure in Section 7.3, and give an expression for the covariance matrix of the estimated parameters. In Sections 7.4 and 7.5 we use this expression to compute the optimal sinusoidal and square wave signals and DOF that minimise the experiment time for the estimation of permeability and porosity for the Direct and Indirect Methods. In the absence of a physical set-up, we illustrate the experiment design results by simulating the noise-corrupted physical system and applying the optimal square wave signal in Section 7.6. Lastly, we draw conclusions in Section 7.7.

## 7.2 The Dynamic Darcy Cell

### 7.2.1 The Set-Up

To investigate the estimation problem the Dynamic Darcy Cell by Heller et al. (2002) is considered. A detailed and schematic layout of this set-up are depicted in Figs. 7.1 and 7.2. A cylindrically-shaped porous core sample is mounted vertically in a core holder under a specific confined pressure $p_{init}$, with the inlet at the bottom (upstream side) and outlet at the top (downstream side). The sample with length $L$ and cross-sectional area $A$ is sealed at the top from the environment. The spatial coordinate axis $x$ is oriented towards the outlet and is perpendicular to the cross-sectional plane. The bottom of the sample is located at $x = 0$. A vibration exciter with equilibrium position $x = -L_i$, also called the actuator, is moved according to the user-defined oscillatory signal $r(t)$. As in Chapter 6, we suppose that the excitation signal is a continuous-time signal. The actuator position is either a sinusoid, i.e.,

$$r(t) = C_\gamma \sin(\omega_{ex}t), \tag{7.1}$$

or a square wave[2],

$$r(t) = \frac{4}{\pi}C_\gamma \sum_{m=1}^{\infty} \frac{\sin([2m-1]\,\omega_c t)}{2m-1}. \tag{7.2}$$

In these expressions, $\omega_{ex}$ and $\omega_c$ in respectively (7.1), (7.2) represent the excitation frequency of the sinusoid and cycle frequency (slowest mode) of the square wave. In the sequel, our objective will be to determine the optimal pair $\{C_\gamma, \omega_{ex}\}$ for the parameterisation (7.1) or the optimal pair $\{C_\gamma, \omega_c\}$ for (7.2) in order to identify the sample's permeability and porosity values. This situation is very close to the one of Chapter 4 and we will see that, here also, we will be able to determine the solution analytically. Finally, note that, since we only identify two parameters, the single sinusoid (7.1) is sufficient to lead to consistent estimates (under Assumption 4.1).

---

[2]Until now, such a signal has not yet been considered. However, this signal can be seen as a multi-sine with a specific amplitude end-phase pattern.
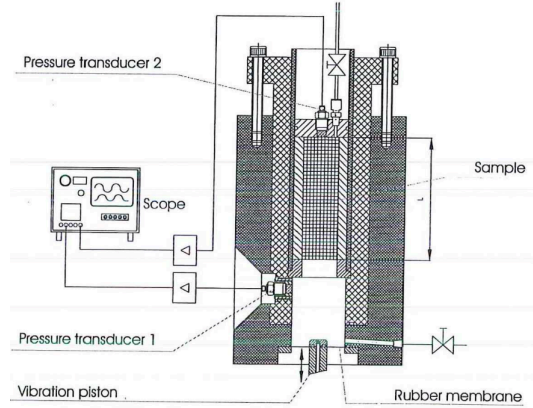
Figure 7.1: The Dynamic Darcy Cell. The core sample is mounted vertically in the holder. The actuator induces a pressure signal at inlet, measured by pressure transducer 1. The wave propagates through the porous core and is measured at the outlet by pressure transducer 2. Courtesy of Heller et al. (2002). The bandwidth of the actuator is much larger than the bandwidth of the system.

The symbol $C_\gamma$ represents the amplitude of the actuator signal defined by

$$C_\gamma = \gamma L_i, \ \ 0 < \gamma \leq \gamma_m. \tag{7.3}$$

Obviously, the actuator amplitude can not exceed the length $L_i$ as can be seen from Fig. 7.2, so the user-chosen factor $\gamma$ has a geometric constraint $\gamma \leq \gamma_m = 1$. However, the actuator amplitude may not necessarily be limited by the geometry of the setup but by its own movement restrictions, yielding a $\gamma_m$ that is smaller than unity.

The square wave signal can be generated in practice by switching abruptly between $+C_\gamma$ and $-C_\gamma$. The actuator induces an upstream (inlet) pressure signal at position $x = 0$, i.e.,

$$p_i(t) = p(x = 0, t), \tag{7.4}$$

within the inlet volume $V_i$ that is connected to the sample. This signal is measured by pressure transducer 1 (see Fig. 7.1) and assumed to be corrupted by sensor noise. At the sample outlet, which is connected to the end volume $V_e$, the output (downstream) pressure

$$p_e(t) = p(x = L, t) = y_{nf}(t) \tag{7.5}$$

is measured by pressure transducer 2 at $x = L$, see Fig. 7.1. Here, $y_{nf}(t) = p_e(t) = p(x = L, t)$ is the noise-free pressure response of the core sample[3]. The measurements taken by this pressure transducer are corrupted by sensor noise. We shall return to this point when we explain the estimation method in Section 7.3. The inlet and outlet volumes $V_i$ and $V_e$ can be set by the experimenter and are part of the DOF of the experiment set-up[4]. Prior to the experiment the core, the inlet and outlet volume are filled with a gas (e.g. air) at pressure $p_{init}$.

---

[3]The input and output are continuous time signals. In Section 7.3 we will use sampled input and output data for parameter estimation.

[4]The set-up can for instance be designed to have easily-adaptable inlet and outlet volumes.
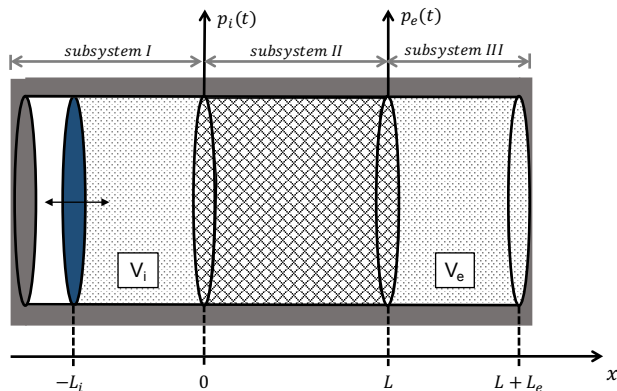
Figure 7.2: A sketch of the Dynamic Darcy Cell, rotated ninety degrees clock-wise. The cylindrical core sample is depicted in between the inlet volume $V_i$ and outlet volume $V_e$. The sample has a cross-sectional area $A$ and length $L$. The signals $p_i(t)$ and $p_e(t)$ are measured by pressure transducer 1 and 2 respectively, see Fig. 7.1. The actuator is visualised by the blue disk that can oscillate around its equilibrium position $x = -L_i$.

| Quantity | Value |
| --- | --- |
| Length $L$ | 0.0512 m |
| Cross-sectional area $A$ | $\pi\, 0.0375^2/4$ m$^2$ |
| Permeability $k_0$ | $2.0 \times 10^{-13}$ m$^2$ |
| Porosity $\phi_0$ | 0.2 |
| Fluid density $\rho$ | 1.225 kg m$^{-3}$ |
| Viscosity $\mu$ | $1.84 \times 10^{-5}$ Pa s |
| Bulk modulus $K$ | $1.0 \times 10^5$ Pa |

Table 7.1: Parameters defining the Dynamic Darcy Cell and the core sample. The parameters $k_0$ and $\phi_0$ need to be estimated.

## 7.2.2    System of Coupled Equations in the Time Domain

In the set-up we consider a porous cylindrical core that is homogeneous and isotropic with constant porosity $\phi$ and permeability $k$, and assume that the compressibility of the medium is small compared with the compressibility of the gas and therefore considered constant. Usually, both $\phi$ and $k$ have to be identified. The core is defined in Table 7.1. Gravity forces and pressure dependencies of the viscosity $\mu$ are neglected and isothermal conditions are assumed.

We now derive the dynamics within the experiment set-up. We shall consider the inlet volume, the porous medium, and outlet volume as three subsystems with their own dynamics, input and output, and boundary conditions. The subsystems are interconnected at the inlet ($x = 0$) and outlet ($x = L$) locations. We shall use the dynamics to derive the relationship between the inlet pressure to outlet pressure signals, and the actuator position to outlet pressure signals in Section 7.2.4.

### Subsystem I: The Inlet Volume

The actuator is a piston that vibrates in the $x$-direction within a confined gas in the inlet volume $V_i = AL_i$, where $L_i$ is the length of the inlet. The dynamics of the gas volume as a consequence of the moving piston is governed by the momentum and mass conservation laws, which for this particular configuration read

$$\frac{\partial w}{\partial t} + w\frac{\partial w}{\partial x} + \frac{1}{\rho}\frac{\partial p}{\partial x} \;=\; 0, \tag{7.6}$$

$$\frac{\partial \rho}{\partial t} + w\frac{\partial \rho}{\partial x} + \rho\frac{\partial w}{\partial x} \;=\; 0, \tag{7.7}$$

where $w = w(x,t)$ is the velocity profile of the gas in the $x$-direction, $\rho$ the density of the gas, and $p = p(x,t)$ the pressure profile. We assume that the actuator has a small amplitude. In this case we may linearise (7.6)-(7.7) around the pressure $p_{init}$ and $w_{init}$[5]. Furthermore, we assume isothermal conditions and therefore replace $\frac{1}{\rho}\frac{\partial \rho}{\partial t}$ with $\frac{1}{K}\frac{\partial p}{\partial t}$, where $K = \rho\frac{\partial p}{\partial \rho}$ the Bulk modulus. Equations (7.6)-(7.7) then reduce to

$$\frac{\partial w}{\partial t} + \frac{1}{\rho}\frac{\partial p}{\partial x} \;=\; 0, \tag{7.8}$$

$$\frac{1}{K}\frac{\partial p}{\partial t} + \frac{\partial w}{\partial x} \;=\; 0. \tag{7.9}$$

Lastly, we take the derivative of (7.8) with respect to $x$ and the derivative of (7.9) with respect to $t$ and combine the two, resulting in

$$\frac{\partial^2 p}{\partial x^2} = \frac{\rho}{K}\frac{\partial^2 p}{\partial t^2}, \tag{7.10}$$

$$\frac{\partial w}{\partial t} = -\frac{1}{\rho}\frac{\partial p}{\partial x}. \tag{7.11}$$

---

[5]The factor $\gamma_m$ in (7.3) is thus either defined by limitations in the actuator movement or by the linearisation condition, whichever is most restrictive.
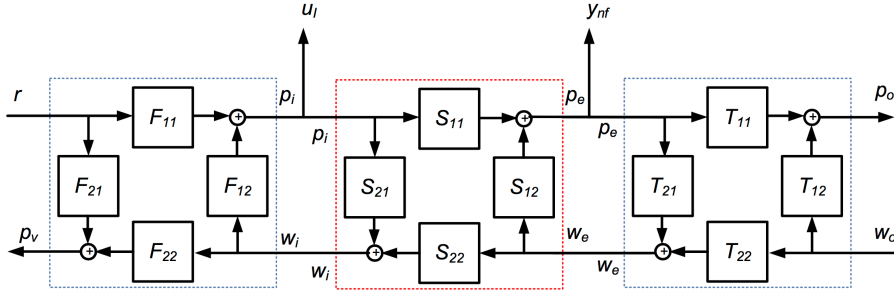
Figure 7.3: The network representation of the experimental setup. The dynamics inside the subsystems I and III are contained in respectively the left and right blue-dotted squares, whereas the dynamics in subsystem II is contained in the centre, red-dotted square.

The boundary conditions, i.e. inputs, of this subsystem are given by

$$w(x = -L_i, t) = \frac{\partial r(t)}{\partial t}, \ \ w(x = 0, t) = w_i(t), \quad (7.12)$$

where $r(t)$ is the movement of the actuator as a function of time, and $w_i(t)$ the inlet gas speed. We neglect friction effects between the wall of the inlet volume and the actuator[6]. The outputs of this subsystem are

$$p(x = -L_i, t) = p_v(t), \ \ p(x = 0, t) = p_i(t). \quad (7.13)$$

This subsystem is shown in Fig. 7.3 in the left blue-dotted square. Notice that it is connected to subsystem II through the output $p_i(t)$, being the inlet pressure, and the inlet gas speed $w_i(t)$. We now continue with the dynamics in the porous medium.

**Subsystem II: The Porous Medium**

For the second system, i.e. the porous medium, mass conservation and Darcy's law show that the pressure change in the core is governed by the diffusion equation

$$\frac{\partial p(x, t)}{\partial t} = \frac{kK}{\mu \phi} \frac{\partial^2 p(x, t)}{\partial x^2}. \quad (7.14)$$

The specific discharge, or Darcy velocity, inside the porous medium is related to pressure by

$$w(x, t) = -\frac{k}{\mu} \frac{\partial p(x, t)}{\partial x}. \quad (7.15)$$

---

[6]The signal distortion caused by friction depends on how the set-up is actually designed, and has to be tested on the actual set-up. Square wave actuator signals are generated in practice by switching abruptly between $+C_\gamma$ and $-C_\gamma$. Hence, as long as the actuator driving mechanism is strong enough, friction effects do not play a role. Sinusoidal actuator signals can, depending on the severity of the friction, be distorted by the nonlinear friction. In that case one could opt for measuring the actuator position, which can be done with high accuracy. A feedback control scheme can then be designed that ensures that the actual movement of the actuator follows the designed sinusoidal signal.

Note that this velocity is different to those in the inlet and outlet volumes (subsystems I and III). The boundary conditions, i.e. inputs, for this subsystem read

$$p(x=0,t) = p_i(t), \ w(x=L,t) = w_e(t),$$  (7.16)

in which $p_i(t)$ is the inlet pressure defined previously, and $w_e(t)$ the outlet gas speed. The outputs are defined by

$$w(x=0,t) = w_i(t), \ p(x=L,t) = p_e(t).$$  (7.17)

This subsystem is shown in Fig. 7.3 in the centre, red-dotted square. Note that the first and second subsystem are now connected. What remains is to connect subsystem II with subsystem III. We shall now derive the dynamics in the latter.

### Subsystem III: The Outlet Volume

In the third subsystem, following the same reasoning as for the first subsystem, the dynamics are determined by the conservation of mass and momentum. The pressure profile follows the wave equation and reads (c.f. (7.10))

$$\frac{\partial^2 p}{\partial x^2} = \frac{\rho}{K}\frac{\partial^2 p}{\partial t^2},$$  (7.18)

$$\frac{\partial w}{\partial t} = -\frac{1}{\rho}\frac{\partial p}{\partial x}.$$  (7.19)

The boundary conditions are however different from subsystem I and are given by

$$p(x=L,t) = p_e(t), \ w(x=L+L_e,t) = w_o(t),$$  (7.20)

in which $w_o(t)$ is an as-of-yet unspecified input for subsystem III. The outputs are defined by

$$w(x=L,t) = w_e(t), \ p(x=L+L_e,t) = p_o(t),$$  (7.21)

where $w_e(t)$ is the gas speed at the outlet and $p_o(t)$ the pressure at the boundary $x=L+L_e$.

At this point, we have defined all dynamics in the experiment set-up. The three subsystems are now connected through their boundary conditions and outputs. We proceed by introducing the scaled set-up. The scaled equations are then used to find the dynamic relationship between the actuator, inlet pressure, and outlet pressure.

## 7.2.3   Scaling

We are interested to identify the porosity and the permeability of the porous medium. As shown in Table 7.1, the values of these parameters differ by twelve orders of magnitude. It is thus very important for the sake of numerical computations to scale the dynamical equations in such a way that the to-be-identified parameters are both of $O(1)$. To this end, we first choose $k_s$ and $\phi_s$ equal to the order of magnitude of $k$ and $\phi$ (which are usually

known) and define the dimensionless parameters

$$\tilde{k} = \frac{k}{k_s}, \ \tilde{\phi} = \frac{\phi}{\phi_s}. \tag{7.22}$$

Furthermore, we also define the following dimensionless variables

$$\tilde{x} = \frac{x}{L}, \ \tilde{p}(\tilde{x},\tilde{t}) = \frac{p(x/x_s, t/t_s)}{p_s}, \ \tilde{t} = \frac{t}{t_s}, \ \tilde{w}(\tilde{x},\tilde{t}) = \frac{w(x/x_s, t/t_s)}{w_s}. \tag{7.23}$$

We note that the actuator signal $r(t)$ should be scaled in time and space according to the above definitions, resulting in $\tilde{r}(\tilde{t}) = \frac{r(t/t_s)}{L}$. The scaled frequency $\tilde{\omega}$ follows from the above-defined time scaling and is given by $\tilde{\omega} = \omega t_s$. Lastly, choosing

$$p_s = \frac{K}{\phi_s}, \ t_s = \frac{\phi_s \mu L^2}{k_s K}, \ w_s = \frac{k_s p_s}{\mu L}, \tag{7.24}$$

leads to equations with $O(1)$ terms when substituting (7.22)-(7.24) into the equations of subsystem I to III (7.10)-(7.18). The scaled system is thus given by

$$\frac{\partial^2 \tilde{p}(\tilde{x},\tilde{t})}{\partial \tilde{x}^2} = \frac{\rho L^2}{K} t_s^{-2} \frac{\partial^2 \tilde{p}(\tilde{x},\tilde{t})}{\partial \tilde{t}^2}, \tag{7.25}$$

$$\frac{\partial \tilde{w}}{\partial \tilde{t}} = -\frac{t_s p_s}{\rho w_s L} \frac{\partial \tilde{p}}{\partial \tilde{x}}, \tag{7.26}$$

$$\frac{\partial \tilde{p}(\tilde{x},\tilde{t})}{\partial \tilde{t}} = \frac{\tilde{k}}{\tilde{\phi}} \frac{\partial^2 \tilde{p}(\tilde{x},\tilde{t})}{\partial \tilde{x}^2}, \tag{7.27}$$

$$\tilde{w}(\tilde{x},\tilde{t}) = -\tilde{k} \frac{\partial \tilde{p}(\tilde{x},\tilde{t})}{\partial \tilde{x}}, \tag{7.28}$$

with the scaled boundary conditions (7.12), (7.16), (7.20)

$$\tilde{w}(\tilde{x} = -\frac{L_i}{L}, \tilde{t}) = \frac{\partial \tilde{r}(\tilde{t})}{\partial \tilde{t}}, \ \tilde{w}(\tilde{x} = 0, \tilde{t}) = \tilde{w}_i(\tilde{t}), \tag{7.29}$$

$$\tilde{p}(\tilde{x} = 0, \tilde{t}) = \tilde{p}_i(\tilde{t}), \ \tilde{w}(\tilde{x} = 1, \tilde{t}) = \tilde{w}_e(\tilde{t}), \tag{7.30}$$

$$\tilde{p}(\tilde{x} = 1, \tilde{t}) = \tilde{p}_e(\tilde{t}), \ \tilde{w}(\tilde{x} = 1 + \frac{L_e}{L}, \tilde{t}) = \tilde{w}_o(\tilde{t}), \tag{7.31}$$

and outputs (7.13), (7.17), (7.21)

$$\tilde{p}(\tilde{x} = -\frac{L_i}{L}, \tilde{t}) = \tilde{p}_v(\tilde{t}), \ \tilde{p}(\tilde{x} = 0, \tilde{t}) = \tilde{p}_i(\tilde{t}) \tag{7.32}$$

$$\tilde{w}(\tilde{x} = 0, \tilde{t}) = \tilde{w}_i(\tilde{t}), \ \tilde{p}(\tilde{x} = 1, \tilde{t}) = \tilde{p}_e(\tilde{t}), \tag{7.33}$$

$$\tilde{w}(\tilde{x} = 1, \tilde{t}) = \tilde{w}_e(\tilde{t}), \ \tilde{p}(\tilde{x} = 1 + \frac{L_e}{L}, \tilde{t}) = \tilde{p}_o(\tilde{t}). \tag{7.34}$$

From now on we shall work with the scaled system and omit the tildes for the sake of simplicity. The unscaled results can easily be deduced using the scaling defined in this section. We proceed with the determination of the dynamic relationships between the actuator and the inlet and outlet pressures.

### 7.2.4   System of Coupled Equations in the Laplace Domain

For the estimation of the physical parameters we require explicit expressions of the transfer functions between the actuator and the outlet pressure, as well as the inlet to outlet pressure. For this purpose, we transform the equations for each system into the Laplace domain.

#### Subsystem I

The dynamics in subsystem I are defined by (7.10)-(7.13). Their scaled equivalents are given by (7.25)-(7.26), (7.29), and (7.32). We take the Laplace transform of (7.25) and assume zero initial conditions. The resulting equation reads

$$\frac{\partial^2 P(x,s)}{\partial x^2} = \frac{\rho L^2 s^2}{K t_s^2} P(x,s), \tag{7.35}$$

where $P(x,s)$ is the Laplace transform of the scaled pressure profile $p(x,t)$. This equation has the general solution

$$P(x,s) = m_1 \sinh\left(x\frac{L}{t_s}\sqrt{\frac{\rho}{K}}s\right) + m_2 \cosh\left(x\frac{L}{t_s}\sqrt{\frac{\rho}{K}}s\right), \tag{7.36}$$

in which $m_1$ and $m_2$ are two unknown scalars. We solve the coefficients $m_1, m_2$ with the equation for the gas speed (7.26), which we transform into the Laplace domain (assuming zero initial conditions), giving

$$W(x,s) = -\frac{t_s p_s}{\rho w_s L s}\frac{\partial P(x,s)}{\partial x}. \tag{7.37}$$

Substitution of (7.36) into (7.37) then yields

$$W(x,s) = -\frac{p_s}{w_s\sqrt{\rho K}}\left\{m_1 \cosh\left(x\frac{L}{t_s}\sqrt{\frac{\rho}{K}}s\right) + m_2 \sinh\left(x\frac{L}{t_s}\sqrt{\frac{\rho}{K}}s\right)\right\}. \tag{7.38}$$

Using the Laplace transformed boundary conditions (7.29) then leads to

$$m_1 = -\frac{w_s}{p_s}\sqrt{\rho K}W_i(s),$$

$$m_2 = -\frac{w_s}{p_s}\sqrt{\rho K}\left\{\sinh^{-1}\left(-s\frac{L_i}{t_s}\sqrt{\frac{\rho}{K}}\right)sR(s) - \coth\left(-s\frac{L_i}{t_s}\sqrt{\frac{\rho}{K}}\right)W_i(s)\right\}.$$

Substitution of these expressions into (7.36) and using the Laplace transformed outputs (7.32) allows us to determine the dynamical relationship between $R(s)$, $W_e(s)$ and $P_v(s)$, $P_i(s)$:

$$\begin{bmatrix} P_i(s) \\ P_v(s) \end{bmatrix} = \frac{w_s}{p_s}\sqrt{\rho K}\begin{bmatrix} F_{11}(s) & F_{12}(s) \\ F_{21}(s) & F_{22}(s) \end{bmatrix}\begin{bmatrix} R(s) \\ W_i(s) \end{bmatrix},$$

in which

$$
\begin{bmatrix} F_{11}(s) & F_{12}(s) \\ F_{21}(s) & F_{22}(s) \end{bmatrix} = \begin{bmatrix} -s\sinh^{-1}(-s\frac{L_i}{t_s}\sqrt{\frac{\rho}{K}}) & \coth(-s\frac{L_i}{t_s}\sqrt{\frac{\rho}{K}}) \\ -s\coth(-s\frac{L_i}{t_s}\sqrt{\frac{\rho}{K}}) & \sinh^{-1}(-s\frac{L_i}{t_s}\sqrt{\frac{\rho}{K}}) \end{bmatrix}.
\tag{7.39}
$$

The argument in each of the above hyperbolic functions contains the fraction $\frac{L_i\sqrt{\rho}}{t_s\sqrt{K}} = \frac{k_s L_i\sqrt{\rho K}}{L^2\mu\phi_s}$. Since this expression evaluates to a small number for typical values of each parameter (order $10^{-7}$ for the parameters used in this chapter), we approximate these hyperbolic functions with $\coth(z) \approx \frac{1}{z}$ and $\sinh(z) \approx z$ where $z \ll 1$. The transfer functions then reduce to the expressions

$$
\begin{bmatrix} F_{11}(s) & F_{12}(s) \\ F_{21}(s) & F_{22}(s) \end{bmatrix} = \frac{\phi_s L}{L_i s} \begin{bmatrix} s & -1 \\ s & -1 \end{bmatrix} = \frac{f_i}{s} \begin{bmatrix} s & -1 \\ s & -1 \end{bmatrix},
\tag{7.40}
$$

where $f_i$ is defined as

$$
f_i = \frac{\phi_s A L}{V_i} = \frac{\phi_s L}{L_i}.
\tag{7.41}
$$

**Subsystem II**

We recall that the dynamics in subsystem II are defined by the equations (7.14)-(7.17). Their scaled equivalents are given by (7.27)-(7.28), (7.30), and (7.33). We apply the Laplace transform to the diffusion equation (7.27), again assuming zero initial conditions, and write it as

$$
\left( \frac{\partial^2}{\partial x^2} - \frac{s}{k/\phi} \right) P(x,s) = 0,
$$

where $P(x,s)$ is the Laplace transformed scaled pressure. The general solution to this equation reads

$$
P(x,s) = c_1 e^{x\sqrt{\frac{s\phi}{k}}} + c_2 e^{-x\sqrt{\frac{s\phi}{k}}},
\tag{7.42}
$$

where $c_1$ and $c_2$ are as-of-yet unknown scalar coefficients. Taking the Laplace transform of (7.28) and using the previous equation shows that the speed of gas in the porous medium is given by

$$
W(x,s) = -kc_1\sqrt{\frac{s\phi}{k}}e^{x\sqrt{\frac{s\phi}{k}}} + kc_2\sqrt{\frac{s\phi}{k}}e^{-x\sqrt{\frac{s\phi}{k}}}.
\tag{7.43}
$$

The unknown coefficients $c_1$ and $c_2$ are then determined with the Laplace transformed boundary conditions (7.30). We then substitute these into (7.42) and use (7.33) to find the dynamical relationships between $P_e(s)$, $W_i(s)$ and $P_i(s)$, $W_e(s)$:

$$
\begin{bmatrix} P_e(s) \\ W_i(s) \end{bmatrix} = \begin{bmatrix} S_{11}(s) & S_{12}(s) \\ S_{21}(s) & S_{22}(s) \end{bmatrix} \begin{bmatrix} P_i(s) \\ W_e(s) \end{bmatrix},
\tag{7.44}
$$

in which

$$
\begin{bmatrix} S_{11}(s) & S_{12}(s) \\ S_{21}(s) & S_{22}(s) \end{bmatrix} = \begin{bmatrix} \cosh^{-1}\left(\sqrt{s\phi/k}\right) & \frac{-1}{\sqrt{s\phi k}}\tanh\left(\sqrt{s\phi/k}\right) \\ \sqrt{s\phi k}\tanh\left(\sqrt{s\phi/k}\right) & \cosh^{-1}\left(\sqrt{s\phi/k}\right) \end{bmatrix}. \tag{7.45}
$$

Note that the argument in all hyperbolic functions are of $O(1)$ or higher. We therefore do not approximate these functions as we did for subsystem I.

## Subsystem III

The dynamics in subsystem III are defined by the equations (7.18)-(7.21). Their scaled equivalents are given by (7.25)-(7.26), (7.31), and (7.34). We follow the exact same derivation as for subsystem I, albeit with the boundary conditions and outputs in (7.31) and (7.34). The result for subsystem III is that

$$
\begin{bmatrix} P_o(s) \\ W_e(s) \end{bmatrix} = \begin{bmatrix} T_{11}(s) & T_{12}(s) \\ T_{21}(s) & T_{22}(s) \end{bmatrix} \begin{bmatrix} P_e(s) \\ W_o(s) \end{bmatrix} \tag{7.46}
$$

in which

$$
\begin{bmatrix} T_{11}(s) & T_{12}(s) \\ T_{21}(s) & T_{22}(s) \end{bmatrix} = \begin{bmatrix} \cosh^{-1}\left(\frac{L_e}{t_s}\sqrt{\frac{\rho}{K}}s\right) & -\frac{w_s}{p_s}\sqrt{\rho K}\tanh\left(\frac{L_e}{t_s}\sqrt{\frac{\rho}{K}}s\right) \\ \frac{p_s}{w_s\sqrt{\rho K}}\tanh\left(\frac{L_e}{t_s}\sqrt{\frac{\rho}{K}}s\right) & \cosh^{-1}\left(\frac{L_e}{t_s}\sqrt{\frac{\rho}{K}}s\right) \end{bmatrix}.
$$

Following the derivation for subsystem I we remark that the arguments in all the hyperbolic functions are small. We approximate these functions around zero and find that we may write

$$
\begin{bmatrix} T_{11}(s) & T_{12}(s) \\ T_{21}(s) & T_{22}(s) \end{bmatrix} = \begin{bmatrix} 1 & -\frac{k_s^2 K\rho}{\mu^2 L^2}\frac{s}{f_e} \\ \frac{s}{f_e} & 1 \end{bmatrix},
$$

where $f_e$ is defined as

$$
f_e = \frac{\phi_s A L}{V_e} = \frac{\phi_s L}{L_e}. \tag{7.47}
$$

## The Experiment Set-Up System

At this point we have coupled the different inputs and outputs of the total system. In the Dynamic Darcy Cell experiment set-up, however, we do not have gas entering the system at $x = 1 + \frac{L_e}{L}$ and thus $w_o(t) = 0$. Consequently, we can remove the transfer functions $T_{12}(s)$ and $T_{22}(s)$ from the network, see Fig. 7.3. In addition, the transfer functions $F_{21}(s)$, $F_{22}(s)$ may be removed as they do not influence $p_i(t)$, $r(t)$, nor $p_e(t)$. Lastly, $T_{11}(s)$ can be discarded as it does not influence $p_e(t)$. The reduced network is depicted in Fig. 7.4. From this figure, we see the output signal $y_{nf}(t) = p_e(t)$ that we shall use to estimate permeability and porosity. For the two experiment types we consider (see Introduction), observe that $r(t) = u_{II}(t)$ is the input in the Indirect Method, and $u_I(t) = p_i(t)$ the input in the Direct Method.

For the least-squares procedure that we shall introduce in Section 7.3 we require the transfer function between $r(t)$ and $y_{nf}(t) = p_e(t)$ and the transfer function between $p_i(t)$
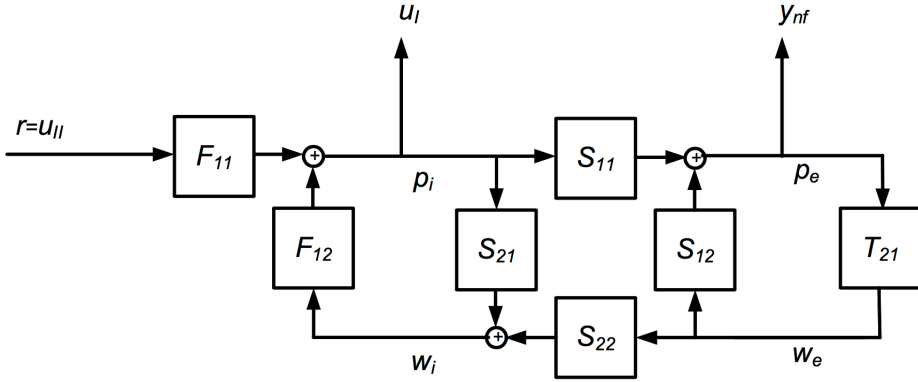
Figure 7.4: The network representation of the experimental setup after simplification.

and $y_{nf}(t) = p_e(t)$. We shall derive these transfer functions now. We start with the relationship between $P_i$ and $P_e$, which we shall use to find the time-domain connection between $p_e(t)$ and $p_i(t)$. We find from Fig. 7.4 that

$$P_e(s) = \frac{S_{11}(s)}{1 - S_{12}(s)T_{21}(s)} P_i(s). \tag{7.48}$$

This equation shows that the outlet pressure depends on both the inlet pressure $P_i$ as well as itself through $W_e$. This feedback mechanism is clearly seen in Fig. 7.4. Next, the relationship between $R(s)$ and $P_i(s)$ can be deduced from (7.40), (7.44)-(7.45), and (7.46) or Fig. 7.4 and reads

$$P_i(s) = F_{11}(s) \left[ 1 - F_{12}(s) \left( S_{21}(s) + S_{22}(s)T_{21}(s)\frac{S_{11}(s)}{1 - S_{12}(s)T_{21}(s)} \right) \right]^{-1} R(s). \tag{7.49}$$

Equations (7.48) and (7.49) reveal the transfer functions between the Laplace-transformed measurement variables $r(t)$, $p_i(t)$, and $p_e(t)$. In the next section we show how to calculate the time-domain response of $p_i(t)$ and $p_e(t)$ as a function of the actuator signal $r(t)$ using these transfer functions. These responses are a function of the physical parameters that we seek to estimate, and will be used as estimation functions in Section 7.3.

## 7.2.5 Input-Output Dynamics in the Time Domain

Suppose that an input signal $u(t)$ (which in our case can either be $p_i(t)$ or $r(t)$) affects some noise-free output $y_{nf}(\boldsymbol{\theta},t)$. In the Laplace domain, their relation is

$$Y_{nf}(\boldsymbol{\theta},s) = G(s,\boldsymbol{\theta})U(s), \tag{7.50}$$

where $G(s,\boldsymbol{\theta})$ is a function of the physical parameters collected in the vector $\boldsymbol{\theta}$. This vector represents a family of physical systems, whereas $\boldsymbol{\theta} = \boldsymbol{\theta}_0$ refers to a particular physical system characterised by its parameters $\boldsymbol{\theta}_0$. We shall refer to the system with $\boldsymbol{\theta}_0$ as the data-generating system, and $\boldsymbol{\theta}_0$ contains the physical parameters we need to estimate. For the identification, we shall use discrete-time input and output data to estimate the param-

eters using a least-squares method. Consequently, as in Chapter 6, we require a function that simulates the noise-free response $y_{nf}(\boldsymbol{\theta},t)$ of the system. In this section, we derive this response for sinusoidal (7.1) and square wave (7.2) actuator signals using Method 1 of Section 6.3.

Suppose we have a closed-form expression of $G(s,\boldsymbol{\theta})$ in (7.50). The time-domain signal $y_{nf}(\boldsymbol{\theta},t)$ for an input signal of the form, assuming zero initial conditions, reads

$$u(t) = C_\gamma \sin(\omega t). \tag{7.51}$$

The corresponding noise-free output is then given by (Ljung (1999))

$$y_{nf}(\boldsymbol{\theta},t) = C_\gamma |G(i\omega,\boldsymbol{\theta})| \sin(\omega t + \alpha), \tag{7.52}$$

where $G(i\omega,\boldsymbol{\theta})$ is defined in (7.50) and $\alpha = \angle G(i\omega,\boldsymbol{\theta})$. For the square wave input signal (7.2) with amplitude $C$ and cycle frequency $\omega_c$ the output $y_{nf}(\boldsymbol{\theta},t)$ reads

$$y_{nf}(\boldsymbol{\theta},t) = \frac{4}{\pi} C_\gamma \sum_{m=1}^{\infty} \frac{|G(i[2m-1]\omega_c,\boldsymbol{\theta})|}{2m-1} \sin([2m-1]\omega_c t + \alpha_m), \tag{7.53}$$

where $\alpha_m = \angle G(i[2m-1]\omega_c,\boldsymbol{\theta})$.

At this point a general expression of a linear system's response for sinusoidal and square wave input signals is defined. What remains is to find a closed-form expression for the transfer function $G(s,\boldsymbol{\theta})$ that connects the actuator signal $r(t)$ with the inlet and outlet pressures $p_i(t)$ and $p_e(t)$. In the next two subsections we derive this transfer function for $p_i(t)$ to $p_e(t)$ and $r(t)$ to $p_e(t)$.

### Direct Method: Inlet Pressure-Outlet Pressure Measurements

The first measurement method uses inlet and outlet pressure measurements and is called the Direct Method; see Chapter 2. This is one way to collect data in pressure oscillation experiments, see e.g. (Heller et al. (2002)). The input signal $u(t) = u_I(t) = p_i(t)$ and the output is $y_{nf}(\boldsymbol{\theta},t) = p_e(t)$, see Fig. 7.4. In the previous section we have derived the relationship between $P_i(s)$ and $Y_{nf}(s) = P_e(s)$ (c.f. (7.48)), being

$$P_e(s) = \frac{S_{11}}{1 - S_{12}T_{21}} P_i(s).$$

Substitution of $S_{11}$, $S_{12}$, and $T_{21}$ defined in (7.45) and (7.46) results in

$$P_e(s) = G_{f_e}(s,\boldsymbol{\theta})P_i(s),$$

in which

$$G_{f_e}(s,\boldsymbol{\theta}) = \frac{1}{\cosh\sqrt{\phi s/k} + f_e^{-1}\sqrt{s(\phi k)^{-1}}\sinh\sqrt{\phi s/k}}. \tag{7.54}$$

Note that $\boldsymbol{\theta} = (k,\phi)^T$ and that $G_{f_e}$ also depends on the degree of freedom $f_e$. We have now obtained the closed-form expression of the transfer function between $p_i(t)$ and $p_e(t)$. Hence, we can easily calculate the output response in the time domain using (7.52). We remark that the dynamics between $p_i(t)$ and $p_e(t)$ have also been derived in (Heller et al.
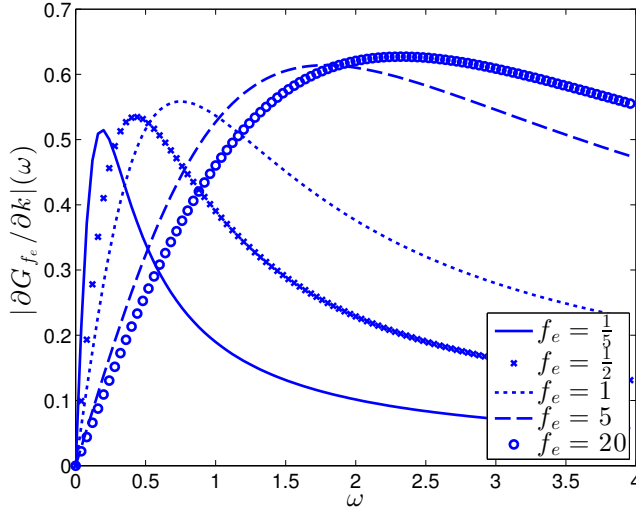
Figure 7.5: Absolute value of the derivative of the transfer function (7.54) with respect to permeability as a function of the scaled frequency $\omega$, see (7.55). Observe that for increasing values of $f_e$, the maximum of the curve shifts to higher frequencies and higher values. A small (large) $f_e$ value means that the outlet volume is large (small).

(2002)), but that in that paper the concept of transfer function has not been used; see Appendix 7.C for a discussion.

For future reference we also calculate the gradient of (7.54) with respect to $\boldsymbol{\theta} = (k, \phi)^T$:

$$\frac{\partial G_{f_e}(i\omega, \boldsymbol{\theta})}{\partial k} = \frac{f_e \left\{ i\phi\omega \cosh\left(\sqrt{\frac{i\omega\phi}{k}}\right) + k\left[f_e\phi + 1\right]\sqrt{\frac{i\omega\phi}{k}}\sinh\left(\sqrt{\frac{i\omega\phi}{k}}\right)\right\}}{2k^2\phi\left\{f_e\cosh\left(\sqrt{\frac{i\omega\phi}{k}}\right) + \sqrt{i\omega(k\phi)^{-1}}\sinh\left(\sqrt{\frac{i\omega\phi}{k}}\right)\right\}^2}, \tag{7.55}$$

$$\frac{\partial G_{f_e}(i\omega, \boldsymbol{\theta})}{\partial \phi} = \tag{7.56}$$

$$-\frac{f_e\left\{i\omega/k\cosh\left(\sqrt{\frac{i\omega\phi}{k}}\right) + \left[f_e\sqrt{\frac{i\omega\phi}{k}} - \sqrt{i\omega(k\phi)^{-1}}\right]\sinh\left(\sqrt{\frac{i\omega\phi}{k}}\right)\right\}}{2\phi\left\{f_e\cosh\left(\sqrt{\frac{i\omega\phi}{k}}\right) + \sqrt{i\omega(\phi k)^{-1}}\sinh\left(\sqrt{\frac{i\omega\phi}{k}}\right)\right\}^2}.$$

We shall use these expressions in Section 7.4 to find the optimal input signals. The absolute values of the derivatives are shown in Figs. 7.5 and 7.6 as a function of $\omega$ for several values of $f_e$.

### Indirect Method: Actuator-to-Outlet Pressure Measurements

Another possible method uses the actuator and outlet pressure signal for parameter estimation and is equivalent to the Indirect Method introduced in Chapter 2. These signals have so far not been considered in pressure oscillation literature, but we will see in the remainder of this chapter that this configuration will be beneficial for a series of reasons. In
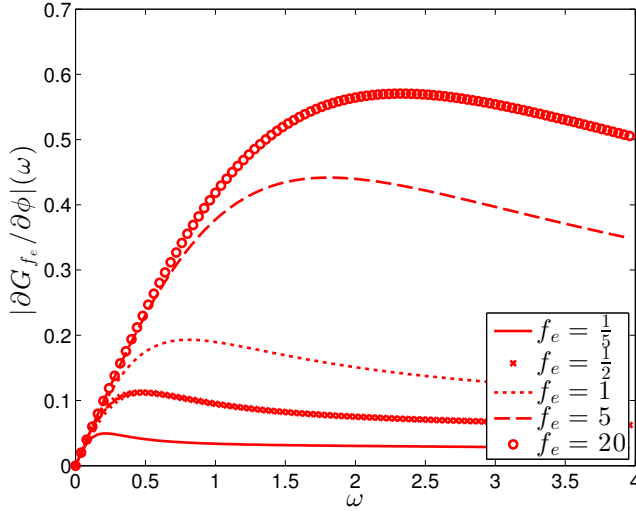
Figure 7.6: Absolute value of the derivative of the transfer function (7.54) with respect to porosity as a function of the scaled frequency $\omega$, see (7.56). For a given ratio $f_e$, the absolute value of $\partial G_{f_e}(i\omega,\boldsymbol{\theta})/\partial\phi$ is smaller at almost all frequencies than the absolute value of $\partial G_{f_e}(i\omega,\boldsymbol{\theta})/\partial k$, see Figure 7.5.

this configuration, the input $u(t) = u_{II}(t) = r(t)$ and the output $y_{nf}(\boldsymbol{\theta},t) = p_e(t)$, see Fig. 7.4. The relationship between $r(t)$ and $p_e(t)$ in the Laplace domain is found by combining (7.48), (7.49) and using (7.54), i.e.,

$$P_e(s) = \left[1 - F_{12}\left(S_{21} + S_{22}T_{21}G_{f_e}(s,\boldsymbol{\theta})\right)\right]^{-1} F_{11}(s)G_{f_e}(s,\boldsymbol{\theta})R(s)$$

Substitution of $F_{11}$, $F_{12}$ (7.40), $S_{11},\ldots,S_{22}$ (7.45), and $T_{21}$ (7.46), into the previous expression results in

$$P_e(s) = L_{f_i,f_e}(s,\boldsymbol{\theta})G_{f_e}(s,\boldsymbol{\theta})R(s),$$

in which

$$L_{f_i,f_e}(s,\boldsymbol{\theta}) = \left[\frac{1}{f_i} + \frac{1}{s}\left(k\sqrt{\frac{s\phi}{k}}\tanh\sqrt{\frac{s\phi}{k}} + \frac{sG_{f_e}(s,\boldsymbol{\theta})}{f_e\cosh\sqrt{\frac{s\phi}{k}}}\right)\right]^{-1}. \qquad (7.57)$$

This is an interesting result. It shows that the relationship between $R(s)$ and $P_e(s)$ is equal to the relationship between $P_i(s)$ and $P_e(s)$ multiplied by a complex filter $L_{f_i,f_e}(s,\boldsymbol{\theta})$. Thus, we have that $P_i(s) = L_{f_i,f_e}(s)R(s)$ and $P_e(s) = G_{f_e}(s)P_i(s)$. The input-output connection between $R(s)$ and $P_e(s)$ is thus $P_e(s) = L_{f_i,f_e}(s,\boldsymbol{\theta})G_{f_e}(s,\boldsymbol{\theta})R(s) = G_{f_i,f_e}(s,\boldsymbol{\theta})R(s)$, where

$$G_{f_i,f_e}(s,\boldsymbol{\theta}) = \left[\frac{1}{f_i} + \frac{1}{s}\left(k\sqrt{\frac{s\phi}{k}}\tanh\sqrt{\frac{s\phi}{k}} + \frac{sG_{f_e}(s,\boldsymbol{\theta})}{f_e\cosh\sqrt{\frac{s\phi}{k}}}\right)\right]^{-1} G_{f_e}(s,\boldsymbol{\theta}). \qquad (7.58)$$
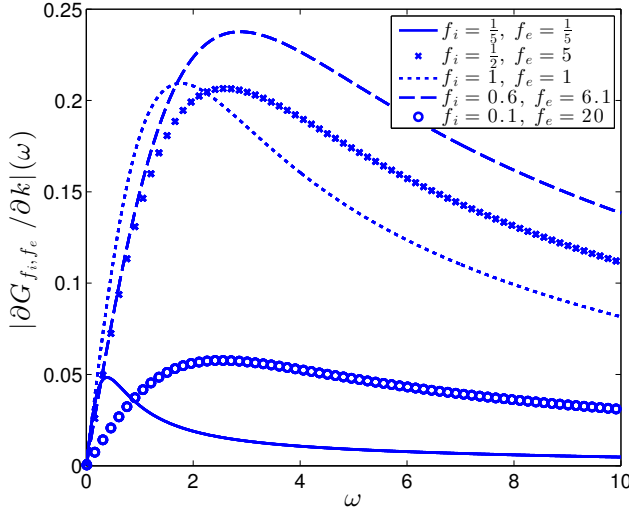
Figure 7.7: Absolute value of the derivative of the transfer function (7.58) with respect to permeability as a function of the scaled frequency $\omega$, see (7.59). Observe that for increasing values of $f_i$ and $f_e$, the maximum of the curve increases and shifts to higher frequencies. A small (large) $f_e$ value means that the outlet volume is large (small). A small (large) $f_i$ value means that the inlet volume is large (small).

For future reference, we also calculate the derivatives of (7.58) with respect to $k$ and $\phi$:

$$\frac{\partial G_{f_i,f_e}(i\omega,\boldsymbol{\theta})}{\partial k} = \tag{7.59}$$

$$\frac{k\phi G_{f_e}(i\omega,\boldsymbol{\theta})\left[\sqrt{\frac{i\omega\phi}{k}}\,\text{sech}^2\sqrt{\frac{i\omega\phi}{k}} - \tanh\sqrt{\frac{i\omega\phi}{k}}\right] - if_e^{-1}\phi\omega G_{f_e}^2(i\omega,\boldsymbol{\theta})}{}$$

$$\frac{\times\,\text{sech}\sqrt{\frac{i\omega\phi}{k}}\tanh\sqrt{\frac{i\omega\phi}{k}} + 2f_i^{-1}k^2\frac{\partial G_{f_e}(i\omega,\boldsymbol{\theta})}{\partial k}\left[\sqrt{\frac{i\omega\phi}{k}} + f_i\phi\tanh\sqrt{\frac{i\omega\phi}{k}}\right]}{2k^2\sqrt{\frac{i\omega\phi}{k}}\left(f_i^{-1} + f_e^{-1}G_{f_e}(i\omega,\boldsymbol{\theta})\,\text{sech}\sqrt{\frac{i\omega\phi}{k}} + \phi\sqrt{\frac{k}{i\omega\phi}}\tanh\sqrt{\frac{i\omega\phi}{k}}\right)^2},$$

$$\frac{\partial G_{f_i,f_e}(i\omega,\boldsymbol{\theta})}{\partial\phi} = \tag{7.60}$$

$$i\phi\omega\left(\sqrt{k}G_{f_e}(i\omega,\boldsymbol{\theta})\,\text{sech}^2\sqrt{\frac{i\omega\phi}{k}} - 2f_i^{-1}\sqrt{k}\frac{\partial G_{f_e}(i\omega,\boldsymbol{\theta})}{\partial\phi} + \frac{\tanh\sqrt{\frac{i\omega\phi}{k}}}{\sqrt{i\omega\phi}}\right.$$

$$\left.\frac{\times\left[kG_{f_e}(i\omega,\boldsymbol{\theta}) - i\omega f_e^{-1}G_{f_e}^2(i\omega,\boldsymbol{\theta})\,\text{sech}\sqrt{\frac{i\omega\phi}{k}} - 2k\phi\frac{\partial G_{f_e}(i\omega,\boldsymbol{\theta})}{\partial\phi}\right]\right)}{2k^{3/2}\left(f_e^{-1}\sqrt{\frac{i\omega\phi}{k}}G_{f_e}(i\omega,\boldsymbol{\theta})\,\text{sech}\sqrt{\frac{i\omega\phi}{k}} + f_i^{-1}\left[\sqrt{\frac{i\omega\phi}{k}} + f_i\phi\tanh\sqrt{\frac{i\omega\phi}{k}}\right]\right)^2}.$$

In these expressions, the transfer function $G_{f_e}$ and its derivatives are defined in (7.54)-(7.56). The absolute values of the above derivatives are shown in Figs. 7.7 and 7.8 as a function of $\omega$ for several values of $f_e$ and $f_i$.
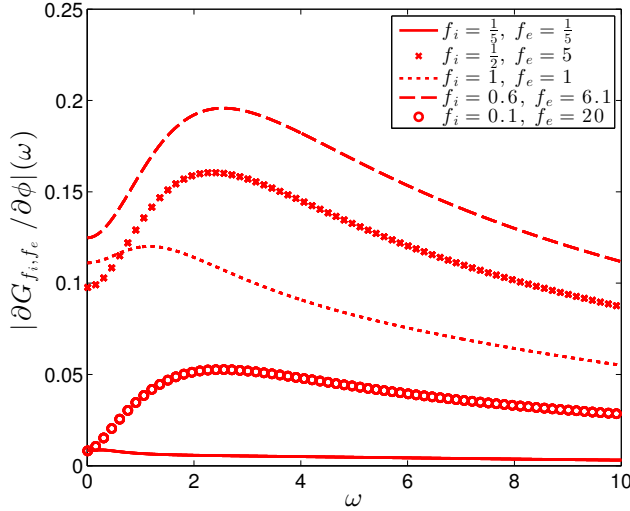
Figure 7.8: Absolute value of the derivative of the transfer function (7.58) with respect to porosity as a function of the scaled frequency $\omega$, see (7.60).

## 7.3   Estimation Procedure

In this section we introduce the estimation procedure. Our goal is to estimate the physical parameters $k$ and $\phi$ of the coupled system defined in Section 7.2.2 for the Direct and Indirect Method.

We first rewrite the expression of the actuator amplitude $C_\gamma$ (c.f. (7.3)). Since $C_\gamma$ and the ratio $f_i$ (7.41) are related to the inlet length $L_i$, we write the actuator amplitude as a function of $f_i$, i.e.

$$C_\gamma(f_i) = \gamma \frac{L_i}{L} = \gamma \frac{\phi_s}{f_i}, \tag{7.61}$$

where we still have that $0 < \gamma \leq \gamma_m$. It is already mentioned that $\gamma_m \leq 1$ due to the movement limitations of the actuator. However, it is now also clear that $\gamma_m$ can not be chosen large as otherwise the inlet volume is no longer approximately constant due to the actuator movement, and hence our above derivations no longer hold[7]. The value $\gamma_m \leq 1$ should be determined by the experimenter.

We continue with determining the data collection procedure and then define the least-squares method.

### Indirect Method

Let us for simplicity first explain the identification of the parameters for the Indirect Method. For the Indirect Method the input signal for the identification is a discrete-time form $u_D[n]$ of the user-chosen actuator signal $r(t)$ and the output signal is a discrete-time form $y_D[n]$ of the outlet pressure $p_e(t)$. The identification procedure can be performed following the same steps as in Section 6.3 (Method 1). In the case of the square wave

---

[7]It is important to use the above definition of the actuator amplitude as otherwise unphysical (wrong) results are obtained when using optimal experiment design.

excitation signal (7.2), the discrete-time input data $u_D[n]$ obtained after the anti-aliasing filter and the sampling at rate $1/T_s$ is given by:

$$u_D[n] = \frac{4}{\pi} C_\gamma(f_i) \sum_{m=1}^{M(T_s)} \frac{\sin([2m-1]\omega_c n T_s)}{2m-1}, \; n = 1, \ldots, N, \tag{7.62}$$

where we recall that $\omega_c$ is the cycle frequency of the square wave (7.2). Furthermore, note that the sum no longer extends to infinity but to the finite integer $M(T_s) = \left\lfloor \frac{1}{2} \left( \frac{\pi}{\omega_c T_s} + 1 \right) \right\rfloor$: it determines the highest mode that can be observed in the discrete-time data. Here, $\lfloor \cdot \rfloor$ represents the *floor* function. This integer can be easily deduced from the radial Nyquist rate $\frac{\pi}{T_s}$.

We suppose as in Section 6.3 that the corresponding discrete-time output data $y_D[n]$ is corrupted with white noise of variance $\sigma_e^2$. These data are thus given by (6.8) in which $y_{sim}[n; \boldsymbol{\theta}]$ is given by:

$$y_{sim}[n; \boldsymbol{\theta}] = \frac{4}{\pi} C_\gamma(f_i) \sum_{m=1}^{M(T_s)} \frac{|G_{f_i, f_e}(i[2m-1]\omega_c, \boldsymbol{\theta})|}{2m-1} \sin([2m-1]\omega_c n T_s + \alpha_m), \tag{7.63}$$

with $G_{f_i, f_e}$ the transfer function defined in (7.58), and $\alpha_m = \angle |G_{f_i, f_e}(i[2m-1]\omega_c, \boldsymbol{\theta})|$. Based on $N$ input-output data, the estimate of the parameters can be deduced using the prediction error criterion (6.9):

$$\hat{\boldsymbol{\theta}}_N = \arg \min_N \frac{1}{N} \sum_{n=1}^{N} (y_D[n] - y_{sim}[n; \boldsymbol{\theta}])^2, \tag{7.64}$$

where $y_{sim}[n; \boldsymbol{\theta}]$ is defined in (7.63). Note that in the remaining sections, the number of data $N$ will be a decision variable of the optimal experiment design problem. Note also that the case of a sinusoidal excitation signal (7.1) can be similarly treated.

**Remark 7.1** *The scaling introduced in the previous section should also be applied to the measured data set $Z_N$. This is explained in Section 6.3.2.*

### Direct Method

In the Direct Method we will also apply a square wave or sinusoidal excitation signal $r(t)$ to the system via the actuator. However, we will not use this signal as input for the identification, but we will use the measured inlet pressure $p_i(t)$ instead. The output signal remains to be the outlet pressure and is measured in the same way as in the Indirect Method, yielding $\{y_D[n]\}_{n=1}^N$. This method is also followed by Heller et al. (2002). The input signal is transformed into a discrete-time signal $u_D[n]$ using the same measurement mechanism (anti-aliasing filter and sampling with $T_s$ time steps). Since the signal $p_i(t)$ is measured (and not directly applied as $r(t)$), we are not able to retrieve precisely the inlet pressure (the measurements are indeed corrupted by noise). The signal entering the system is thus not known exactly, and consequently, we are facing an Errors-In-Variables (EIV) identification problem that may lead to serious problems in practice (Söderström (2007); Söderström et al. (2013)). As shown by Mansoori et al. (2015) on another problem, a way to deal with this EIV problem is to apply a two-stage strategy (Van den Hof and

Schrama (1993)). First, identify a model $\hat{L}$ of the relation $L_{f_i,f_e}$ (c.f. 7.57) between the actuator signal and the noise-corrupted measurements of $p_i(t)$. Second, the actuator signal $r(t)$ is filtered by that model $\hat{L}$ to lead to new input data. These new input data converge asymptotically to the noise-free inlet pressure if a good model structure is chosen for the identification. While this method alleviates the EIV issue, it will nevertheless increase the variance of the estimate $\hat{\theta}_N$. For the sake of comparison between the Direct and Indirect Method, we will disregard here this increase of variance and suppose that we can obtain the noise-free discrete-time inlet pressure using this procedure. This is the same as supposing that we know precisely the filter $L(s) = L_{f_i,f_e}(s,\theta_0)$.

For a square wave signal $r(t)$, the discrete-time signal $p_i[n]$ reads

$$u_D[n] = \frac{4}{\pi}C_\gamma(f_i) \sum_{m=1}^{M(T_s)} |L_{f_i,f_e}(i[2m-1]\omega_c,\theta_0)| \times \tag{7.65}$$

$$\frac{\sin([2m-1]\omega_c n T_s + \angle L_{f_i,f_e}(i[2m-1]\omega_c,\theta_0))}{2m-1}.$$

The output signal can therefore also be written as (7.64) with $y_{sim}[n;\theta]$ now defined as

$$y_{sim}[n;\theta] = \frac{4}{\pi}C_\gamma(f_i) \sum_{m=1}^{M(T_s)} |L_{f_i,f_e}(i[2m-1]\omega_c,\theta_0)| \frac{|G_{f_e}(i[2m-1]\omega_c,\theta)|}{2m-1} \times \tag{7.66}$$

$$\sin([2m+1]\omega_c n T_s + \alpha_m),$$

where $\alpha_m = \angle G_{f_e}(i[2m-1]\omega_c,\theta) + \angle L_{f_i,f_e}(i[2m-1]\omega_c,\theta_0)$. Based on the above expressions, we can use a set of $N$ data to estimate $\hat{\theta}_N$ using (7.64), but now with the new definitions of $y_{sim}[n;\theta]$. Note that we now identify the parameter vector in the transfer function $G_{f_e}$ while the considered transfer function was $G_{f_i,f_e}$ for the Indirect Method.

**Remark 7.2** *The zero noise assumption on the inlet pressure signal is alleviated in (Heller et al. (2002)) by averaging points of the signal $p_i(t)$ over a three-sample window to reduce the measurement noise. This downsampling of data leads to information loss since high frequency dynamics is discarded, and consequently to higher parameter variances.*

## 7.4 Experiment Design using the Direct Method

### 7.4.1 Problem Statement

In the previous section we have defined the identification experiment and the identification criterion. Suppose now that our objective is, like in Chapter 6, to obtain estimates of both parameters with a variance that is smaller than a given threshold, i.e.,

$$\begin{aligned}
\text{var}(\hat{k}_N) &= e_1^T P_{N,\theta} e_1 \leq c_k, \\
\text{var}(\hat{\phi}_N) &= e_2^T P_{N,\theta} e_2 \leq c_\phi,
\end{aligned}$$

where the covariance matrix will be defined below. We would like to optimise the frequency content and the amplitude of the excitation signal $r(t)$ as well as the DOF $f_i$ and $f_e$ in such a way that the above constraints are fulfilled with the shortest possible identification length $N$.

In this section we address this problem for the Direct Method. For the sake of brevity, we only derive the solution for the square wave actuator signal (7.2). The case of a sinusoidal excitation signal (7.1) can be treated in a similar way. Furthermore, we recall that, even though the excitation signal $r(t)$ is induced by the actuator, the signals that are used for the identification are the reconstructed inlet pressure $p_i(t)$ and the measured outlet pressure $p_e(t)$. The transfer function that is to be identified is thus $G_{f_e}(s, \boldsymbol{\theta}_0)$.

The spectrum of the sampled inlet pressure signal with amplitude $C_\gamma(f_i)$ and cycle frequency $\omega_c$ is given by

$$\Phi_{u_D}(\omega) = \frac{16}{\pi^2} \frac{\pi C_\gamma^2(f_i)}{2T_s} \sum_{m=1}^{M(T_s)} \frac{|L_{f_i,f_e}(i[2m-1]\omega_c, \boldsymbol{\theta}_0)|^2}{(2m-1)^2} \sum_{l=\{-1,1\}} \delta(\omega - l[2m-1]\omega_c). \tag{7.67}$$

Since the filter $L_{f_i,f_e}(s, \boldsymbol{\theta}_0)$ is not identified but only $G_{f_e}(s, \boldsymbol{\theta})$, $L_{f_i,f_e}$ for the Direct Method is not a function of $\boldsymbol{\theta}$ anymore, but assumed known and therefore always evaluated at $\boldsymbol{\theta} = \boldsymbol{\theta}_0$. Using the same reasoning as in Section 6.4.2, we obtain the following expression for the inverse of the covariance matrix for the Direct Method is given by

$$P_{N,\boldsymbol{\theta}}^{-1}[\omega_c, C_\gamma(f_i), f_i, f_e] = \frac{16}{\pi^2} \frac{N C_\gamma^2(f_i)}{2\sigma_e^2} \sum_{m=1}^{M(T_s)} \frac{|L_{f_i,f_e}(i[2m-1]\omega_c, \boldsymbol{\theta}_0)|^2}{(2m-1)^2} \times \tag{7.68}$$

$$\text{Re}\left\{\left[\nabla_{\boldsymbol{\theta}} G_{f_e}(i[2m-1]\omega_c, \boldsymbol{\theta})\right]_{\boldsymbol{\theta}=\boldsymbol{\theta}_0} \cdot [\text{C.C.}]\right\},$$

where C.C. stands for complex conjugate.

## 7.4.2 Optimisation Problem and Its Solution

Due to the amplitude limitation of the actuator, the optimisation problem for the Direct Method is defined mathematically as

$$\min_{\omega_c, C_\gamma(f_i), f_i, f_e} \text{Experiment length } N \tag{7.69}$$

subject to

$$\text{var}(\hat{k}_N) = e_1^T P_{N,\boldsymbol{\theta}}[\omega_c, C_\gamma(f_i), f_i, f_e] e_1 \leq c_k, \tag{7.70}$$

$$\text{var}(\hat{\phi}_N) = e_2^T P_{N,\boldsymbol{\theta}}[\omega_c, C_\gamma(f_i), f_i, f_e] e_2 \leq c_\phi \tag{7.71}$$

in which $c_k$ and $c_\phi$ are the scaled user-imposed constraints on respectively the variance of the estimates $\hat{k}_N$ and $\hat{\phi}_N$, $e_i$ the $i$-th unit vector, and $P_{N,\boldsymbol{\theta}}$ the inverse of matrix (7.68). The optimisation problem for a sinusoidal actuator signal is defined and solved in Appendix 7.A.

We wish to ensure that the variances of the estimates in $\hat{\boldsymbol{\theta}}_N = (\hat{k}_N, \hat{\phi}_N)^T$ do not exceed their respective bounds $c_k$ and $c_\phi$ using the smallest experiment length. The solution is found as follows:

1. Set the factor $\gamma = \gamma_m$ in the actuator amplitude $C_\gamma(f_i)$.

2. Define the functions

$$N_k(f_i, f_e, \omega_c) = \frac{1}{c_k} e_1^T P_{1,\theta} [\omega_c, C_{\gamma_m}(f_i), f_i, f_e] e_1, \qquad (7.72)$$

$$N_\phi(f_i, f_e, \omega_c) = \frac{1}{c_\phi} e_2^T P_{1,\theta} [\omega_c, C_{\gamma_m}(f_i), f_i, f_e] e_2, \qquad (7.73)$$

where $P_{1,\theta}$ is the inverse of (7.68) for $N = 1$, and we note that $\gamma$ has been replaced by $\gamma_m$.

3. Using the functions from the previous item, define

$$N_{min}(f_i, f_e) = \min_{\omega_c} \left\{ \max \left[ N_k(f_i, f_e, \omega_c), N_\phi(f_i, f_e, \omega_c) \right] \right\}, \qquad (7.74)$$

where $\omega_c(f_i, f_e)$ is the frequency $\omega_c$ leading to the minimum in (7.74).

4. The optimal experiment length is given by

$$N_{opt} = N_{min}(f_{i,opt}, f_{e,opt}), \text{ where } \left\{ f_{i,opt}, f_{e,opt} \right\}. \qquad (7.75)$$

The solution to the problem is given by the quartet $N_{opt}$, $f_{i,opt}$, $f_{e,opt}$, and $\omega_{c,min}(f_{i,opt}, f_{e,opt}) = \arg N_{min}(f_{i,opt}, f_{e,opt})$.

In step 1 the coefficient $\gamma$ in the actuator amplitude $C_\gamma(f_i)$ is set to $\gamma = \gamma_m$. Equation (7.68) shows that the parameter variances scale inversely proportional to $C_\gamma(f_i)$. Thus, selecting the largest possible amplitude of the actuator is a requirement to find the minimal experiment time. The actuator amplitude is now only a function of $f_i$. In step 2 the functions $N_k$ and $N_\phi$ respectively define the required experiment length to ensure that (i) $\text{var}(\hat{k}_N) = c_k$ and (ii) $\text{var}(\hat{\phi}_N) = c_\phi$. Smaller values than $N_k$ and $N_\phi$ violate the respective constraints in (7.71), whereas larger ones lead to longer experiment lengths than required. Both constraints are honoured simultaneously, i.e. satisfying situation (i) and (ii), with the function $N_{min}(f_i, f_e)$ calculated in step 3. It returns the minimal required experiment length as a function of $f_i$ and $f_e$ by finding the optimal cycle frequency. The last step then finds the optimal values of $f_i$ and $f_e$ such that the global minimum of $N_{min}(f_i, f_e)$, i.e. $N_{opt}$, is obtained.

Previously it was mentioned that in order to compute the optimal input signal the true parameter vector $\theta_0$ should be used. However, it is this parameter that we want to identify. Unfortunately, this so-called chicken-and-egg problem is unavoidable in (optimal) Experiment Design. In order to design an optimal signal, some knowledge of the system (in this case the true parameter vector) is required. Consequently, to solve the optimisation problem (7.69)-(7.71), we require a prior estimate or an initial estimate $\theta_{init}$ to evaluate the inverse of the covariance matrix (7.68). This substitution inevitably leads to suboptimal experiment lengths. However, the case study in Chapter 6 showed that much better estimates can be obtained using Experiment Design compared to an arbitrary selection of signals and frequencies, and that in many cases the variance constraints are still honoured.

### 7.4.3  Numerical Results

In this section we follow the four steps defined in the previous section to numerically find the solution (7.75) that solves (7.69)-(7.71). To this end, we grid the frequency $\omega_c \in$

$[0, \pi/T_s]$ and ratios $f_i \in [0.05, 20]$, and $f_e \in [0.05, 20]$. The grid resolutions are respectively $\Delta \omega_c = 0.05$, $\Delta f_i = \Delta f_e = 0.05$. The minimum (maximum) values in the interval of $f_i$ and $f_e$ correspond to unscaled maximum (minimum) inlet and outlet lengths of respectively $L_i = L_e = 0.2$ meters ($L_i = L_e = 0.5$ mm). Values outside these intervals are assumed to practically infeasible. The physical system is defined through the values in Table 7.1; the experiment conditions and experiment design values in Table 7.2. We wish to ensure that the standard deviation of the estimate $\hat{k}_N$ and $\hat{\phi}_N$ are respectively less than or equal to 5% of their true values $k_0$ and $\phi_0$, defined in Table 7.1, using minimal experiment time. We remark that the optimal experiment lengths found in this section depend strongly on the choice of noise variance $\sigma_e^2$ and actuator amplitude bound $\gamma_m$. Thus, comparison with results in the existing literature is only fair under the same experiment conditions.

We first discuss separate parameter estimation results, followed by joint parameter estimation results.

### Separate Parameter Estimation

Separate parameter estimation refers to the situation where either $k_0$ or $\phi_0$ is known, and respectively $\phi_0$ and $k_0$ is unknown and needs to be estimated. We thus wish to ensure that the standard deviation of the estimate $\hat{k}_N$ or $\hat{\phi}_N$ is less than or equal to 5% of their true value $k_0$ or $\phi_0$ in minimal time. Separate estimation is a special case of one in which both parameters are identified simultaneously (joint estimation), and the optimal experiment design problem in this case can thus be solved following a very similar procedure as the one presented in the previous section. This procedure is given in Appendix 7.A for the case of the sinusoidal excitation signal. The problem and solution for a square wave excitation signal can also be trivially formulated using that appendix.

The different results for separate estimation of $k$ and $\phi$ with sinusoidal or square wave excitation are summarised in Table 7.3. In order to interpret these results, it makes sense to start discussing the result corresponding to the sinusoidal excitation and in particular the function $N_{min}(f_i, f_e)$ defined for the sinusoidal signal in (7.85) in Appendix 7.A. This function is represented in Fig. 7.13 of that appendix for the case where the parameter $k$ is identified. We observe the following:

- For any value of $f_i$ the required experiment length reduces with increasing $f_e$. Inspection of $N_{min}(f_i, f_e)$ (c.f. (7.85)) shows that increasing $\partial G_{f_e}(i\omega_{ex}, \theta)/\partial \theta$ decreases $N_{min}$. From Fig. 7.5 we see that increasing $f_e$ results in a larger absolute value of the derivative. At $f_e = 20$ we find a maximum at $\omega_{ex} \approx 2.4$. Similar behaviour is shown for the case $\theta = \phi$. The optimal value is $f_{e,opt} = 20$.

- For any value of $f_e$ the required experiment length reduces with decreasing $f_i$. Let us analyse this result. Note first that $f_i$ is only present in the term $C_{\gamma_m}(f_i)|L_{f_i,f_e}(i\omega, \theta_0)|$, i.e. the amplitude of the inlet pressure $p_i(t)$. Obviously, by decreasing $f_i$, we increase the inlet volume and thus also the maximal amplitude of the actuator $C_{\gamma_m}(f_i)$ (see remark below (7.3) and (7.61)), which in turn decreases the required experiment time (c.f. (7.85)). However, the inlet amplitude attenuation due to the filter $|L_{f_i,f_e}|$ decreases with decreasing $f_i$, yet increases with frequency. It is easy to show that

$$\forall f_i, f_e : \ \max_{\omega} C_{\gamma_m}(f_i)|L_{f_i,f_e}(i\omega, \theta_0)| = \gamma_m \phi_s.$$

Thus, the maximal amplitude of the inlet pressure is equal to $\gamma_m \phi_s$ and independent

| Quantity | Scaled Value | Real Value |
|---|---|---|
| Sampling time | $\tilde{T}_s = 0.021$ | $T_s = 0.01$ s |
| Sensor noise variance | $\tilde{\sigma}_e^2 = 0.05$ | $\sigma_e^2 = 1.25 \times 10^9$ Pa$^2$ |
| Permeability variance constraint | $\tilde{c}_k = 2.5 \times 10^{-3}$ | $c_k = 2.5 \times 10^{-3} k_0^2$ m$^4$ |
| Porosity variance constraint | $\tilde{c}_\phi = 2.5 \times 10^{-3}$ | $c_\phi = 2.5 \times 10^{-3} \phi_0^2$ |
| Actuator amplitude constraint | $\gamma_m = 0.1$ | $\gamma_m = 0.1$ |

Table 7.2: The experiment is designed using the above quantities. The scaled system is defined through the choices $L = 0.05$, $k_s = k_0$, $\phi_s = \phi_0$. These scalars define the scaled system in Section 7.2.3.

of $f_i$ and $f_e$. However, for small $f_i$ this asymptotic value is reached quicker at lower frequencies than for larger $f_i$, see Fig. 7.10. It is also reached quicker for larger $f_e$. This explains why one should opt for taking $f_{i,opt} = 0.1$ for any $f_e$. It is also at low frequencies where the derivative of $G_{f_e}(i\omega, \theta)$ with respect to $k$ is large, as explained in the previous item.

- The optimal ratios are $f_{i,opt} = 0.1$ and $f_{e,opt} = 20$. The corresponding optimal experiment length $N_{opt} = 2.86 \times 10^5$ at optimal frequency $\omega_{opt} = 2.45$, see Table 7.3. The value of $f_{e,opt}$ corresponds with a choice made in literature (Heller et al. (2002)): minimising the outlet volume. The optimal values occur at the boundary of the considered intervals of $f_i$ and $f_e$. The aim in practice is thus to maximise the inlet volume and minimise the outlet volume.

- Quantitatively the same results and analysis holds for the case where $\theta = \phi$. The experiment lengths in Table 7.3 show that porosity is more difficult to estimate than permeability, as $\partial G_{f_e}/\partial \phi$ is smaller than $\partial G_{f_e}/\partial k$ for all values of $f_e$ depicted in Fig. 7.6.

- Square wave actuator signals result in shorter experiment lengths than sinusoidal ones. This reason for that is explained in Appendix 7.D.

**Joint Parameter Estimation**

We follow the procedure outlined at the start of this section, using the same experiment conditions, to analyse the joint parameter estimation experiment design solutions. The optimisation problem is given by (7.69)-(7.71). The results are also given in Table 7.3 for the case of the sinusoidal and square wave signals. The logarithm of the $N_{min}(f_i, f_e)$ (c.f. 7.74)) is shown in Fig. 7.9 as a function of $f_i$ and $f_e$. Starting once again the discussion with the sinusoidal signal, we observe the following:

- The optimal input signal for joint estimation, defined through (7.75), is found for $\omega_{opt} = \omega_{ex,min}(f_{i,opt}, f_{e,opt}) = 2.35$ at optimal ratios $f_{i,opt} = 0.1$ and $f_{e,opt} = 1.0$, see Table 7.3 and Fig. 7.9. The minimal experiment length for this combination is $N_{opt} = 4.47 \times 10^7$, and corresponds to an unscaled experiment time of about five days ($T_s = 0.01$ seconds). The experiment lengths for a square wave actuator signal are also tabulated. Note that $N_{opt}$ is smaller for the square wave signal than when using a sinusoidal actuator signal, as expected from the result in Appendix 7.D.

- For any value of $f_e$ it is clear from the figure that by lowering $f_i$ shorter experiment times are obtained. This effect has already been explained in Section 7.4.3.

| Direct Method | $k$ | | $\phi$ | | $\{k,\phi\}$ | |
|---|---|---|---|---|---|---|
| | Sine | SW | Sine | SW | Sine | SW |
| $N_{opt}$ | $2.86 \cdot 10^5$ | $1.66 \cdot 10^5$ | $3.46 \cdot 10^5$ | $2.0 \cdot 10^5$ | $4.47 \cdot 10^7$ | $2.51 \cdot 10^7$ |
| $\omega_{opt}$ | 2.45 | 2.3 | 2.45 | 2.3 | 2.35 | 2.1 |
| $f_{i,opt}$ | 0.1 | 0.1 | 0.1 | 0.1 | 0.1 | 0.1 |
| $f_{e,opt}$ | 20 | 20 | 20 | 20 | 1.0 | 1.0 |

Table 7.3: Optimal experiment lengths, scaled frequencies, and optimal ratios $f_{i,opt}$, $f_{e,opt}$ of input using the Direct Method for sinusoidal (Sine) and square wave (SW) actuator signal. Three cases are shown: estimation of only $k$ or $\phi$, and the joint estimation of the parameters $\{k,\phi\}$.
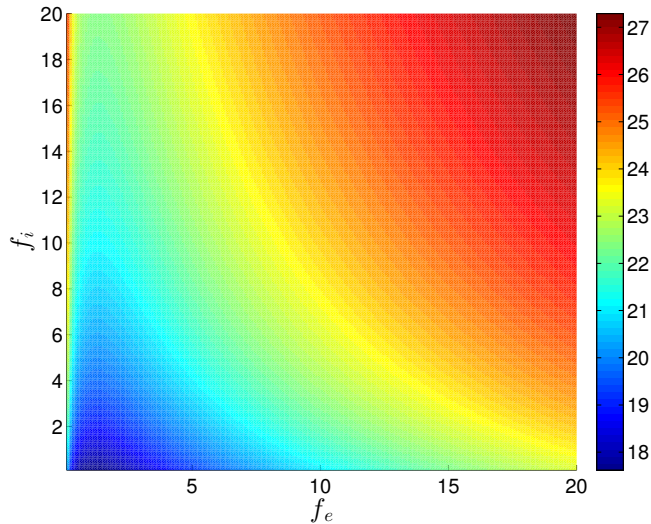


Figure 7.9: The natural logarithm of the minimal experiment length $N_{min}(f_i, f_e)$ (7.75) for the simultaneous estimation of $k$ and $\phi$ using a sinusoidal excitation signal, required to honour their respective variance constraint and the amplitude constraint $\gamma_m = 0.1$, is plotted against the ratios $f_i$ and $f_e$. In sharp contrast to single parameter estimation experiments, the optimal ratio $f_{e,opt} = 1.0$. The optimal inlet ratio $f_{i,opt} = 0.1$.
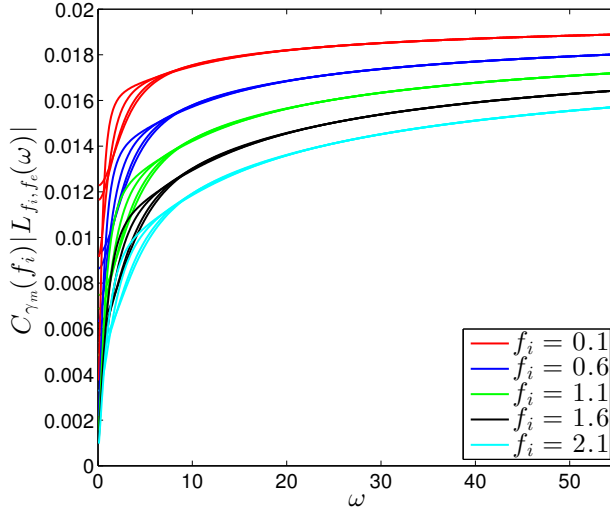
Figure 7.10: The inlet pressure amplitude $C_{\gamma_m}(f_i)|L_{f_i,f_e}(i\omega,\theta_0)|$ as a function of frequency $\omega$ for various values of $f_i$. For each ratio $f_i$ the inlet amplitude is shown for various values of $f_e$ in the same color. For the same $f_i$ value, smaller values of $f_e$ correspond to smaller amplitudes. Observe that a smaller $f_i$ leads to a higher amplitude at any given frequency, although all ratios of $f_i$ lead to the same asymptotic value of $\gamma_m\phi_s = 0.02$. Notice that $f_e$ only affects the amplitude at low frequencies and after $\omega = 7.0$ all ratios $f_e$ yield the same amplitude at their respective value of $f_i$.

- In sharp contrast to the single parameter experiments (see Table 7.3), we observe that now, instead, $f_e$ should be chosen equal to $f_e = f_{e,opt} = 1.0$ as opposed to $f_e \gg 1$. The experiment length $N$ is affected by $f_e$ through the gradient of $G_{f_e}$, see (7.68). In Figs. 7.5 and 7.6 we see that both components of this gradient increase with increasing $f_e$, which in principle should shorten $N$. This is not the result we obtain from the optimal experiment design results.

In order to understand the curiosity mentioned in the last item, i.e. why the optimal ratio is now $f_{e,opt} = 1.0$ instead of $f_e = 20$, we need to analyse the physical system further. To this end, we require the following theorem.

**Theorem 7.1** *The parameters $k$ and $\phi$ are not identifiable in the limit $f_e \to \infty$.*

**Proof:** The general condition for identifiability is given by (Ljung (1999))

$$G(i\omega,\theta_1) = G(i\omega,\theta_2)\forall\omega \Rightarrow \theta_1 = \theta_2. \tag{7.76}$$

Taking the limit $f_e \to \infty$ of the frequency response $G_{f_e}(i\omega,\theta)$ in (7.54) yields

$$\lim_{f_e\to\infty} G_{f_e}(i\omega,\theta) = \frac{1}{\cosh\sqrt{i\omega\phi/k}}. \tag{7.77}$$

Suppose that $\theta_1 = (k_1,\phi_1)^T$ and $\theta_2 = (\kappa k_1,\kappa\phi_1)^T$, where $\kappa \in \mathbb{R}$. Substitution in (7.77) then shows that $G_\infty(i\omega,\theta_1) = G_\infty(i\omega,\theta_2)$ for any frequency $\omega$, whereas $\theta_1 \neq \theta_2$. This concludes the proof. $\square$

The proof shows that in the limit of $f_e \to \infty$ the transfer function $G_{f_e}$ contains the quotient $\frac{\phi}{k}$. As a consequence, infinitely many equal quotients exist by multiplying $k$ and $\phi$ with

the same scalar $\kappa$. This problem does not exist for the estimation of only one parameter, as the other one is known. How is this effect then reflected in (7.75)?

**Theorem 7.2** *The components of the gradient $\nabla_{\boldsymbol{\theta}} G_{f_e}(i\omega, \boldsymbol{\theta})$ are linearly dependent for all frequencies in the limit $f_e \to \infty$. Consequently, the inverse of the covariance matrix $P_{N,\boldsymbol{\theta}}^{-1}$ is rank deficient for any input spectrum $\Phi_{u_D}(\omega)$.*

**Proof:** The derivative of the transfer function (7.54) with respect to the parameters $k$ and $\phi$ have been calculated previously, see (7.55) and (7.56). Dividing the numerator and denominator of each derivative by $f_e^2$ and taking the limit $f_e \to \infty$ shows that

$$\frac{\partial G_{f_e}(i\omega, \boldsymbol{\theta})}{\partial k} = -\frac{k}{\phi} \frac{\partial G_{f_e}(i\omega, \boldsymbol{\theta})}{\partial \phi}.$$

This shows that the elements in $\nabla_{\boldsymbol{\theta}} G_{f_e}(i\omega, \boldsymbol{\theta})$ are linearly dependent at all frequencies.

Consequently, for any input spectrum $\Phi_{u_D}$ the inverse of the covariance matrix for the Direct Method in this limit, i.e.

$$P_{N,\boldsymbol{\theta}}^{-1} = \frac{NT_s}{2\pi\sigma_e^2} \begin{pmatrix} k^2/\phi^2 & -k/\phi \\ -k/\phi & 1 \end{pmatrix} \int_{-\pi/T_s}^{\pi/T_s} \left| \frac{\partial G_{f_e}(i\omega, \boldsymbol{\theta})}{\partial \phi} \right|^2_{\boldsymbol{\theta}=\boldsymbol{\theta}_0} |L_{f_i,f_e}(i\omega, \boldsymbol{\theta}_0)|^2 \Phi_{u_D}(\omega) \, d\omega$$

is rank deficient for all $\omega$. Indeed, we find that $\det(P_{N,\boldsymbol{\theta}}^{-1}) = 0$. It is clear that the variances of the estimates $\hat{k}_N$ and $\hat{\phi}_N$ approach infinity when increasing $f_e$ towards the limit $f_e \to \infty$.

□

**Discussion**

Theorem 7.2 shows that when identifying the two parameters jointly, high values of $f_e$ should be avoided. We see now that there are two competing mechanisms. One the one hand, the sensitivity of the physical system with respect to the parameters increases with increasing $f_e$, which is beneficial to reduce the individual variances of the parameters (and thus shorten the required experiment time). On the other hand, joint estimation of the two parameters becomes more difficult as the derivatives become more and more similar for large $f_e$. Hence, the parameters become increasingly correlated for increasing $f_e$ for any excitation frequency (or, in fact, any input spectrum), making the covariance matrix singular in the limit $f_e \to \infty$. This effect already plays a dominant role at $f_e \approx 20$, as can be observed from Figs. 7.5 and 7.6. Consequently, a trade-off between these two mechanisms has to be made. Optimal experiment design shows that the best trade-off is reached by choosing $f_e = 1.0$ and using an optimal frequency of $\omega_{c,opt} = 2.1$. Due to this trade-off, the minimal experiment time increases to $N = 2.51 \times 10^7$ (approximately five days), which is two orders of magnitude larger than the experiment lengths obtained for separate parameter estimation.

## 7.5 Experiment Design using the Indirect Method

### 7.5.1 Problem Statement

In this section we consider experiment design for the Indirect Method. We recall that we estimate the parameters in the transfer function $G_{f_i,f_e}(s,\boldsymbol{\theta}_0) = L_{f_i,f_e}(s,\boldsymbol{\theta}_0)G_{f_e}(s,\boldsymbol{\theta}_0)$. The input in this case is the actuator signal $r(t)$ and the output is the outlet pressure $p_e(t)$, see Fig. 7.4. We use the same core sample values and scaling as in the previous section, see Tables 7.1 and 7.2. As in Section 7.4, we only derive the results for the square wave signal. The results for the sinusoidal excitation can be treated in a very similar way. The optimisation problem in the case of a single parameter estimation is delegated to Appendix 7.B.

The power spectrum of the square wave actuator signal, corresponding to the input signal (7.62), is defined by

$$\Phi_{u_D}(\omega) = \frac{16}{\pi^2} \frac{\pi C_\gamma^2(f_i)}{2T_s} \sum_{m=1}^{M(T_s)} \frac{1}{(2m-1)^2} \sum_{l=\{-1,1\}} \delta(\omega - l[2m-1]\omega_c). \tag{7.78}$$

The corresponding inverse covariance matrix reads

$$\boldsymbol{P}_{N,\boldsymbol{\theta}}^{-1}[\omega_c, C_\gamma(f_i), f_i, f_e] = \frac{16}{\pi^2} \frac{NC_\gamma^2(f_i)}{2\sigma_e^2} \times \tag{7.79}$$

$$\sum_{m=1}^{M(T_s)} \frac{1}{(2m-1)^2} \mathrm{Re}\left\{ \left[ \nabla_{\boldsymbol{\theta}} G_{f_i,f_e}(i[2m-1]\omega_c, \boldsymbol{\theta}) \right]_{\boldsymbol{\theta}=\boldsymbol{\theta}_0} \cdot [\,\mathrm{C.C.}\,] \right\},$$

where C.C. stands for complex conjugate and the transfer function $G_{f_i,f_e}$ is given by (7.58). As in the previous section, we search for the minimal identification length $N$ that nonetheless fulfils variance constraints on the estimates, and respects the actuator amplitude limitations, by finding optimal values for $\gamma$, $\omega_c$, $f_i$, and $f_e$.

### 7.5.2 Optimisation Problem and Its Solution

The optimisation problem in the Indirect Method is given by

$$\min_{\omega_c, f_i, f_e, C_\gamma(f_i)} \text{Experiment length } N \tag{7.80}$$

subject to

$$\mathrm{var}(\hat{k}_N) = \boldsymbol{e}_1^T \boldsymbol{P}_{N,\boldsymbol{\theta}}[\omega_c, C_\gamma(f_i), f_i, f_e]\boldsymbol{e}_1 \leq c_k, \tag{7.81}$$

$$\mathrm{var}(\hat{\phi}_N) = \boldsymbol{e}_2^T \boldsymbol{P}_{N,\boldsymbol{\theta}}[\omega_c, C_\gamma(f_i), f_i, f_e]\boldsymbol{e}_2 \leq c_\phi, \tag{7.82}$$

in which the inverse of the covariance matrix for two parameters is given by (7.79) for the transfer function $G_{f_i,f_e}$ (7.58). Notice that the optimisation problem is similar to (7.69)-(7.71), although we now consider the transfer function is $G_{f_i,f_e}$ and the amplitude of the input is different.

The solution is found by following the same reasoning as in Section 7.4.2. We follow the steps 1-4 in Section 7.4.2, where we instead use (7.79) for $\boldsymbol{P}_{N,\boldsymbol{\theta}}^{-1}$.

### 7.5.3 Numerical Results

Let us now investigate the experiment design solutions, where we use the same physical set-up, experiment parameters, and gridding method as defined in Section 7.4.3. For convenience we recall that we wish to ensure that the variance of the estimate $\hat{k}_N$ and $\hat{\phi}_N$ are respectively less than or equal to 5% of their true values $k_0$ and $\phi_0$, defined in Table 7.1. All parameters defining the porous medium are also mentioned in this table. Other parameters are defined in Table 7.2. We will first consider separate parameter estimation experiment design results, followed by the joint parameter results.

**Separate parameter estimation**

In Appendix 7.B the optimisation problem (7.83)-(7.84) and solution are given for the separate parameter estimation problem in case of a sinusoidal signal. The case of a square wave input signal is trivially formulated and solved with the use of (7.79).

The optimal experiment times are tabulated in Table 7.4. The function $N_{min}(f_i, f_e)$ (c.f. (7.88)) plotted against $f_i$ and $f_e$ is qualitatively similar to the Direct Method case (see Fig. 7.13) for both $\theta = k$ and $\theta = \phi$. Furthermore, we observe the following:

- For both $\theta = k$ and $\theta = \phi$ the optimal ratios are $f_{i,opt} = 0.1$ and $f_{e,opt} = 20$. Apparently, it is best practice to maximise the inlet volume and minimise the outlet volume.

- From (7.88) we find that $f_e$ influences the gradient $\nabla_\theta G_{f_i, f_e}(i\omega_{ex}, \theta)$. The larger the gradient, the smaller $N_{min}(f_i, f_e)$ for any value of $f_i$. Figures 7.7 and 7.8 show that increasing $f_e$ increases the gradient of both $k$ and $\phi$. This explains why one should opt for maximising $f_e$.

- The same figures also show that decreasing $f_i$ decreases the gradient, which increases the required experiment length. Yet, we see from Table 7.4 that $f_i$ should be minimised. The actuator amplitude $C_{\gamma_m}(f_i)$ scales inversely proportional to $f_i$, and so minimising $f_i$ increases the amplitude and reduces the required experiment length. The two effects are thus competing, but the latter one is dominant. Hence, $f_i$ should me minimised.

- The optimal excitation frequencies lie close to those values where the gradients are maximal, see Figs. 7.7 and 7.8.

**Joint parameter estimation**

The solution for the joint estimation of permeability and porosity is also presented in Table 7.4 and is discussed now. The numerical results are obtained through the same procedure as in Section 7.4, but using (7.79) to define $P_{N,\theta}$. We discuss here directly the case of the square wave signal:

- The function $N_{min}(f_i, f_e)$ attains its minimum for $f_{i,opt} = 0.6$ and $f_{e,opt} = 6.1$, giving $N_{opt} = N_{min}(0.6, 6.1) = 1.8 \times 10^6$ (5 hours) and an optimal cycle frequency of $\omega_{c,opt} = 1.0$, see Fig. 7.11.

- These optimal values differ significantly from the separate estimation results, see Table 7.4. From Figs. 7.7 and 7.8 we see that for $f_i = 0.1, f_e = 20$ the gradients of $k$

| Indirect Method | $k$ | | $\phi$ | | $\{k, \phi\}$ | |
|---|---|---|---|---|---|---|
| | Sine | SW | Sine | SW | Sine | SW |
| $N_{opt}$ | $3.00 \times 10^5$ | $1.74 \times 10^5$ | $3.6 \times 10^5$ | $2.1 \times 10^5$ | $3.3 \times 10^6$ | $1.8 \times 10^6$ |
| $\omega_{opt}$ | 2.55 | 2.4 | 2.5 | 2.4 | 1.2 | 1.0 |
| $f_{i,opt}$ | 0.1 | 0.1 | 0.1 | 0.1 | 0.6 | 0.6 |
| $f_{e,opt}$ | 20 | 20 | 20 | 20 | 6.4 | 6.1 |

Table 7.4:  Scaled optimal experiment lengths, frequencies, and ratios $f_i$, $f_e$ of input for the Indirect Method. The scaled system is defined through Table 7.1. These scalars define the scaled system in Section 7.2.3. For simultaneous estimation in case of a SW actuator signal, note that $f_{i,opt}$ and $f_{e,opt}$ translate into an inlet length of $L_i = L/3 \approx 1.7$ cm and an outlet length of $L_e = L/30 \approx 1.7$ mm, both of which are feasible in practice.
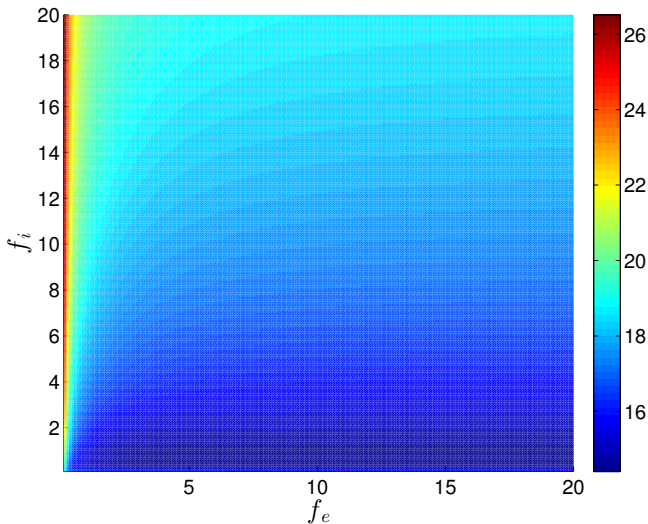


Figure 7.11: The natural logarithm of the minimal experiment length $N_{min}(f_i, f_e)$ as a function of the ratios $f_i$ and $f_e$. Note that the shortest experiment length is obtained for $f_{i,opt} = 0.6$, $f_{e,opt} = 6.1$.

and $\phi$ are very similar, resulting in high correlation between the two parameters in a joint estimation. This increases the required experiment length. However, we have here no identifiability problem as for the Direct Method.

- In Section 7.5.3 it is explained that the actuator amplitude is maximised by minimising $f_i$ and therefore for those cases $f_{i,opt} = 0.1$. By virtue of the previous item, a trade-off between parameter correlation and amplitude maximisation has to be made. We see from Figs. 7.7 and 7.8 that the gradients are large and not identical at the optimal ratios of $f_i$ and $f_e$, so the increase in $f_i$ (reducing the amplitude and thus increasing the required experiment length) is compensated by larger gradients.

**Discussion**

We now discuss some differences between the Indirect and Direct Method results.

Let us first discuss the case of separate estimation. For this specific case, observe from Tables 7.3 and 7.4 that permeability or porosity is estimated with slightly shorter experiment times when using the Direct Method. However, we point out that we have assumed the input signal $p_i(t)$ is noise free, corresponding to the assumption that we know the filter $L_{f_i,f_e}(i\omega, \theta_0)$. In reality, this is not the case, and will increase the variance of the estimates. Probably the Indirect Method is then preferred.

Let us now go to the more interesting case of joint estimation of the two parameters. Experiment Design has revealed that the optimal experiment length strongly depends on the selected input signals. Indeed, the experiment time for the Indirect Method is a factor fourteen smaller for joint estimation compared to the Direct Method. We have seen for the latter method that $f_e$ had to be reduced due to singularity issues at $f_e \gg 1$. This back-off reduces both the inlet pressure amplitude and the gradients, hereby increasing the required experiment length enormously compared to the separate estimations. For the Indirect Method, the combination $(f_i = 0.1, f_e = 20)$ corresponds to highly correlated parameters and thus a long experiment time. However, we found that for $f_{i,opt} = 0.6$ and $f_{e,opt} = 6.1$ the gradients can be increased significantly even though the actuator amplitude is less. The difference in the required experiment length for joint estimation compared to the separate estimations is therefore less drastic than in the Direct Method.

## 7.6 Simulation of the Experiment Set-Up: Estimation Results

In this last section we apply the optimal square wave input signal for the Indirect Method detailed in Section 7.5, Table 7.4, to the core sample. All parameters are defined in Tables 7.1 and 7.2. In the absence of a physical set-up, we instead generate numerical experiment data $Z_N = \{u_D[n], y_D[n]\}_{n=1}^N$ by applying our optimal input signal $u_D$ (using the values in Table 7.4 and (7.62)) and generating noise-corrupted output sequences $y_D$ using (7.63). We then follow the estimation procedure for the Indirect Method detailed in Section 7.3.

We consider the simultaneous estimation of permeability and porosity from a single experiment. We performed five thousand Monte Carlo simulations yielding the estimated pairs $\{\hat{k}_N, \hat{\phi}_N\}$. The optimal square wave signal has a cycle frequency of $\omega_{c,opt} = 1.0$, the experiment length is $N_{opt} = 1.8 \times 10^6$, and the optimal ratio $f_{i,opt} = 0.6$, $f_{e,opt} = 6.1$, see Section 7.5. A scatter plot of the estimates is shown in Fig. 7.12. The mean of all points is
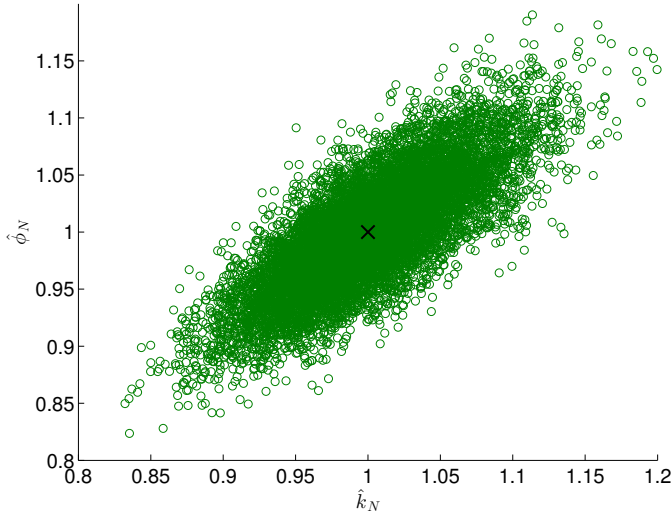
Figure 7.12: Scatter plot of the couples $\{\hat{k}_N, \hat{\phi}_N\}$ resulting from $5 \times 10^3$ experiments. The variance of permeability is $\sigma_k^2 = 9.9183 \times 10^{-5}$ and of porosity $\sigma_\phi^2 = 5.1211 \times 10^{-5}$. The black cross indicates the coordinate of the mean values of permeability and porosity, which were $< \hat{k}_N > = 1.0$ and $< \hat{\phi}_N > = 1.0$ and hence respectively equal to $k_0 = 1.0$ and $\phi_0 = 1.0$.

$(1.0, 1.0)$, corresponding to the true scaled parameter values $k_0 = \phi_0 = 1.0$. The variance of the estimates $\hat{k}_N$ and $\hat{\phi}_N$ are respectively $\sigma_k^2 = 2.49 \times 10^{-3}$ and $\sigma_\phi^2 = 2.5 \times 10^{-3}$. The variance constraints defined in Table 7.2 are clearly respected.

In conclusion, we see the optimal input signal and set-up conditions indeed generate estimates that respect the variance constraints that we set prior to the experiment.

**Remark 7.3** *In the experiment design sections we have made use of the fact that we know $\theta_0$ in order to find the optimal input spectra, since the inverse of the covariance matrix depends on $\theta_0$. Unfortunately, this dependence is universal in experiment design: no optimal experiment can be designed without prior knowledge of the system. Although we here chose to use the true parameter values, we have shown in Chapter 6 that by replacing the true vector by an initial guess $\theta_{init}$ nonetheless delivers better results than arbitrary input signal or degrees-of-freedom in the set-up.*

**Remark 7.4** *Our results are based on the values $k_0$ and $\phi_0$ shown in Table 7.1. Different values will lead to different optimal frequencies and optimal ratios $f_{i,opt}$ and $f_{e,opt}$. However, the Indirect Method will remain a better estimation method than the Direct Method, regardless of the actual values of permeability and porosity. Indeed, Theorem 7.1 is independent of the scaling or the values of $k$ and $\phi$.*

## 7.7  Summary

In this chapter we have introduced a novel estimation method that allows finding the minimal experiment time that is required to estimate permeability and porosity under user-specified parameter variance constraints and actuator limits. We have illustrated our

methodology on the Dynamic Darcy Cell. We have approached the problem by introducing a classical least-squares estimation procedure, from which we derived an expression for the covariance matrix of the estimates. This expression was used to compute the optimal input signal (either a sinusoid or square wave) and optimal experiment set-up degrees of freedom, being the ratios of the pore volume to inlet volume, $f_i$, and pore volume to outlet volume, $f_e$ using Experiment Design techniques. We considered sinusoidal and square wave actuator signals and two measurement types: actuator position/ outlet pressure measurements (the Indirect Method) and inlet pressure/outlet pressure measurements (Direct Method).

We have proven that square wave signals deliver shorter experiment lengths than sinusoidal ones under the same variance constraints and actuator limits.

The experiment design results for the Direct Method were as follows. For the joint estimation of permeability and porosity, we found that the optimal ratios $f_{e,opt} = 1.0$ and $f_{i,opt} = 0.1$, in contrast to separate parameter experiments for which $f_{e,opt} = 20$. This curiosity originates from a trade-off between variance reduction of permeability and porosity (which is obtained for high $f_e$ values, and reduces the variance of each separate parameter) and their correlation (which increases with increasing $f_e$, and drives the inverse of the covariance matrix to singularity). As a result, the minimum experiment time in this case is two orders of magnitude larger than for the separate parameter experiments.

We also investigated the Indirect Method, novel in this chapter. We found it superior to the Direct Method for joint parameter estimation: experiment lengths of a factor fourteen less are found. This difference originates mainly from the fact that, compared to the Direct Method, the sensitivity of the system with respect to changes in permeability and porosity for the Indirect Method is large over a broader range of $f_i$ and $f_e$ values.

Our analytical results are verified by simulating the Dynamic Darcy cell numerically, and we found excellent agreement between the numerical results and theoretical predictions.

Experiment design, and the introduction of the novel estimation method, clearly have enormous potential in practice. This theoretical work is therefore also an invitation to experimentalists to apply our techniques in practice. Future research could be focussed on extending the methodology to large-scale identification problems in e.g. oil reservoirs and aquifers.

## 7.A    Single Parameter Experiment Design for the Direct Method

In this appendix we consider the estimation of either permeability of porosity using a sinusoidal actuator signal. The true parameter vector is denoted by $\theta_0$ and is thus either equal to $k_0$ or $\phi_0$. To find the minimal experiment time that honours the variance constraint on one of the estimates given the amplitude constraints on the inlet pressure signal reads:

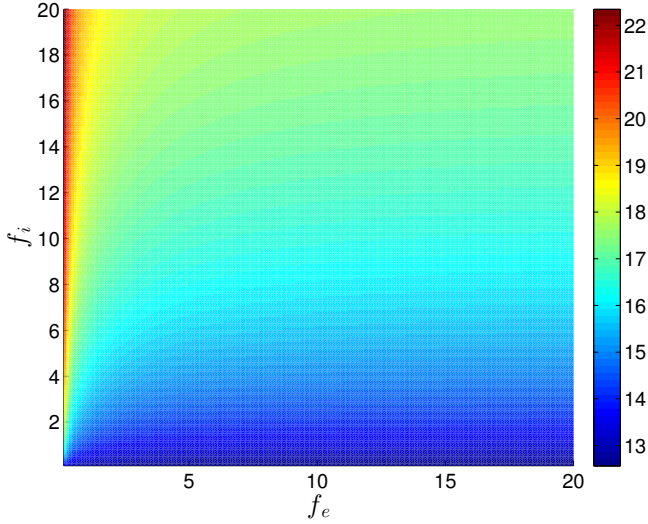$$\min_{\omega_{ex}, C_{\gamma}(f_i), f_i, f_e} \text{Experiment length } N \tag{7.83}$$

Figure 7.13: The logarithm of $N_{min}(f_i, f_e)$ as a function of $f_i$ and $f_e$ for $\theta = k$. The optimal ratios are $f_{i,opt} = 0.1$ and $f_{e,opt} = 20$.

subject to

$$\text{var}(\hat{\theta}_N) = P_{N,\theta}[\omega_{ex}, C_\gamma(f_i), f_i, f_e] \leq c_\theta, \qquad (7.84)$$

where $c_\theta$ is either $c_k$ (constraint value for permeability) or $c_\phi$ (constraint value for porosity), $G_{f_e}$ is given by (7.54), and the inverse of the covariance matrix is given by the scalar

$$P_{N,\theta}^{-1} = \frac{N C_\gamma^2(f_i)}{2\sigma_e^2} \left| L_{f_i,f_e}(i\omega_{ex}, \theta) \right|^2 \left| \frac{\partial G_{f_e}(i\omega_{ex}, \theta)}{\partial \theta} \right|^2_{\theta=\theta_0}.$$

From this expression it is clear that a requirement to find the optimal solution is that the condition $\text{var}(\hat{\theta}_N) \equiv P_\theta = c_\theta$ is met, and that furthermore that we should select $\gamma = \gamma_m$, see previous sections for motivation. The solution to (7.83)-(7.84) for given ratios of $(f_i, f_e)$ is then trivially found to be

$$N_{min}(f_i, f_e) = \frac{2\sigma_e^2}{c_\theta C_{\gamma_m}^2(f_i)} \min_{\omega_{ex}} \left[ \left| L_{f_i,f_e}(i\omega_{ex}, \theta_0) \right|^{-2} \left| \frac{\partial G_{f_e}(i\omega_{ex}, \theta)}{\partial \theta} \right|^{-2}_{\theta=\theta_0} \right], (7.85)$$

where the optimal excitation frequency $\omega_{ex,min}(f_i, f_e)$ is a function of $f_i$ and $f_e$ and is the frequency at which the minimum in (7.85) is obtained. The shortest possible experiment length is then found to be:

$$N_{opt} = N_{min}(f_{i,opt}, f_{e,opt}), \quad (f_{i,opt}, f_{e,opt}) = \arg\min_{f_i, f_e} N_{min}(f_i, f_e). \qquad (7.86)$$

The logarithm of the function $N_{min}(f_i, f_e)$ (c.f. (7.85)) is plotted for $\theta = k$ in Fig. 7.13 as a function of $f_i$ and $f_e$. The result for porosity is qualitatively the same. All optimal values are reported in Table 7.3. All other parameters are defined in Tables 7.1 and 7.2. The constraint value is respectively $c_\theta = c_k$ and $c_\theta = c_\phi$ for these cases, see Table 7.2.

## 7.B Single Parameter Experiment Design for the Indirect Method

In this appendix we follow the exact same procedure as in Appendix 7.A, but now for actuator to outlet measurements. The actuator limit is given by $\gamma_m = 0.1$. All parameters are defined in Tables 7.1 and 7.2. The optimisation problem for the Indirect Method is given by (7.83)-(7.84), where $P_\theta$ should be replaced with

$$P_{N,\theta}^{-1}[\omega_c, C_\gamma(f_i), f_i, f_e] = \frac{NC_\gamma^2(f_i)}{2\sigma_e^2} \left| \frac{\partial G_{f_i,f_e}(i\omega_{ex}, \theta)}{\partial \theta} \right|^2_{\theta=\theta_0}. \tag{7.87}$$

Following the same arguments as in the previous appendix we find that the minimal experiment time for a given set of $\{f_i, f_e\}$ is given by

$$N_{min}(f_i, f_e) = \frac{2\sigma_e^2}{c_\theta C_{\gamma_m}^2(f_i)} \min_{\omega_{ex}} \left| \frac{\partial G_{f_i,f_e}(i\omega_{ex})}{\partial \theta} \right|^{-2}_{\theta=\theta_0}, \tag{7.88}$$

where $G_{f_i,f_e}$ is defined in (7.58). The optimal experiment length $N_{opt}$ is then found as in the previous appendix.

## 7.C Dynamical Relationship between the Inlet and Outlet Pressure

An alternative way to find the dynamical relationship between the inlet pressure $p_i(t)$ and outlet pressure $p_e(t)$ has been considered in (Heller et al. (2002)). In that paper, the expression for the system output when applying an input signal $u(t) = C\cos(\omega t)$ was found to be

$$y_{nf}(t) = p(x=1,t) = C\frac{\Psi_1(\omega)\cos(\omega t) + \Psi_2(\omega)\sin(\omega t)}{\Psi_1^2(\omega) + \Psi_2^2(\omega)} \tag{7.89}$$

in which (after some additional algebraic manipulation to their expressions)

$$\Psi_1(\omega) = \cosh\left(\sqrt{\frac{\omega\phi}{2k}}\right)\cos\left(\sqrt{\frac{\omega\phi}{2k}}\right) + \sqrt{\frac{\omega\phi}{2k}}f \times$$

$$\left[\sinh\left(\sqrt{\frac{\omega\phi}{2k}}\right)\cos\left(\sqrt{\frac{\omega\phi}{2k}}\right) - \cosh\left(\sqrt{\frac{\omega\phi}{2k}}\right)\sin\left(\sqrt{\frac{\omega\phi}{2k}}\right)\right],$$

$$\Psi_2(\omega) = \sinh\left(\sqrt{\frac{\omega\phi}{2k}}\right)\sin\left(\sqrt{\frac{\omega\phi}{2k}}\right) + \sqrt{\frac{\omega\phi}{2k}}f \times$$

$$\left[\sinh\left(\sqrt{\frac{\omega\phi}{2k}}\right)\cos\left(\sqrt{\frac{\omega\phi}{2k}}\right) + \cosh\left(\sqrt{\frac{\omega\phi}{2k}}\right)\sin\left(\sqrt{\frac{\omega\phi}{2k}}\right)\right].$$

It is clear that (7.52) is more compact and easier to use, especially for more complex input signals. A simple time plot of these two signals shows that the expressions (7.52)

and (7.89) are indeed equivalent for $u(t) = C\cos(\omega t)$ (not shown here). Note that for this comparison, $\sin(\cdot)$ in (7.52) needs to be replaced by $\cos(\cdot)$. In fact, one can show with trigonometric identities that their amplitude ratio between the outlet and inlet pressure

$$R = \frac{2}{\sqrt{\Psi_1^2 + \Psi_2^2}}$$

is equal to $|G_{f_e}|$ in (7.54), and that their phase shift $\Theta$ between outlet and inlet pressure

$$\Theta = \arctan\frac{-\Psi_2}{\Psi_1}$$

is equal to $\alpha = \angle G_{f_e}$.

Importantly, regardless of the different notations, the way of deriving the expression of the ratio $R$ and phase shift $\Theta$ in (Heller et al. (2002)) is more involved than when considering the coupled subsystems in Section 7.2. This becomes especially true when considering the full inlet to outlet dynamics, i.e. subsystems I until III.

## 7.D   Square Wave versus Sinusoid

In this appendix we prove that a square wave input signal can deliver shorter experiment times under the same variance constraints compared to a sinusoidal input signal, and give a lower bound on how much shorter the experiment time can be. This result is valid for the estimation of one or two parameters simultaneously. Indeed, one can not identify more than two parameters with one single sinusoid. The result derived here does not only pertain to the Direct and Indirect Methods, but holds in general. The dimension of $\boldsymbol{\theta}$ must however be equal to or less than two.

We introduce some notations. The spectrum for a sinusoidal input signal with frequency $\omega_{ex}$ and amplitude $C$ reads

$$\Phi_u(\omega) = \frac{\pi C^2}{2T_s} \sum_{l=\{-1,1\}} \delta(\omega - l\omega_{ex}), \tag{7.90}$$

in which $T_s$ is the sample time. The spectrum for a square wave with cycle frequency $\omega_c$ and amplitude $C$ reads

$$\Phi_u(\omega) = \frac{8C^2}{\pi T_s} \sum_{m=1}^{M(T_s)} \frac{1}{(2m-1)^2} \sum_{l=\{-1,1\}} \delta(\omega - l[2m-1]\omega_c), \tag{7.91}$$

where $M(T_s) = \left\lfloor \frac{1}{2}\left(\frac{\pi}{\omega_c T_s} + 1\right) \right\rfloor$.

Lastly, for an input $u(t)$ that is connected to output $y(t)$ through a transfer function $G_\Xi(i\omega, \theta_0)$, where $\Xi$ contains all degrees-of-freedom of the set-up, assuming white measurement noise and no feedback, the inverse of the covariance matrix of the estimates $\hat{\theta}_N$

is given by

$$P^{-1}[\Phi_u(\omega)] = \frac{NT_s}{2\pi\sigma_e^2} \int_{-\pi/T_s}^{\pi/T_s} [\nabla_\theta G_\Xi(i\omega,\theta)]_{\theta=\theta_0} [\nabla_\theta^* G_\Xi(i\omega,\theta)]_{\theta=\theta_0} \Phi_u(\omega)\,d\omega, \quad (7.92)$$

where $\sigma_e^2$ is the variance of the white noise, $N$ the experiment length, and the asterisk denotes complex conjugation. We are now ready to prove the following lemma.

**Lemma 7.1** *Let $N_1$, $\omega_{ex} = \omega_{opt}$, $\Xi_{opt}$, $C$ be respectively the minimal experiment time, optimal excitation frequency, optimal set of degrees-of-freedom in the set-up, and amplitude $C$ of the sinusoid $u(t) = C\sin(\omega_{ex}t)$ that solve the optimisation problem*

$$\min_{\omega_{ex},\Xi} N \qquad (7.93)$$

*subject to*

$$\forall \theta_i \in \boldsymbol{\theta}: \ var(\hat{\theta}_{i,N}) \leq c_{\theta_i}, \qquad (7.94)$$

*where $c_{\theta,i}$ is the variance constraint for estimate $\hat{\theta}_{i,N}$. Then, using a square wave signal with cycle frequency $\omega_c = \omega_{opt}$ and amplitude $C$, the minimal experiment time $N_{SW}$ that fulfil constraint (7.94) can be guaranteed to be at least a factor $\pi^2/16$ times smaller than $N_1$.*

**Proof:** The expression of the covariance matrix (7.92) for a single sinusoid with spectrum (7.90) using the optimal parameters $N = N_1$, $\omega_{ex} = \omega_{opt}$, $\Xi = \Xi_{opt}$, and amplitude $C$ reads

$$P_{1,opt}^{-1} = \frac{N_1 C^2}{2\sigma_e^2} \mathrm{Re}\left\{ \left[\nabla_\theta G_{\Xi_{opt}}(i\omega_{opt},\theta)\right]_{\theta=\theta_0} \left[\nabla_\theta G_{\Xi_{opt}}(i\omega_{opt},\theta)\right]_{\theta=\theta_0}^* \right\}. \qquad (7.95)$$

By definition this covariance matrix honours the variance constraints. The substitution of (7.91), $\omega_c = \omega_{opt}$, and $N = N_{SW}$ into the covariance matrix (7.92) results in

$$P_{SW}^{-1} = \frac{16}{\pi^2} \frac{N_{SW}C^2}{2\sigma_e^2} \sum_{m=1}^{M(T_s)} \frac{1}{(2m-1)^2} \mathrm{Re}\left\{ \left[\nabla_\theta G_{\Xi_{opt}}(i[2m-1]\omega_{opt},\theta)\right]_{\theta=\theta_0} \times \right.$$
$$\left. \left[\nabla_\theta G_{\Xi_{opt}}(i[2m-1]\omega_{opt},\theta)\right]_{\theta=\theta_0}^* \right\}. \qquad (7.96)$$

Separating the expression $P_{N,\theta,SW}^{-1}$ into the sum of modes $m = 1$ and $m > 1$ we find

$$P_{SW}^{-1} = \frac{16}{\pi^2} \frac{N_{SW}C^2}{2\sigma_e^2} \mathrm{Re}\left\{ \left[\nabla_\theta G_{\Xi_{opt}}(i\omega_{opt},\theta)\right]_{\theta=\theta_0} \left[\nabla_\theta G_{\Xi_{opt}}(i\omega_{opt},\theta)\right]_{\theta=\theta_0}^* \right\}$$
$$+\text{extra positive definite terms.}$$

Clearly, by choosing $N_{SW} = \frac{\pi^2}{16}N_1 < N_1$ and using (7.95), (7.96), the above equation may be rewritten as

$$P_{SW}^{-1} = P_{1,opt}^{-1} + \text{extra positive definite terms.} \qquad (7.97)$$

What remains to show is that the variance(s) of $\hat{\theta}_{N,i}$ has (have) not increased. To this end, using Schur's complement, we rewrite the constraints in (7.94) for covariance matrix $P_{SW}^{-1}$

as:

$$\forall \theta_i \in \boldsymbol{\theta} : \begin{pmatrix} c_{\theta_i} & \boldsymbol{e}_i \\ \boldsymbol{e}_i^T & \boldsymbol{P}_{SW}^{-1} \end{pmatrix} \succeq \boldsymbol{0}.$$

Denote $\boldsymbol{\Omega} \succeq 0$ the extra positive definite terms in (7.97). For the constraint on $\hat{\theta}_{N,i}$, we find by substitution of (7.97) that we require

$$\forall \theta_i \in \boldsymbol{\theta} : \begin{pmatrix} c_{\theta_i} & \boldsymbol{e}_i \\ \boldsymbol{e}_i^T & \boldsymbol{P}_{1,opt}^{-1} + \boldsymbol{\Omega} \end{pmatrix} = \begin{pmatrix} c_{\theta_i} & \boldsymbol{e}_i \\ \boldsymbol{e}_i^T & \boldsymbol{P}_{1,opt}^{-1} \end{pmatrix} + \begin{pmatrix} 0 & 0 \\ 0 & \boldsymbol{\Omega} \end{pmatrix} \succeq \boldsymbol{0}.$$

The first terms on the r.h.s. of this equation is positive definite by virtue of the fact that the constraint is satisfied for $\boldsymbol{P}_{1,opt}^{-1}$. Multiplying this equation on the left by an arbitrary vector $[\boldsymbol{\xi}, \boldsymbol{\theta}]^T$ and $[\boldsymbol{\xi}, \boldsymbol{\theta}]$ on the right, with $\boldsymbol{\xi}$ a scalar entry, shows that we require that $\boldsymbol{\theta}^T \boldsymbol{\Omega} \boldsymbol{\theta} > 0$ for all $\boldsymbol{\theta}$. This condition is clearly honoured since $\boldsymbol{\Omega} \succeq 0$. Hence, by selecting $N_{SW} = \pi^2/16N_1 < N_1$ we can honour the constraints with a shorter experiment time when using a square wave signal.                                                                           $\square$

# 8

# LCED for Systems with Time-Domain Signal Amplitude Constraints

*"A theory with mathematical beauty is more likely to be correct than an ugly one that fits some experimental data."* - Paul M.J. Dirac

## 8.1   Introduction

In many practical problems, the amplitude of the input signal and/or of the output signal in the time-domain should not exceed a certain value during the identification experiment. An example is given in Chapter 7 where the amplitude of the input/excitation signal is constrained to be smaller than a maximal value. These types of constraints are not treated in neither the classical experiment design contributions nor the least-costly framework. Indeed, in these works, the power of the input and/or output signals are constrained and/or minimised. The reason of considering the power instead of the time-domain amplitude is that it yields convex optimisation problems (see e.g. Chapter 3).[1]

In this chapter, we will consider optimal experiment design combining constraints of the type of Section 3.2.3 (i.e. constraints on the minimal accuracy the model must have) and time-domain amplitude constraints. The optimal experiment design problem can then be formulated as in (Ebadat et al. (2014b,a)), where the experiment length $N$ is minimised subject to both the time-domain amplitude and an accuracy constraint. Note that this is also the formulation chosen in Chapter 7. However, in Chapter 7 we restricted attention to the design of a single sinusoid or a square wave (with one decision variable for the input spectrum). Here, we will design the amplitudes and phases of a multi-sine containing fixed frequencies (see the formula below (3.6)). This is also the main difference with the very interesting contribution of Ebadat et al. (2014a) where the signal is limited to be a stationary process with finite memory and alphabet. In (Ebadat et al. (2014b)) this restriction is not present, but the approach cannot be applied for closed-loop identification unlike the method introduced in this chapter. Our approach tackles the general case of multiple accuracy constraints (see (3.2)) while (Ebadat et al. (2014b,a)) treated the case of one single

---

[1]Parts of this chapter have been published in (Potters et al. (2016b)).

constraint (see (3.10)).

Our approach is based on the nonlinear optimisation algorithm proposed by Guillaume et al. (1991) that is adapted by Manchester (2009), where multi-sines are considered to construct excitation signals. We will refer to this adapted algorithm as the Guillaume-Manchester algorithm. It allows to treat optimisation problems minimising a scalar measure of the covariance matrix under input and output constraints. The scalar measure can be e.g. the determinant of the covariance matrix (D-optimality, as considered by Manchester (2009)), and its largest eigenvalue (E-optimality).

In order to use this efficient algorithm for the optimal experiment design problem considered in this chapter, we use the fact that it is a generalised eigenvalue problem (Boyd and Vandenberghe (2003)). The parameter accuracy constraints are indeed first transformed in an equivalent scalar one stating that the experiment time should be larger than the largest eigenvalue of a generalised and weighted covariance matrix of the parameter estimate. The amplitudes and phases of the multi-sine can then be determined by minimising the largest eigenvalue of this weighted covariance matrix while respecting the amplitude bounds on the input and output signals. This optimisation problem is efficiently solved with the nonlinear algorithm presented in (Guillaume et al. (1991); Manchester (2009)). We provide analytical expressions for the gradients that support fast convergence of this algorithm, the derivation of which is more involved than in (Manchester (2009)) where $D$-optimality is considered. The minimal experiment time is then deduced straightforwardly as the optimal value of the objective function of this optimisation problem, i.e., the largest eigenvalue of the weighted covariance matrix evaluated at the amplitudes of the optimal multi-sine.

The outline of this chapter is as follows. We first recapitulate some concepts of the Direct Identification method in Section 8.2, formulated for multi-sine signals. We introduce the parameter accuracy constraints in Section 8.3 and prove that any finite number of LMI constraints of the form (3.2) can be written as a single scalar one. We then proceed with the Minimum Experiment Time Algorithm that we introduce in Section 8.4. Two illustrations are provided in Section 8.5.

## 8.2   A Brief Refresher

In this section we will briefly review the identification framework presented in Chapter 2 and we will particularise it to the case considered in this chapter. We will do that for the Direct closed-loop identification method for discrete-time systems. Note that open-loop identification is a special case of this method and the Indirect closed-loop identification method can be seen as an open-loop identification method with a tailored choice of parametrisation of the model structure. Continuous-time transfer functions can also be identified with slight modification of this framework as shown in Chapters 6 and 7. Indeed, one can rather easily replace the discrete-time transfer functions by continuous-time ones, as we shall see in this chapter.

To this end, consider a discrete-time linear data-generating system, called the true system, defined by

$$u[n] \quad = \quad r[n] - C(q)y[n], \tag{8.1}$$
$$y[n] \quad = \quad G(q,\boldsymbol{\theta}_0)u[n] + H(q,\boldsymbol{\theta}_0)e[n], \tag{8.2}$$

where $r[n] \in \mathbb{R}$ is the to-be-designed excitation signal, $u[n] \in \mathbb{R}$ and $y[n] \in \mathbb{R}$ represent the discrete-time input and output of the true system, $e[n] \in \mathbb{R}$ a sampled white-noise with variance $\sigma_e^2$, $C(q)$ a linear, time-invariant controller, and $G(q, \theta_0)$ and $H(q, \theta_0)$ are stable, rational, finite-order transfer functions. Furthermore, $H(q, \theta_0)$ is monic and minimum phase. The sampling time $T_s = 1$ is chosen for notational brevity. The excitation signal is parameterised as a multi-sine with $M$ harmonics:

$$r[n] = \sum_{m=1}^{M} A_m \sin(m\omega_f n + \phi_m), \tag{8.3}$$

in which $A_m$ and $\phi_m$ are the amplitude and phase of the $m^{th}$ harmonic, where $m = 1, \ldots, M$. We define $\mathbf{A} = \{A_m\}_{m=1}^{M}$, $\phi = \{\phi_m\}_{m=1}^{M}$ and $\Omega = \{\mathbf{A}, \phi\}$. Unlike in optimal experiment design with power constraints where the phases did not appear in the optimisation problem (see Chapter 3), we will here optimise both the amplitudes and the phases in the multi-sines. The multi-sine (8.3) is periodic with period $T = \frac{2\pi}{\omega_f}$ and has a fundamental frequency $\omega_f$. Suppose now that we apply $N$ samples of the signal $\{r[n]\}_{n=1}^{N}$ to the true system. We collect the input and output data in the set $Z_N = \{u[n], y[n]\}_{n=1}^{N}$. The true parameter vector $\theta_0$ can then be estimated using a full-order model structure $\mathscr{M} = \{G(z, \theta), H(z, \theta)\}$ with a prediction error method (c.f. Chapter 2):

$$\hat{\theta}_N = \arg\min_{\theta} \frac{1}{N} \sum_{n=1}^{N} \varepsilon^2[n; \theta],$$

where $\varepsilon[n; \theta] = H^{-1}(z, \theta)\left(y[n] - G(z, \theta)u[n]\right)$ is the prediction error. In the limit $N \to \infty$ the estimate $\hat{\theta}_N$ will be asymptotically normally distributed around $\theta_0$ under conditions that can be found in Chapter 2. Using Parseval's relation a frequency-domain expression of $\mathbf{P}_{N,\theta}^{-1}$ for the input signal (8.3) can be deduced and reads (Ljung (1999))

$$\mathbf{P}_{N,\theta}^{-1}[\mathbf{A}] = \frac{N}{2\sigma_e^2} \sum_{m=1}^{M} A_m^2 \mathrm{Re}\left\{\mathbf{F}_r(e^{-im\omega_f}, \theta_0)\mathbf{F}_r^*(e^{-im\omega_f}, \theta_0)\right\} + \mathbf{R}_0, \tag{8.4}$$

where $\mathbf{P}_{N,\theta}$ is the covariance matrix for an experiment with $N$ samples. For instance, if $N = 1$, then the corresponding covariance matrix is denoted by $\mathbf{P}_{1,\theta}$. Furthermore, the terms $\mathbf{F}_r$ and $\mathbf{R}_0$ in (8.4) are defined as

$$\mathbf{F}_r(e^{-im\omega_f}, \theta_0) = H_0^{-1}(e^{-im\omega_f})S_0(e^{-im\omega_f}, \theta_0)\Lambda_G(e^{-im\omega_f})$$

and

$$\mathbf{R}_0 = \frac{N}{2\pi} \int_{-\pi}^{\pi} \mathbf{F}_v(e^{-i\omega}, \theta_0)\mathbf{F}_v^*(e^{-i\omega}, \theta_0)\, d\omega,$$

where $\mathbf{F}_v(e^{-i\omega}, \theta_0) = H_0^{-1}(e^{-i\omega})\Lambda_H(e^{-i\omega}) - C(e^{-i\omega})S_0(e^{-i\omega})\Lambda_G(e^{-i\omega})$. In these equations, $S_0 = (1 + CG_0)^{-1}$ is the sensitivity function of the closed-loop system, $\Lambda_G(e^{-i\omega}) = [\nabla_\theta G(e^{-i\omega})]_{\theta=\theta_0}$, $\Lambda_H(e^{-i\omega}) = [\nabla_\theta H(e^{-i\omega})]_{\theta=\theta_0}$, and the asterisk denotes complex conjugation. The inverse of the covariance matrix is a strictly positive definite symmetric matrix, i.e. $\mathbf{P}_{N,\theta}^{-1} \succ \mathbf{0}$.

Note that, like in Chapter 7, the experiment length $N$ will also be considered in this chapter

as an extra decision variable of the optimal experiment design problem: the objective will indeed be to minimise this length $N$.

## 8.3   Parameter Accuracy Constraints

In the introduction we mentioned that we consider the optimal experiment design problem of Ebadat et al. (2014b). As mentioned in Section 8.1, the parameter accuracy constraint in that paper is of the form $\mathbf{P}_{N,\theta}^{-1} \succeq \mathbf{R}_{adm}$. Using the sensitivity analysis of Hjalmarsson (2009) that is based on a second-order Taylor approximation, such a constraint guarantees an acceptable performance level for the loop made up by the true system and the controller designed with the identified model (see Section 3.2.3). As also shown in that section, we can, however, be faced in practice with multiple constraints of the above type, i.e.,

$$P_{N,\theta}^{-1}[A] \succeq R_{adm}(j) \text{ for all } j = 1, \ldots, J, \tag{8.5}$$

in which $J \in \mathbb{N}^+$ the number of constraints, and the matrices $\{R_{adm}(j)\}_{j=1}^{J}$ are symmetric and $(\kappa \times \kappa)$-dimensional, where $\kappa = \dim(\theta_0)$. These constraints are the same as the LCED problem (3.1)-(3.2). The case in (Ebadat et al. (2014b)) corresponds to $J = 1$ in which $R_{adm}$ is non-singular. In the case of $J \leq \kappa$ variance constraints on $J$ to-be-identified parameters, (8.5) is used with (3.14).

We recall that our goal is to minimise the experiment time $N$ while respecting the constraints (8.5) and the amplitude constraints on the input $u$ and output $y$ of the closed-loop (8.1) during the identification experiment. In the introduction, we mentioned that we will solve this problem with the nonlinear optimisation algorithm in (Guillaume et al. (1991); Manchester (2009)). To apply this algorithm, we first need to transform the LMI constraints (8.5) into a single scalar one. This is done in the following theorem.

**Theorem 8.1** *Consider the LMI constraints in (8.5). These constraints are equivalent to the following scalar one:*

$$N \geq \lambda_{max} \left( \mathcal{P}_{1,\theta}[A] \mathcal{R}_{adm} \right). \tag{8.6}$$

with $\mathcal{P}_{1,\theta}$ and $\mathcal{R}_{adm}$ given by the two $J\kappa \times J\kappa$-dimensional block-diagonal symmetric matrices

$$\mathcal{P}_{1,\theta}[A] = \text{diag}(P_{1,\theta}[A], \ldots, P_{1,\theta}[A]) \succ 0, \tag{8.7}$$
$$\mathcal{R}_{adm} = \text{diag}(R_{adm}(1), \ldots, R_{adm}(J)), \tag{8.8}$$

in which $P_{1,\theta}[A]$ is the inverse of (8.4) for $N = 1$.
**Proof:**  Using Lemma 4.1 we first rewrite the constraints (8.5) as

$$\forall j = 1, \ldots, J : N \geq \lambda_{max} \left( P_{1,\theta}[A] R_{adm}(j) \right), \tag{8.9}$$

which are equivalent to the single constraint

$$N \geq \max \left[ \lambda_{max}(P_{1,\theta} R_{adm}(1)), \ldots, \lambda_{max}(P_{1,\theta} R_{adm}(J)) \right]. \tag{8.10}$$

Then, since $\mathcal{P}_{1,\theta}$ and $\mathcal{R}_{adm}$ are block-diagonal matrices, we have

$$\det(\mathcal{P}_{1,\theta}\mathcal{R}_{adm} - \lambda I_{J\kappa \times J\kappa}) = \prod_{j=1}^{J} \det(P_{1,\theta}R_{adm}(j) - \lambda I_{\kappa \times \kappa}).$$

Thus, the $J\kappa$ eigenvalues of $\mathcal{P}_{1,\theta}[A]\mathcal{R}_{adm}$ are equal to the eigenvalues of the following matrices: $P_{1,\theta}R_{adm}(1), \ldots, P_{1,\theta}R_{adm}(J)$. Equation (8.10) is therefore equivalent to $N \geq \lambda_{max}(\mathcal{P}_{1,\theta}[A]\mathcal{R}_{adm})$, see (8.6). This concludes the proof. $\qquad\square$

**Remark 8.1** *Since (8.6) is equivalent to (3.2), this theorem shows that the LCED problem (3.1)-(3.2) is a dual of a generalised and weighted E-optimality problem.*

**Remark 8.2** *The single constraint (8.6) is equivalent to*

$$\lambda_{min}\left(\mathcal{P}_{N,\theta}^{-1}\mathcal{R}_{adm}^{-1}\right) \geq 1 \tag{8.11}$$

*in the case that all $\{R_{adm}(j)\}_{j=1}^{J}$ are non-singular. This follows from the analysis in Section 3.3, or from ((Larsson, 2014, Ch. 5)). There, it is proven for a non-singular $R_{adm}$ that a single constraint given by (8.9) for $J = 1$, is equivalent to $\lambda_{min}(T^{-1}P_{N,\theta}^{-1}T^{-1}) \geq 1$, where $R_{adm} = TT^{H}$. Following similar steps as taken in Lemma 4.1, generalising to $J > 1$, and defining the block-diagonal matrices $\mathcal{P}_{N,\theta}^{-1}$ and $\mathcal{R}_{adm}$ then also leads to (8.11).*

**Remark 8.3** *Although (4.5) could be used in the remainder of this text, it will be convenient to use (8.6) instead since this eigenvalue does not contain the square root of $\mathcal{P}_{1,\theta}$ in its argument. This property will be important in the Guillaume-Manchester algorithm that is used in Section 8.4.*

## 8.4 Minimal Experiment Time Algorithm

Let us now formulate mathematically the optimisation problem of Ebadat et al. (2014b) using Theorem 8.1 to replace the accuracy constraint with its scalar equivalent (8.6). The input and output signal amplitude bounds that we want to respect during the closed loop identification are respectively $u_{max}$ and $y_{max}$. This yields

$$\min_{A,\phi,N} N \tag{8.12}$$

subject to

$$f_u(A, \phi) \triangleq ||u_r(A, \phi)||_\infty / u_{r,max} \leq 1, \tag{8.13}$$

$$f_y(A, \phi) \triangleq ||y_r(A, \phi)||_\infty / y_{r,max} \leq 1, \tag{8.14}$$

$$N \geq \lambda_{max}\left(\mathcal{P}_{1,\theta}[A]\mathcal{R}_{adm}\right), \tag{8.15}$$

where $||u_r(A, \phi)||_\infty = \max_n |u_r[n]|$ and $||y_r(A, \phi)||_\infty = \max_n |y_r[n]|$ represent the maximum absolute value of the noise-free input $u_r[n] = S_0(q)r[n]$ and noise-free output $y_r[n] = S_0(q)G_0(q)r[n]$ (i.e. the amplitudes), $\mathcal{R}_{adm}$ as defined in Section 8.3, and $u_{r,max} \in \mathbb{R}^+$ and

$y_{r,max} \in \mathbb{R}^+$ are the amplitude bounds of $u_r$ and $y_r$:

$$u_{r,max} = u_{max} - \Delta u, \ \ y_{r,max} = y_{max} - \Delta y. \tag{8.16}$$

Here, $\Delta u$ and $\Delta y$ are user-chosen maximum noise disturbances caused on respectively $u[n]$ and $y[n]$. These deviations can be computed with for instance the simulation of $u_e[n] = -S_0(q)C(q)H_0(q)e[n]$ and $y_e[n] = S_0(q)G_0(q)H_0(q)e[n]$, where it is understood that $u[n] = u_r[n] + u_e[n]$ and $y[n] = y_r[n] + y_e[n]$[2].

Problem (8.12)-(8.15) is a Generalised EigenValue Problem (GEVP). The aim is to find the smallest value of $N$ for which (8.13)-(8.15) are feasible for some values of $N$, $\boldsymbol{A}$, and $\phi$. It is obvious that the optimal experiment time $N^*$ and the optimal amplitudes $\boldsymbol{A}^*$ are related by the following optimality condition[3]:

$$N^* = \lambda_{max} \left( \mathcal{P}_{1,\theta}[\boldsymbol{A}^*]\mathcal{R}_{adm} \right). \tag{8.17}$$

The solution to (8.12)-(8.15) is found with the following steps:

1. Solve the optimisation problem

$$\min_{\{\boldsymbol{A},\phi\}} J = \lambda_{max} \left( \mathcal{P}_{1,\theta}[\boldsymbol{A}]\mathcal{R}_{adm} \right) \tag{8.18}$$

   subject to

$$f_u(\mathbf{A},\phi) \leq 1, \ \ f_y(\mathbf{A},\phi) \leq 1, \tag{8.19}$$

   where the objective function is the r.h.s. of the constraint (8.15), $f_u(\mathbf{A},\phi)$ and $f_y(\mathbf{A},\phi)$ defined in (8.13)-(8.14), and $\mathcal{P}_{1,\theta}$ given by (8.7). This problem is solved with the Guillaume-Manchester algorithm detailed in Appendix 8.A. Denote $\Omega^* = \{\mathbf{A}^*,\phi^*\}$ as the solution of this problem, and $J^*$ as the minimum value of the objective function.

2. Use the optimality condition (8.17) to set the minimal experiment time:

$$N^* = J^* = \lambda_{max} \left( \mathcal{P}_{1,\theta}[\mathbf{A}^*]\mathcal{R}_{adm} \right). \tag{8.20}$$

   Note that in this step, we do no additional computation: we merely use the result from step 1. However, we stress that we here set the optimal experiment length $N^*$, whereas in step 1 we used $N = 1$ to find the optimal amplitudes and phases.

This two-step approach is valid due to the special form of condition (8.17). It allows us to design $\mathbf{A},\phi$ independently of $N$. It is obvious from inspecting (8.12)-(8.15) that the amplitudes $\mathbf{A}^*$ determined via (8.18)-(8.19) are the ones that fulfil the parameter accuracy constraint (8.15) with the smallest experiment time $N$. Moreover, since the excitation signal $r[n]$ is periodic, the signals $u_r[n]$ and $y_r[n]$ are also periodic with the same period. Consequently, it is sufficient to verify (8.19) over one single period of the excitation signal to guarantee that these constraints hold for any experiment length $N$. This is how (8.18)-(8.19) is solved in Appendix 8.A.

---

[2]The simulations of $u_e$ and $y_e$ are performed by replacing $\theta_0$ by an estimate $\theta_{init}$

[3]$N$ being an integer, (8.17) is of course rounded up to the nearest integer.

The optimal excitation signal $\{r_{opt}[n]\}_{n=1}^N$ (c.f. (8.3)) used for identification is then defined by $N = N^*$ and $\Omega = \Omega^*$ that are found with steps 1) and 2).

**Remark 8.4** *In some problems the matrix $\mathcal{R}_{adm}$ is non-singular. The constraints $\forall j = 1, \ldots, J : \mathbf{P}_{N,\theta}^{-1}[A] \succeq \mathbf{R}_{adm}(j)$ in Section 8.3 can then be recast into (8.11). Consequently, the constraint (8.15) may be replaced with $N\lambda_{min}(\mathcal{P}_{1,\theta}^{-1}\mathcal{R}_{adm}^{-1}) \geq 1$, and the optimality condition (8.17) becomes $N^*\lambda_{min}(\mathcal{P}_{1,\theta}^{-1}[A^*]\mathcal{R}_{adm}^{-1}) = 1$. Furthermore, the objective function in (8.18) becomes $-\lambda_{min}(\mathcal{P}_{1,\theta}^{-1}[A]\mathcal{R}_{adm})$ and (8.20) is changed to*

$$N^* = \frac{1}{\lambda_{min}(\mathcal{P}_{1,\theta}^{-1}[A^*]\mathcal{R}_{adm}^{-1})}.$$

*It can be beneficial to use the above criterion if $\mathcal{R}_{adm}$ is non-singular. Indeed, the convergence of the Guillaume-Manchester algorithm may in this case be faster than when using (8.6) due to a simpler eigenvalue gradient.*

## 8.5   Numerical Illustrations

### 8.5.1   Introduction

This section provides several examples that illustrate the Minimal Experiment Time (MET) algorithm. In particular, these will show the advantage of using the approach presented in Section 8.4 over a design that would consist of using a classical design with power constraints (see Chapter 3), and subsequently scaling this result to furthermore respect amplitude constraints.

First, we will revisit the case study of Chapter 6 and show that the optimal solution $r_{opt}[n] = A_{opt}\sin(\omega_{opt}n)$ computed there can be improved when, instead of minimising the power of the signal under the considered accuracy constraints, we minimise the experiment length under the same accuracy constraints and furthermore impose the constraint that the input amplitude cannot exceed the value $A_{opt}$. We will see that under the same conditions the experiment time resulting from the MET algorithm is much less than the ones resulting from the classical approach.

Second, we consider a four-parameter, discrete-time, black-box system. We compare the classical approach to the novel one in the case of an active input constraint, and active output constraint. We will also compare these solutions and provide interpretation.

Third, we revisit the Pressure Oscillation experiment of Chapter 7. In that chapter, we have proven that when identifying two parameters, a square wave delivers shorter experiment times than sinusoidal ones (under the same conditions). We have however not shown that square waves deliver the shortest possible experiment times. To this end, we compare as a last example the optimal square wave signal for the Indirect Method, computed in Section 7.5, with the one calculated here using the MET algorithm. We take the same input and parameter accuracy constraints and show that it is very likely that the optimal solution computed in Chapter 7 is indeed the one delivering the shortest possible experiment time. (We say *very likely* since the MET algorithm is not convex, so the solution obtained here might still be sub-optimal).

All three examples consider open-loop identification, i.e., $\mathbf{R}_0 = 0$, $C(z) = 0$, and $S(z) = 1$.

| Algorithm Parameters | Front-Face | Four-Parameter Model | | PO Experiment |
|---|---|---|---|---|
| | | Input Active | Output Active | |
| $M$ | 100 | 75 | 75 | 50 |
| $\omega_f$ | $\pi/10$ | 0.1 | 0.1 | 0.37 |
| $u_{max}$ | $A_{opt} = 1.7067$ | 1.0 | 1.0 | 0.0313 |
| $y_{max}$ | $10^3$ | $10^3$ | 3.7 | $10^3$ |
| $\gamma_u$ | 1.0 | 1.0 | $10^3$ | 1.0 |
| $\gamma_y$ | $10^3$ | $10^3$ | 1.0 | $10^3$ |
| $L$ | 256 | $10^3$ | $10^3$ | 512 |
| $p_{end}$ | 5 | 5 | 5 | 6 |
| $T_s$ | 0.1 | 0.419 | 0.419 | $4 \times 0.021$ |

Table 8.1: Parameters used to initialise the Guillaume-Manchester algorithm in Appendix 8.A for respectively the example in Section 8.5.2, 8.5.3, and 8.5.4. The sampling times $T_s$ are not independently chosen but given by $T_S = \pi/(M\omega_f)$.

Furthermore, for the sake of simplicity, we take a noise model $H(z) = 1$ and $\Delta u = \Delta y = 0$. For all examples, we compare the minimum time of (8.12)-(8.15) with the problem (8.23)-(8.26) defined in Appendix 8.A, in which the values of $u_{max}$, $y_{max}$, $L$, $\omega_f$, $M$, $\mathcal{R}_{adm}$, $\gamma_u$, and $\gamma_y$ can be found in Table 8.1 for each case, and of which the optimal amplitudes are scaled to $\mathbf{A}^*_{LCED}$ using (8.28) to satisfy the input and output amplitude constraints. The optimal experiment length found with (8.23)-(8.26) is then subsequently scaled to $N^*_{LCED}$, which ensures that (8.15) is also satisfied. The optimal phases $\phi^*_{LCED}$ for all cases are selected using Schroeder phases, see (8.27). The LCED-like solution $\Omega^*_2 = \{A^*_{LCED}, \phi^*_{LCED}\}$ is used to initialise the Guillaume-Manchester algorithm at $p = 2$, see Section 8.A.

## 8.5.2 Front-face Experiment Revisited

Chapter 6 considered the LCED problem (3.1)-(3.2) for a scaled front-face experiment, in which the scaled input $u[n]$ and scaled output $y[n]$ were connected through [4]

$$G(s, \boldsymbol{\theta}_0) = \frac{1}{\lambda_0} \sqrt{\frac{\alpha_0}{i\omega}} \tanh\left(\sqrt{\frac{i\omega}{\alpha_0}}\right).$$

The output was corrupted with Gaussian white noise of variance $\sigma_e^2 = 0.05$. The true scaled parameter vector was defined by $\boldsymbol{\theta}_0 = (\alpha_0, \lambda_0)^T = (1.0, 1.0)^T$, i.e., the thermal diffusivity and conductivity, respectively. The solution to the LCED problem at an experiment length of $N = 9000$ and parameter variance constraints (6.37) was one scaled sinusoid of amplitude $A_{opt} = 1.7067$ and frequency $\omega_{opt} = 1.57$, see (6.40). We have there considered a multi-sine parameterisation of the excitation signal (3.6) defined by $M = 100$ and $\omega_f = \pi/10$ ($T_s = 0.1$ seconds).

Now, we pose the question whether we can reduce the experiment length while conserving the amplitude bound $A = A_{opt} = 1.7067$ if we also optimise the phases of the multi-sine. We thus consider exactly the same experiment, but instead use the MET algorithm. To this end, the Guillaume-Manchester algorithm is initialised with the parameter values tabulated in Table 8.1, and the ones specified above. Furthermore, the matrix $\mathcal{R}_{adm}$

---

[4]We have dropped all tildes on the scaled variables and parameters for notational simplicity.
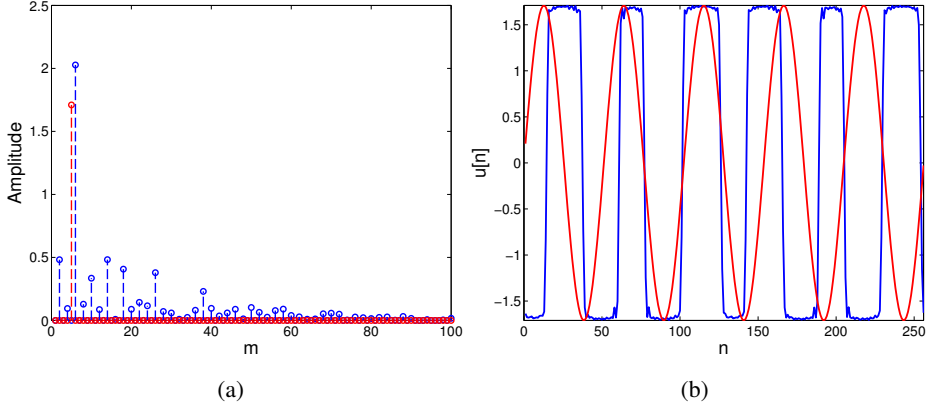
Figure 8.1: (a) The optimal input spectrum of the solution of the MET algorithm (blue) compared with the optimal spectrum found with the classical LCED method (red). (b) Time-domain realisation of the optimal input signals as a function of time for the optimal spectra in Fig. 8.1a (same color coding).

is constructed using $J = 2$ and the constraints (6.37).

Let us now compare the results. The optimal input spectrum resulting from the MET algorithm (8.12)-(8.15) and the LCED solution $\Omega_2^* = \{A_{LCED}^* = A_{opt}, \phi_{LCED}^* = 0\}$, $N_{LCED}^* = 9000^5$, are respectively shown in blue and red in Fig. 8.1a, and their time-domain realisations in Fig. 8.1b.

The LCED optimal input frequency appears at the mode $m = 5$, corresponding to $\omega_5 = \omega_{opt} = 1.57$ rad/s. Notice that the dominant frequency of the optimal signal using the MET algorithm is close to $\omega_{opt}$. This is intuitively pleasing, as the LCED solution attempts to minimise the sum of squared amplitudes (i.e. the power). Minimising the amplitude is indeed also effective in minimising the experiment length under the amplitude constraints. The MET algorithm is able to increase the amplitude close to $\omega_{opt} = 1.57$ rad/s with a factor of about 1.17 by adding higher modes to the input signal. The result is a signal that has a block-like structure. The minimum experiment length using the MET algorithm is $N^* = 5926$, a reduction of almost 34%.

**Remark 8.5** *Since the MET algorithm (8.12)-(8.15) is not convex, the solution obtained for the front-face experiment might still be suboptimal. Indeed, the square wave*

$$u[n] = \frac{4A}{\pi} \sum_{m=1}^{M} \frac{\sin([2m-1]\omega_c n)}{2m-1} \tag{8.21}$$

*with $M = 100$, $A = A_{opt} = 1.7067$ and $\omega_c = 1.57$ yields a minimal experiment time $N_{SW}$ that, by virtue of Lemma 7.1, is guaranteed to be a factor $16/\pi^2$ smaller than $N_{LCED}^* = 9000$, i.e., $N_{SW} \leq 5552$. (This solution clearly also respects the input and parameter accuracy constraints.) We see that it is also smaller than $N^* = 5926$ found with the MET algorithm; an improvement of about 6%.*

---

[5]This is simply the solution (6.40) from Chapter 6.

### 8.5.3    A Four-Parameter Rational Transfer Function Model

We proceed with an example that we have not considered so far. Consider the open-loop discrete-time system (2.1)-(2.2) in which the transfer function is given by

$$G(z, \theta_0) = \frac{\theta_1 z^{-1} + \theta_2 z^{-2}}{1 + \theta_3 z^{-1} + \theta_4 z^{-2}}, \tag{8.22}$$

with $\theta_0 = (0.8, 0, -0.9854, 0.8187)^T$. Furthermore, $H(z) = 1$ and the Gaussian noise variance $\sigma_e^2 = 1.20$. We consider an accuracy constraint defined by $J = 1$ and $\mathcal{R}_{adm} = \mathbf{R}_{adm} = 10^4 \mathbf{I}_{4 \times 4}$, i.e. $\mathbf{P}_{N,\theta}^{-1} \succeq \mathbf{R}_{adm} = 10^4 \mathbf{I}_{4 \times 4}$.

As for the previous example, we compare the LCED-like solution $\Omega_2^* = \{A_{LCED}^*, \phi_{LCED}^*\}$, $N_{LCED}^*$ (detailed at the start of this section) to the solution of the MET algorithm (8.12)-(8.15). We will do this for the cases in which either (i) the input constraint is active ($u_{max} = 1$, $y_{max} = 10^3$), or (ii) the output constraint is active ($u_{max} = 10^3$, $y_{max} = 3.7$). The Guillaume-Manchester algorithm is initialised with the parameters shown the third and fourth column of Table 8.1 for the respective cases (i) and (ii), and the ones specified above. The results are as follows.

We start with case (i). The optimal input spectrum of the MET and LCED-like solutions are respectively shown in blue and red in Fig. 8.2a, and their time-domain realisations in Fig. 8.2b. We see that the two frequencies corresponding to the optimal signal in the LCED-like formulation (8.23)-(8.26) are also present in the MET solution. Note that, as in the previous example, the MET spectrum contains high amplitudes around, and at, the optimal frequencies of the LCED-like solution. Clearly, minimising the sum of squared amplitudes also plays a dominant role in finding the minimal experiment time under amplitude constraints. As in the previous example, we also observe that the blue time-domain signal has a block-like structure. To satisfy the input and output bounds, as well as the accuracy constraint, the LCED experiment length $N_{LCED}^* = 10^4$, whereas $N^* = 4587$ using the MET algorithm; a reduction of about 56%.

Let us now consider case (ii), i.e. the situation with an active output constraint. The solution spectra of the MET algorithm of the cases (i) and (ii) are shown in Fig. 8.2c in respectively purple and blue. In this figure, we also superimposed the absolute value of $G(e^{-i\omega}, \theta_0)$ (8.22) as a function of frequency (scaled by a factor ten). The four grey curves show the real part of the four elements in the gradient $\nabla_\theta G(z, \theta)$ evaluated at $\theta = \theta_0$ (scaled by a factor fifty). Figure 8.2d shows the time-domain output signals corresponding to the optimal spectra in Fig. 8.2c (same color coding). Comparing the optimal spectra from the MET algorithm for the cases (i) and (ii), we observe the following. First, notice that in both cases the dominant frequencies reside at the modes where both the elements in the gradient of (8.22) and the frequency response (8.22) are large. That these frequencies are selected is not surprising for case (i), since the LCED-like solution (see red spectrum in Fig. 8.2a) has already shown that the sum of amplitudes is then minimised, which also eases the minimisation of the experiment length under an input amplitude constraint (c.f. (2.9)). Second, we see from Fig. 8.2c that the optimal spectrum for case (ii) (blue) has dominant frequencies that are shifted away from the peak of the frequency response of (8.22) (shown in black). This is an intuitively pleasing result. Indeed, in order to minimise the experiment length under the active output constraint $y_{max}$, modes should be selected at which the amplitudes $A_m$ of the input signal are not amplified too much by
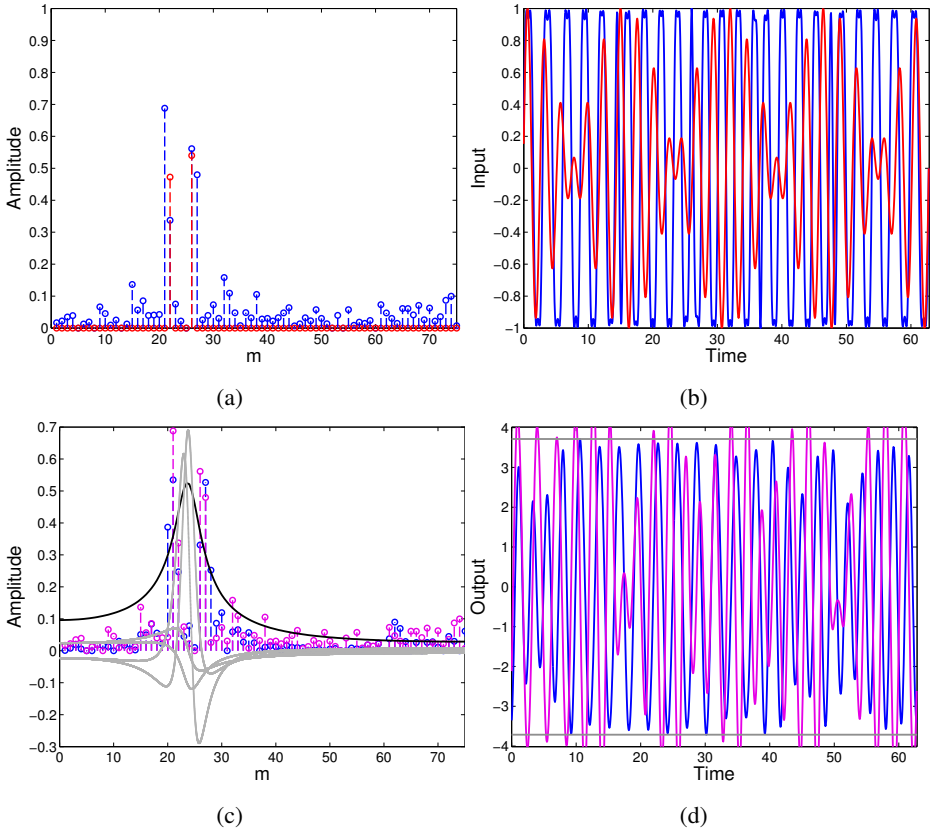
(a)

(b)

(c)

(d)

Figure 8.2: (a) The optimal input spectrum for the four-parameter example under an active input constraint using the MET algorithm (blue) compared with the optimal spectrum found with the classical LCED method (red). (b) Time-domain realisation of the input signals for the optimal spectra shown in Fig. 8.2a (same color coding). (c) The optimal input spectrum of the MET algorithm for the four-parameter example under an active output constraint (blue) and active input constraint (purple). The absolute value of (8.22) scaled by a factor ten is shown in black. The four elements of the gradient of (8.22) evaluated at $\theta = \theta_0$, scaled by a factor fifty, are shown in grey. (d) Time-domain realisation of the output signal as a function of time for the optimal spectra in Fig. 8.2c (same color coding). The dark grey horizontal lines indicate the output constraint $|y_{max}|$.

(8.22) (otherwise the input amplitudes have to be drastically reduced to still satisfy the output constraint, leading to an increased experiment time, see (2.9)). On the other hand, it is beneficial to select frequencies where the elements of the gradient are large, as for case (i). Hence, in this example, a trade-off has to be made between these two competing effects. This trade-off consequently leads to a minimal experiment time $N^* = 5810$ that is about 27% longer than the minimal experiment time of case (i). We note that this trade-off becomes more pronounced when decreasing $y_{max}$, i.e., the dominant frequencies in this case shift away even more from the peak of the frequency response of (8.22).

### 8.5.4   Pressure Oscillation Experiment Revisited

In this last example, we consider the scaled pressure oscillation experiment from Chapter 7[6]. There, the experiment time was minimised subject to an input amplitude constraint and variance constraints on the permeability $k$ and porosity $\phi$ parameters. The input constraint was given by $u_{max} = C_{\gamma_m} = 0.0313$, and the variance constraints on the estimates by $\text{var}(\hat{k}_N) \leq 2.5 \times 10^{-3}$ and $\text{var}(\hat{\phi}_N) \leq 2.5 \times 10^{-3}$. We will in particular re-examine the optimal square wave signal that was obtained for the Indirect Method, see Section 7.5. There, the optimal square wave solution had a cycle frequency $\omega_{c,opt} = 1.0$ and an amplitude $A = A_{opt} = 0.0313$ (equal to the limit of the actuator: $C_{\gamma_m} = \gamma_m \frac{\phi_s}{f_{i,opt}}$). The optimal degrees of freedom in this case were $f_{i,opt} = 0.6$ and $f_{e,opt} = 6.1$. The variance of the white noise was $\sigma_e^2 = 0.05$. The minimal experiment length corresponding to this optimal square wave was $N_{opt} = 1.8 \times 10^6$ at a sampling time of $T_s = 0.021$ seconds.

We assumed in Chapter 7 that a square wave is a good choice to minimise the experiment length under the input amplitude and parameter accuracy constraints. Let us in this section validate this assumption by considering, under the exact same conditions, the solution to the MET algorithm. As done in all the previous examples, the algorithm is initialised with the parameters reported in Table 8.1[7]. We furthermore fix $f_i$ and $f_e$ to their optimal values reported above.

The optimal input spectrum resulting from the MET algorithm is shown in Fig. 8.3a. Its corresponding time-domain signal is shown in Fig. 8.3b. Notice that we obtain a signal that is essentially a square wave signal. It is not a perfect square wave due to the fact that we have a sampling time larger than zero (the number of modes $M$ in (8.21) is therefore not infinite). The corresponding optimal cycle frequency is located at the mode $m = 3$, i.e., $\omega_{c,opt} = 1.11$ rad/s.

The optimal experiment length is $N^* = 2.076 \times 10^6$, which is about 15% longer than $N_{opt} = 1.8 \times 10^6$ found in Section 7.5. This difference could be the result of an $\omega_f$ that is too large, and due to the fact that the solution corresponds to a local minimum that is close to the global one of the problem (8.12)-(8.15).

Notwithstanding this difference, the numerical solution obtained with the MET algorithm validates (to some extent) the assumption of Chapter 7 that a square wave is a good signal to minimise the experiment length.

---

[6]All the results reported in this section correspond to the *scaled* system considered in Section 7.5.

[7]Note that we artificially increased the sampling time to four times of the ones used in Section 7.5. This ensures that the number of modes $M = 50$ (for which $T_s = 4 \times 0.021$) instead of $M = 200$ (for which $T_s = 0.021$) for the fundamental frequency $\omega_f = 0.37$ rad/s. This speeds up the numerical algorithm.
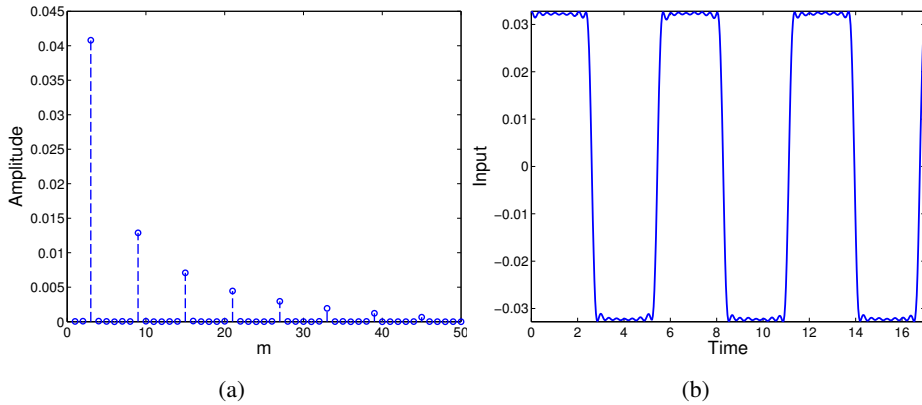
(a)  (b)

Figure 8.3: (a) Optimal input spectrum resulting from the MET algorithm for the Pressure Oscillation experiment. (b) The corresponding optimal input signal. Notice that it resembles a square wave signal.

## 8.6   Summary

We considered the input design problem of finding the minimal required experiment time such that accuracy constraints on the parameter estimate of an identification experiment are satisfied, while also respecting signal amplitude bounds. The input signal is parameterised as a multi-sine. We first show how multiple linear matrix inequalities from the least-costly and applications-oriented experiment design frameworks can be transformed into a generalised $E$-optimality constraint. Then, the solution to our problem is found by: (i) designing a multi-sine of one period with the Guillaume-Manchester algorithm (Guillaume et al. (1991); Manchester (2009)) that minimises the generalised $E$-optimality criterion under signal amplitude bounds, and (ii) utilising periodicity and an optimality condition to scale the experiment time such that the imposed accuracy constraints are also respected. Examples show experiment time reductions of more than 40% compared with the traditional least-costly experiment design approach from Chapter 3.

The numerical results in this chapter seem to suggest that block-shaped signals form the right basis to find optimal experiment times. Instead of designing the optimal multi-sine input signal, one could instead consider designing the optimal block-shaped signal, i.e., a binary input signal with optimally chosen switches between the two values. Probably, the dominant frequencies in this signal would be close to the optimal frequencies obtained from the traditional LCED problem. Developing an algorithm to compute such signals is an interesting future research possibility.

## 8.A   Guillaume-Manchester Algorithm

In this appendix we solve (8.18)-(8.19) using the Guillaume-Manchester algorithm defined below. We refer the reader to (Guillaume et al. (1991); Manchester (2009)) for more details. Conceptually, the idea is to solve (8.18)-(8.19) iteratively by replacing the amplitude of $u_r, y_r$ by the $p$-norms of these signals and by increasing the value of $p$ at each iteration. We have indeed that the maximal amplitude of a a signal is given by its $p$-norm for $p = \infty$.

Before presenting the algorithm, we make two observations. First, since $r$ is a multi-

sine, the signals $u_r$ and $y_r$ are also multi-sines (with the same period). Consequently, we have to only consider one period of these signals to verify the amplitude constraints. Second, if the actual sampling frequency is not very high, taking the maximal values of $u_r[n]$ and $y_r[n]$ may result in poor estimates of the actual amplitudes of their continuous-time equivalents. However, we are not obliged to use the actual sampling frequency to solve (8.18)-(8.19). We can artificially increase the sampling frequency to more accurately determine the amplitudes by deducing analytically the continuous-time expressions of $u_r$ and $y_r$. We assume that the excitation signal $r$ is also continuous and that the discrete-time closed-loop transfer functions relating $r$ with $u_r, y_r$ are equal to their continuous-time counterparts in the frequency range $[0, \pi]$ (we assume $T_s = 1$ for simplicity). With these analytical expressions we can sample these signals at any sampling rate. Let us assume that for this high sampling frequency, $L+1$ is the number of samples of one period of $r, u_r$ and $y_r$. In the sequel, we will subsequently compute the $p$-norms of $u_r, y_r$ for the Guillaume-Manchester algorithm using $u_r[l]$ and $y_r[l]$ for $l = 0, \ldots, L$.

The Guillaume-Manchester algorithm is defined as follows. The input and output signals are constructed with the amplitudes and phases, i.e. $\Omega$, of the excitation signal $r$. We define $\mathbf{A}_p = \{A_1, \ldots, A_M\}_p$ and $\phi_p = \{\phi_1, \ldots, \phi_M\}_p$ as its amplitude and phase variables at step $p \in [2, 4, 8, \ldots, p_{end}]$, and their elements are denoted by $A_{p,m}$ and $\phi_{p,m}$.

*Initialisation.* Select the fundamental frequency $\omega_f$ and number of harmonics $M$ of the multi-sine $\{r[l]\}_{l=0}^{L}$ (8.3). The solution for $p = 2$ is $\{\mathbf{A}_2^*, \phi_2^*\} = \Omega_2^*$ and given by the user. It initialises the Guillaume-Manchester algorithm. One way to initialise $\Omega_2^*$ is to solve the following optimisation problem (of the LCED type) that considers power constraints instead of amplitude ones. Define the multi-sine (8.3) for the user-chosen values $\omega_f$ and $M$ and solve the Generalised EigenValue Problem (GEVP):

$$\min_{\mathbf{A}} N \tag{8.23}$$

subject to

$$\frac{1}{2} \sum_{m=1}^{M} |S_0(e^{-im\omega_f})|^2 A_m^2 \leq \gamma_u, \tag{8.24}$$

$$\frac{1}{2} \sum_{m=1}^{M} |S_0(e^{-im\omega_f})|^2 |G_0(e^{-im\omega_f})|^2 A_m^2 \leq \gamma_y, \tag{8.25}$$

$$N \mathcal{P}_{1,\theta}^{-1}[\mathbf{A}] \succeq \mathcal{R}_{adm}, \tag{8.26}$$

where $\gamma_u, \gamma_y$ are bounds on respectively the input and output power, and the last constraint equal to (8.15).

Furthermore, we define the phases at $p = 2$ using Schroeder phases (see also Manchester (2009)), i.e.,

$$\phi_{2,m}^* = -2\pi \sum_{q=1}^{m-1} (m-q) A_{2,m}^*, \tag{8.27}$$

which reduce the amplitudes of the input and output signals.

The optimal amplitudes from the above problem and the phases $\phi_{2,m}^*$ are then used to design $\{u_r[l]\}_{l=0}^{L}$ and $\{y_r[l]\}_{l=0}^{L}$. To ensure that the constraints (8.13)-(8.14) are respected,

the amplitudes are then uniformly scaled until we have the solution $\Omega^*$ for which either $f_u(\Omega_2^*) = 1, f_y(\omega_2^*) \leq 1$ or $f_u(\Omega_2^*) \leq 1, f_y(\Omega_2^*) = 1$ (see (8.28)), and $N$ is subsequently scaled such that (8.15) is furthermore respected.

*Iterative steps.* Solve for $p = 4, 8, 16, \ldots, p_{end}$ the following optimisation problem:

Use the solution of previous step, $\mathbf{A}_{p/2}^*$ and $\phi_{p/2}^*$, and scale to fit constraints and provide the next initial guess:

$$\mathbf{A}_p = \frac{\mathbf{A}_{p/2}^*}{\max\left[f_{u,p}(\mathbf{A}_{p/2}^*, \phi_{p/2}^*), f_{y,p}(\mathbf{A}_{p/2}^*, \phi_{p/2}^*)\right]}, \quad (8.28)$$

$$\phi_p = \phi_{p/2}^*, \quad (8.29)$$

where $f_{u,p} = ||u_r(\mathbf{A}, \phi)||_p^p$, $f_{y,p} = ||y_r(\mathbf{A}, \phi)||_p^p$, and $||x(k)||_p \triangleq \left(\frac{1}{K}\sum_{k=1}^{K}|x(k)|^p\right)^{1/p}$. Then solve

$$\mathbf{A}_p^*, \phi_p^* = \arg \min_{\{\mathbf{A}_p, \phi_p\}} \lambda_{max}\left(\mathcal{P}_{1,\theta}[\mathbf{A}_p]\mathcal{R}_{adm}\right) \quad (8.30)$$

subject to

$$f_{u,p}(\mathbf{A}_p, \phi_p) \leq 1, \quad f_{y,p}(\mathbf{A}_p, \phi_p) \leq 1. \quad (8.31)$$

The nonlinear optimisation problem (8.30)-(8.31) is solved with any nonlinear optimisation solver (e.g. the *fmincon* function of Matlab) using $\mathbf{A}_p$ and $\Phi_p$ as initial guess for the solution. After the last iteration, the solution to (8.18)-(8.19) in Section 8.4 is provided by the solution of the Guillaume-Manchester algorithm and is denoted by $\Omega^* = (\mathbf{A}_{p_{end}}^*, \phi_{p_{end}}^*)$.

# 8.B    Gradients for the Guillaume-Manchester Algorithm

The gradients of the objective function and constraints can be numerically computed with the *fmincon* function used to solve (8.30)-(8.31). However, the speed of convergence can be greatly improved when providing *fmincon* with analytical gradients. Here these gradients are provided.

### Objective function in (8.30)

We assume that the eigenvalues of matrix $\mathcal{P}_{1,\theta}\mathcal{R}_{adm}$ are simple, and that this matrix is non-defective. Denote $\mathbf{v}_{max}$ as the right eigenvector corresponding $\mathcal{P}_{1,\theta}\mathcal{R}_{adm}$, i.e., we have

$$\left(\mathcal{P}_{1,\theta}[\mathbf{A}_p]\mathcal{R}_{adm}\right)\mathbf{v}_{max}[\mathbf{A}_p] = \lambda_{max}[\mathbf{A}_p]\mathbf{v}_{max}[\mathbf{A}_p]. \quad (8.32)$$

Furthermore, define $\mathbf{w}_{max}$ as the right eigenvector of $\left(\mathcal{P}_{1,\theta}\mathcal{R}_{adm}\right)^T$, i.e., $\mathbf{w}_{max}^T$ is the left eigenvector of $\mathcal{P}_{1,\theta}\mathcal{R}_{adm}$:

$$\mathbf{w}_{max}^T[\mathbf{A}_p]\left(\mathcal{P}_{1,\theta}[\mathbf{A}_p]\mathcal{R}_{adm}\right) = \lambda_{max}[\mathbf{A}_p]\mathbf{w}_{max}^T[\mathbf{A}_p]. \quad (8.33)$$

We normalise the vectors $\mathbf{w}_{max}$ and $\mathbf{v}_{max}$ such that $\mathbf{w}_{max}^T\mathbf{v}_{max} = 1$. Define the matrix $\mathbf{B}[\mathbf{A}_p] = \mathcal{P}_{1,\theta}[\mathbf{A}_p]\mathcal{R}_{adm}$, then taking the derivative of (8.32) w.r.t. $A_{p,m}$ on both sides

results in

$$\left(\frac{\partial}{\partial A_{p,m}}\mathbf{B}[\mathbf{A}_p]\right)\mathbf{v}_{max}[\mathbf{A}_p] + \mathbf{B}[\mathbf{A}_p]\left(\frac{\partial}{\partial A_{p,m}}\mathbf{v}_{max}[\mathbf{A}_p]\right) =$$
$$\left(\frac{\partial}{\partial A_{p,m}}\lambda_{max}[\mathbf{A}_p]\right)\mathbf{v}_{max}[\mathbf{A}_p] + \lambda_{max}[\mathbf{A}_p]\left(\frac{\partial}{\partial A_{p,m}}\mathbf{v}_{max}[\mathbf{A}_p]\right).$$

Multiplying both sides with $\mathbf{w}_{max}^T$ from the left and using (8.33), $\mathbf{w}_{max}^T\mathbf{v}_{max} = 1$, and the definition of $\mathbf{B}[\mathbf{A}_p]$, we obtain

$$\frac{\partial}{\partial A_{p,m}}\lambda_{max}[\mathbf{A}_p] = -\mathbf{w}_{max}^T[\mathbf{A}_p]\left(\mathcal{P}_{1,\theta}[\mathbf{A}_p]\frac{\partial}{\partial A_{p,m}}\left(\mathcal{P}_{1,\theta}^{-1}[\mathbf{A}_p]\right)\mathcal{P}_{1,\theta}[\mathbf{A}_p]\mathcal{R}_{adm}\right)\mathbf{v}_{max}[\mathbf{A}_p],$$

where we furthermore made use of the identity $\frac{\partial}{\partial x}\mathbf{X}^{-1} = -\mathbf{X}^{-1}(\frac{\partial}{\partial x}\mathbf{X})\mathbf{X}^{-1}$. The gradient at $\mathbf{A}_p = \overline{\mathbf{A}}_p$ is then easily found with (8.4) by evaluating the above equation for all $\{A_{p,m}\}_{m=1}^M$ at $\overline{\mathbf{A}}_p$. Note that the gradient of $\mathcal{P}_{1,\theta}[\mathbf{A}_p]\mathcal{R}_{adm}$ can be calculated analytically, whereas the gradient of $\mathcal{P}_{1,\theta}^{1/2}[\mathbf{A}_p]\mathcal{R}_{adm}\mathcal{P}_{1,\theta}^{1/2}[\mathbf{A}_p]$ cannot. This observation motivated the last step taken in Lemma 8.1, see also Remark 1.

Since (8.34) is not dependent on $\phi_p$, we trivially have that the gradient

$$\nabla_{\phi_p}\lambda_{max}\left(\mathcal{P}_{1,\theta}[\mathbf{A}_p]\mathcal{R}_{adm}\right) = \mathbf{0}.$$

### Constraints (8.31)

The derivatives of the constraints are now calculated. We assume that the excitation multisine $r$ is continuous. Following (Manchester (2009)) the functions $f_{u,p}$ and $f_{y,p}$ in (8.31) are written as

$$f_{u,p}(\mathbf{A}_p,\phi_p) = \eta_{u,p}^T\eta_{u,p}, \; f_{y,p}(\mathbf{A}_p,\phi_p) = \eta_{y,p}^T\eta_{y,p},$$

with $\eta_{u,p}[l] = u_r^k[l]/u_{r,max}^k$, $\eta_{y,p}[l] = y_r^k[l]/y_{r,max}^k$, $k = p/2$, and $\dim(\eta_{u,p}) = \dim(\eta_{y,p}) = L+1$. The derivatives of these functions with respect to the amplitudes and phases are then easily found:

$$\frac{\partial f_{u,p}}{\partial A_{p,m}} = 2\eta_{u,p}^T\frac{\partial \eta_{u,p}}{\partial A_m}, \; \frac{\partial f_{u,p}}{\partial \phi_m} = 2\eta_{u,p}\frac{\partial \eta_{u,p}}{\partial \phi_{p,m}},$$
$$\frac{\partial f_{y,p}}{\partial A_{p,m}} = 2\eta_{y,p}^T\frac{\partial \eta_{y,p}}{\partial A_{p,m}}, \; \frac{\partial f_{y,p}}{\partial \phi_m} = 2\eta_{y,p}\frac{\partial \eta_{y,p}}{\partial \phi_{p,m}},$$

in which

$$\frac{\partial \eta_{u,p}}{\partial A_{p,m}}[l] = k\frac{u_r^{k-1}[l]}{u_{r,max}^k}|S_0(z_m)|\sin(\omega_m l\Delta L + \phi_{p,m} + \phi_S),$$
$$\frac{\partial \eta_{u,p}}{\partial \phi_{p,m}}[l] = k\frac{u_r^{k-1}[l]}{u_{r,max}^k}A_{p,m}|S_0(z_m)|\cos(\omega_m l\Delta L + \phi_{p,m} + \phi_S),$$

in which $\phi_S = \angle S_0(z_m)$. The derivatives for $\eta_{y,p}$ can be found analogously.

# 9

# Conclusions

*"Measure what is measurable, and make measurable what is not so."* - Galileo
Galilei

## 9.1  Contribution of this thesis

The main contribution of this thesis is the development of several techniques that widen
the scope of the classical Least-Costly Experiment Design (LCED) framework (defined
in Chapter 3). In particular, we have extended the framework to include structured and
unstructured linear systems regulated by arbitrary controllers, and relevant costs and prac-
tical constraints.

The conclusions at a high level are as follows. The novel techniques from this thesis
can be used to solve more of the problems indicated in Fig. 9.1. (It is the same schematic
as shown in Chapter 1, here shown again for convenience.) We have generalised in Chap-
ter 6 the classical LCED framework such that we can now select at step I a system in the
class of linear PDEs with constant coefficients. In that chapter, we have also extended
the LCED framework to include degrees of freedom in the experiment set-up by intro-
ducing an efficient subdivision algorithm. The Stealth and Sensitivity methods introduced
in Chapter 5 allows experiment design on a system operated in closed-loop with an un-
known linear or (possible unknown) nonlinear controller, addressing step III. Lastly, with
the Minimum Experiment Time (MET) algorithm introduced in Chapter 8, another optimi-
sation problems (IV) can be solved. This novel algorithm finds the optimal input spectrum
(and degrees of freedom) that minimise the experiment time (the experiment cost) under
parameter accuracy constraints and input/output amplitude bounds (system constraints).
Next to these extensions, we have provided analytical solutions for some classical LCED
problems.

In the remainder of this section, we provide detailed conclusions of the specific prob-
lems that have been addressed in this thesis.

*Design optimal input signal and experiment conditions for:*

I.    Structured and Unstructured Systems (PDEs, ODEs, networks)

*with or without*

II.    degrees of freedom in experiment set-up

*in*

III.    Open Loop    *or*    Closed Loop

MPC    LTI    Nonlinear    Unknown

*by solving the optimization problem*

IV.

$$\min_{\Xi} \ \text{Experiment cost}$$

subject to

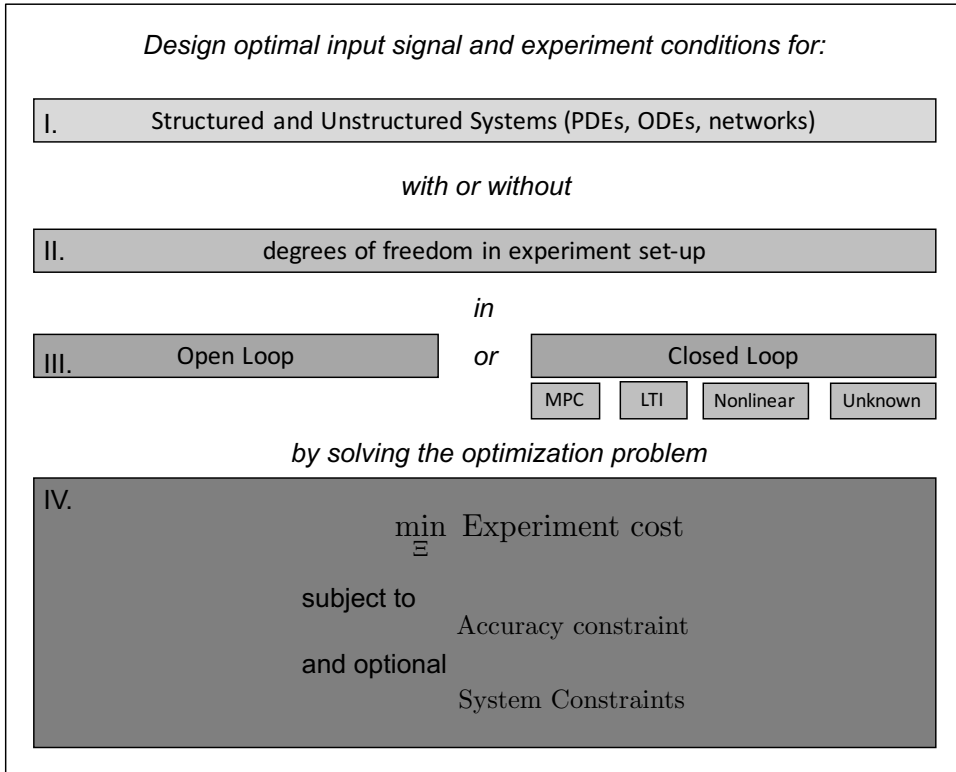Accuracy constraint

and optional

System Constraints

Figure 9.1: This diagram shows the type of problems that need to be solved with Experiment Design. The aim is to solve the optimisation problem IV for any structured or unstructured system, with or without degrees of freedom in the experiment set-up, and that can be in either open- or closed-loop. The symbol $\Xi$ indicates the set of design variables in the optimisation problem, which usually contains only the input spectrum $\Phi_r$, but can also include degrees of freedom of an experiment set-up.

**Analytical Solutions and Interpretation**

We have calculated in Chapter 4 analytical solutions to the classical LCED problem, defined in Chapter 3, for continuous- and discrete-time uni- and bi-parametric models. The solutions derived in Chapter 4 are general in the sense that they hold for an arbitrary but finite number of parameter accuracy constraints, in which all or some of the constraint matrices may be non-singular. For bi-parametric models, we motivate that a single-sine solution is probably almost always optimal, whereas for uni-parametric models we prove that this solution is in fact always optimal.

The solutions also aid in the interpretation of the optimal input spectra that would otherwise have been obtained with convex numerical methods. These analytical solutions can also be used to validate the numerical ones, as is done for several problems in Chapters 4, 6, and 8.

Several side results have also been obtained from the analytical approach. First, it likely that no analytical solutions exist for systems with more than four unknown parameters, a statement that traces back to Lemma 4.1. Indeed, in this lemma we have proven that the Linear Matrix Inequalities used in the LCED framework may be equivalently written as a single scalar constraint stating that the maximum eigenvalue of the weighted covariance matrix should be smaller than unity. By virtue of Galois theory, we know that no solutions exist for general polynomial equations of a degree higher than four. Consequently, no analytical expressions for the eigenvalues of matrices larger than dimension four exist. Therefore, it is unlikely that analytical solutions of the LCED problem exists for systems with more than four unknown parameters.

Second, in Chapter 8 we have proven, using Lemma 4.1, that the classical LCED problem is in fact a generalised and weighted dual $E$-optimality problem. This nice result that formally classifies the LCED problem within the $A$-, $C$-, $D$-, and $E$-optimality problems.

**LCED for (Un)structured Systems with Unknown or Nonlinear Controllers**

We have extended the LCED framework such that optimal spectra can now also be computed for linear systems that are regulated by nonlinear or unknown controllers.

To this end, we have introduced the Stealth and Sensitivity methods in Chapter 5. These methods generalise the framework considerably, since nonlinear controllers are essentially the norm in industry. The Stealth Method adapts the usual Direct Method identification scheme such that the excitation signal is no longer observed by the controller. This consequently leads to a LCED optimisation problem that is again numerically tractable. The Sensitivity method, however, does not alter the identification scheme, but instead uses prior data to estimate the sensitivity function between the input and excitation signal (for instance using data that has also been used to provide an initial estimate of the true parameter vector in order to circumvent the chicken-and-egg issue; see Section 3.2.2). This estimate can then be used to solve the LCED problem.

**LCED for Structured Systems with Degrees-of-Freedom in the Experiment Set-Up**

The vast majority of works on experiment design in the System Identification literature deal solely with optimal input design. In the physical literature, however, the degrees-of-freedom in the experiment set-up are optimised. In this thesis, we generalised the LCED

framework to simultaneously optimise the input signal and such degrees of freedom. Examples of the latter are input and output measurement locations, and inlet and outlet volumes in a Pressure Oscillation experiment (see Chapter 7). To this end, we have introduced in Chapter 6 an efficient algorithm to compute the optimal input and degrees of freedom for structured systems. It can be applied to discrete-time systems arising from Ordinary Differential Equations, as well as continuous-time linear Partial Differential Equations with constant coefficients. We have in particular studied diffusion-advection-reaction processes.

### Minimum Experiment Time Algorithm

We have introduced in Chapter 8 a novel algorithm, called the Minimal Experiment Time (MET) algorithm, that computes the solution of an optimisation problem first formulated by Ebadat et al. (2014b): minimise the experiment time subject to constraints on parameter accuracies and input and output amplitude constraints. However, we solved this optimisation problem by designing the amplitudes and phases of a multi-sine input signal containing fixed frequencies. The MET algorithm is applicable to (un)structured systems in open and closed loop, and can cope with the general case of multiple parameter accuracy constraints (contrary to the existing methods).

It utilises the Guillaume-Manchester algorithm and generalises a method introduced by Manchester (2009). It is applicable to (discrete- or continuous-time) open- and closed-loop systems. This new formulation is better suited to real-life problems, in the sense that input and output amplitude constraints are taken into account; the classical LCED problem does not. On the other hand, the LCED problem in Chapter 3 is convex, whereas the novel algorithm is not. Nonetheless, for many different types of systems experiment lengths have been obtained that are at least 40% shorter than when scaling the classical LCED solutions to satisfy input and output constraints. This mainly stems from the fact that the new method optimises the phases of the multi-sine harmonics, compressing the overall input or output amplitude (i.e. the crest of the input or output signal).

### Optimal Input Signal Construction for Pressure Oscillation Experiments

Chapter 7 focusses on the application of experiment design to Pressure Oscillation experiments. The goal of such an experiment is to estimate the permeability and/or porosity value(s) of a core sample obtained from e.g. an underground oil reservoir. Such estimates can then e.g. be used to calibrate computer reservoir models. Accurate estimates are therefore crucial. However, in the literature, it is mentioned that obtaining such estimates is difficult.

In this thesis, we show how to optimally design the input signal and degrees-of-freedom of the set-up used in Pressure Oscillation experiments. We developed an algorithm that finds the minimal experiment time while nonetheless satisfying a-priori set parameter accuracy constraints and input amplitude bounds. In particular, we compared two input-output measurement configurations, and found that one delivers much shorter experiment times under the same constraints. This result traces back to an identifiability issue in one of the measurement configurations.

## 9.2   Recommendations for future research

### Linear Partial Differential Equations with Spatially-Dependent Coefficients

In this thesis Distributed Parameter Systems governed by linear PDEs with spatially-independent coefficients have been considered. It will be interesting to generalise the theory to systems governed by linear PDEs in which the coefficients are spatially dependent. In this case, single-input single-output systems no longer suffice to estimate all physical parameters as identifiability issues arise. Instead, multiple-input multiple-output or single-input multiple-output systems should be considered.

### Pressure Oscillation Experiments on a Real Set-Up

The theoretical and numerical results in Chapter 7 on Pressure Oscillation experiments should be validated in practice on an actual experiment set-up. Since there is in principle no limitation on the number of Pressure Oscillation experiments that can be performed in a lab, one can easily test the theoretical results from this thesis. This would be a safe environment to test the potential of experiment design on a relevant real-life problem.

### Networks and MIMO Systems

The ability to extend Experiment Design to networks and MIMO systems is a difficult but important step. Currently, the majority of the literature considers SISO systems, although some work has been done on MIMO systems (Barenthin et al. (2008)). Theoretical analysis and software to compute optimal input signals in a MIMO or network setting are needed to push the field of Experiment Design forward. Furthermore, using Stealth Identification for identification in networks can be very useful as the number of unknown parameters that need to be estimated can then be drastically reduced. Indeed, by adding the Stealth component to the closed loop, all the feedback from the output to the input signal need not be known. In other words, the unknown parameters in the feedback transfer functions do not need to be estimated. This can lead to e.g. much shorter experiment lengths or less powerful excitation signals.

In this thesis it has been shown that the Direct and Indirect Identification Methods can lead to entirely different inverse covariance matrices. As a consequence, the required experiment length between these two methods can differ drastically under the same parameter accuracy constraints (see Chapter 7). In networks the freedom to select the input and output for identification is in principle enormous.

Suppose a particular transfer function $G(z, \theta_0)$ has to be identified in the network with minimum cost, using Experiment Design. Then the following steps can be considered:

1. Identify all input-output combinations that lead to a consistent estimate of $\theta_0$

2. Formulate the LCED optimisation problem for each combination and compute the optimal input signals

3. Select the best solution from the set of solutions

It would be interesting to test these steps on a simple network and see how much the experiment costs can differ when using different input-output combinations. To compute all these spectra in a reasonable time, the current numerical codes need to be optimised as much as possible.

**Linear Parameter Varying Systems**

In this thesis linear systems have been considered. Extending the Experiment Design method to nonlinear systems is a difficult step. As an intermediate step, research into Experiment Design in Linear Parameter Varying Systems should be considered. This brings the field into an entirely new domain and many physical systems can then also be analysed. It would be very interesting to generalise the Stealth and Sensitivity method to such systems, both for structured and unstructured systems.

# Bibliography

Aoun, M., Malti, R., Levron, F., and Oustaloup, A. (2004). Numerical simulations of fractional systems: An overview of existing methods and improvements. *Nonlinear Dynamics*, 38:117–131.

Barenthin, M., Bombois, X., Hjalmarsson, H., and Scorletti, G. (2008). Identification for control of multivariable systems: controller validation and experiment design via LMIs. *Automatica*, 44(12):3070–3078.

Bernabé, M. and Evans, B. (2006). A note on the oscillating flow method for measuring rock permeability. *International Journal of Rock Mechanics and Mining Sciences*, 43:311–316.

Boitnott, G. (1997). Use of complex pore transients to measure permeability of rocks. In *SPE Annual Technical Conference and Exhibition*, pages 37–45, San Antonio, Texas, US.

Bombois, X., den Dekker, A., Rojas, C., Hjalmarsson, H., and Van den Hof, P. (2011). Optimal experiment design for hypothesis testing applied to functional magnetic resonance imaging. In *18$^{th}$ IFAC World Congress, Milano, Italy*, pages 9953–9958, Milan,Italy.

Bombois, X. and Scorletti, G. (2012). Design of least-costly identification experiments - the main philosophy accompanied by illustrative examples. *Journal Europeen des Systems Automatises*, 46(6):587–610.

Bombois, X., Scorletti, G., den Hof, P. V., and Gevers, M. (2004). Least costly identification experiment for control. A solution based on a high-order model approximation. In *Proc. American Control Conference, Boston*, pages 2818–2823, Boston, US.

Bombois, X., Scorletti, G., Van den Hof, P., and Hilderbrand, R. (2006). Least-costly identification experiment for control. *Automatica*, 42:1651–1662.

Boyd, S. and Grant, M. (2013). Cvx: Matlab software for disciplined convex programming.

Boyd, S. and Vandenberghe, L. (2003). *Convex Optimization*. Cambridge University Press.

Cardiff, M., Bakhos, T., Kitanidis, P., and Barrash, W. (2013). Aquifer heterogeneity characterisation with oscillatory pumping: Sensitivity analysis and imaging potential. *Water Resources Research*, 49:5395–5410.

Crank, J. and Nicolson, P. (1947). A practical method for numerical evaluation of solutions of partial differential equations of the heat conduction type. *Proc. Camb. Phil. Soc.*, 43(1):50–67.

Dankers, A. (2014). *System Identification in Dynamical Networks*. PhD thesis, Delft University of Technology.

Ebadat, A., Valenzuela, P., Rojas, C., Hjalmarsson, H., and Wahlberg, B. (2014a). Applications oriented input design for closed-loop system identification: a graph-theory approach. In *53rd IEEE Annual Conference on Decision and Control (CDC)*, pages 4125–4130, Los Angeles, US.

Ebadat, A., Wahlberg, B., Hjalmarsson, H., Rojas, C., Hägg, P., and Larsson, C. (2014b). Applications oriented input design in time-domain through cyclic methods. In *In $19^{th}$ IFAC World Congress*, Cape Town, South Africa.

Emery, A. and Nenarokomov, A. (1998). Optimal experiment design. *Meas. Sci. Technol.*, 9:864–876.

Eykhoff, P. (1974). *System Identification - Parameter and System Estimation*. John Wiley and Sons, New York.

Federov, V. (1972). *Theory of Optimal Experiments*. Academic Press.

Ferreres, G. and Fromion, V. (1997). Computation of the robustness margin with the skewed $\mu$-tool. *System Control Letters*, 32:193–202.

Fischer, G. (1992). The determination of permeability and storage capacity: Pore pressure oscillation method. *International Geophysics Series*, 51:187–211.

Forgione, M., Bombois, X., and Van den Hof, P. (2013). Experiment design for batch-to-batch model-based learning control. In *Proceedings of the 2013 American Control Conference*, pages 3918–3923, Washington, DC, US.

Fromion, V. and Scorletti, G. (2002). Performance and robustness analysis of nonlinear closed loop systems using $\mu_{nl}$ analysis: Applications to nonlinear pi controllers. In *Proceedings of the 41st IEEE Conference on Decision and Control*, pages 2480–2485, Las Vegas, Nevada, US.

Gabano, J.-D. and Poinot, T. (2009). Fractional modelling applied to heat conductivity and diffusivity estimation. *Physica Scripta*, 136.

Gabano, J.-D. and Poinot, T. (2011). Fractional modelling and identification of thermal systems. *Signal Processing*, 91:531–541.

Gerencsèr, L., Hjalmarsson, H., and Mårtensson, J. (2009). Identification of arxx systems with non-stationary inputs - asymptotic analysis with applications to adaptive input design. *Automatica*, 45:623–633.

Gergonne, J. (1974). The application of the method of least squares to the interpolation of sequences. *Historica Mathematica*, 1(4):439–447.

Goodwin, G. and Payne, R. (1977). *Dynamic System Identification: Experiment Design and Data Analysis*. Academic Press.

Guillaume, P., Schoukens, J., Pintelon, R., and Kollar, I. (1991). Crest-factor minimization using nonlinear chebyshev approximation methods. *IEEE Transactions on Instrumentation and Measurement*, 40(6):982–989.

Hasanov, A. and Batzle, M. (2013). Pore pressure pulsing effects on reservoir transport properties. In *Second International Workshop on Rock Physics*, pages 2866–2872, Houston, TX, USA.

Haug, E., Choi, K., and Komkov, V. (1986). *Design Sensitivity Analysis of Structured Systems*. Academic Press.

Heller, K., Bruining, H., and Smeulders, D. (2002). Permeability obtained from pressure oscillation experiments, part i, one phase flow. *Computational Methods in Water Resources*, 47:201–207.

Hjalmarsson, H. (2005). From experiment design to closed-loop control. *Automatica*, 41(3):393–438.

Hjalmarsson, H. (2009). System identification of complex and structured systems. 3:275–310.

Jansen, J. (2013). *A Systems Description of Flow Through Porous Media*. Springer.

Jansson, H. and Hjalmarsson, H. (2005). Input design via LMIs admitting frequency-wise model specifications in confidence regions. *IEEE Transactions on Automatic Control*, 50(10):1534–1549.

Javaherian, H. (1974). Optimal input experiment design for parameter estimation. Master's thesis, Dept. of Computing and Control, Imperial College, London.

Karlin, S. and Studden, W. (1966). Optimal experimental designs. *Ann. Math. Stat.*, 37:783–815.

Kiefer, J. (1959). Optimal experimental designs. *J. Royal Stat. Soc. B21*, pages 272–319.

Kiefer, J. (1961). Optimum designs in regression problems, ii. *Ann. Math. Stat.*, 32:298–325.

Kiefer, J. and Wolfowitz, J. (1959). Optimum designs in regression problems. *Ann. Math. Stat.*, 30:271–294.

Kiefer, J. and Wolfowitz, J. (1960). The equivalence of two extremum problems. *Canadian Journal of Mathematics*, 12:363–366.

Kranz, R., Saltzman, J., and Blacic, J. (1990). Hydraulic diffusivity measurements on laboratory rock samples using an oscillating pore pressure method. *International Journal of Rock Mechanics and Mining Sciences & Geomechanics Abstracts*, 27:345–352.

Larsson, C. (2014). *Applications-oriented Experiment Design for Industrial Model Predictive Control*. PhD thesis, KTH Royal Institute of Technology.

Larsson, C., Annergren, M., Hjalmarsson, H., Rojas, C., Bombois, X., Mesbah, A., and Modén, P. (2013). Model predictive control with integrated experiment design for OE systems. In *Proceedings of the 2013 European Control Conference*, pages 3790–3795, Zürich, Switzerland.

Larsson, C., Rojas, C., and Hjalmarsson, H. (2011). Mpc oriented experiment design. In *Proceedings of the 18$^{th}$ IFAC World Congress*, Milan,Italy.

Levadi, V. (1966). Design of input signals for parameter estimation. *IEEE Transactions AC-11*, 2:205–211.

Levin, M. (1960). Optimal estimation of impulse response in the presence of noise. *IRE Transactions on Circuity Theory*, pages 50–56.

Ljung, L. (1971). Characterization of the concept of 'persistently exciting' in the frequency domain. Report 7119, Div. of Automatic Control, Lund Inst. of Teechnology.

Ljung, L. (1978). Convergence analysis of parametric identification methods. *IEEE Transactions on Automatic Control*, 23(5):770–783.

Ljung, L. (1985). Asymptotic variance expressions for identified black-box transfer function models. *IEEE Transactions on Automatic Control*, 30(9):834–844.

Ljung, L. (1999). *System Identification: Theory for the User*. Prentice Hall.

Ljung, L. (2008). Perspectives on system identification. In *In Plenary talk at the proceedings of the 17th IFAC World Congress, Seoul, South Korea*.

Maciejowski, J. (2002). *Predictive Control with Constraints*. Pearson - Prentice Hall.

Malti, R., Abrashov, S., Moze, M., and Moreau, X. (2014). Experiment design in system identification using fractional models. In *International Conference on Fractional Differentiation and Its Applications*, pages 1–7, Catania, Spain.

Manchester, I. (2009). An algorithm for amplitude-constrained input design for system identification. In *Proceedings of the 48$^{th}$ IEEE Conference on Decision and Control*, pages 1551–1556, Shanghai, China.

Manchester, I. (2010). Input design for system identification via convex relaxation. In *49th IEEE Conference on Decision and Control (CDC)*, pages 2041–2046, Atlanta, GA, US.

Manchester, I. (2012). Amplitude-constrained input design: Convex relaxation and application to clinical neurology. In *16$^{th}$ IFAC Symposium on System Identification, Brussels, Belgium*.

Mansoori, M., Dankers, A., and Van den Hof, P. (2014). Errors-in-variables identification in bilaterally coupled systems with application to oil well testing. In *accepted in the Proceedings of the* 19$^{th}$ *IFAC World Congress*, Cape Town, South Africa.

Mansoori, M., Van den Hof, P., Jansen, J., and Rashtchian, D. (2015). Pressure transient analysis of bottomhole pressure rate measurements using system identification techniques. *SPE Journal*, 20(5):1005–1027.

Mehra, R. (1973). Frequency domain synthesis of optimal inputs for parameter estimation. Report 645, Div. of Eng. and Appl. Physics, Harvard University.

Mehra, R. (1974a). Synthesis of optimal inputs for mimo systems with process noise. Report 649, Div. of Eng. and Appl. Physics, Harvard University.

Mehra, R. K. (1974b). Optimal input signals for parameter estimation in dynamic systems - survey and new results. *IEEE Transactions on Automatic Control*, 19(6):753–768.

Payne, R. and Goodwin, G. (1974). Simplification of frequency domain experiment design for siso systems. Technical report, Dept. of Computing and Control, Imperial College, London.

Pierce, C. (1876). Note on the theory of the economy of research. *Coast Survery Report*, pages 197–201.

Pintelon, R. and Schoukens, J. (2001). *System Identification: A Frequency Domain Approach*. IEEE Press.

Pintelon, R., Schoukens, J., Pauwels, L., and Van Gheem, E. (2005). Diffusion systems: Stability, modeling, and identification. *IEEE Transactions on Instrumentation and Measurement*, 54(5):2061–2067.

Poinot, T. and Trigeassou, J. (2003). A method for modelling and simulation of fractional systems. *Signal Processing*, 83:2319–2333.

Poinot, T., Trigeassou, J., and Lin, J. (2002). Parameter estimation of fractional models: application to modeling of diffusive systems. In 15$^{th}$ *Triennial World Congress*, pages 462–468, Barcelona, Spain.

Potters, M., Bombois, X., Mansoori, M., and Van den Hof, P. (2016a). Estimating parameters with pre-specified accuracies in distributed parameter systems. *International Journal of Control*, 89(6):1–21.

Potters, M., Bombois, X., and Van den Hof, P. (2016b). Experiment time minimisation under parameter accuracy constraints and time-domain signal amplitude bounds. *accepted to European Control Conference 2016*.

Potters, M., Forgione, M., Bombois, X., Hjalmarsson, H., Modén, P., Lundh, M., and Van den Hof, P. (2014). Optimal experiment design in closed loop with unknown, nonlinear or implicit controllers using stealth identification. In *Proceedings of the 2014 European Control Conference, Strasbourg, France*, pages 726–731, Strasbourg, France.

Potters, M., Forgione, M., Bombois, X., and Van den Hof, P. (2015). Least-costly experiment design for uni-parametric linear models: An analytical approach. In *Proceedings of the 2015 European Control Conference*, pages 848–853, Linz, Austria.

Potters, M., Mansoori, M., Bombois, X., Jansen, J., and Van den Hof, P. (2016c). Optimal input experiment design for parameter estimation in core-scale pressure oscillation experiments. *Journal of Hydrology*, 534(3):534–552.

Rensfelt, A., Mousavi, S., Mossberg, M., and Söderström, T. (2008). Optimal sensor locations for nonparametric identification of viscoelastic materials. *Automatica*, 44:28–38.

Schorsch, J., Garnier, H., Gilson, M., and Young, P. (2013). Instrumental variable methods for identifying partial differential equation models. *International Journal of Control*, 86(12):2325–2335.

Söderström, T. (2007). Errors-in-variables methods in system identification. *Automatica*, 43(939–958).

Söderström, T. and Stoica, P. (1989). *System Identification*. Prentice Hall.

Söderström, T., Wang, L., Pintelon, R., and Schoukens, J. (2013). Can errors-in-variables systems be identified from closed-loop experiments. *Automatica*, 49:681–684.

Song, I. and Renner, J. (2007). Analysis of oscillatory fluid flow through rock samples. *International Journal of Geophysics*, 170:195–204.

St John, R. and Draper, N. (1975). D-optimality for regression designs. *Technometrics*, 17(1):15–23.

Suri, P., Azeemuddin, M., Zaman, M., Kukreti, A., and Roegiers, J.-C. (1997). Stress-dependent permeability measurements using the oscillating pulse technique. *Journal of Petroleum Science and Engineering*, 17:247–264.

Thomas, L. (1949). Elliptic problems in lienar differential equations over a network. Technical report, Watson Sci. Comput. Lab Report, Columbia University.

Uciński, D. (2004). *Optimal Measurement Methods for Distributed Parameter System Identification*. CRC Press.

Van den Hof, P., Dankers, A., Heuberger, P., and Bombois, X. (2013). Identification of dynamic models in complex networks with prediction error methods - basic methods for consistent module estimates. *Automatica*, 49(10):2994–3006.

Van den Hof, P. and Schrama, R. (1993). Indirect method for transfer function estimation from closed loop data. *Automatica*, 29(6):1523–1527.

Wagner, H. (1997). Experiment design for estimating parameters of rate-limited mass transfer: Analysis of stream tracer studies. *Water Resources Research*, 33(7):1731–1741.

Wahlberg, B., Annergren, M., and Rojas, C. (2011). On optimal input signal design for identification of output error models. In *50th IEEE Conference on Decision and Control, Orlando, FL, USA*, pages 5118–5124, Orlando, FL, USA.

Walter, E. and Pronzato, L. (1997). *Identification Of Parametric Models from Experimental Data*. Springer.

Wang, Y. and Knabe, R. (2011). Permeability characterisation on tight gas samples using pore pressure oscillation method. *Petrophysics*, 52:437–433.

Whittle, P. (1973). Some general points in the theory of optimal experiment design. *Journal Royal Stat. Soc. B35*, (123–130).

Yeh, W. (1986). Review of parameter identification procedures in groundwater hydrology: The inverse problem. *Water Resources Research*, 22(2):96–18.

Zarrop, M. (1979). *Optimal Experiment Design for Dynamic System Identification*. Springer Verlag, New York.

# Summary

**Experiment Design for Identification of Structured Linear Systems**

M.G. Potters

**E**xperiment Design for system identification involves the design of an optimal input signal with the purpose of accurately estimating unknown parameters in a system. Specifically, in the Least-Costly Experiment Design (LCED) framework, the optimal input signal results from an optimisation problem in which a weighted input power (the cost) is minimised subject to parameter accuracy constraints. In this particular formulation, the problem is convex and can be solved with efficient numerical tools. The LCED framework, however, has the following limitations: (i) no interpretation follows from its numerical solutions, (ii) it can not be applied to systems with unknown or nonlinear controllers, (iii) it cannot be applied in full generality to structured (physical) systems, and (iv) the problem formulation has so far mainly considered input power as the cost, whereas other possibilities exist. In this thesis these four limitations are addressed.

Firstly, we calculate analytical solutions for a class of LCED problems for models with one or two parameters. For uni-parametric models we have proven that the solution is always a single sinusoid, whereas for bi-parametric models we have provided arguments that a single sinusoid is often the solution. From our theoretical analysis we also, at a formal level, classify the LCED problems as generalised and weighted dual E-optimality problems.

Secondly, we introduce Stealth and Sensitivity methods that enable the applicability of the LCED framework to structured and unstructured systems regulated by unknown or nonlinear controllers. The requirement of an explicit and known expression of the sensitivity function, necessary to solve the LCED problems, is circumvented with the above two novel methods. The Stealth method adapts the classical Direct Identification scheme such that the controller does not sense the excitation signal, reducing the sensitivity function to unity. The Sensitivity method, instead, relies on the usual Direct Identification scheme and finds an approximation of the sensitivity function. Three numerical studies show the strength of both methods.

Thirdly, we generalise the LCED framework such that it can be applied to structured systems governed by linear partial differential equations with constant coefficients. We use a systematic approach to simulate such systems using harmonic signals, which in turn are designed by the LCED framework. Issues such as stability and scaling will be formally addressed. Since structured systems are concomitant with degrees of freedom in the experiment set-up, we also develop a progressive subdivision algorithm that can efficiently solve the corresponding LCED problems.

Fourthly, we introduce the novel Minimum Experiment Time (MET) algorithm that, by designing an optimal harmonic input signal, solves an optimisation problem formulated by Ebadat et al. (2014b): minimise the experiment time subject to parameter accuracy constraints and amplitude bounds on the input and output signal. The MET algorithm is applicable to systems that are in open or closed loop, and is relevant for many industrial processes. It can also deal with multiple accuracy constraints, in contrast to traditional methods. We show with several examples that optimal experiment times can be achieved that are up to 50% shorter compared with the solutions of the classical LCED framework.

Finally, using the above methods, we address an important problem in petrophysics: the estimation of permeability and porosity values of a porous rock sample using Pressure Oscillation experiments. We show how to design the optimal input spectrum and inlet and outlet volumes of the experiment set-up such that the experiment time is minimised, while respecting parameter accuracy and actuator constraints. Furthermore, we design such signals for the Direct and Indirect identification methods. We show that identifiability issues can arise with the former method. The latter method has no such issues. Consequently, the Indirect method delivers optimal experiment times that are a factor fourteen shorter compared with those of the Direct Method.

# Samenvatting

## Experiment Ontwerp voor de Identificatie van Gestructureerde Lineaire Systemen

M.G. Potters

Experiment ontwerp voor systeemidentificatie bestaat uit het ontwerpen van een optimaal ingangssignaal met als doel het nauwkeurig schatten van onbekende parameters van een systeem. In het zgn. *Least-Costly Experiment Design* (LCED) raamwerk volgt het optimale ingangssignaal uit een optimalisatieprobleem waarin een gewogen vermogen van het ingangssignaal wordt geminimaliseerd onder kwaliteitsvoorwaarden op de parameterschattingen. Met deze formulering is het optimalisatieprobleem met convexe numerieke methodes op te lossen. Het LCED raamwerk kent echter de volgende beperkingen: (i) de numerieke oplossingen hebben geen fysische interpretatie, (ii) het kan niet worden toegepast op systemen met onbekende en niet-lineaire regelaars, (iii) het kan niet worden toegepast op generieke gestructureerde (fysische) systemen, en (iv) de te minimaliseren functie in het LCED optimalisatieprobleem is tot nu toe met name gedefinieerd als een gewogen vermogen van het ingangssignaal, terwijl andere functies betere alternatieven kunnen zijn. Dit proefschrift behandelt de vier bovenstaande beperkingen.

Ten eerste worden in dit proefschrift analytische oplossingen berekend voor een klasse van LCED problemen met één of twee onbekende parameters. Voor het eerste type model bewijzen we dat de oplossing altijd gegeven is door een enkele sinus, terwijl voor het tweede type dit niet altijd het geval is. De theoretische analyse heeft ook geleid tot de formele classificering van het LCED probleem: het is een duaal van een gegeneraliseerde en gewogen $E$-optimaliteit probleem.

Ten tweede zijn er de *Stealth* en *Sensitivity* methodes ontwikkeld die het toepassen van het LCED raamwerk op systemen met onbekende of niet-lineaire regelaars mogelijk maakt. De voorwaarde van het kennen van een expliciete en bekende uitdrukking van de *sensitivity function*, benodigd voor het oplossen van de LCED problemen, wordt omzeild met de twee nieuwe methodes. De *Stealth* methode past de klassieke Directe Identificatie methode zodanig aan dat de regelaar het excitatie signaal niet opmerkt, waardoor de *sensitivity function* effectief gelijk is aan één. De *Sensitivity* methode, daarentegen, maakt gebruik van de klassieke Directe Identificatie methode om de *sensitivity function* te schat-

ten. Drie numerieke studies tonen de kracht van beide methodes aan.

Ten derde wordt het LCED raamwerk gegeneraliseerd zodat het toegepast kan worden op gestructureerde systemen gedreven door lineaire partiële differentiaalvergelijkingen met constante coëfficiënten. Met een systematische aanpak simuleren we dit type systemen door gebruik te maken van een som van een harmonische functies, welke optimaal ontworpen worden in het LCED raamwerk. Stabiliteit en schaling worden formeel aangepakt. Doordat gestructureerde systemen voorkomen in samenhang met vrijheidsgraden in de experimentele opstelling, is in dit proefschrift een progressief onderverdelingsalgoritme ontwikkeld dat de bijbehorende LCED problemen efficiënt kan oplossen.

Ten vierde bevat dit proefschrift het nieuwe Minimale Experiment Tijd (MET) algoritme dat, door middel van het ontwerpen van een optimale som van harmonische functies, het volgende optimalisatie probleem (zoals geformuleerd in (Ebadat et al. (2014b))) oplost: minimaliseer de experimenttijd onder beperkingen op de kwaliteit van de parameter schattingen en het systeem. Het MET algoritme is toepasbaar op (on)gestructureerde open- en gesloten-lus systemen, en is relevant voor veel industriële processen. Het kan tevens meerdere beperkingen op de kwaliteit van parameterschattingen aan, in tegenstelling tot eerder gepubliceerde methodes. Verschillende voorbeelden tonen aan dat optimale experimenteertijden bereikt kunnen worden die tot 50% korter zijn dan de oplossingen die volgen uit het klassieke LCED raamwerk.

Tenslotte passen we enkele van de bovenstaande nieuwe methodes toe om een belangrijk probleem in petrofysica op te lossen. Het betreft het schatten van de permeabiliteit en porositeit van een poreus monster door middel van Druk-Inducerende experimenten. In dit proefschrift minimaliseren we de tijd van dit experiment onder kwaliteitsvoorwaarden van de parameterschattingen door het berekenen van het optimale ingangssignaal, alsook de optimale inlaat en uitlaat volumes van de experimentele opzet. Deze optimale signalen en volumes worden uitgerekend voor de Directe en Indirecte identificatie methodes. Er wordt bewezen dat identificeerbaarheid een probleem is voor de eerste methode. De tweede methode heeft dit probleem niet. De optimale experimenteertijden voor de tweede methode zijn hierdoor een factor veertien korter ten opzichte van de eerste methode.

# Curriculum Vitae



Max Potters was born on December 28 1987 in Wijk bij Duurstede, The Netherlands. He obtained his B.Sc. degree in Physics and Astronomy, and his M.Sc. degrees in Physics and Mathematics at University of Utrecht in The Netherlands. His M.Sc. project involved statistical predictions and simulations of long-lived large-scale structures in two-dimensional Eulerian flows and Shallow Water flows under the supervision of Prof. Freddy Bouchet at École Normale Supérieure de Lyon, and Prof. Henk Dijkstra and Dr. Heinz Hanßmann at University of Utrecht. For this work he was awarded the *Vliegenthart Scriptieprijs* in 2012, for writing the best thesis in all beta sciences in that year.

In January 2012 he started his Ph.D. at Delft Centre for Systems and Control, and worked on Optimal Experiment Design methods under the supervision of Prof.dr.ir. Paul Van den Hof and Prof.dr.ir. Xavier Bombois. His research focused on providing insight and analytical solutions to optimization problems, generalising current methods to be applicable to more closed-loop systems, and applying the method to distributed parameter systems. During his Ph.D. he was nominated for *Best Presenter* at the 2015 Benelux Meeting.

His main research interests are statistical mechanics, geophysical flows, and optimal experiment design.